Università
degli Studi
di Ferrara

DOCTORAL COURSE IN
PHYSICS

CYCLE XXXIV

COORDINATOR Prof.ssa Eleonora Luppi

Investigating Cosmology with angular power spectra from small to large scales

Scientific/Disciplinary (SDS) FIS/02

Candidate
Caterina Chiocchetta

Supervisor
Dr. Luca Pagano

Supervisor
Dr. Mattia Negrello

Years 2018-2021

Università
degli Studi
di Ferrara

DOCTORAL COURSE IN
PHYSICS

CYCLE XXXIV

COORDINATOR Prof.ssa Eleonora Luppi

Investigating Cosmology with angular power spectra from small to large scales

Scientific/Disciplinary (SDS) FIS/02

Candidate
Caterina Chiocchetta

Supervisor
Dr. Luca Pagano

Supervisor
Dr. Mattia Negrello

Years 2018-2021

Non ti fidar di me se il cuor ti manca

Abstract

Among the most promising topics in Cosmological investigation we can certainly consider the polarization of the Cosmic Microwave Background (CMB) and the multiwavelenght analysis of extragalactic emissions. On one side, CMB polarization allows to better constrain the cosmological parameters and to test the standard model. On the other side, the study of millimeter and submillimeter data opens the door for investigation of the matter distribution on large scales in order to understand the formation and evolution of the Large Scale Structure. After a brief review of the Standard Model and the theory of cosmological perturbation (first and second chapter), this thesis focuses on the study of the large scale Cosmic Microwave Background anomalies in polarization (third chapter) and on the distribution of galaxies within dark matter halos, through the analysis of millimeter and submillimeter data (fourth chapter).

In the first project described in this thesis we present an assessment of the large-scale CMB anomalies in polarisation using the two-point correlation function as a test case. We employ the state of the art of large scale polarisation datasets: the first based on a *Planck* 2018 HFI 100 and 143 GHz cross-spectrum analysis, based on `SRoll2` processing, and the second from a map-based approach derived through a joint treatment of *Planck* 2018 LFI and WMAP-9yr. We consider the well-known $S_{1/2}$ estimator, which measures the distance of the two-point correlation function from zero at angular scales larger than 60°, and rely on realistic simulations for both datasets to assess confidence intervals. By focusing on the pure polarisation field described by either the Q and U Stokes parameters or by the local $E-$modes, we show that the first description is heavily influenced by the quadrupole (which is poorly constrained in both datasets) while the second one is more suited for an analysis containing higher multipoles up to $\ell \sim 10$, limit above which both datasets become markedly noise dominated. We find that

both datasets exhibit a lack-of-correlation anomaly in local $E-$modes, similar to the one observed in temperature, which is better constrained by the less noisy *Planck* HFI 100×143 data, where its significance lies at about 99.5%. We perform our analysis using realizations that are either constrained or non-constrained by the observed temperature field, and find similar results in the two cases. The analysis has been carried out with the best datasets currently available at large angular scales, which are however limited by the still significant amount of noise in polarisation observations. This issue will be hopefully overcome by the advent of new data, such as those from LiteBIRD, which are expected to be cosmic variance limited at all scales. The prospect to perform this analysis in the context of future experiments is then attractive, in order to shed light on the presence of the lack-of-power anomaly in CMB polarization.

In the second project presented we developed a tool for data analysis designed for the millimeter and sub-millimeter wavelength datasets. We fit with a unique model data from the South Pole Telescope and the Hershel/SPIRE experiment. Our formalism describes the emission of radio galaxies, the thermal Sunyaev Zeldovich (tSZ) effect, the kinetic Sunyaev Zeldovich (kSZ) effect and the Cosmic Infrared Background (CIB) clustered and Poisson contribution. We use a halo model approach to describe the clustering of dark matter together with a halo occupation distribution model to parametrize the galaxy power spectrum. We fit for the so-called clustering parameters, i.e. minimum mass of the hosting halo and the index regulating the accretion of galaxies in the halo outskirts. We consider two populations of galaxies: early and late-type populations. The former experienced the phase of star formation at redshift larger than 1.5 and now is passively evolving, while the second is star-forming at low redshift. We use a halo formalism also for the tSZ effect and for its correlation with the CIB clustering. The key parameter in modelling the tSZ is the hydrostatic mass bias, which strongly depends on cosmology and contains all the uncertainties we have in the determination of the SZ clusters mass. Our code has been validated with two tools already available online and it is flexible in order to fit for next generation datasets and to vary cosmological parameters. With our analysis we improved the constraints on the clustering parameters of the late-type population, confirming that it is hosted in less massive structures with respect to the early-type one. We find a minimum mass of $10^{12.5}[M_{\odot}h^{-1}]$ and $10^{11.4}[M_{\odot}h^{-1}]$ for the early and late-type population respectively, when fitting for SPIRE data. We find a minimum mass of $10^{12.1}[M_{\odot}h^{-1}]$ and $10^{10.8}[M_{\odot}h^{-1}]$ for the early and late-type population respectively, when fitting for SPT data. For both datasets we find values of the hydrostatic mass bias, $b = 0.57 \pm 0.16$, higher than those found

by Planck, although the amplitude of the tSZ power spectrum obtained with this value of b is in line with the findings of previous SPT analysis. We also derive a more severe constraint on the amplitude of the kSZ with respect to previous literature, detecting it at 2σ level, and investigate its degeneracy with the tSZ-CIB correlation. These results are obtained using the state of the art data available but our tool will be of great utility in the analysis of future datasets, such as the Simons Observatory, CMB-Stage 4 and CONCERTO.

Contents

Introduction

The Standard Model of Cosmology relies on a theory proposed in the '20 and called Hot Big Bang. It assumed that Universe was very hot and dense at the beginning and gradually expanded and cooled with time. This theory predicted the existence of an homogeneus bath of photons permeating Universe in all directions. This bath was the relic of a primordial era, in which photons and baryons were in thermal equilibrium. Fourty years later, the discovery of Cosmic Microwave Background (CMB) was the proof of the reliability of this theory [1]. Since the measurement of the CMB black body distribution [2], this observable became one of the milestones of Cosmology. The theory also predicted the presence of small temperature anisotropies in the CMB photons spatial distribution, derived from perturbations in the primordial plasma. Also those anisotropies have been found by [3]. They allowed to constrain the parameters of the Standard Model, making Cosmology for the first time a precise science. On the other side, CMB represented a challenge for the Standard Cosmology, as it was homogeneus at scales larger than expected. This observational evidence brought to an extention of the Standard model, which has been enriched with a new primordial phase, called Inflation, able to explain homogeneity on scales larger than the horizon at CMB formation time. On WMAP data, however, there were other discrepancies with respect to the Standard model, which are still waiting for an explanation: they have taken the generic name of CMB *anomalies*. Their low statistical significance, between 2 and 3 σ, in addition to a possible instrumental origin, led the comunity to wonder if anomalies were real features in the microwave sky. More detailed informations arrived with the Planck satellite data release [4], which was cosmic variance limited at all angular scales in temperature. For this reason, Planck observations have been of great utility in improving the constraints on the cosmological parameters. Nevertheless, also Planck observed the CMB anomalies, almost at the same statistical significance of WMAP. This made an instrumental origin unlikely, even if not completely excluded. If we assume that CMB anomalies are real features in the sky, we can conclude to live in a mildy rare statistical fluctuation of the Standard Cosmology. The alternative, and for sure more intriguing, point of view is that, to explain these features, some modifications of the ΛCDM cosmology are required. As CMB temperature measurements are already cosmic variance limited at all scales, the information contained in the large angle tail of the anisotropy power spectrum has already been exausted. One way to bypass this problem is to extend the analysis to another observable, possibly correlated with CMB temperature. Luckily, CMB photons are slightly polarized. Polarization arises from the same primordial perturbations that originates temperature anisotropies, so the two observables are correlated. Planck observations can then be used to start the investigation of large angle anomalies in polarization. Nevertheless, Planck data in polarization are still really noisy, so, to give a definitive assessment on the presence of these features in polarization, we have to wait for next generation datasets. In particular we are waiting for data coming from the LiteBIRD satellite, recently approved by the JAXA (Japan Aerospace Exploration Agency), whose launch is expected in the next decade [5].

CMB observations, in addition to the analysis of the rotation curves of the galaxies, led to the idea that luminous matter was just a small fraction of the total amount of matter in the Universe. Consequently, the Standard Model has been extended with the introduction of a new component, of unknown nature, interacting only gravitationally with the other components of the Universe: the dark matter. A lot of studies try to understand what dark matter is made of, but we are still far from an answer. Something we now, in any case, is that dark matter tends to cluster and form giant structures growing with time. This knowledge has opened the door to another field of cosmological investigation: the study of Large Scale Structure. With the support of numerical simulations, astronomers developed an idea of how dark matter structures form and evolve. The tool used to describe the clustering of dark matter with redshift is called *halo model*. It is an analytical description of the matter distribution in the Universe, which assumes that all matter resides in separated units, called halos. To describe the matter distribution through a halo approach, we need three fundamental quatities: the halo bias, the halo mass function and the halo density profile. First, to properly relate the distribution of halos to the underlying density field, we have to consider that they are biased tracer of the background matter distribution, and introduce the so-called halo bias. Then, we have to describe the halos spatial distribution: for this purpose we use functions predicting the numbers of halos occupying a certain mass bin. These tools are called halo mass functions. To conclude the picture, we need to parametrize the distribution of matter within a specific halo, using a halo density profile. All these quantities evolve with redshift, and can then account for the evolution of dark matter structures. As we can not detect dark matter, to constrain our halo models we use data from visible matter, and try to relate the distribution of the astrophysical sources to that of dark matter. An incredible source of information in this sense is contained in millimeter and submillimeter data. They combine the CMB with several other emissions and effects: the Cosmic Infrared Background (CIB), the Sunyaev Zeldovich effect, the radio sources emission, the galactic cirrus. If we want to constrain the cosmological parameters, we have to clean maps from all emissions, or *foregrounds*, other from CMB primary anisotropies. The proper modelling of the foregrounds is then necessary in order to avoid the misleading of the cosmological parameters constraints. However, these emissions are *per se* full of information. The extragalactic (or in some case galactic) sources originating them are located in the potential wells of the dark matter halos and are then the visible tracers of the dark matter distribution.

The CIB is generated during the star formation phase of galaxies, when the high energy radiation emitted by the young stars is absorbed and re-emitted by the dust grains at lower frequencies. Unfortunately, while numerical simulations allowed a quite good comprehension of the dark halo structures, the relation with the dusty galaxies located within halos is still a matter of debate. We know that star formation is influenced by the mass and rotation of the hosting halo, but the connection beween the dark matter and the galaxy power spectrum remain unclear. The main models in literature are two: the oldest one [6], and all its variations [7], try to parametrize in an empirical way the number of galaxies that occupy an halo (*halo occupation distribution*) as function of the halo mass. The emission of those galaxies is then accounted for through the so-called *emissivity function*. The second model has been released more recently by [8] and try to directly relate the halo accretion to the star formation rate. Both models are still used in literature and, at the moment, none of them is clearly favoured by data.

The CIB is definitely the dominant contribution to millimeter and submillimeter data power spectrum, but not the only one. The y-type spectral distortion of the CMB black body distribution, caused by the thermal Sunyaev Zeldovich (tSZ) effect [9], is a tracer of matter distribution in massive local structures, i.e. the low redshift halos hosting galaxy clusters. Again, the tSZ effect is described by a

halo model, with some small difference with respect to the CIB case. First of all, in this case we do not need to model the galaxy emission, secondly, the halo density profile is replaced with the electron pressure profile. The CIB and the tSZ effect are correlated observable, so the modelling of their correlation is also required: we use for it a halo model and investigate its degeneration with the kinetic Sunyaev Zeldovich (kSZ) effect. Despite it is a subdominant contribution in the power spectra, the correct modelling of kSZ effect is fundamental, as it can give informations about the duration and timing of the Reionization epoch. The acquisition of data in these frequency ranges and the modelling of the different foregrounds contribution is one of the most active field in Cosmology nowadays. The most constraining datasets available have been released by the South Pole Telescope, in the millimeter, and by the Hershel/SPIRE, in the submillimeter. However, several experiments are going to be active in the next decade, for example the Simons Observatory [10], CMB-S4 [11] and CONCERTO [12].
This thesis is organized as follows:

- In the first two chapters we briefly review the basis of the Standard Cosmological model, with a description of the main energy-matter components, the phases of the cosmic history and some basic definitions. We then describe the origin and evolution of cosmological perturbations trough a simple treatment of the Inflation epoch and a study of the Boltzmann equations for photons and dark matter. We describe in detail the CMB power spectrum, both in temperature and polarization.

- In the third chapter we analyse the large scales of CMB power spectrum, investigating the large angle anomalies. We give the details of the context in which these features have been detected and studied. Then we describe the anomaly on which we focus, the so-called lack-of-power in CMB temperature correlation function, explaining why we decide to look for this feature also in polarization. We describe the dataset and methodology used and the results we obtain comparing the value of the correlation on simulations and on data for the Q and U stokes parameters and local E-modes. This work has been published on JCAP:

  - [13] Caterina Chiocchetta, Alessandro Gruppuso, Massimiliano Lattanzi, Paolo Natoli, Luca Pagano *"Lack-of-correlation anomaly in CMB large scale polarisation maps"*;

On the same topic, another work, which is not described in this thesis, is in preparation:
-In preparation *"LiteBird E-modes anomalies"*.

- In the fourth chapter we analyse data from the SPT and SPIRE in order to constrain the parameters of the model describing the foregrounds contributing to the data power spectrum. We describe in detail the halo model used for the CIB and the tSZ. We also explain the parametrization chosen for the kSZ, the radio sources and the galactic cirrus. Then we extensively discuss the result of the comparison between data and model, both at low and high frequencies.

  The code is available on GitHub `https://github.com/paganol/CIB_project`.

- In the conclusions we summarize the most important results of our work. We also give an overview of the experiments and surveys which will be active in the next decade and will be dedicated, on one side, to the measurements of CMB polarization, and, on the other side, to the acquisition of new millimeter data.

1

The Standard cosmological scenario

Cosmology has become a precise science in less than a hundred years. In the first chapter of this thesis we briefly review the main achievements of this century of investigations. We describe the basis of our Standard Cosmological model and the main phases of the cosmic history. We also outline the origin and evolution of cosmological perturbations trough a simple treatment of the Inflation epoch.

1.1 The Friedman-Lemaitre-Robertson-Walker Universe

The Standard Cosmological Scenario [14], [15], [16], [17] is based on the assumption that Universe is statistically homogeneus and isotropic at zero order. Such a Universe is described by the metric of Friedman-Lemaitre-Robertson-Walker (FLRW):

$$ds^2 = -(cdt)^2 + a^2(t)\left[\frac{dx^2}{1-Kx^2} + x^2(d\theta^2 + sin^2\theta d\phi^2)\right], \tag{1.1}$$

where θ, ϕ and x are spherical comoving coordinates and $a(t)$ is the scale factor, which regulates the dynamical evolution of the Universe. The factor K represents the curvature of the space-like hypersurfaces. The case $K = 0$ corresponds to a flat space with no curvature; $K = 1$ corresponds to a positive curvature, which implies a closed Universe, and $K = -1$ to a negative curvature, i.e. an open space. In the standard scenario the theory of gravity is based on the General Relativity. The metric enters in the left side of the field equation, which is related to the geometry of the space-time. On the right side of the field equation we find instead the energy-momentum tensor. Considering a FLRW metric and a Universe filled of a perfect fluid, we can find a set of analytical solutions to the field equations, called *Friedmann equations*:

$$\left(\frac{\dot{a}(t)}{a(t)}\right)^2 = \frac{8G\pi\rho}{3} - \frac{K}{a(t)^2}, \tag{1.2}$$

$$\frac{\ddot{a}(t)}{a(t)} = -\frac{4G\pi}{3}(\rho + 3P). \tag{1.3}$$

Here ρ and P are the density and pressure of the fluid that dominates the energy-density content of the Universe at a certain time. Defining the *Hubble parameter* as:

$$H(t) \equiv \left(\frac{\dot{a}}{a}\right), \tag{1.4}$$

one can compute the energy content in the case of a flat Universe, called *critical density*:

$$\rho_c = \frac{3H^2}{8\pi G}. \tag{1.5}$$

To derive the evolution of both $a(t)$, ρ and P, we need a relation between density and pressure, which is given by the equation of state:

$$\rho = wP. \tag{1.6}$$

The value of w depends on the fluid considered: $w = 1/3$ corresponds to a fluid of relativistic particles, hereafter denoted with the subscript r. In the case of massive particles, generically called *matter* and denoted with the letter m, $w = 0$. Observations suggest the presence of a third component filling the Universe, other than matter and radiation, which is referred to as dark energy and usually denoted by the letter Λ. It is driving the Universe accelerated expansion at the present time and it is characterized by negative pressure $w \sim -1$ (in the case of $w = -1$ it would take the name of Cosmological constant). Observations are also able to constrain the density parameter of these components, which is defined with respect to the critical density of the Universe:

$$\Omega_{0,m} = \rho_{0,m}/\rho_{0,c} \sim 0.27, \quad \Omega_{0,\Lambda} = \rho_{0,\Lambda}/\rho_{0,c} \sim 0.73, \quad \Omega_{0,r} = \rho_{0,r}/\rho_{0,c} \sim 10^{-5}. \tag{1.7}$$

Here $\Omega_{0,m}$, $\Omega_{0,r}$, $\Omega_{0,\Lambda}$ are the desntity parameters of matter, radiation and dark energy respectively. The picture that emerges is that of a Universe dominated by the dark energy, in which radiation occupies a small fraction of the energy density content, while matter constitutes almost one third of it. Until now we have generically used the term 'matter' for all the components that have an equation of state with $w = 0$. Nevertheless we know that there is a mismatch between the quantity of visible matter we can derive from observations and the total amount of matter inferred from gravity. The fraction of matter responsible for this mismatch is called dark matter and its nature is unkonwn. We only know that, at least a fraction of it, has to be non-baryonic matter, as deduced from the constraints placed on the baryonic matter from the primordial Nucleosynthesis. This process, which will be briefly described in section *1.3*, is responsible for the chemical abundances of the light elements in the Universe. Following these considerations, we can operate a further division in the energy content of the Universe, separating the contribution of the baryonic matter from that of dark matter:

$$\Omega_{0,DM} = \rho_{0,DM}/\rho_{0,c} \sim 0.23, \qquad \Omega_{0,b} = \rho_{0,b}/\rho_{0,c} \sim 0.04. \tag{1.8}$$

The matter content of the Universe is hence dominated by matter interacting only gravitationally, with a much smaller contribution coming from ordinary matter.

To trace the evolution of all the mentioned components through the cosmic history, we use the continuity equation:

$$\dot{\rho} = -3H(\rho + p). \tag{1.9}$$

Combining the equation of state (1.6) with the continuity equation (1.9) we can express the evolution of the energy-density parameter as function of the scale factor:

$$\rho \propto a^{-3(w+1)}. \tag{1.10}$$

Using this relation, we can then rewrite the first Friedmann equation as a relation between scale factor and time:

$$\frac{\dot{a}(t)}{a(t)} = H_0 \sqrt{\Omega_i} a_i^{-3/2(1+w_i)}, \tag{1.11}$$

where the subscript i denotes the considered component. We can then resume the behaviour of the three main constituens of the Universe during time as follows:

- relativistic matter $\rho \propto \; a^{-4}$ and $a \propto t^{\frac{1}{2}}$,
- non relativistic matter: $\rho \propto \; a^{-3}$ and $a \propto t^{\frac{2}{3}}$,
- dark energy: $\rho = const$ and $a \propto e^{Ht}$.

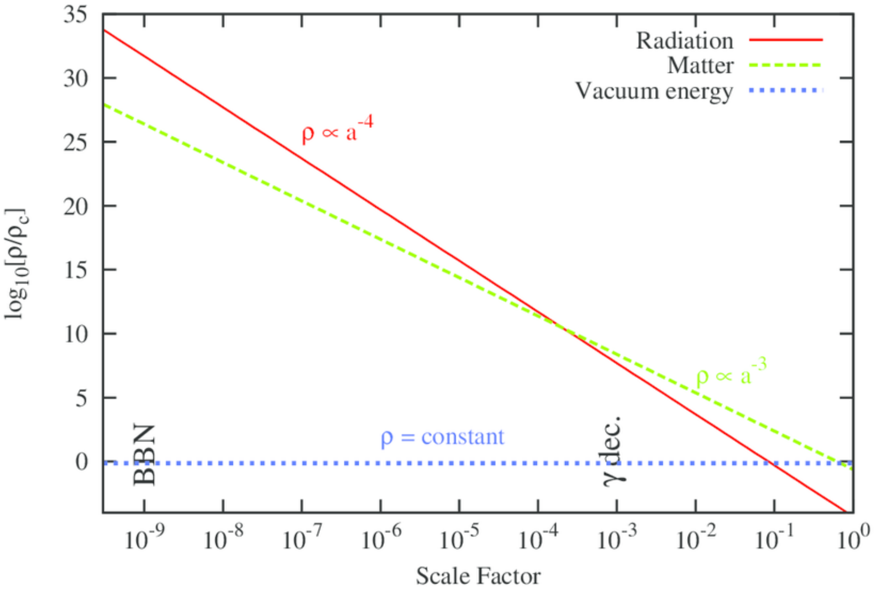

Figure 1.1: *Evolution of radiation, matter and dark energy density with the scale factor.*

A picture of the behaviour of these components is given in figure 1.1. It is clear how, going back in time, Universe becomes denser and hotter. In a finite time in the past, around 13.78 billion years ago, density diverged: this singularity is the well known Big Bang. The high temperature, and the consequent high scattering rate between particles, ensures that primordial Universe was in thermal equilibrium. Following the so-called Hot Big Bang Model, Universe adiabatically expanded and cooled during time. This model is validated by observations, that show an homogeneous and isotropic Universe on large scales.

The scenario just described is a zero order approximation and, if we want to analyse the structure of Universe on smaller scales, we need to allow for deviations from this behaviour. One of the main observable of Universe is the spatial distribution of galaxies. Several surveys have revealed that galaxies are not distributed randomly, but, as opposite, that Universe has a structure on large scales. As baryons are a small fraction of the total matter, we can guess that galaxies are located in the potential wells of dark matter, which likely drive the formation of cosmological structures. This implies that, to understand the actual distribution of matter in the Universe, we have to allow for deviation from smoothness. We then need a tool that allows us to study perturbations around the isotropic background predicted by the Standard Model. A similar scenario is found when we focus on Cosmic Microwave Background (CMB) photons. This bath of primordial radiation seems to uniformly permeate all the Universe. Nevertheless, last decades experiments have shown also in this case the presence of spatial anisotropies in the photons temperature distribution. These fluctuations around the mean, present both in the radiation and in the matter fields, have a common origin in the primordial Universe, but evolved differently in time, as we will see in the next chapters. The mechanism generating the primordial perturbations is called *Inflation* and will be briefly described in the next section [18], [19], [20], [21], [22].

To conclude, and before moving on, it is usefull to introduce a quantity that can account for the stretching of the light wavelenghts of photons travelling in a expanding Universe. The definition of the *redshift* is fundamental, as basically all informations we have about Universe are given by observations of photons emitted by distant sources. We know that there is a relation between the photon momentum and wavelenght, $\lambda = h/p$. From the equation of the geodesic of a photon travelling in a FLRW Universe, we can derive the relation between momentum and scale factor, $p \propto a^{-1}$, which impies $\lambda \propto a$. If we consider a photon emitted with wavelenght λ_e at time t_e and received at t_0 with wavelenght λ_0, we have:

$$\lambda_0 = \frac{a(t_0)}{a(t_e)}\lambda_e. \tag{1.12}$$

As the scale factor increases, also λ increases i.e it is redshifted. Redshift is then defined as:

$$z \equiv \frac{\lambda_0 - \lambda_e}{\lambda_e}, \tag{1.13}$$

and the relation between redshift and scale factor turns out to be:

$$1 + z = \frac{a(t_0)}{a(t_e)}. \tag{1.14}$$

1.2 Initial conditions

The origin and main features of the CMB will be described in the next chapter. For the moment we just say that CMB has been a key observable in our understanding of the Universe [23]. One of the main characteristic of this radiation is to be homogeneus on very large scales. When this large scale homogeneity was discovered, it represented at first a problem for the Standard Model, known as the *horizon problem.* To understand why, we first introduce the concept of horizon. There are two main types of horizon: the Hubble radius and the particle horizon. The *Hubble radius* is a quantity related to the finite velocity of light. It contains all regions that light can reach in a Hubble characteristic time and is defined as:

$$R_c = \frac{c}{H(t)} = c\tau(t), \tag{1.15}$$

where

$$\tau_h = \frac{1}{H(t)}. \tag{1.16}$$

The Hubble time, $\tau(t)$, can be described as the characteristic time of expansion in a particular epoch. All regions inside the Hubble radius are in causal contact at a particular time in the expansion history. The *particle horizon*, instead, contains all the regions that have been in causal contact since the beginning of time. The comoving particle horizon is defined as:

$$d_h = \int_0^t \frac{cdt}{a(t')} \tag{1.17}$$

It is an integral over time of the Hubble horizon and keeps into account the past history of the observer. The ratio between the two horizons depends on the expansion rate of the Universe. When the Hubble radius grows, it gradually includes and put in causal contact more and more regions of space. The process is called horizon entering. The most interesting entering event is that of cosmological perturbations, as they determine the fluctuations of the potential and density field of matter and radiation.

The CMB formed early in the cosmic history, about $380'000$ years after the Big Bang. After that event, called Recombination, CMB photons decoupled from matter and their distribution remained freezed to that we observe now. The comoving Hubble horizon at the CMB formation time is seen today under an angle of $2°$ in the sky. In this scheme, the high level of homogeneity we observe on large scales is not possible, as scales larger than the comoving Hubble radius

at the time of Recombination have never been in causal contact.
The solve this problem we have to consider the possibility that large scales of perturbations, which weren't in the Hubble radius at the time of CMB formation, were instead inside the particle horizon. In other words, these regions have been in causal contanct in the primordial Universe, for some reason they went out the Hubble horizon and, now, we are just seeing them **re-entering** in it. For this to be possible, the Hubble Horizon must have experienced a fast and dramatic decrease in the early times, caused by an equally fast and impressive expansion of the Universe. This process is called Inflation.

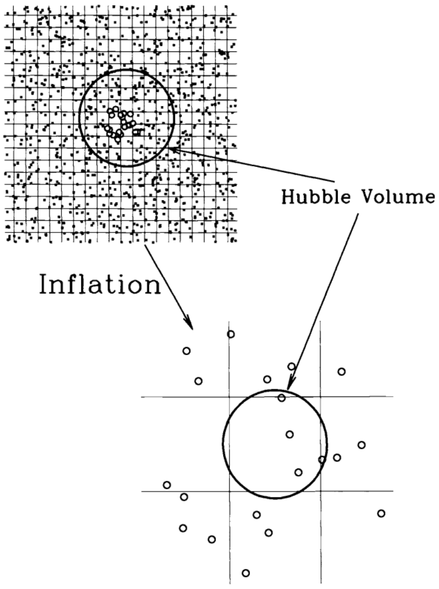

Figure 1.2: *Expansion of the Universe and consequent decrease of Hubble horizon. Particles in causal contact in the primordial epoch are pushed out of the horizon due to Inflation. Picture taken from Dodelson et al. [24].*

In figure 1.2 we see the effect of the accelerated expansion on the Hubble radius. The horizon is depicted as the black thick circle, the small circles are region of space in causal contact one with the other. The expansion of universe, represented by the evolution of underlying grid, causes a decrease of the Hubble horizon and pushes some regions out of it.

In figure 1.3 we see the effect of the Universe accelerated expansion on a spatial scale of perturbation. During Inflation the Hubble horizon decrease and the process we assist is that of the Horizon exit. After the end of Inflation, Hubble Horizon starts to grow again and gradually includes perturbations on larger scale, which then re-enter the Horizon.

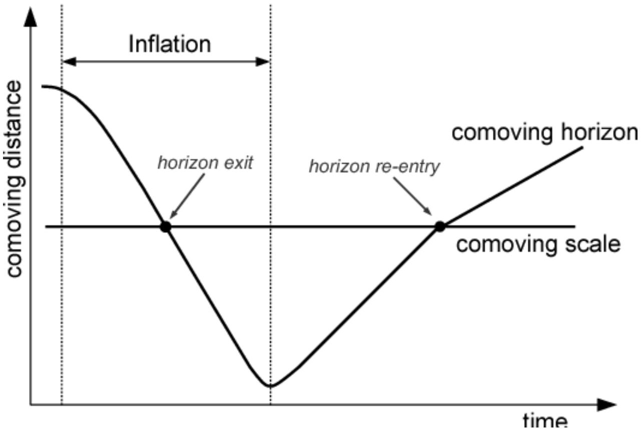

Figure 1.3: *The effect of Inflation on a scale of preturbation. As the Hubble radius decreases, the perturbation exits the horizon. At later times, when Inflation is ended and the Hubbble radius starts growing again, the same scale re-enters the horizon and perturbes the matter-radiation density field.*

To understand how these primordial perturbations affected the photons-baryon fluid at later epochs, we assume a standard description of Inflation, in which the cause of the acceletared expansion is a scalar field with negative pressure. Recalling the second Friedmann equation, (1.3), to have an accelerated expansion we need negative pressure:

$$\ddot{a}(t) > 0 \rightarrow (\rho + 3P) < 0 \rightarrow P < -\frac{1}{3}\rho. \tag{1.18}$$

As the energy density ρ is always positive, P has to assume negative values. In the simplest model of Inflation the scalar field is static and homogeneous and the component of the energy momentum tensor are:

$$T^0_0 = -\frac{1}{2}\dot{\psi}^2 - V(\psi) = -\rho \tag{1.19}$$

$$T^i_j = \left(\frac{1}{2}\dot{\psi}^2 - V(\psi)\right)\delta^i_j = p\delta^i_j \tag{1.20}$$

Many models of Inflation assume that the scalar field slowly rolls toward its true ground state. The kinetic term of this field is close to a constant, so that we can impose the so called *slow-roll condition*: $\frac{1}{2}\dot{\psi}^2 \ll V(\psi)$. The equation of state for this fluid is then:

$$p \approx -\rho. \tag{1.21}$$

The Klein Gordon equation in a FLRW metric represents the equation of motion of the inflaton field at zero order.

$$\ddot{\psi} + 3H\dot{\psi} - \frac{\nabla^2\psi}{a^2} = -V'(\psi). \tag{1.22}$$

We can neglect the term $\frac{\nabla^2\psi}{a^2}$ as we assumed that the field is static. The quantistic perturbations of primordial Universe were gaussian distributed and small with respect to the background, so we can treat them with linear theory. The perturbed field can be written as:

$$\psi(x,t) = \psi(t) + \delta\psi(x,t). \tag{1.23}$$

The zero order part depend only on time and is responsible for the acceleration of the Universe expansion. The first order term, instead, induces metric perturbations. We can then wonder what is the behaviour of these fluctuations, both in the case they remain within the horizon and in the case they exit from it, due to the expansion driven by the background. The dynamic of perturbations is again described by the Klein Gordon equation. Now the spatial derivative has to be taken into account, differently from the zero order case. For simplicity we assume a massless field, $V'' = \frac{dV^2}{d^2\psi} = 0$, and obtain:

$$\ddot{\delta\psi}(x,t) + 3H\dot{\delta\psi}(x,t) - \frac{\nabla^2\delta\psi}{a^2} = 0. \tag{1.24}$$

Moving to harmonic space we have:

$$\ddot{\delta\psi}_k + 3H\dot{\delta\psi}_k - \frac{k^2\delta\psi_k}{a^2} = 0. \tag{1.25}$$

The solution to this equation can then be divided in two different regimes:

- Inside horizon: the scale of the perturbation satisfies the condition $\lambda \ll H^{-1} \rightarrow \frac{k}{aH} \gg 1$. The equation reduces to:

  $$\ddot{\delta\psi}_k - \frac{k^2\delta\psi_k}{a^2} \simeq 0, \tag{1.26}$$

  which is the equation of an harmonic oscillator with decreasing amplitude. These perturbations vanish over time.

- Outside horizon: the scale of the perturbation satisfies the condition $\lambda \gg$

> $H^{-1} \rightarrow \frac{k}{aH} \ll 1$. The equation reduces to:
>
> $$\delta\ddot{\psi}_k + 3H\delta\dot{\psi}_k \simeq 0. \tag{1.27}$$
>
> This equation have a decresing solution and a constant one. Perturbations that exit the horizon are freezed until they re-enter it. For this reason we say that long wave modes preserve their primordial features.

We want to relate the perturbations of the Inflaton field that re-enters the horizon and the fluctuations of the matter-radiation field. Let's start saying that fluctuations of the inflaton field are connected to metric perturbations, as they cause different expansion rates in different regions of the Universe. The resulting temporal shift can be written as:

$$\delta t = \frac{-\delta\psi}{\dot{\psi}} \tag{1.28}$$

If we combine equations (1.19), (1.20) and (1.22) with the continuity equation and impose again the slow roll condition, we have:

$$\frac{1}{2}\dot{\psi}^2 + V(\psi) = \rho \rightarrow \delta\rho = V'\delta\psi \tag{1.29}$$

$$\ddot{\psi} + 3H\dot{\psi} = -V' \tag{1.30}$$

$$\frac{\delta\rho}{\dot{\rho}} = \frac{V'\delta\psi}{-3H(p+\rho)} = \frac{-3H\dot{\psi}\delta\psi}{-3H\dot{\psi}^2} = \frac{\delta\psi}{\dot{\psi}} \tag{1.31}$$

Equation (1.31) tells that the perturbations of the primordial scalar field, when entering the horizon, are turned into fluctuations of the cosmic fluid density field. They then serve as initial conditions for the growth of structure and anisotropy in the Universe.
If we write the perturbation in Fourier modes, it can be factorized into distinct k-modes. Every mode is associated to a gaussian distribution with zero mean and non-zero variance. The variance is computed as:

$$\langle \delta\psi(k)\delta\psi(k)^{\star} \rangle = (2\pi)^3 P_{\psi}(k)\delta^3(k-k') \tag{1.32}$$

where $P_{\psi}(k)$ is the power spectrum of the scalar perturbations. Considering the solution of the Klein Gordon equation for super horizon modes and doing some calculation, we can obtain a common parametrization of the power spectrum:

$$P_\psi = \frac{50\pi^2}{9k^3}\left(\frac{k}{H_0}\right)^{n_s-1}\delta_H^2\left(\frac{\Omega_m}{D(a=1)}\right)^2 \tag{1.33}$$

In this equation δ_H is the amplitude of the perturbation at the horizon crossing and n_s is the spectral index of the scalar perturbations. A index equal to unity would imply a spectrum independent on the wavelenght mode. It is almost the case, as cosmological observations give $n \approx 0.96$. The quantity $D(a = 1)$ is the so-called growth factor. It is computed at late times, when dark matter dominates the energy density of Universe, as it will be described in the next chapter. To conclude, we give a normalized version of the power spectrum, which is useful to collect all constants in a unique amplitude and highlight the k-mode dipendence:

$$\Delta_\psi^2 = \frac{k^3}{2\pi^2}P_\psi(k), \tag{1.34}$$

which becomes:

$$\Delta_\psi^2 = A_s(k_0)\left(\frac{k}{k_0}\right)^{n_s-1}, \tag{1.35}$$

where k_0 is a chosen pivoting scale.

1.3 Short thermal history of Universe

We have seen that Inflation set the initial conditions for the growth of structures and anisotropies. Now we will briefly describe the main processes that occourred in the Universe after Inflation [25].
The *baryogenesis* happened around 10^{-12} seconds after the Big Bang, when temperature was $T \sim 10^{15}K$ [26], [27]. During the baryogenesis the production of a small matter-antimatter asymmetry took place. This slight imbalance became dramatic during time, and now we have a dominant presence of the matter particles with respect to their anti-matter counterparts. Another remarcable result of the process which gave rise to baryogenesis (the so-called electroweak phase transition) is that it led matter to have mass. At the end of this transition the cosmic plasma was made by leptons and quarks.
Quarks have been confined into hadrons when Universe cooled to temperature of $10^{12}K$, during the so-called quantum chromodynamics phase transition. After this event the only relativistic particles left in the cosmic fluid were photons,

neutrinos and electrons.
When Universe reached a temperature of $10^{10}K$, neutrinos decoupled from electrons and started to propagate freely, with their temperature scaling as a^{-1}. We have to wait temperature to drop of another order of magnitude, up to 10^9K, to assist at the *Big Bang Nucleosinthesis* (BBN) [28]. The first element to form was deuterium:

$$n + p \iff D + \gamma \tag{1.36}$$

Once the production of deuterium was stabilized, also other elements started to form: Tritium, ^3H, and Helium, ^3He, ^4He, first and, in a second moment, also Lithium, ^7Li, and Berillium, ^7Be. When temperature was $T \sim 10^7K$, the BBN ended and the ordinary matter content (which from now on can be called baryon content) was basically made by H nuclei ($\sim 75\%$) and ^4He. Moreover, there were traces of other light elements and, of course, electrons and photons.
In this phase there was thermal equilibrium: protons and electrons interacted through Coulomb scattering, while electrons and photons were tightly coupled through Compton scattering, as we will see in details in the next chapters. The Universe energy-density content was dominated by photons, but, as radiation density diluits faster than matter density with time, at some point matter became the dominant component. The transition is called *equivalence* and can be computed as:

$$\frac{\rho_m^{eq}}{\rho_r^{eq}} = \frac{\rho_m^0 a^{-3}}{\rho_r^0 a^{-4}} = \frac{\rho_m^0}{\rho_r^0} a \implies a_{eq} = \frac{\rho_r^0}{\rho_m^0} \implies z_{eq} = 4.3 \times 10^4 \Omega_0 h^2. \tag{1.37}$$

Well inside matter domination era, hydrogen was still fully ionized. The fraction of ionized atoms is governed by Saha equation:

$$\frac{X_e^2}{1 - X_e} = \frac{10^9}{T^3} \left(\frac{m_e T}{2\pi} \right)^{3/2} e^{-\frac{B_H}{T}}, \tag{1.38}$$

where X_e is the free electron fraction:

$$X_e \equiv \frac{n_e}{n_p n_H} \tag{1.39}$$

and $B_H \equiv (m_e + m_p - m_H)$ is the binding energy of the hydrogen atom. As long as $T \gtrsim B_H$, then $X_e \approx 1$, i.e. all hydrogen was ionized. When T dropped below B_H, X_e went to zero and the hydrogen atoms formed. *Recombination* happened when almost 90% of electrons were forming hydrogen atoms. We have then:

$$X_e(T_{rec}) \sim 0.1 \implies T_{rec} \sim 3600K. \tag{1.40}$$

This process occourred at resdhift $z_{rec} \simeq 1320$. As already mentioned, before Recombination photons and electrons were tightly coupled via Compton scattering. When atoms started to form, the number of free electrons decreased and the scattering events became less frequent. Photons started to free stream and decoupled from matter. This epoch is called *decoupling* and occurred at redshift $z \simeq 1100$, when the scattering rate became lower than the Hubble rate of expansion. The last moment in which photons interacted with baryons is called *last scattering surface*. The temporal separation bewteen Recombination and Decoupling causes the last scattering surface to have a finite thikness. In anycase, its size is negligible compared with the cosmic history. We can then consider the last scattering as a real surface, as well as using both terms, Recombination and Decopling, to adress the CMB formation epoch.

1.4 Distance measurement in cosmology

The way in which we measure distances in Cosmology depends on the geometry of Universe. If we assume to live in a FLRW space-time, then the line element for photons travelling from the source to the observer along the line of sight is:

$$-c^2dt^2 + a^2(t)\left[\frac{dx^2}{1-kx^2}\right] = 0, \tag{1.41}$$

which implies:

$$\int_{t_1}^{t_2} \frac{cdt}{a(t)} = \int_0^x \frac{dx}{\sqrt{1-kx^2}}. \tag{1.42}$$

The integral on the right, over the line of sight, represents the definition of *comoving distance*. In this sistem of measure the coordinates follow the expansion of the Universe and are then fixed: the comoving distance of an object with respect to the observer is then constant in space and time. The solutions to equation (1.42) depend on the value of the curvature parameter k:

$$d = \begin{cases} k^{-1/2} \arcsin (k^{1/2}x), & \text{if } k > 0 \\ x, & \text{if } k = 0 \\ |k|^{-1/2} \operatorname{arcsinh} (|k|^{1/2}x), & \text{if } k < 0 \end{cases} \tag{1.43}$$

The comoving distance can be expressed also as function of cosmological parameters involving a integral over redshift:

$$d_0 = \int_{t_1}^{t_0} \frac{cdt}{a(t)} = \int_0^z \frac{cdz}{H(z)}, \tag{1.44}$$

where the function $H(z)$ gives the redshift evolution of the Hubble constant and is defined as:

$$H(z) = H_0\sqrt{\Omega_{r,0}(1+z)^4 + \Omega_{m,0}(1+z)^3 + \Omega_{k,0}(1+z)^2 + \Omega_{\Lambda,0}}. \tag{1.45}$$

Turning the comoving distance into the *proper distance* involves a simple multiplication by the scale factor. We have indeed:

$$d_p = a(t)d. \tag{1.46}$$

This quantity represents the distance between object and observer computed with the assumption that they are placed at the same cosmic time. As the Universe expands, the proper distance increases over time.
From an observational point of view, we see an astrophysical object as a flux of incoming photons. We can then define a distance measure related to the flux of the source. The *luminosity distance* involves the relation between the intrinsic luminosity of the source and the flux we receive:

$$d_L^2 = \frac{L}{4\pi F}. \tag{1.47}$$

In a expanding Universe with a FLRW metric, the relation betweeen the luminosity and comoving distance is:

$$d_L = d(1+z). \tag{1.48}$$

Writing the flux in term of its luminosity and the comoving distance, we obtain then:

$$F = \frac{L}{4\pi d^2(1+z)^2}. \tag{1.49}$$

Equation (1.49) clearly shows that the flux from distant sources is reduced by a factor $(1+z)^2$ with respect to what we wuold receive in a static Universe. Luminosity distance has a key role to draw information about the geometry of the Universe and the expansion rate.
To conclude this list of definitions we consider the case in which we are looking at extended objects. We can then compute their distance through a comparison between their proper size, l, and their apparent angular size, θ. The ratio between these two quantities is called *angular diameter distance*:

$$d_A = \frac{l}{\theta}, \tag{1.50}$$

The relation between d_A and the comoving distance is:

$$d_A = \frac{d}{(1+z)}. \tag{1.51}$$

2

Cosmological perturbations: radiation and matter anisotropies

Here we briefly review the basis of theory we will use in the next chapters, that are instead dedicated to the two projects we present in this thesis. The first two sections of the present chapter focus on the origin of the Cosmic Microwave Background (CMB) anisotropies in temperature and polarization. The study of CMB anisotropy pattern on large scales is the focus of the project I will present in Chapter 3. The last section, instead, regards the origin and evolution of Large Scale Structure in the linear theory. The computation of the linear matter power spectrum is the starting point for the development of the halo model used to investigate the clustering properties of dusty galaxies and Sunyaev Zeldovich clusters, which will be usefull for the analysis I will present in Chapter 4. This chapter is mainly based on [24], but more specific references are provided in the corresponding section.

2.1 *The radiation field: Cosmic Microwave Background*

The CMB has been a key observable in our understanding of the Universe. Discovered in the ′60 [1], this radiation has a primordial origin and offers a view on the Universe when it was almost 380 kyr old. At that time Universe was filled by a hot plasma of protons and electrons and radiation interacted with free electrons through Thomson scattering. As the Universe expanded, it cooled enough to allow for the formation of hydrogen athoms in a process called *Recombination*. At this point radiation and baryons decoupled and photons started travelling freely through the Universe. Due to the high rate of scattering before Recombination, photons and baryons were in thermal equilibrium, as it is proved by the specific intensity of the CMB phothons today which shows a blackbody spectrum:

$$I_\nu = \frac{4\pi\hbar\nu^3/c^2}{exp(2\pi\hbar\nu/k_bT) - 1}, \tag{2.1}$$

where $\hbar = h/2\pi$, h is the Planck constant and k_b is the Boltzmann constant. As the last scattering surface is located at $z \sim 1100$, photons temperature decreased due to the expansion of the Universe, as $\rho_{rad} \propto T^4 \propto a^{-4}$, and it is now around $2.7K$. According to the Wien's law, this temperature implies that the peak of the intensity distribution is now in the microwaves:

$$\lambda_{peak}T = const \rightarrow \lambda \approx 2\text{mm}. \tag{2.2}$$

As predicted by the Standard Model [29], observations showed that the spatial distribution of CMB photons is isotropic and homogeneus at zero order, but, if we increase the resolution of our observations [30], [31], [32], we find a pattern of small anisotropies around the smooth backgroud. In order to study this pattern of perturbations we need the Boltzmann equation, a tool able to describe the distribution of photons in the moment of Recombination, when the cosmic fliud momentarily came out from a condition of equilibrium [33], [34].

2.1.1 Boltzmann equation for photons

The Boltzmann equation relates the distribution function of the particles of a fluid to the collisional term, that accounts for the interactions of that particles:

$$\frac{\mathbf{d}f}{\mathbf{d}t} = \hat{\mathbf{C}}(f). \tag{2.3}$$

Here **d** represents the total derivative of the distribution of the particles, which is function of their position and velocity $f = f(\vec{x}, v)$, while **C** represents the collisional term. In order to compute the Boltzmann equation for photons we should at first specify the form of the metric, which has to take into account of small perturbations around the background:

$$g_{00}(\vec{x},t) = -1 - 2\Psi(\vec{x},t), \tag{2.4a}$$

$$g_{0i}(\vec{x},t) = 0, \tag{2.4b}$$

$$g_{ij}(\vec{x},t) = a^2\delta_{ij}(1 + 2\Phi(\vec{x},t)). \tag{2.4c}$$

The functions Ψ and Φ account for small deviations from the FLRW metric. In their absence we recover a homogeneus, expanding universe, simply described by the time dependent scale factor $a(t)$. Using this perturbed metric we can compute the Liouville term (left side of the Boltzmann equation) for photons:

$$\frac{df}{dt} = \frac{\partial f}{\partial t} + \frac{\hat{p}^i}{a}\frac{\partial f}{\partial x^i} - p\frac{\partial f}{\partial p}\left[H + \frac{\partial \Phi}{\partial t} + \frac{\hat{p}^i}{a}\frac{\partial \Psi}{\partial x^i}\right], \tag{2.5}$$

where $\hat{p}^i$ is the angular direction vector of the momentum. Here the first two terms on the right are related to the standard hydrodynamics and their integrals represent respectively the continuity and Euler equations. The third term includes the Hubble expansion rate and describes the photon energy loss during expansion. The last two terms are related to the potential and describe the effect of photons escaping from over/underdense regions. To proceed we need to specify the form of $f(\vec{x},t)$, which is a Bose-Einstein distribution:

$$f(\vec{x},p,\hat{p},t) = \left[\exp\left(\frac{p}{T(t)[1+\Theta(\vec{x},\hat{p},t)]}\right)\right]^{-1}. \tag{2.6}$$

Here $\Theta = \delta T/T$ is the perturbation around the zero-order temperature, which, differently from T, depends not only on time but also on momentum and position. As we consider small perturbations, we can expand equation (2.6) at the first order and we get:

$$\begin{aligned} f &\simeq \frac{1}{e^{p/T}-1} + \left(\frac{\partial}{\partial T}\left[\exp\left(\frac{p}{T}\right) - 1\right]\right) T\Theta \\ &= f^0 - p\frac{\partial f^{(0)}}{\partial p}\Theta, \end{aligned} \tag{2.7}$$

where we used $T\partial f^{(0)}/\partial T = -p\partial f^{(0)}/\partial p$ and, in the last equality of equation (2.7), we set:

$$f^{(0)} \equiv \left[\exp\left(\frac{p}{T}\right) - 1\right]^{-1}. \tag{2.8}$$

Inserting equation (2.7) into (2.5), we obtain the final expression for the Liouville term in the case of radiation. At first order we get:

$$\left.\frac{df}{dt}\right|_{\text{first order}} = -p\frac{\partial f^{(0)}}{\partial p}\left[\frac{\partial\Theta}{\partial t} + \frac{\hat{p}^i}{a}\frac{\partial\Theta}{\partial x^i} + \frac{\partial\Phi}{\partial t} + \frac{\hat{p}^i}{a}\frac{\partial\Psi}{\partial x^i}\right]. \tag{2.9}$$

We need now to compute the collissional term $\mathbf{C}$. The process we want to describe is Compton scattering:

$$\gamma(\vec{p}) + e^-(\vec{q}) \Leftrightarrow \gamma(\vec{p'}) + e^-(\vec{q'}). \tag{2.10}$$

The collisional operator for this process is:

$$\begin{aligned}\mathbf{C}[f(p)] = \frac{(2\pi)^4}{p}\int\frac{d^3q}{(2\pi)^3 2E(q)}\int\frac{d^3q'}{(2\pi)^3 2E(q')} \\ \int\frac{d^3p'}{(2\pi)^3 2E(p')}|\mathcal{M}|^2(\delta^3(\vec{p}+\vec{q}-\vec{p'}-\vec{q'}) \\ \delta[E(p)+E_e(q)-E(p')-E_e(q')][f_e(\vec{q'})f(\vec{p'})-f_e(\vec{q})f(\vec{p})],\end{aligned} \tag{2.11}$$

where the amplitude of the Thomson scattering process is:

$$|\mathcal{M}|^2 = 6\pi\sigma_T m_e^2(1+\hat{p}\cdot\hat{p'}). \tag{2.12}$$

Inserting equation (2.7) into (2.11) and doing some math we can get the final expression for the collisional operator:

$$\mathbf{C}(f(\vec{p})) = -p\frac{\partial f^{(0)}}{\partial p}n_e\sigma_T[\Theta_0 - \Theta(\hat{p}) + \hat{p}\cdot\vec{v_b}], \tag{2.13}$$

where n_e is the electron number density, σ_T is the Thomson scattering cross section and v_b the peculiar velocity of the cosmic fluid. Here we have also introduced the quantity Θ_0 which is defined as:

$$\Theta_0(\vec{x},t) \equiv \frac{1}{4\pi}\int d\Omega'\Theta(\hat{p}',\vec{x},t) \tag{2.14}$$

and represents the monopole of the distribution. Collecting together the right and left side of the Boltzmann equation we obtain:

$$\left[\frac{\partial\Theta}{\partial t} + \frac{\hat{p}^i}{a}\frac{\partial\Theta}{\partial x^i} + \frac{\partial\Phi}{\partial t} + \frac{\hat{p}^i}{a}\frac{\partial\Psi}{\partial x^i}\right] = n_e\sigma_T[\Theta_0 - \Theta + \hat{p}\cdot\vec{v_b}]. \tag{2.15}$$

Perturbations in the radiation field are small, so, if we Fourier transform all the variables in equation (2.15), we obtain a set of decoupled equations in which every Fourier mode evolves independently. The Fourier convention chosen is:

$$\Theta(\vec{x},\eta) = \int \frac{d^3k}{(2\pi)^3} e^{i\vec{k}\cdot\vec{x}} \tilde{\Theta}(\vec{k},\eta), \tag{2.16}$$

where $\eta = \frac{dt}{a(t)}$ is the conformal time. Using the conformal time as time coordinate and writing the Boltzmann equation in Fourier space, we obtain:

$$\dot{\tilde{\Theta}} + ik\mu\tilde{\Theta} - \dot{\tilde{\Phi}} + ik\mu\tilde{\Psi} = -\dot{\tau}\left[\tilde{\Theta}_0 - \tilde{\Theta} + \mu\tilde{v}_b\right]. \tag{2.17}$$

Here $\mu \equiv \hat{k}\cdot\hat{p}$ is the angle between the wavenumber and the photon direction and τ is the optical depth defined as:

$$\tau(\eta) \equiv \int_{\eta}^{\eta_0} d\eta' n_e \sigma_T a. \tag{2.18}$$

Equation (2.17) allows to understand how perturbations manifest themselves in the radiation distribution. The evolution of these perturbations gives the pattern of anisotropies we see today in the CMB. The evolution of perturbations followed two distinct phases, temporally separated by the advent of the matter-radiation decoupling. Before Recombination photons were coupled trought Compton scattering to baryons and the two components acted as a single fluid. After Recombination photons were free from interactions with matter and 'free-streamed' to us. The decoupling of photons from matter prevented them following the collapse of matter perturbations due to gravity: their perturbation remained always small so that it is possible to deal with them through linear theory.

2.1.2 Anisotropies

2.1.2.1 Large scale anisotropies

Combining Boltzmann with Einstein equation and considering the initial conditions given by Inflation, we find the equation for the observed large scale anisotropy:

$$(\Theta_0 + \Psi)(k,\eta_\star) = \frac{1}{3}\Psi(k,\eta_\star) = -\frac{1}{6}\delta(\eta_\star) \tag{2.19}$$

On the left side of the equation we don't have only the monopole of the perturbation but also the gravitational potential Ψ. This happens because the photons we see today had to travel out of the potential they were in at the time of Recombination. Emerging from the potential wells caused a decrease of energy, so that the temperature we observe now is that at Recombination, Θ_0, plus Ψ. The last equality on the right is obtained from the relation between the density perturbation and the gravitational potential, given by the Einstein equations. This equality shows that the observed anisotropy of an overdense region is going to be negative. Even if photons in denser regions were hotter at Recombination, the loss of energy employed in escaping the potential wells more than compensate for their higher initial temperature. It means that a cold spot in the sky today corresponds to an overdense region at the decoupling.

2.1.2.2 Small scale anisotropies

Before Recombination photons and baryons were tightly coupled through Compton scattering and the mean free path of the photons was much smaller than the horizon of the Universe. In this regime the perturbations had an oscillatory behaviour due to the competition between gravity, which drives the collapse of the perturbation, and the radiation pressure, which tends to push the photons out of the potential wells. Moreover it can be shown that, due to the short free mean path of photons, only the monopole and the dipole of the perturbation give visible effects: we are in the so called *fluid approximation.* The solution to the Boltzmann equation for the monopole and the dipole of the radiation fluid, in the case of tight coupling with baryons, are:

$$\begin{aligned}\Theta_0(\eta)+\Phi(\eta) &= [\Theta_0(0)+\Phi(0)]\cos(kr_s)\\ &\quad+\frac{k}{\sqrt{3}}\int_0^\eta d\eta'[\Phi(\eta')-\Psi(\eta')]\sin[k(r_s(\eta)-r_s(\eta'))],\end{aligned} \tag{2.20}$$

$$\begin{aligned}\Theta_1(\eta) &= \frac{1}{\sqrt{3}}[\Theta_0(0)+\Phi(0)]\sin(kr_s)\\ &\quad-\frac{k}{3}\int_0^\eta d\eta'[\Phi(\eta')-\Psi(\eta')]\cos[k(r_s(\eta)-r_s(\eta'))].\end{aligned} \tag{2.21}$$

Here the factor $\sqrt{3}$ represents the sound speed of the relativistic fluid, generically denoted as c_s, while r_s is the sound horizon, defined as:

$$r_s(\eta)\equiv\int_0^\eta d\eta' c_s(\eta'). \tag{2.22}$$

Let us first focus on equation (2.20): if we consider the limit in which the term multiplied by the cosine dominates, we have an expression for the frequency of the oscillations and we can compute the location of the acoustic peaks:

$$k_p = n\pi/r_s \qquad n = 1, 2, ... \tag{2.23}$$

Equation (2.21) instead gives the solution for the dipole of the perturbation and it is obtained differentiating equation (2.20). The first term is out of phase with respect to the behaviour of the monopole and this will have important implications on the power spectra. The oscillatory behaviour of the perturbations is affected by the diffusion of photons which tends to damp the anisotropies. The process is called *diffusion damping* [35] and it is characterized by a small but non-negligible quadrupole moment, that has to be combined to the equation of the monopole and dipole. The damping process affects anisotropies on a scale of $1/k_D \sim [\eta/n_e\sigma_T a]^{1/2}$, where n_e is the electron density and σ_T, the Thomson scattering cross section.

2.1.2.3 Free streaming

After Recombination photons free streamed toward us. In order to understand how the monopole and dipole of the perturbations at the decoupling have evolved in the photons moments today, $\Theta_\ell(\eta_0)$, we have to go back to the Boltzmann equation for photons, see equation (2.15). We can rewrite it as:

$$\dot{\Theta} + (ik\mu - \dot{\tau})\Theta = e^{-ik\mu\eta+\tau}\frac{d}{d\eta}[\Theta e^{ik\mu\eta-\tau}] = \tilde{S}, \tag{2.24}$$

where $\tilde{S}$ is the source function, defined as:

$$\tilde{S} \equiv +\dot{\Phi} - ik\mu\Psi - \dot{\tau}[\Theta_0 + \mu v_b]. \tag{2.25}$$

Integrating equation (2.24) between a time before Recombination, which we can assume to be zero with respect to the present epoch, $\eta_{ini} \approx 0$, and the conformal time today, η_0, we obtain:

$$\Theta(k,\mu,\eta_0) = \Theta(k,\mu,\eta_{ini})e^{ik\mu(\eta_{ini}-\eta_0)}e^{-\tau(\eta_{ini})} + \int_{\eta_{ini}}^{\eta_0} d\eta\tilde{S}(\eta)e^{ik\mu(\eta-\eta_0)-\tau(\eta)}. \tag{2.26}$$

With the assumption that the Universe was completely opaque at early times, $\tau(\eta_{ini}) \to \infty$, while it is transparent now, $\tau(\eta_0) \equiv 0$, we get:

$$\Theta(k,\mu,\eta_0) = \int_0^{\eta_0} d\eta\tilde{S}(k,\mu,\eta)e^{ik\mu(\eta-\eta_0)-\tau(\eta)}. \tag{2.27}$$

In order to turn equation (2.27) into an expression for each of the Θ_ℓ, we want to rewrite the equation without the μ dependence. We start by multiplying each side by the Legendre polynomial $\mathcal{P}_\ell(\mu)$ and integrate over μ. On the right side we will have:

$$\int_{-1}^{1} \frac{d\mu}{2} \mathcal{P}_\ell(\mu) e^{ik\mu(\eta-\eta_0)} = \frac{1}{(-i)^\ell} j_\ell[k(\eta-\eta_0)], \tag{2.28}$$

where j_ℓ is the spherical Bessel function. After this operation we still have a μ dependence, hidden in the source term. In order to account for this, we performe a variable change:

$$\mu \to \frac{1}{ik}\frac{d}{d\eta}. \tag{2.29}$$

The source term becomes:

$$\tilde{S}(k,\eta) \simeq g(\eta)[\Theta_0(k,\eta) + \Psi(k,\eta)] + \frac{d}{d\eta}\left(\frac{iv_b(k,\eta)g(\eta)}{k}\right) + e^{-\tau}[\dot{\Psi}(k,\eta) - \dot{\Phi}(k,\eta)]. \tag{2.30}$$

Here $g(\eta)$ is the *visibility function* defined as:

$$g(\eta) \equiv -\dot{\tau}e^{-\tau}. \tag{2.31}$$

This function can be interpreted as a probability density, indeed $\int_0^{\eta_0} d\eta g(\eta) = 1$. It is the probability for a photon to have the last scatter at the conformal time η. Using the new shape of the source term, equation (2.27) becomes:

$$\Theta(k,\eta_0) = \int_0^{\eta_0} d\eta \tilde{S}(k,\eta) j_\ell[k(\eta-\eta_0)]. \tag{2.32}$$

Rewriting this equation in a more explicit form we obtain:

$$\begin{aligned} \Theta_\ell(k,\eta_0) = &\int_0^{\eta_0} d\eta g(\eta)[\Theta_0(k,\eta) + \Psi(k,\eta)] j_\ell[k(\eta-\eta_0)] \\ &- \int_0^{\eta_0} d\eta g(\eta)\left(\frac{iv_b(k,\eta)}{k}\right)\frac{d}{d\eta} j_\ell[k(\eta-\eta_0)] \\ &\int_0^{\eta_0} d\eta e^{-\tau}[\dot{\Psi}(k,\eta) - \dot{\Phi}(k,\eta)] j_\ell[k(\eta-\eta_0)]. \end{aligned} \tag{2.33}$$

To perform the integrals we make the assumption that the visibility function is tightly peaked around the time of the Recombination. In fact τ was high in the epochs before last scattering and the exponential $e^{-\tau}$ brought g to zero. After recombination $\dot{\tau}$ dropped, bringing again the visibility function to zero. Considering the visibility function as a Dirac Delta peacked around $\eta = \eta_\star$ and using $v_b(\nu_\star) = -3i\Theta_1(\eta_\star)$, equation (2.33) becomes:

$$\begin{aligned}\Theta_\ell(k,\eta_0) \simeq\ & [\Theta_0(k,\eta_\star) + \Psi(k,\eta_\star)] j_\ell[k(\eta_0-\eta_\star)] \\ & + 3\Theta_1(k,\eta_\star)\left(j_{\ell-1}[k(\eta_0-\eta)] - \frac{(\ell+1)j_{\ell-1}[k(\eta_0-\eta)]}{k(\eta_0-\eta)]}\right) \\ & + \int_0^{\eta_0} d\eta e^{-\tau}[\dot{\Psi}(k,\eta) - \dot{\Phi}(k,\eta)] j_\ell[k(\eta_0-\eta)].\end{aligned} \tag{2.34}$$

Equation (2.34) shows that the anisotropy we see today is given mainly from three contributions: the first term is related to an effective temperature given by the monopole of the perturbation plus a the gravitational contribution. It is called Sachs-Wolfe effect: if the region we observe was denser at the time of Recombination, we will see a cold spot in the distribution of photons today. The second term is a Doppler effect, given by the peculiar motion of the cosmic fluid at the epoch of Recombination. Inside regions with a positive velocity in our direction, photons had a slight higher frequency: they will seem hotter with respect to those coming from regions with negative peculiar velocity at last scattering. The third term is weighted for $e^{-\tau}$, so it contributes to the anisotropy only after Recombination, when $\tau \lesssim 1$. This term, which survives only if the gravitational potential evolves, is called Integrated Sachs-Wolfe effect and it is subdominant with respect the other two terms. To understand the impact that a perturbation with wavenumber k has on an angular scale ℓ^{-1}, let's consider a perturbation on small angular scale:

$$\lim_{\ell\to\infty} j_\ell(x) = \frac{1}{\ell}\left(\frac{x}{\ell}\right)^{\ell-1/2}. \tag{2.35}$$

In this case the spherical Bessel funtion is small for $x < \ell$. The perturbation $\Theta_\ell(k,\eta_0)$ is close to zero for $\ell > k\eta_0$ i.e. small angular scales anisotropies receive a very little contribution from large wavelenght perturbations. In the same way, large scales are poorly affected by perturbations with small wavelenght. To conclude, a perturbation with wavenumber k contributes mainly on angular scales of the order of $\ell \sim k\eta_0$.

2.1.2.4 The CMB temperature power spectrum today

When looking at the sky, observers tipically make 'maps', in which anisotropies show up as 'hot or cold spots in the sky'. This is because we observe the CMB at coordinates (x_0, η_0), so our description of the anisotropy is entirely based on the direction of the incoming photons. In other words, we receive photons which follow a black body spectral distribution, but, depending on the observation direction, these black bodies are characterized by slightly different temperatures. We can then write the CMB temperature field as:

$$T(\vec{x},\hat{p},\eta) = T(\eta)[1+\Theta(\vec{x},\hat{p},\eta)]. \tag{2.36}$$

The anisotropy $\Theta(\vec{x},\hat{p},\eta)$ can be expanded in terms of spherical harmonics:

$$\Theta(\vec{x},\hat{p},\eta) = \sum_{\ell=1}^{\infty}\sum_{m=-\ell}^{\ell} a_{\ell m}(\vec{x},\eta)Y_{\ell m}(\hat{p}). \tag{2.37}$$

The spherical harmonics, $Y_{\ell,m}$, represent a complete set of eigenfunctions for the expansion on the sphere and all the information contained in the temperature field T is also contained in the weights $a_{\ell,m}$. We can now invert equation (2.37) by multiplying both side by $Y^{\star}_{\ell,m}(\hat{p})$ and exploiting the orthogonality of spherical harmonics:

$$a_{\ell,m}(\vec{x},\eta) = \int \frac{d^3k}{(2\pi)^3}e^{i\vec{k}\cdot\vec{x}}\int d\Omega Y^{\star}_{\ell,m}(\hat{p})\Theta(\vec{k},\hat{p},\eta). \tag{2.38}$$

The theory doesn't predict a specific value for the $a_{\ell,m}$ but just their distribution. If we assume the inflationary scenario, we expect a random field of quantum perturbations: the coefficients of the anisotropy expansion are drawn from a gaussian distribution. The mean of the $a_{\ell,m}$ is zero but they have some nonzero variance, called C_ℓ:

$$\langle a_{\ell,m}\rangle = 0, \qquad \langle a_{\ell,m}a^{\star}_{\ell,m}\rangle = \delta_{\ell,\ell'}\delta_{m,m'}C_\ell. \tag{2.39}$$

When we measure the $a_{\ell,m}$ we are sampling the distribution from which they are drawn. In this notation the index ℓ represents the angular scale we are looking at, while m represents all the possible configurations of the anisotropy that we can observe at that scale: for this reason $m = l-1,...,l+1$. For a given ℓ we will sample the distribution $2\ell+1$ times and thus there is an unavoidable uncertainty in the knowledge of the C_ℓ. It is the sample variance, called in this case *cosmic variance*:

$$\left(\frac{\Delta C_\ell}{C_\ell}\right) = \sqrt{\frac{2}{2\ell+1}}. \tag{2.40}$$

Through equation (2.38) we can relate the anisotropy directly to the C_ℓs. In order to take the expectation value of the $a_{\ell,m}$s we need to compute the expectation value of the anisotropy:

$$\langle\Theta(\vec{k},\hat{p})\Theta^{\star}(\vec{k}',\hat{p}')\rangle = \langle\delta(\vec{k})\delta^{\star}(\vec{k}')\rangle\frac{\Theta(\vec{k},\hat{p})}{\delta(\vec{k})}\frac{\Theta^{\star}(\vec{k}',\hat{p})}{\delta^{\star}(\vec{k}')}, \tag{2.41}$$

where we have factorized the initial perturbation generated by Inflation, δ, and the evolution of the perturbation when entering the horizon, $\left(\frac{\Theta}{\delta}\right)$. The first factor on the right is the *primordial power spectrum*:

$$\langle\delta(\vec{k})\delta^{\star}(\vec{k}')\rangle = (2\pi)^3\delta^3(\vec{k}-\vec{k}')P(k). \tag{2.42}$$

Expanding the anisotropy in spherical harmonics:

$$\Theta(k,\hat{k}\cdot\hat{p}) = \sum_{\ell}(-i)^{\ell}(2\ell+1)\mathcal{P}_{\ell}(\hat{k}\cdot\hat{p})\Theta_{\ell}(k), \tag{2.43}$$

and inserting equation (2.42) in (2.41) we find:

$$\begin{aligned} C_{\ell} = &\int\frac{d^3k}{(2\pi)^3}P(k)\sum_{\ell',\ell''}(-i)^{\ell'}(i)^{\ell''}(2\ell'+1)(2\ell''+1)\frac{\Theta_{\ell'}(k)\Theta^{\star}_{\ell''}(k)}{|\delta(k)|^2} \\ &\times\int d\Omega\mathcal{P}_{\ell'}(\hat{k}\cdot\hat{p})Y^{\star}_{\ell,m}(\hat{p})\int d\Omega'\mathcal{P}_{\ell''}(\hat{k}\cdot\hat{p}')Y_{\ell,m}(\hat{p}'). \end{aligned} \tag{2.44}$$

Using the properties of spherical harmonics [36] and of Legendre polynomials we get the final relation between anisotropy and power spectrum:

$$C_{\ell} = \frac{2}{\pi}\int_0^{\infty}dkk^2P(k)\left|\frac{\Theta_{\ell}(k)}{\delta(k)}\right|^2. \tag{2.45}$$

2.1.2.5 Sachs-Wolfe plateau: large scales

Large scales were out of the horizon at Recombination. In this case only the monopole contributes to the anisotropy, which is determined by the "effective temperature" $\Theta_0+\Psi$ at the decoupling. We start from equation (2.19) and consider that Recombination occours in a matter dominated Universe: the potential can be written as the potential today modulo the growth factor. We have then:

$$\Theta_0(\eta_{\star})+\Psi(\eta_{\star}) \simeq \frac{1}{3D_1(a=1)}\Psi(\eta_0) = -\frac{1}{3D_1(a=1)}\Phi(\eta_0). \tag{2.46}$$

The quantity D_1 is the growth factor, which describes the evolution of matter perturbations with time and, in equation (2.46), is computed at redshift zero. The second equality is valid at late time, when we consider $\Phi = -\Psi$. If we write the potential in terms of the dark matter perturbation, the previous equation becomes:

$$\Theta_0(\eta_\star) + \Psi(\eta_\star) \simeq -\frac{\Omega_m H_0^2}{2k^2 D_1(a=1)}\delta(\eta_0). \tag{2.47}$$

The expression for the effective temperature in equation (2.47) can be plugged in the monopole term of equation (2.34) in order to obtain the value of the anisotropy. Once we have computed Θ_ℓ, we use equation (2.45) to get the C_ℓ:

$$C_\ell^{SW} \simeq \pi H_0^{1-n}\left(\frac{\Omega_m}{D_1(a=1)}\right)^2 \delta_H^2 \int_0^\infty \frac{dk}{k^{2-n}} j_\ell^2[k(\eta_0 - \eta_\star)] \tag{2.48}$$

The superscript SW stands for *Sachs-Wolfe* [37], the people who first derived the equation for the large scales effect. Starting from equation (2.48) and doing some math we obtain:

$$\ell(\ell+1)C_\ell^{SW} = \frac{\pi}{2}\left(\frac{\Omega_m}{D_1(a=1)}\right)\delta_H^2. \tag{2.49}$$

At large scales, which means low ℓs, we expect a plateau when plotting $\ell(\ell+1)C_\ell^{SW}$ as function of the multipoles. Small deviations from the flat shape are due to the residual effect of the dipole and, most of all, to the Integrated Sachs-Wolfe effect, which gains importance as dark energy becomes dominant.

2.1.2.6 Acoustic peaks: small scales

When studying the small-scale anisotropy spectrum, we must consider not only the effect of the monopole but also the dipole and the Integrated Sachs-Wolfe effect. The monopole at Recombination $\Theta_0 + \Psi(k, \eta_\star)$ contains most of the structure of the final anisotropy spectrum. Using equation (2.35) we have seen that, when the monopole free stream to us, it generates an anisotropy on angular scales $\ell \sim k\eta_0$. Going more in details, it can be shown that the peak of the spherical Bessel function is at slightly lower values than $k\eta_0$. In addition, the position of the peak in k-space is at values lower than $\pi\eta_0/r_s$. Considering these two corrections the position of the peak results at $\ell_p \simeq 0.75\pi\eta_0/r_s$, with a shift towards larger scales with respect to the behaviour of the monopole at Recombination. The second relevant feature is that the 'zeroes' are smoothed: this is due to the fact that the value of a particular C_ℓ is determined not only by the mode $k = \ell/\eta_0$, but also by many other modes with wavenumber greater than k, whose contribution turn the zero point into a trough. The second block of equation (2.34) represents the dipole of the perturbation. Adding this term to the final spectrum raises the overall anisotropy level and in particular fills the troughs: an effect originated from the shift in phase between the monopole and the dipole. The last contribution to consider is that of the ISW effect, which is related to potential changes and affects in particular the scale of the horizon. One of its manifestations is called *early integrated Sachs-Wolfe effect* and is due to the residual radiation at the epoch of Recombination, when Universe isn't purely matter-dominated yet. It can be seen as a boost of the first acoustic peak in the anisotropy power spectrum.

2.1.2.7 Cosmological parameters

The anisotropy power spectrum depends on cosmological parameters. This makes it a fundamental probe for precision cosmology. The parameters affecting the position and separation of the peaks are several and often present strong degeneracies. To describe the ΛCDM model and to fit it to CMB data we need to choose six of these parameters and take care to reduce the degeneracy [38]. In Planck 2018 [39] the baseline parameters are the amplitude of primordial perturbations, the spectral index of primordial scalar perturbations, the baryon and matter density, the optical depth and the angular size of the sound horizon. The first two parameters are related to the shape of the power spectrum of primordial scalar perturbations, defined as:

$$P(k) = A_s(k_\star)\left(\frac{k}{k_\star}\right)^{n_s-1}, \tag{2.50}$$

where $k_\star$ is a pivoting scale and it is fixed to $k_\star = 0.05 Mpc^{-1}$ in Planck analysis. In the following list we enter a bit the details of the Planck baseline parameters.
Scalar amplitude, A_s: affects the magnitude of the primordial perturbations and hence shifts the CMB spectrum up and down;
Spectral index of primordial scalar perturbations, n_s: represents the tilt of the scalar perturbations and indeed it tilts the CMB spectrum, see [21], [19]. The condition $n_s = 1$ implies that the $\ell(\ell+1)C_\ell$ has equal power on all scales, while for $n_s > 1 (n_s < 1)$ it has more power on small (large) scales;
Barion density: variations in baryon density, $\omega_b h^2$, affect the heights of the peaks. Here $h = H_0/(100 kms^{-1}Mpc^{-1})$ is the reduced Hubble constant. The presence of baryons increases the deepness of the peaks adding extra force to the potential

wells of dark matter (baryon loading) and breaks the symmetry between even and odd peaks.
Matter density: the matter content of the Universe, $\omega_m h^2$, determines the matter-radiation equality and therefore which scales enter the horizon before or after this transition and how they evolve. Lowering the matter density shifts matter-radiation equality to later times, i.e. closer to Recombination. In this situation radiation density must be taken into account in the formation of the inhomogeneities at the decoupling. The decay of the potential due to the photon pressure provides a strong driving force for the oscillations. Moreover, since the potential is no more constant, there is a higher contribution of the early-ISW, which increases the large scale anisotropies.
Optical depth, τ: it is related to Reionization. The hot radiation produced by the born of stars is supposed to reionize Universe at a redshift around $z \sim 6$. This casues an increase of the optical depth towards the last scattering surface. The scales which has entered the horizon before Reionization are suppressed by a factor $e^{-\tau}$ due to the re-scattering of the photons.
Acoustic scale, $\theta_\star$: changing this parameter has the effect of horizontally shifting the acoustic peaks. It is defined as $\theta_\star \equiv r_\star / D_A$, where $r_\star$ is the comoving sound horizon at Recombination and D_A is the comoving angular diameter distance. The presence of the angular diameter distance involves another parameter that has not been mentioned yet: *curvature*. If Universe was open rather than flat, the geodesics of photons starting from the last scattering surface wuoldn't be parallel but slowly diverge. This cause the first peak to be moved at a smaller angular scale than in a flat universe, i.e. to a larger ℓ. Indeed, if in a flat Universe the angular diameter distance is simply $\eta_0 - \eta_\star$, in a open Universe it turns to be:

$$D_A = \frac{a}{H_0\sqrt{|\Omega_k|}} \sin\left(\sqrt{-\Omega_k} H_0 \chi\right) \tag{2.51}$$

where χ is the comoving distance. In addition to these parameters we should also consider the effect of the *dark energy density parameter*, Ω_Λ, which becomes dominant at reshift $z \sim 0.3$. It introduces a late Integrated Sachs-Wolfe effect, as the gravitational potential stops being time independent. This leads to a boost of the power of the low$-\ell$ modes of CMB power spectrum.

2.1.3 CMB Polarization

The Compton scattering that CMB photons underwent at the epoch of Recombination is expected to generate polarization. The electric and magnetic fields of a photon propagating in the x-direction oscillate in the y-z plane, i.e. tranverse to the direction of propagation. If the intensity along the two transverse directions is equal, then the light is unpolarized. Suppose that this photon scatter off an electron and gets deflected into the z direction: none of the intensity along the z-axis gets transmitted. As opposite, all of the intensity along the y-axis is transmitted. The resulting radiation is polarized along the y-axis. In this configuration Compton scattering can be considered a good mechanism to produce polarization. Unfortunately, in the early Universe every electron interacted with several photons coming from different directions. In the case of isotropic radiation all contributions from different photons are cancelled and the resulting radiation is still unpolarized: we need some sort of anisotropy to produce a net effect of polarization for CMB radiation. Polarization can be described as an headless vector, with a lenght corresponding to its magnitude and the orientation on the axis along which the intensity is gratest. In the plane perpendicular to the direction of propagation, we can decompose the intensity into:

$$I_{i,j} = \begin{pmatrix} T+Q & U \\ U & T-Q \end{pmatrix},$$

where T is the temperature while Q and U are the Stokes parameters. In principle we could include also the fourth Stokes parameter, V, which describes the circular polarization, but Compton scattering only produces linear polarization so we can set $V = 0$. To make quantitative predictions for the polarizations of CMB photons we have to consider a situation before Recombination, in which many electrons are coupled to an evolving photons distribution. We have then to write the Boltzmann equation for the polarization anisotropy, Θ_P, and then relate it to the Stokes parameters Q and U. We start from:

$$\dot{\Theta_P} + ik\mu\Theta_P = -\dot{\tau}\left[-\Theta_P + \frac{1}{2}\left(1 - \mathcal{P}_2(\mu)\right)\Pi\right], \tag{2.52}$$

$$\Pi = \Theta_2 + \Theta_{P2} + \Theta_{P0}, \tag{2.53}$$

where $\mu \equiv \hat{k} \cdot \hat{n}$, Θ_2 is the quadrupole of the temperature field and Θ_{P0}, Θ_{P2} are the monopole and the quadrupole of the polarization field respectively. In analogy to the temperature case the solution of equation (2.24) is:

$$\Theta_P(\hat{n}, \vec{k}) = \int_0^{\eta_0} d\eta e^{i\vec{k}\cdot\hat{n}(\eta-\eta_0)-\tau(\eta)} S_P(k, \mu, \eta), \tag{2.54}$$

where the source term is:

$$S_P(k,\mu,\eta) = -\frac{3}{4}\dot{\tau}(1-\mu^2)\Pi. \tag{2.55}$$

Equation (2.54) can be re-written introducing the visibility function $g(\eta) = -\dot{\tau}e^{-\tau}$ and writing explicitly the source term:

$$\Theta_P(\hat{n},\vec{k}) = \frac{3}{4}(1-\mu^2)\int_0^{\eta_0} d\eta e^{i\vec{k}\cdot\hat{n}(\eta-\eta_0)}g(\eta)\Pi(k,\eta). \tag{2.56}$$

Evaluating the integrand at the time of decoupling, where the visibility function integrates to unity, we find:

$$\Theta_P(\hat{n},\vec{k}) \simeq \frac{3\Pi(k,\eta_\star)}{4}(1-\mu^2)e^{i\vec{k}\cdot\hat{n}(\eta_\star-\eta_0)}. \tag{2.57}$$

To get the moments $\Theta_{P\ell}$, we neglect $\eta_\star$ with respect to η_0, multiply both side of the equation (2.57) by $\mathcal{P}_\ell(\mu)$ and integrate over all μ:

$$\Theta_{\ell P}(k) \simeq \frac{3\Pi(k,\eta_\star)}{4}\frac{\ell^2}{(k\eta_0)^2}j_\ell(k\eta_0). \tag{2.58}$$

In tight coupled limit the term Π can be expressed in term of the quadrupole, which is in turn related to the dipole. As $\Pi = 5\Theta_2/2$, equation (2.58) becomes:

$$\Theta_{\ell P}(k) \simeq \frac{15\Theta_2(k,\eta_\star)}{8}\frac{\ell^2}{(k\eta_0)^2}j_\ell(k\eta_0). \tag{2.59}$$

In the tightly coupled limit the quadrupole is proportional to the dipole and we obtain:

$$\Theta_{\ell P}(k) \simeq \frac{5k\Theta_1(k,\eta_\star)}{6\dot{\tau}(\eta_\star)}\frac{\ell^2}{(k\eta_0)^2}j_\ell(k\eta_0). \tag{2.60}$$

From equation (2.59) it is clear that polarization arises in presence of the a quadrupole moment. As in tight coupled limit the quadrupole is suppressed in Compton scattering, we expect polarization signal to be lower than the temperature power spectum. This suppression is of a factor $k/\dot{\tau}$, as emerges from equation (2.60). Moreover, from the fact that polarization anisotropy is proportional to the dipole, we expect it to be out of phase with respect to the monopole, i.e. to the temperature spectum. To conclude we notice that there is no analogous of the Integrated Sachs-Wolfe effect: changings in the gravitational potential has no effect on polarization anisotropies field.

2.1.3.1 CMB Polarization power spectra

To link the anisotropy computed in equation (2.59) to the polarization power spectrum that we observe today, we expand also the polarization perturbations in spherical harmonics, see [40], [15]. Doing this we must keep into account for the fact that polarization is a tensor. While temperature is invariant under a right handed rotation in the plane perpendicular to the direction $\hat{\mathbf{n}}$, Q and U trasform under rotation as:

$$Q' = Q\cos 2\psi + U\sin 2\psi, \tag{2.61}$$

$$U' = -Q\sin 2\psi + U\cos 2\psi, \tag{2.62}$$

where ψ is the rotation angle, $\hat{e}_1' = \cos\psi\hat{e}_1 + \sin\psi\hat{e}_2$ and $\hat{e}_2' = -\sin\psi\hat{e}_1 + \cos\psi\hat{e}_2$. Using the Q and U Stokes parameters we can then write two quantities that have a definite value of the spin:

$$(Q \pm iU)'(\hat{\mathbf{n}}) = e^{\mp 2i\psi}(Q \pm iU)(\hat{\mathbf{n}}). \tag{2.63}$$

If we expand these two quantities in the spin-weighted basis, we obtain:

$$(Q + iU)(\hat{\mathbf{n}}) = \sum_{\ell m} a_{2,\ell m\,2}Y_{\ell m}(\hat{\mathbf{n}}), \tag{2.64}$$

$$(Q - iU)(\hat{\mathbf{n}}) = \sum_{\ell m} a_{-2,\ell m\,-2}Y_{\ell m}(\hat{\mathbf{n}}), \tag{2.65}$$

where Q and U are defined at a given direction $\mathbf{n}$ with respect to the spherical coordinate system $(\hat{e}_\theta,\, \hat{e}_\phi)$. When computing the power spectrum of polarization we must take care to the fact that the Stokes parameters are not invariant under rotations in the plane perpendicular to $\mathbf{n}$. Equation (2.59) is the expression for the polarization moments from a single plane wave, but in the real Universe the anisotropy is given by the superposition of many waves. Then, in order to compute the power spectrum, for each wavevector $\mathbf{k}$ and direction on the sky $\hat{\mathbf{n}}$, one should rotate the Q and U parameters from the $\mathbf{k}$ and $\hat{\mathbf{n}}$ basis into a fixed basis on the sky. To avoid this issue one can use the spin raising and lowering operator to obtain spin zero quantities, which have the advatage to be rotationally invariant. These operators are defined as:

$$\eth_s f(\theta,\phi) = -\sin^s(\theta)\left[\frac{\partial}{\partial\theta} + i\csc(\theta)\frac{\partial}{\partial\phi}\right]\sin^{-s}(\theta)_s f(\theta,\phi), \tag{2.66}$$

$$\bar{\eth}_s f(\theta,\phi) = -\sin^{-s}(\theta)\left[\frac{\partial}{\partial\theta} - i\csc(\theta)\frac{\partial}{\partial\phi}\right]\sin^{s}(\theta)_s f(\theta,\phi) \tag{2.67}$$

and have the property of raising or lowering the spin-weight of the spin-s function, $(\eth_s f)' = e^{-i(s+1)\psi}\eth_s f$, $(\bar{\eth}_s f)' = e^{-i(s-1)\psi}\bar{\eth}_s f$. Using these operators one can express the quantity ${}_sY_{\ell m}$ in terms of the spin zeros spherical harmonics $Y_{\ell m}$:

$${}_sY_{\ell m} = \left[\frac{(\ell-s)!}{(\ell+s)!}\right]^{\frac{1}{2}}\eth^s Y_{\ell m} \quad 0 \le s \le \ell, \tag{2.68}$$

$${}_sY_{\ell m} = \left[\frac{(\ell+s)!}{(\ell-s)!}\right]^{\frac{1}{2}}(-1)^s\bar{\eth}^{-s} Y_{\ell m} \quad -\ell \le s \le 0. \tag{2.69}$$

Applying these operators to the polarization field we obtain then:

$$\bar{\eth}^2(Q+iU)(\hat{\mathbf{n}}) = \sum_{\ell m}\left[\frac{(\ell+2)!}{(\ell-2)!}\right]^{\frac{1}{2}} a_{2,\ell m}Y_{\ell m}(\hat{\mathbf{n}}), \tag{2.70}$$

$$\eth^2(Q-iU)(\hat{\mathbf{n}}) = \sum_{\ell m}\left[\frac{(\ell+2)!}{(\ell-2)!}\right]^{\frac{1}{2}} a_{-2,\ell m}Y_{\ell m}(\hat{\mathbf{n}}). \tag{2.71}$$

The expression for the expansion coefficients are:

$$\begin{aligned} a_{2,\ell m} &= \int d\Omega {}_2Y^\star_{\ell,m}(\hat{\mathbf{n}})(Q+iU)(\hat{\mathbf{n}}) \\ &= \left[\frac{(\ell+2)!}{(\ell-2)!}\right]^{-\frac{1}{2}}\int d\Omega Y^\star_{\ell,m}(\hat{\mathbf{n}})\eth^2(Q+iU)(\hat{\mathbf{n}}), \end{aligned} \tag{2.72}$$

$$\begin{aligned} a_{-2,\ell m} &= \int d\Omega {}_{-2}Y^\star_{\ell,m}(\hat{\mathbf{n}})(Q-iU)(\hat{\mathbf{n}}) \\ &= \left[\frac{(\ell+2)!}{(\ell-2)!}\right]^{-\frac{1}{2}}\int d\Omega Y^\star_{\ell,m}(\hat{\mathbf{n}})\eth^2(Q-iU)(\hat{\mathbf{n}}). \end{aligned} \tag{2.73}$$

We can also replace $a_{-2,\ell m}$ and $a_{2,\ell m}$ with their linear combination:

$$a_{E,\ell m} = -(a_{2,\ell m} + a_{-2,\ell m})/2, \tag{2.74}$$

$$a_{B,\ell m} = i(a_{2,\ell m} - a_{-2,\ell m})/2. \tag{2.75}$$

The E and B modes behave differently under parity transformations: while E remains unchanged, B changes sign. As B shows an opposite parity with respect to E, the EB cross correlation vanishes and, to characterize the polarization perturbations, we just need the E and B autospectra. These power spectra can be defined as rotationally invariant quantities:

$$C_\ell^{EE} = \frac{1}{2\ell+1}\sum_m \langle a^\star_{E,\ell m} a_{E,\ell m}\rangle, \tag{2.76}$$

$$C_\ell^{BB} = \frac{1}{2\ell+1}\sum_m \langle a^\star_{B,\ell m} a_{B,\ell m}\rangle, \tag{2.77}$$

in terms of which,

$$\langle a^\star_{E,\ell' m'} a_{E,\ell m}\rangle = C_\ell^{EE}\delta_{\ell'\ell}\delta_{m'm}, \tag{2.78}$$

$$\langle a^\star_{B,\ell' m'} a_{B,\ell m}\rangle = C_\ell^{BB}\delta_{\ell'\ell}\delta_{m'm}. \tag{2.79}$$

We are interested in relating the power spectrum to the perturbation computed in equation (2.59). The power spectrum is generated by the superposition of many Fouries modes characterized by a vawevector k. For a given Fourier mode we choose a coordinate system where $k||\hat{z}$ and $(\hat{e}_1, \hat{e}_2) = (\hat{e}_\theta, \hat{e}_\phi)$. As the symmetry is azimutal, only Q Stokes parameter is generated. Its amplitude only depends on the angle between the photon direction and the wavevector, $\mu = \hat{n}\cdot\hat{k}$. For a single mode we have $U = 0$ and $Q = \Theta_P(\hat{n}, \vec{k})$, where the perturbation $\Theta_P(\hat{n}, \vec{k})$ is given by equation (2.56). We have then that $\bar{\eth}^2(Q+iU) = \eth^2(Q-iU)$, so that ${}_2a_{\ell m} = {}_{-2}a_{\ell m}$: scalar modes contribute only to the E combination while B vanishes. Applying the spin raising operator twice on the integral solution for the polarization anisotropy, we obtain an expression for the perturbation of the E modes:

$$\begin{aligned}\Theta_E(\eta_0, k, \mu) &= -\frac{3}{4}\int_0^{\eta_0} d\eta g(\eta)\Pi(k,\eta)\partial_\mu^2[(1-\mu^2)^2 e^{ix\mu}] \\ &= \frac{3}{4}\int_0^{\eta_0} d\eta g(\eta)\Pi(k,\eta)(1+\partial_x^2)^2(x^2 e^{ix\mu}),\end{aligned} \tag{2.80}$$

where $\mu = \vec{k} \cdot \hat{n}$ and $x = k(\eta - \eta_0)$. To obtain the polarization spectrum today we use the equation (2.76) for the C_ℓ and integrate over all the Fourier modes:

$$\begin{aligned} C_\ell^{EE} &= \frac{1}{2\ell+1}\frac{(\ell-2)!}{(\ell+2)!} \\ &\times \int d^3k P_\phi(k) \sum_m \left| \frac{3}{4} \int d\Omega Y^\star_{\ell m}(\hat{n}) \int_0^{\eta_0} d\eta g(\eta)\Pi(k,\eta)(1+\partial_x^2)^2(x^2 e^{ix\mu}) \right|^2 \\ &= (4\pi)^2 \frac{(\ell-2)!}{(\ell+2)!} \int k^2 dk P_\phi(k) \left[\frac{3}{4} \int_0^{\eta_0} d\eta g(\eta)\Pi(k,\eta) \frac{j_\ell(x)}{x^2} \right]^2, \end{aligned} \tag{2.81}$$

where $P_\phi(k)$ is the initial power spectrum. If we consider:

$$\Theta^{(S)}_{E\ell}(k) = \sqrt{\frac{(\ell-2)!}{(\ell+2)!}} \frac{3}{4} \int_0^{\eta_0} d\eta g(\eta)\Pi(k,\eta)\frac{j_\ell(x)}{x^2}, \tag{2.82}$$

we obtain the final equation for the E modes power spectrum, originated by scalar perturbations:

$$C_\ell^{EE} = (4\pi)^2 \int k^2 dk P_\phi(k) [\Theta^{(S)}_{E\ell}(k)]^2. \tag{2.83}$$

2.1.3.2 Power spectrum from tensor perturbations

Until now we have focused on scalar perturbations. In this paragraph, instead, we will briefly describe the contribution to the power spectra given by tensor modes of perturbation, both for temperature and polarization. Tensor perturbations are able to produce B-modes, but their contribution is subdominant with respect to the scalar one and their detection is still an active field of research. In the following analysis we will employ some mathematical tools we have already seen when dealing with the Stokes parameters to obtain rotationally invariant quantities. Let's start saying that gravity has two independent polarizations, usually denoted with × and +. It is convenient to work with two linear combinations:

$$\xi^1 = (\xi^+ - i\xi^\times)/\sqrt{2}, \tag{2.84}$$

$$\xi^2 = (\xi^+ + i\xi^\times)/\sqrt{2}, \tag{2.85}$$

with ξ^1 and ξ^2 independent random variables with the following statistical properties:

$$\langle \xi^{1\star}(k_1)\xi^1(k_2)\rangle = \langle \xi^{2\star}(k_1)\xi^2(k_2)\rangle = \frac{P_h(k)}{2}\delta(k_1-k_2), \quad \langle \xi^{1\star}(k_1)\xi^2(k_2)\rangle = 0. \tag{2.86}$$

The perturbations generated by tensor modes, i.e. gravity waves, satisfy the following Boltzmann equations:

$$\dot{\tilde\Theta}^{(T)}_T + ik\mu\tilde\Theta^{(T)}_T = -\dot h - \dot\tau[\tilde\Theta^{(T)}_T - K], \tag{2.87}$$

$$\dot{\tilde\Theta}^{(T)}_P + ik\mu\tilde\Theta^{(T)}_P = -\dot\tau[\tilde\Theta^{(T)}_P + K], \tag{2.88}$$

$$K \equiv \left[\frac{1}{10}\tilde\Theta^{(T)}_{T_0} + \frac{1}{7}\tilde\Theta^{(T)}_{T_2} + \frac{3}{70}\tilde\Theta^{(T)}_{T_4} - \frac{3}{5}\tilde\Theta^{(T)}_{P_0} + \frac{6}{7}\tilde\Theta^{(T)}_{P_2} - \frac{3}{70}\tilde\Theta^{(T)}_{P_4}\right]. \tag{2.89}$$

The term $\dot h$, in equation 2.87, is the derivative of the tensor perturbation of the metric with respect to the conformal time. If we choose the coordinate frame where $\hat k || \hat z$ and $(e_1, e_2) = (e_\theta, e_\phi)$ the tensor perturbations pattern is related to $\tilde\Theta^{(T)}_T$ and $\tilde\Theta^{(T)}_P$ as:

$$\begin{aligned}\Theta^{(T)}_T(\eta,\hat n,k) = {} & [(1-\mu^2)e^{2i\phi}\xi^1(k) + (1-\mu^2)e^{-2i\phi}\xi^2(k)] \\ & \times \tilde\Theta^{(T)}_T(\eta,\mu,k),\end{aligned} \tag{2.90}$$

$$\begin{aligned}(\Theta^{(T)}_Q + i\Theta^{(T)}_U)(\eta,\hat n,k) = {} & [(1-\mu)^2 e^{2i\phi}\xi^1(k) + (1+\mu)^2 e^{-2i\phi}\xi^2(k)] \\ & \times \tilde\Theta^{(T)}_P(\eta,\mu,k),\end{aligned} \tag{2.91}$$

$$\begin{aligned}(\Theta^{(T)}_Q - i\Theta^{(T)}_U)(\eta,\hat n,k) = {} & [(1+\mu)^2 e^{2i\phi}\xi^1(k) + (1-\mu^2)e^{-2i\phi}\xi^2(k)] \\ & \times \tilde\Theta^{(T)}_P(\eta,\mu,k).\end{aligned} \tag{2.92}$$

In order to obtain the pattern of anisotropies today we have to integrate along the line of sight:

$$\begin{aligned}\Theta^{(T)}_T(\eta_0,\hat n,k) = {} & [(1-\mu^2)e^{2i\phi}\xi^1(k) + (1-\mu^2)e^{-2i\phi}\xi^2(k)] \\ & \times \int_0^{\eta_0} d\eta e^{ix\mu} S^{(T)}_T(k,\eta),\end{aligned} \tag{2.93}$$

$$\begin{aligned}(\Theta^{(T)}_Q + i\Theta^{(T)}_U)(\eta_0,\hat n,k) = {} & [(1-\mu)^2 e^{2i\phi}\xi^1(k) + ((1+\mu)^2 e^{-2i\phi}\xi^2(k)] \\ & \times \int_0^{\eta_0} d\eta e^{ix\mu} S^{(T)}_P(k,\eta),\end{aligned} \tag{2.94}$$

$$(\Theta_Q^{(T)} - i\Theta_U^{(T)})(\eta_0, \hat{n}, k) = [(1+\mu)^2 e^{2i\phi}\xi^1(k) + (1-\mu)^2 e^{-2i\phi}\xi^2(k)] \times \int_0^{\eta_0} d\eta e^{ix\mu} S_P^{(T)}(k,\eta), \tag{2.95}$$

where

$$S_T^{(T)}(k,\eta) = -\dot{h}e^{-\tau} + gK, \tag{2.96}$$

$$S_P^{(T)}(k,\eta) = -gK. \tag{2.97}$$

We act twice with the raising and lowering spin operators both on ξ^1 and ξ^2 and we obtain the expression for the anisotropy for the rotationally invariant quantities $\Theta_T^{(T)}$, $\Theta_T^{(E)}$and $\Theta_T^{(B)}$. As anticipated, it emerges here that, in the case of tensor perturbations, also B-modes are generated:

$$\Theta_T^{(T)}(\eta_0, \hat{n}, k) = [(1-\mu^2) e^{2i\phi}\xi^1(k) + (1-\mu^2) e^{-2i\phi}\xi^2(k)] \int_0^{\eta_0} d\eta e^{ix\mu} S_T^{(T)}(k,\eta), \tag{2.98}$$

$$\Theta_E^{(T)}(\eta_0, \hat{n}, k) = [(1-\mu^2) e^{2i\phi}\xi^1(k) + (1-\mu^2) e^{-2i\phi}\xi^2(k)]\hat{\mathcal{E}} \int_0^{\eta_0} d\eta e^{ix\mu} S_P^{(T)}(k,\eta), \tag{2.99}$$

$$\Theta_B^{(T)}(\eta_0, \hat{n}, k) = [(1-\mu^2) e^{2i\phi}\xi^1(k) - (1-\mu^2) e^{-2i\phi}\xi^2(k)]\hat{\mathcal{B}} \int_0^{\eta_0} d\eta e^{ix\mu} S_P^{(T)}(k,\eta), \tag{2.100}$$

where we have introduced two new operators: $\hat{\mathcal{E}}(x) = -12 + x^2[1-\partial_x^2] - 8x\partial_x$ and $\hat{\mathcal{B}}(x) = 8x + 2x^2\partial_x$. We can then compute the three auto spectra:

$$\begin{aligned} C_{T\ell}^{(T)} &= \frac{4\pi}{2\ell+1}\int k^2 dk P_h(k) \sum_m \left| \int d\Omega Y_{\ell m}^{\star}(\hat{n}) \int_0^{\eta_0} d\eta S_T^{(T)}(k,\eta)(1-\mu^2) e^{2i\phi} e^{ix\mu} \right|^2 \\ &= (4\pi)^2 \frac{(\ell+2)!}{(\ell-2)!} \int k^2 dk P_h(k) \left| \int_0^{\eta_0} d\eta S_T^{(T)}(k,\eta) \frac{j_\ell(x)}{x^2} \right|^2, \end{aligned} \tag{2.101}$$

$$C_{E\ell}^{(T)} = (4\pi)^2 \int k^2 dk P_h(k) \left| \int_0^{\eta_0} d\eta S_P^{(T)}(k,\eta) \hat{\mathcal{E}}(x) \frac{j_\ell(x)}{x^2} \right|^2, \tag{2.102}$$

$$C_{B\ell}^{(T)} = (4\pi)^2 \int k^2 dk P_h(k) \left| \int_0^{\eta_0} d\eta S_P^{(T)}(k,\eta) \hat{\mathcal{B}}(x) \frac{j_\ell(x)}{x^2} \right|^2. \tag{2.103}$$

Applying the $\hat{\mathcal{E}}$ and $\hat{\mathcal{B}}$ operators we obtain:

$$C_{X\ell}^{(T)} = (4\pi)^2 \int k^2 dk P_h(k) [\Theta_{X\ell}^{(T)}(k)]^2, \tag{2.104}$$

where $X = T, E, B$. The quantities $\Theta_{T\ell}^{(T)}$ and $\Theta_{E,B\ell}^{(T)}$ are given by:

$$\Theta_{T\ell}^{(T)} = \sqrt{\frac{(\ell+2)!}{(\ell-2)!}} \int_0^{\eta_0} d\eta S_T^{(T)}(k,\eta) \frac{j_\ell(x)}{x^2}, \tag{2.105}$$

$$\Theta_{E,B\ell}^{(T)} = \int_0^{\eta_0} d\eta S_{E,B}^{(T)}(k,\eta) j_\ell(x). \tag{2.106}$$

Temperature source term is given in equation (2.96), while those of the polarization modes can be written as:

$$S_E^{(T)}(k,\eta) = g\left(K - \frac{\ddot{K}}{k^2} + \frac{2K}{x^2} - \frac{\dot{K}}{kx}\right) - \dot{g}\left(\frac{2\dot{K}}{k^2} + \frac{4K}{kx}\right) - 2\ddot{g}\frac{K}{k^2}, \tag{2.107}$$

$$S_B^{(T)}(k,\eta) = g\left(\frac{4K}{x} + \frac{2\dot{K}}{k}\right) + 2\dot{g}\frac{K}{k}. \tag{2.108}$$

To conclude this section it is worth to note that, until now, we have neglected a fundamental fact: the CMB anisotropy pattern we observe today is not actually the distribution emerged from the last scattering surface. CMB photons interact at some degree with the matter distribution while travelling from Recombination to the present epoch and these interactions cause distortions of the anisotropies field. These distortions are called *secondary anisotropies* and will be extensively discussed in the following sections. We just mention now one of them, which will not be investigated later on: *gravitational lensing*. CMB photons are deflected from their original path due to the presence of mass between the last scattering surface and us. This effect is well predicted by the General Relativity and makes lensing a fundamental tracer of the distribution of matter on large scales. For what concern the effect of the lensing deflection on the CMB power spectrum, it changes depending on the observable considered: in the case of temperature lensing does not generate any additional power, but rather redistributes it from large scales to smaller ones. The impact on E-modes is similar and it shows up as a smoothing of the acoustic peaks and trought of the power spectrum. For what regards the B-modes, instead, the effect is more important: lensing causes an increase of power due the generation of spurious B-modes from the distortion of primordial E-modes. This means that, in the presence of lensing, we will observe B-modes even if no primordial signal is present [41]. Figure 2.1, adapted from [42], shows the temperature, E-mode, lensing B-mode and TE power spectra. Different colours correspond to different experiments, while the dashed line shows the best-fit ΛCDM model.

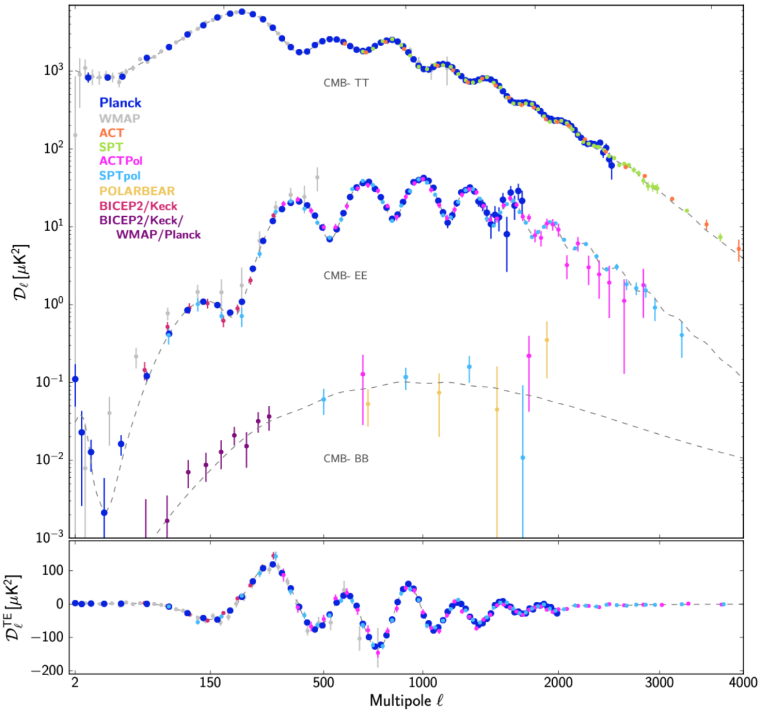

Figure 2.1: *The upper panel shows temperature, E-mode and lensing B-mode polarization power spectra, while the lower panel shows the cross-correlation spectrum between T and E. Different colours correspond to different experiments, while the dashed line shows the best-fit ΛCDM model to the Planck temperature, polarization, and lensing data. This figure is adapted from [42].*

2.2 Large Scale Structure

2.2.1 Boltzmann equation for cold dark matter

In the next chapter we will describe how the CMB power spectra, analysed in details in the previous section, is contamined, on small scale, by the interaction with the Large Scale Structure (LSS) [43]. In order to understand how matter is distributed in the Universe, how it clusters and forms structure, we need to study the evolution of dark matter perturbations. We use again the Boltzmann equation formalism, which can be applied to any component of the Universe. Dark matter distribution differs from that of photons as it does not interact with the other constituens of the Universe and, therefore, we don't have to deal with a collisional term. Moreover, it is a 'cold' component, which means that it is non-relativistic: the energy contribution is given not only by the momentum, as in the photon case, but also by the rest mass. The collsionless Boltzmann equation for non-relativistic matter is:

$$\frac{\partial f_{dm}}{\partial t} + \frac{\hat{p}^i}{a}\frac{p}{E}\frac{\partial f_{dm}}{\partial x^i} - \frac{\partial f_{dm}}{\partial E}\left[\frac{da/dt}{a}\frac{p^2}{E} + \frac{p^2}{E}\frac{\partial \Phi}{\partial t} + \frac{\hat{p}^i p}{a}\frac{\partial \Psi}{\partial x^i}\right] = 0, \tag{2.109}$$

where the term p/E is called velocity and $E \equiv \sqrt{p^2+m^2}$. To compute the first two moments of dark matter particle distribution we do not need to specify a distribution function, as in the case of the Bose-Eistein for photons: we directly take the moments of equation (2.109). In order to obtain the zero order moment we multiply both sides of equation (2.109) by the phase space volume $d^3p/(2\pi)^3$ and integrate. After some calculation we obtain:

$$\frac{\partial n_{dm}}{\partial t} + \frac{1}{a}\frac{\partial (n_{dm} v^i)}{\partial x^i} + 3\left[\frac{da/dt}{a} + \frac{\partial \Phi}{\partial t}\right] n_{dm} = 0, \tag{2.110}$$

having defined the dark matter density:

$$n_{dm} \equiv \int \frac{d^3p}{(2\pi)^3} f_{dm}, \tag{2.111}$$

and velocity:

$$v^i \equiv \frac{1}{n_{dm}} \int \frac{d^3p}{(2\pi)^3} f_{dm} \frac{p\hat{p}^i}{E}. \tag{2.112}$$

The first two terms represent the standard continuity equation of a fluid, while the last term arises due to the perturbation of the FLRW metric. From this equation we can get the evolution of the density background:

$$\frac{\partial n^{(0)}_{dm}}{\partial t} + 3n^{(0)}_{dm}\frac{da/dt}{a} = 0 \quad \rightarrow \quad n^{(0)}_{dm} \propto a^{-3}, \tag{2.113}$$

where we have neglected the terms including velocity and Φ (which are first order) and considered only the zero order part of the density. To obtain the first order of this equation we must retain all the term of equation (2.110) and consider first order perturbations of the density:

$$n_{dm} = n_{dm}^{(0)}[1 + \delta(\vec{x}, t)], \tag{2.114}$$

where the first order piece is $n_{dm}^{(0)}\delta = n_{dm}^{(0)}\delta\rho/\rho$. Considering only the first-order part of equation (2.110) and dividing by $n_{dm}^{(0)}$ we obtain:

$$\frac{\partial \delta}{\partial t} + \frac{1}{a}\frac{\partial v^i}{\partial x^i} + 3\frac{\partial \Phi}{\partial t} = 0. \tag{2.115}$$

In equation (2.110) we have two variables, the density perturbation δ and the velocity. To solve for these variables we need another equation, which we obtain taking the first moment of equation (2.109). We multiply the Boltzmann equation for dark matter by $d^3p/(2\pi)^3(p/E)\hat{p}^j$ and integrate. After some computation we get:

$$\frac{\partial (n_{dm} v^j)}{\partial t} + 4\frac{da/dt}{a}(n_{dm} v^j) + \frac{n_{dm}}{a}\frac{\partial \Psi}{\partial x^j} = 0. \tag{2.116}$$

This equation has no zero-order part, as all terms are multiplied by first order terms, velocity or Ψ. Thus we can consider only the density background, setting $n_{dm} \to n_{dm}^{(0)}$, and use $n_{dm}^{(0)} \propto a^{-3}$. We arrive at:

$$\frac{\partial v^j}{\partial t} + \frac{da/dt}{a} v^j + \frac{1}{a}\frac{\partial \Psi}{\partial x^j} = 0 \tag{2.117}$$

In order to obtain the final expression for the density and velocity we write equations (2.115) and (2.117) in terms of the conformal time η and operate a Fourier tranform. Assuming $\tilde{v}^i = (k^i/k)\tilde{v}$ the density equation becomes:

$$\dot{\tilde{\delta}} + ik\tilde{v} + 3\dot{\tilde{\Phi}} = 0, \tag{2.118}$$

and the velocity one:

$$\dot{\tilde{v}} + \frac{\dot{a}}{a}\tilde{v} + ik\tilde{\Phi} = 0. \tag{2.119}$$

In this analysis we have neglected all terms of second order in (p/E), which are those connected to the higher moments of the distributions. This choice is giustified by the fact that dark matter is cold and the only relevant moments are the first two.

2.2.2 Boltzmann equation for baryons

Ordinary matter occupies the cosmic structures generated by dark matter perturbations. Its emission contaminates the CMB power spectrum and will be extensively described in the next chapter. In order to undestand how this contamination is generated, we need to complete the picture of the cosmological components and describe the Boltzmann equation also for baryons. In Cosmological language the term baryon refers both to protons and electrons which are coupled through Coulomb scattering. Moreover electrons interacts with photons via Compton scattering. As electrons and protons are tightly coupled their overdensity can be set to a common value, δ_b. The same is valid for the velocity, where we consider $\vec{v}_e = \vec{v}_p \equiv \vec{v}_b$. To derive equations for δ_b and v_b we start from the unintegrated Boltzmann equations for electrons and protons:

$$\frac{df_e(\vec{x}, \vec{q}, t)}{dt} = \langle c_{ep} \rangle_{QQ'q'} + \langle c_{e\gamma} \rangle_{pp'q'}, \tag{2.120}$$

$$\frac{df_p(\vec{x}, \vec{Q}, t)}{dt} = \langle c_{ep} \rangle_{qq'Q'}. \tag{2.121}$$

We don't need the explicit form of the collisional term. We just provide some details of the notation appearing in equations (2.120) and (2.121): the simbol $'$ denote the momentum emerging from the scattering. The momentum of photons, electrons and protons are denoted respectively with $\vec{p}, \vec{q}$ and $\vec{Q}$. To conclude, the brackets indicates the integration over all momentum in the subscripts. It is worth to note that we neglected protons Compton scattering, whose cross section is negligible with respect to that of electrons for the same process. To derive an equation for δ_b we start from (2.120), multiply both sides by the phase space volume $d^3q/(2\pi)^3$ and integrate. When we perform the integral on the terms on the right, they vanish. This is due to the fact that the processes we are considering conserve the electron number density: they do not contribute to dn/dt, as the total number of electron produced, for example by Compton scattering, is also lost in the same process. At the end we are left with an equation for baryon density perturbations which is identical to the one of dark matter:

$$\dot{\tilde{\delta}}_b + ik\tilde{v}_b + 3\dot{\tilde{\Phi}} = 0, \tag{2.122}$$

where the subscript b indicates the quantities related to the baryons distribution. To obtain the equation for the velocity we need the first moment of Boltzmann equation. First we multiply the unintegrated equations by $\vec{q}$ (or $\vec{Q}$ for protons) and integrate. Then we add together equations (2.120) and (2.121) obtaining:

$$m_p \frac{\partial (n_b v_b^j)}{\partial t} + 4\frac{da/dt}{a} m_p n_b v_b^j + \frac{m_p n_b}{a}\frac{\partial \Psi}{\partial x^i} = \langle c_{ep}(q^j + Q^j)\rangle_{QQ'qq'} + \langle c_{e\gamma} q^j \rangle_{pp'q'q}. \tag{2.123}$$

The first integral on the right vanishes, for the conservation of the momentum, and we are left only with Compton scattering. Dividing both side by $\rho_b = m_p n_b^{(0)}$ we are left with:

$$\frac{\partial v_b^j}{\partial t} + \frac{da/dt}{a} v_b^j + \frac{1}{a}\frac{\partial \Psi}{\partial x^j} = \frac{1}{\rho_b}\langle c_{e\gamma} q^j \rangle_{pp'q'q}. \tag{2.124}$$

We can write explicitly the collisional term, having already Fourier transformed it:

$$\begin{aligned} \langle c_{e\gamma}\vec{q}\rangle_{pp'q'q} &= -\langle c_{e\gamma}\vec{p}\rangle_{pp'q'q} \\ &= \frac{n_e \sigma_T}{\rho_b}\int \frac{d^3p}{2\pi^2} p^4 \frac{\partial f^{(0)}}{\partial p}\int_{-1}^{1}\frac{d\mu}{2}\mu[\tilde{\Theta}_0 - \tilde{\Theta}(\mu) + \tilde{v}_b \mu], \end{aligned} \tag{2.125}$$

where the first equality is given by the conservation of the total momentum $\vec{q}+\vec{p}$. We integrate and obtain the final equation for the baryons velocity:

$$\dot{\tilde{v}}_b + \frac{\dot{a}}{a}\tilde{v}_b + ik\tilde{\Psi} = \dot{\tau}\frac{4\rho_\gamma}{3\rho_b}\left[3i\tilde{\Theta}_1 + \tilde{v}_b\right]. \tag{2.126}$$

2.2.3 Evolution of dark matter perturbations

The seeds of the formation of the LSS reside in the primordial gravitational instability. Matter tends to accumulate in initially overdense regions, whose growth is regulated by the competition between gravity and thermal pressure: while the first grabs more matter into the potential wells, random thermal motions cause a loss of mass from the overdense regions. As this balancing of forces takes place within the horizon, the described scenario predicts that perturbations grow differently outside or inside it. Moreover, the effect of pressure on the evolution of the perturbations depends on the component that dominates the energy content of the Universe at the moment in which a specific mode crosses the horizon. For this reason, we expect a different behaviour of modes that underwent the horizon crossing before or after the epoch of Equality, when the radiation dominated Universe became matter dominated. The perturbations growth is driven by the shape of the potential at different epochs. Our observations are limited to the distribution of matter at late epochs, so we need to relate the potential today to the primordial potential. We write:

$$\Phi(\vec{k},a) = \Phi_p(\vec{k}) \times [\text{Transfer Function(k)}] \times [\text{Growth Function}(a)] \,, \tag{2.127}$$

where Φ_p is the primordial potential, given by Inflation. The transfer function describes the evolution of perturbations through the epoch of horizon crossing, in the case it happened before or soon after the matter-radiation equality. The growth factor describes the evolution of the potential at late times in a fully matter dominated Universe. Conventionally the transfer function is normalized to the value of the potential at late times, in order to be equal to the unity at present epoch, when the evolution of the potential is driven by the growth factor. The transfer function is then defined as:

$$T(k) \equiv \frac{\Phi(k, a_{late})}{\Phi_{Large-scale}(k, a_{late})}. \tag{2.128}$$

The quantity a_{late} denotes an epoch well after the time of equality and $\Phi_{Large-scale}$ is the potential at such epoch, observed in large scale modes, which are those that enter the horizon at late times. Also the growth factor, D_1, includes a normalization: it is defined as the potential in a epoch after the transfer function regime, $\Phi(a)$, divided by the potential in a flat matter-dominated scenario, $\Phi(a_{late})$:

$$\frac{\Phi(a)}{\Phi(a_{late})} \equiv \frac{D_1(a)}{a} \quad (a > a_{late}). \tag{2.129}$$

The potential Φ can be related to the matter overdensity today through the Poisson's equation:

$$\Phi = \frac{4\pi G \rho_m a^2 \delta}{k^2} \quad (a > a_{late}). \tag{2.130}$$

Considering the background matter density $\rho_m = \Omega_m \rho_c / a^3$ and the first Friedmann's equation $4\pi G \rho_c = (3/2) H_0^2$ we can rewrite equation (2.130) as:

$$\delta(\vec{k},a) = \frac{k^2 \Phi(\vec{k},a) a}{(3/2)\Omega_m H_0^2} \quad (a > a_{late}). \tag{2.131}$$

We write equation (2.127) expliciting the large scales normalization, that will be described more in detail in the next section:

$$\Phi(\vec{k},a) = \frac{9}{10} \Phi_p(\vec{k}) T(k) \frac{D_1(a)}{a} \quad (a > a_{late}). \tag{2.132}$$

Plugging equation (2.132) into (2.131), we obtain a new expression for the matter overdensity:

$$\delta(\vec{k}, a) = \frac{3}{5}\frac{k^2}{\Omega_m H_0^2}\Phi_p(\vec{k})T(k)D_1(a) \quad (a > a_{late}). \tag{2.133}$$

As Φ_p is the inflationary potential, it is drawn from a gaussian distribution, whose variance is the the primodial power spectrum, P_Φ. As we have already seen in equation (1.33), the inflationary power spectrum can written as:

$$P_\Phi = \left(\frac{50\pi^2}{9k^3}\right)\left(\frac{k}{H_0}\right)^{n-1}\delta_H^2\left(\frac{\Omega_m}{D_1(a=1)}\right)^2, \tag{2.134}$$

where δ_H represents a primordial field of perturbations. Using (2.134) we can obtain the equation for the matter spectrum at late times:

$$P(k, a) = 2\pi^2\delta_H^2\frac{k^n}{H_0^{n+3}}T^2(k)\left(\frac{D_1(a)}{D_1(a=1)}\right)^2 \quad (a > a_{late}). \tag{2.135}$$

Equation (2.135) shows that, having the potential, we can compute the overdensity and its power spectrum, which can be compared to the observations of LSS today. We might also use the adimensional definition of the power spectrum:

$$\Delta^2(k) \equiv \frac{k^3 P(k)}{2\pi^2}. \tag{2.136}$$

Small Δ corresponds to small inhomogeneities, while large Δ indicates that the evolutions of perturbations has entered in the non-linear regime and equation (2.135) is no longer a good description of matter power spectrum. The linear power spectrum is shown in figure 2.2. To understand its shape we need to know the transfer function and the growth factor to plug in equation(2.127): their computation will be the focus of the next two sections.

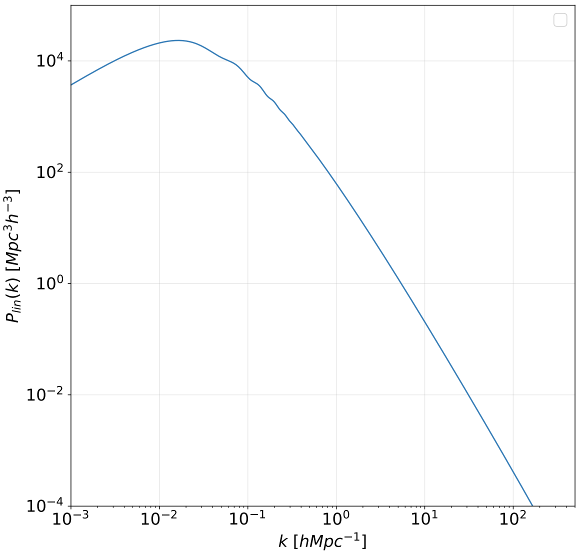

Figure 2.2: *Matter power spectrum computed with CAMB at redshift zero. The turnover corresponds to the scale that enters the horizon at epoch of Equality. Scales smaller than this were inside the horizon during radiation domination and their evolution have been suppressed by the competition between gravity and radiation pressure.*

2.2.4 Transfer function

The evolution of the dark matter overdensity can be obtained from a set of Boltzmann equations for the five variables $\Theta_0, \Theta_1, \delta, v, \Phi$:

$$\dot{\Theta}_{r,0} + k\Theta_{r,1} = -\dot{\Phi}, \tag{2.137}$$

$$\dot{\Theta}_{r,1} - \frac{k}{3}\Theta_{r,0} = -\frac{k}{3}\Phi, \tag{2.138}$$

$$\dot{\delta} + ikv = -3\dot{\Phi}, \tag{2.139}$$

$$\dot{v} + \frac{\dot{a}}{a}v = ik\Phi, \tag{2.140}$$

$$k^2\Phi + 3\frac{\dot{a}}{a}\left(\dot{\Phi} + \frac{\dot{a}}{a}\Phi\right) = 4\pi G a^2[\rho_{dm}\delta + 4\rho_r\Theta_{r,0}]. \tag{2.141}$$

The first two equations give the evolution of the monopole and dipole of the radiation perturbation. We need only the first two moments as, before Recombination, the tight coulping between radiation and baryons suppressed all other moments. After Recombination, instead, potential is fully dominated by matter and we can neglect the effect of radiation. The last equation is the time-time component of Einstein equation and is needed to constrain the gravitational potential. A solution to this set of equations, valid for every mode, can be computed numerically. For our purpose it is enough to sketch the solution for Φ and δ in four example cases:

- super-horizon waves: solving the set of Boltzmann equations in the case of very large modes, which reside outside the horizon, we obtain the following expression for the potential:

  $$\Phi = \frac{\Phi(0)}{10}\frac{1}{y^3}\left[16\sqrt{1+y} + 9y^3 + 2y^2 - 8y - 16\right], \tag{2.142}$$

  where:

  $$y \equiv \frac{a}{a_{eq}} = \frac{\rho_{dm}}{\rho_r}. \tag{2.143}$$

  At large y, once Universe has become matter-dominated, the y^3 term in the brackets dominates, so that $\Phi \to (9/10)\Phi(0)$. This means that the potential drops by a factor $1/10$ when Universe passes from radiation domination to matter domination, even if the mode hasn't entered the horizon. The factor $9/10$ is exactly the one used to normalize the transfer function to the large scales value, see equation (2.132).

- horizon-crossing waves during matter domination: the set of equations needed to solve for the potential in this case are three, as the radiation equations can be safely neglected. Combining the last three equations in (2.141), we obtain that the potential for modes entering the horizon in the matter dominated era is constant. Considering the large scale normalization, the transfer function results equal to unity for all modes of scale:

  $$k \ll k_{eq} = 0.073 Mpc^{-1}\Omega_m h^2. \tag{2.144}$$

- horizon-crossing waves before equality: during the radiation era matter is a subdominant component, and its perturbations simply follow the radiation-driven potential. To find a solution for the gravitational potential we use the radiation equations combined with the Einstein equation (first, second and last line in (2.141)). After some math one can find that:

  $$\Phi = 3\Phi_p\left(\frac{\sin\left(k\eta/\sqrt{3}\right) - (k\eta/\sqrt{3})\cos\left(k\eta/\sqrt{3}\right)}{(k\eta/\sqrt{3})^3}\right), \tag{2.145}$$

where Φ_p is the inflationary potential. Equation (2.145) tells that, if the horizon crossing happens during the radiation dominated era, the potential starts to decay. After the decay it starts oscillating, but the amplitudes of the oscillations decreases with the second power of the conformal time $\Phi \sim \Theta_0/\eta^2$. What happens is that, as the radiation perturbations oscillate in time rather than growing, the potential simply decays for the cosmological diluition of the background density. During this phase of the cosmic history, the density perturbation (which can be derived from line three and four of (2.141), using potential of equation (2.145)) can be written as:

$$\delta(k,\eta) = A\Phi_p \ln(B) + A\Phi_p \ln(k\eta), \tag{2.146}$$

where A and B are two constants. The solution is then the sum of a constant plus a logarithmic term. Despite the potential decaying, equation (2.146) says that the perturbations experience a growth, even if suppressed with respect to the matter dominated case.

- horizon-crossing waves soon after equality: in this epoch Universe isn't still fully matter dominated and there is more radiation than matter. Despite of this, radiation perturbations do not grow, due to pressure, while matter perturbations do. At some points dark matter overdensities become larger than those of radiation and start to evolve together with the potential, insensitive to the radiation effects. The matter perturbations evolution is regulated by the Meszaros equation:

  $$\delta'' + \frac{2+3y}{2y(y+1)}\delta' - \frac{3}{2y(y+1)}\delta = 0, \tag{2.147}$$

  where y is defined as in equation (2.143) and the upperscript $'$ denotes the derivative with respect to y. The solution to equation (2.147) is given by:

  $$\delta(k,y) = C_1 D_1(y) + C_2 D_2(y) \quad y \gg y_H, \tag{2.148}$$

  where y_H is the scale factor at the time of the horizon entering divided by the scale factor at equality. The C_1 and C_2 constants are determined in order to match the logarthmic solution of the previous case. The solution for $\delta(k,y)$ is now given by the sum of a linearly growing mode, $D_1 = y+3/2$, and a decaying mode, $D_2 \propto y^{-3/2}$.

In order to determine the evolution of matter perturbation at all scales we need to turn the matter overdensity into an expression for the transfer function. On large scales we already know that the value of the transfer function is normalized to unity. Consequently, we just need and expression for $T(k)$ in the small scale case. The transfer funtion is determined by the behaviour of δ well after the equality, when only the growing mode affect the evolution of perturbations. The perturbation can be written as:

$$\delta(\vec{k}, a) = \frac{3A\Phi_p(\vec{k})}{2} \ln\left[\frac{4Be^{-3}a_{eq}}{a_H}\right] D_1(a) \quad a \gg a_{eq}, \tag{2.149}$$

where we use the relation between the perturbation and the potential given by equation (2.130). The factors A and B originate from the continuity condition imposed to the coefficient of the growing mode, in order to match the solution before equality. Replacing the left side of equation (2.133) with the expression for δ in (2.149), we obtain the transfer function on small scales:

$$T(k) = \frac{12k_{eq}^2}{k^2} \ln\left[\frac{k}{8k_{eq}}\right] \quad k \gg k_{eq}, \tag{2.150}$$

where we have defined $k_{eq} \equiv a_{eq}H(a_{eq})$. This analytical solution is in good agreement with more complex fitting function, modelled in order to better spline the small and large scales behaviour. For our model we will use the $CAMB$ [44] or in alternative the Eisenstein and Hu [45] fitting functions. A complete expression for the transfer function includes also the effect of baryons. They represent only the 4% of the energy content of the Universe, so their effect on the matter transfer function is small. The presence of baryons causes a smoothing of the peaks on small scales: their coupling with photons before Recombination prevents them to contribute to the collapse of matter perturbations, which results to be smaller with respect to the case in which all matter is dark. Their tight coupling with photons is still visible as small oscillations of the matter power spectrum, located around $k \simeq 0.1hMpc^{-1}$, which are the imprints of the oscillatory behaviour of the photon−baryon fluid before Decoupling.

2.2.5 Growth factor

At redshift $z \lesssim 10$ all scales within the horizon evolve identically, as the modes smoothing due to radiation pressure is now negligible. The transfer function tends to unity and the evolution of the matter perturbatins starts to be driven by the growth factor. In order to correctly derive it we have to modify the *Meszaros equation* to keep into account the contribution of dark energy at very late times.

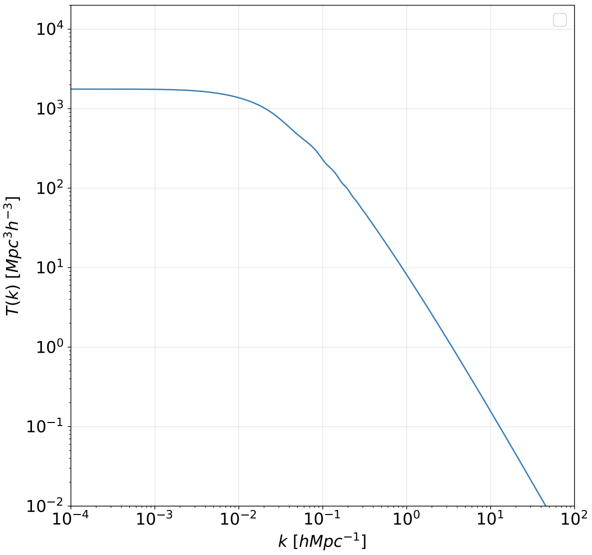

Figure 2.3: *Non normalized Eisenstein and Hu fitting function computed through the HaloMod code [46]*

The equation for the perturbations becomes:

$$\delta'' + ikv\left(\frac{d(aHy)^{-1}}{dy} - \frac{1}{aHy^2}\right) = \frac{3\Omega_m H_0^2}{2y^3a^2H^2a_{eq}}\delta. \tag{2.151}$$

We are looking for a growing mode, of the order of δ/H, as those modes survive long within the horizon. We find:

$$D_1(a) \propto H(a)\int \frac{da'}{(a'H(a'))^3}. \tag{2.152}$$

The proportionality constant is fixed to match the solution for the growth factor when matter still dominates. At that epoch $D_1 = a$ and $H = H_0\Omega_m^{1/2}a^{-3/2}$ so the final expression for the growth factor is:

$$D_1(a) = \frac{5\Omega_m}{2}\frac{H(a)}{H_0}\int_0^a \frac{da'}{(a'H(a')/H_0)^3}. \tag{2.153}$$

If the Universe was flat and matter dominated, the growth factor wuold be simply equal to the scale factor. The presence of dark energy instead suppresses the growth at late times. The conclusion is that, in a Universe dominated by the cosmological constant, the cosmic structures develop earlier in time, while at later times their evolution is suppressed.

3

Lack-of-correlation anomaly in CMB large scale polarisation maps

In this chapter it is reported the first project carried out during my Ph.D. It focuses on CMB large scales, where we have investigated one of the so-called CMB temperature anomalies by looking for its polarization counterpart.

As we have extensively discussed in the previous chapters, the CMB is one of the most important cosmological observables and has greatly contributed to the success of the standard ΛCDM model. Nonetheless, anomalous features exist in the large-angle CMB anisotropy pattern which are in tension with the predictions of ΛCDM. Their statistical significance is assessed at the $2-3\sigma$ level depending on the particular estimator chosen. Several CMB anomalies exist [47]. In the following we will focus on the lack-of-correlation anomaly, which consists of a suppression in the CMB two-point correlation function at large angular scales with respect to the best-fit ΛCDM model [48–52]. This anomaly is directly connected to the so-called CMB lack-of-power anomaly, for which the lack of correlation shows up as a reduction of anisotropy power at large angular scales [53–57] and to others as well [58–61].

Two independent experiments, WMAP and *Planck* [62–65], agree well on these deviations, therefore limiting (but not completely excluding) the possibility of an instrumental origin. An alternative astrophysical explanation of these anomalies is the possible presence of residuals of Galactic emission. However, this explanation seems unlikely given that foreground cleaning at large angular scales is usually performed on maps and an imperfect subtraction would normally result into an increase rather than a decrease of power[1]. A pragmatic approach

---

[1] A possible exception is the presence of chance correlations between foreground and the CMB which appears also unlikely.

is therefore to consider the CMB anomalies as correctly measured features in the CMB temperature pattern and assess their statistical significance, e.g. correctly including look-elsewhere effects [66].

If we accept the above point of view, then there are two possible explanations for these features: either we live in a rare (yet not exceedingly rare) realisation of a ΛCDM cosmology or we need a modification of ΛCDM to account for them. Discriminating between these two hypotheses can only happen based on some acceptable a posteriori probabilities to exceed. Unfortunately, the anomalies show up at large angular scales where the temperature field is already cosmic variance limited, so any additional data, while always useful for consistency tests, are not going to boost statistical significance.

Improvements can however be expected by including the CMB polarisation pattern, whose measurements are still far from reaching cosmic variance accuracy especially at large scales, where the systematic error budget is currently non negligible[2]. In the study of CMB anomalies, several analyses that include polarisation have been performed on the *Planck* legacy data [68], using various estimators to quantify statistical significance jointly in temperature and polarization. The most adopted estimator has been proposed in [69] and only uses temperature to E-mode correlations (TE). It has been extended to incorporate polarization auto-spectra EE and BB information in [70]. The latter is employed, among others, by the *Planck* collaboration in their own analysis [68]. Other estimators have been proposed: see for instance [71] where a one-dimensional statistic involving TT, TE, EE angular power spectra is employed.

Incorporating polarization into a joint estimator calls for a choice. On the one hand, it is desirable to test whether the polarization observations are consistent with ΛCDM once the temperature observations are given. This can be accomplished by using constrained realizations of the joint temperature and polarization fields. On the other hand, it is also useful to test the significance of anomalies in temperature and polarization leaving both fields free to fluctuate within the ΛCDM predictions. This implies dealing with unconstrained (i.e. open) realisations. For instance, authors in [69] work under the first assumption, while the *Planck* collaboration [68] assumes the second.

In our work, we analysed the consequences of either assumptions. We employed two datasets: the first one is based on the cross-spectra between *Planck* 100 and 143 GHz channels obtained with the `SRoll2` processing [72] while the second is based on the auto-spectra obtained combining the *Planck* 70 GHz channel with

---

[2] The power spectrum of *Planck* HFI 100×143 is cosmic variance dominated between $\ell = 3$ and $\ell = 5$; see figure 10 of [67].

the Ka, Q and V bands of WMAP [73]. These two datasets cannot be easily further combined because a proper combination should happen at map level (as it has been done for *Planck* 70 GHz and WMAP) but the *Planck* 100 and 143 GHz channels do not allow for this. Therefore we analysed the two datasets separately. We stress that these datasets have never been employed in the context of CMB anomalies before. This is an aspect where our analysis is entirely novel.

We focused on the lack of correlation anomaly in polarization by considering the correlation functions C^{QQ} and C^{UU}, Q and U being the linear polarization Stokes parameters. We considered also the C^{EE} correlation function as proposed in [70].

3.1 Datasets and methodology

We considered the most constraining large-scale polarization datasets currently available, i.e. the cross-spectra between *Planck* 100 and 143 GHz channels [74] as presented in [67, 72] (hereafter *Planck* HFI 100×143) and the auto-spectra obtained combining the *Planck* 70 GHz channel [75] with the Ka, Q and V bands of WMAP [76] as presented in [73] (hereafter *Planck* LFI+WMAP). Here we briefly provide some general information useful to understand the procedure followed in preparing the former datasets. All the maps contained in the two datasets are mitigated from polarized Galactic foreground emissions (thermal dust and synchrotron) through a template fitting procedure, see e.g., [77, 78]. In the *Planck* LFI+WMAP dataset the auto-spectra are computed from the CMB map, built through an optimal weighting of the four foreground reduced input maps (i.e. 70 GHz, Ka, Q and V). In temperature both datasets employ the `Commander` *Planck* 2018 CMB solution smoothed trough a Gaussian kernel with FWHM of 440 arcminutes and downgraded to a `HEALpix`[3] $\mathrm{N_{side}} = 16$ resolution [79, 80]. The polarization maps are instead smoothed assuming a cosine window profile as suggested in [81, 82], and re-pixelized to the same `HEALpix` resolution as temperature. We selected a useful sky fraction of 50% of *Planck* HFI 100×143 and 54% for *Planck* LFI+WMAP as suggested respectively in [67] and in [73]. Note that, as detailed above, we have chosen to use the Planck HFI polarization data in the form of cross-power spectra, as described in [67]. In order to be consistent, we have adopted the same harmonic based approach also for the other dataset considered.

---

[3] `https://healpix.sourceforge.io/`

In order to estimate the angular power spectra from the CMB maps we employed a Quadratic Maximum Likelihood (hereafter QML) method as presented in [82–84]. For a given map $\mathbf{x} = (\mathbf{T}, \mathbf{Q}, \mathbf{U})$ the QML provides the estimated auto angular power spectra as

$$\hat{C}_\ell^X = \sum_{\ell', X'} (F^{-1})^{X,X'}_{\ell\ell'} \left[\mathbf{x}^t \mathbf{E}^{\ell'}_{X'} \mathbf{x} - \mathrm{Tr}(\mathbf{N}\mathbf{E}^{\ell'}_{X'}) \right], \tag{3.1}$$

where X and X' are one of TT, EE, BB, TE, TB, EB and $F^{\ell\ell'}_{X,X'}$ is the Fisher information matrix defined as

$$F^{\ell\ell'}_{X,X'} = \frac{1}{2}\mathrm{Tr}\left[\mathbf{C}^{-1} \frac{\partial \mathbf{S}}{\partial C_\ell^X} \mathbf{C}^{-1} \frac{\partial \mathbf{S}}{\partial C_\ell^{X'}} \right], \tag{3.2}$$

with $\mathbf{C} \equiv \mathbf{S}(C_\ell) + \mathbf{N}$ being the CMB signal ($\mathbf{S}$) plus noise ($\mathbf{N}$) covariance matrix and C_ℓ a fiducial set of CMB angular power spectra. Finally, the $\mathbf{E}$ matrix in eq. (3.1) is given by

$$\mathbf{E}^\ell_X = \frac{1}{2}\mathbf{C}^{-1} \frac{\partial \mathbf{S}}{\partial C_\ell^X} \mathbf{C}^{-1}. \tag{3.3}$$

Assuming uncorrelated noise between two maps $\mathbf{x}_a$ and $\mathbf{x}_b$, eq. (3.1) can be easily extended to cross-spectrum estimation which reads

$$\hat{C}_\ell^X = \sum_{\ell', X'} (F^{-1})^{X,X'}_{\ell\ell'} \mathbf{x}_a^t \mathbf{E}^{\ell'}_{X'} \mathbf{x}_b, \tag{3.4}$$

having defined

$$\begin{aligned} F^{\ell\ell'}_{X,X'} &= \frac{1}{2}\mathrm{Tr}\left[\mathbf{C}_a^{-1} \frac{\partial \mathbf{S}}{\partial C_\ell^X} \mathbf{C}_b^{-1} \frac{\partial \mathbf{S}}{\partial C_\ell^{X'}} \right], && (3.5) \\ \mathbf{E}^\ell_X &= \frac{1}{2}\mathbf{C}_a^{-1} \frac{\partial \mathbf{S}}{\partial C_\ell^X} \mathbf{C}_b^{-1}, && (3.6) \\ \mathbf{C}_a &= \mathbf{S}(C_\ell) + \mathbf{N}_a, \\ \mathbf{C}_b &= \mathbf{S}(C_\ell) + \mathbf{N}_b. \end{aligned}$$

For the two aforementioned datasets we also considered a set of 500 noise plus residual systematics simulations described in the two dedicated papers [67, 72].

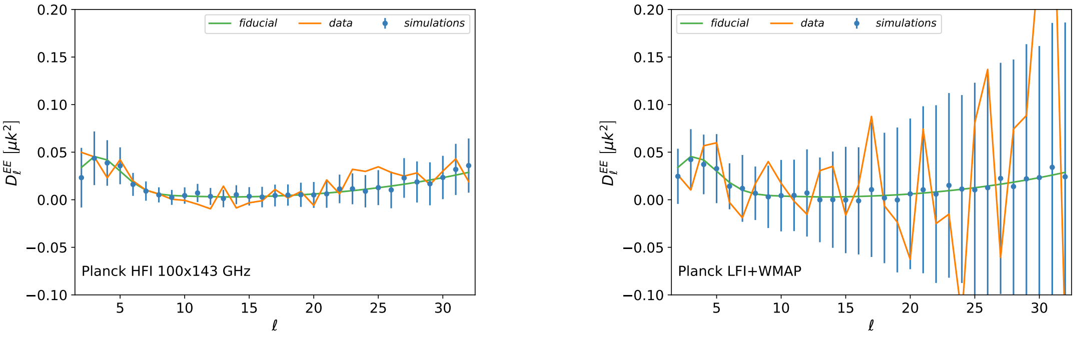

Figure 3.1: *E-mode angular power spectrum $D_\ell^{EE} \equiv \ell(\ell+1)C_\ell^{EE}/2\pi$ for Planck HFI 100×143 GHz (left panel) and Planck LFI+WMAP (right panel). The orange line is the data power spectrum while blue dots are the mean of power spectra extracted from 250000 constrained maps. The error bars have been computed as the standard deviation of the simulations. Note that the range of values on the y-axis is the same for both panels.*

3.2 Analysis

As discussed in the introduction of the chapter we used both constrained and unconstrained simulations of the temperature and polarization fields. To build the set of constrained realizations we followed the procedure described in [69] and generated the polarized spherical harmonic coefficients, $a_{\ell m}^E$ and $a_{\ell m}^B$, as

$$\begin{aligned} a_{\ell m}^E &= \frac{C_\ell^{TE}}{C_\ell^{TT}} a_{\ell m}^{T_{data}} + \zeta_1 \sqrt{C_\ell^{EE} - \frac{(C_\ell^{TE})^2}{C_\ell^{TT}}}, \\ a_{\ell m}^B &= \zeta_2 \sqrt{C_\ell^{BB}}, \end{aligned} \tag{3.7}$$

where ζ_1 and ζ_2 are random Gaussian realizations with zero mean and unit variance, C_ℓ^{XX} are the spectra corresponding to the *Planck* best fit ΛCDM model and $a_{\ell m}^{T_{data}}$ are extracted from the observed temperature map, assuming negligible noise. When building maps from spherical harmonic coefficients, we applied the same aforementioned window functions. Finally, we combined each of the 500 simulated CMB signal maps with all the 500 noise maps described in the previous section, forming a set of 250000 signal plus noise (hereafter `S+N`) realizations. In figure 3.1 we show the E-mode power spectra of the data maps compared with mean and standard deviations of the corresponding spectra of our `S+N` Monte Carlo. Both *Planck* HFI 100×143 and *Planck* LFI+WMAP spectra do not show any evident outlier when compared to `S+N` simulations.

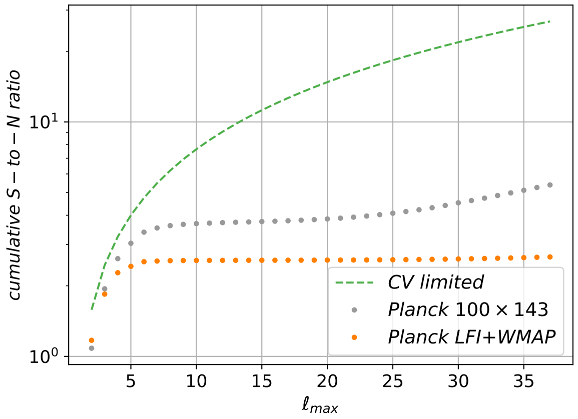

Figure 3.2: *Comparison of the integrated signal to noise ratio for the Planck HFI 100×143 (grey dots) and Planck LFI+WMAP (orange dots) dataset and for a sample of ideal simulations (green dashed line). Both datasets show a plateau above* $\ell_{\max} \simeq 10$*, which is consequently chosen as maximum multipole in the analysis. For Planck HFI 100×143 a rise in trend is visible at* $\ell_{\max} > 20$*, due to the corresponding increase in the E-mode signal. This effect can be safely ignored in our analysis.*

We started computing the signal-to-noise ratio, S/N,

$$\frac{S}{N} = \sqrt{\sum_{\ell=2}^{\ell_{\max}} \left(\frac{C_\ell^{EE}}{\sigma_\ell}\right)^2}, \tag{3.8}$$

where C_ℓ^{EE} is a fiducial power spectrum, σ_ℓ is the standard deviation of the `S+N` simulations and $\ell_{\max}$ is the maximum multipole considered in the sum. In Figure 3.2 it is shown S/N as a function of $\ell_{\max}$ for our two datasets and for a cosmic variance limited full sky survey. As expected, *Planck* HFI 100×143 has a better S/N ratio with respect to *Planck* LFI+WMAP for almost all the $\ell_{\max}$ considered. The only exception is the quadrupole, where the *Planck* HFI 100×143 variance is dominated by residual dipole leakage (see [67, 72] for details [4]). Both datasets considered show a plateau above $\ell_{\max} \simeq 10$ where the variance of the noise starts dominating the total variance. This justifies our choice of $\ell_{\max} = 10$ as maximum multipole in the following analysis.

---

[4] Figure 10 of [72], in particular, shows that, for the lowest multipoles, the dominant contribution to the total uncertainty is the cosmic variance, except for the quadrupole, where a still large amount of extra-variance noise is clearly visible.

3.2.1 Estimators

We focused on an estimator originally suggested by the WMAP team, called $S_{1/2}$ [48]. The idea of this estimator is to measure the distance between the correlation function and zero over a chosen range of angles [51]. We formally define this estimator in the next subsection.

3.2.1.1 Temperature

As anticipated in the previous chapter CMB temperature fluctuations are usually expanded in terms of scalar spherical harmonics:

$$\frac{\Delta T(\hat{n})}{T_0} \equiv \Theta(\hat{n}) = \sum_{\ell m} a^T_{\ell m} Y_{\ell m}(\hat{n}) \,, \tag{3.9}$$

and the covariance of the coefficients $a^T_{\ell m}$ defines the anisotropy angular power spectrum,

$$\langle a^T_{\ell m} a^{T\star}_{\ell' m'} \rangle = C^{TT}_\ell \delta_{\ell\ell'} \delta_{mm'} \,, \tag{3.10}$$

standing the assumption of statistical isotropy and independence of the modes. The angular power spectrum, C^{TT}_ℓ, and the two-point angular correlation function, $C(\theta)$, are related by the following expression,

$$C(\theta) \equiv \langle \Theta\left(\hat{n}_1\right) \Theta\left(\hat{n}_2\right) \rangle = \frac{1}{4\pi} \sum_{\ell=0}^{\infty} \left(2\ell+1\right) C^{TT}_\ell \mathcal{P}_\ell\left(\cos(\theta)\right) , \tag{3.11}$$

where $\hat{n}_1 \cdot \hat{n}_2 = \cos(\theta)$ and $\mathcal{P}_\ell$ are the Legendre Polynomials. The $S_{1/2}$ statistic in temperature, is defined as

$$S^{TT}_{1/2} \equiv \int_{-1}^{1/2} d(\cos\theta) [C^{TT}(\theta)]^2 \,, \tag{3.12}$$

and is used to quantify the lack of correlation at scales larger than 60°. Substituting (3.11) into (3.12) we can rewrite the estimator in terms of the angular power spectrum,

$$S^{TT}_{1/2} = \sum_{\ell=2}^{\ell_{max}} \sum_{\ell'=2}^{\ell'_{max}} \frac{(2\ell+1)}{4\pi} \frac{(2\ell'+1)}{4\pi} C^{TT}_\ell I_{\ell\ell'} C^{TT}_{\ell'} , \tag{3.13}$$

where the matrix $I_{\ell\ell'}$ is defined as

$$I_{\ell\ell'}(x) \equiv \int_{-1}^{x} \mathcal{P}_{\ell}(x')\mathcal{P}_{\ell'}(x')dx', \tag{3.14}$$

and evaluated at $x = 1/2$, with $x = \cos\theta$.

Before proceeding with the details of the polarization analysis, it is worth underlining that the method just described presents some differences with the pixel-based method applied in Ref. [68] on the Planck Commader temperature map. In particular, in our work we have shown that the two-point correlation functions built from harmonic or pixel-space data are equivalent only in the full sky case. See Appendix *0.1*.

3.2.1.2 Polarization

Linear polarization is a spin-2 quantity and can be described by the Stokes parameters Q and U [85]. In analogy with T we can define the corresponding two-point angular correlation function as $C^{QQ}(\theta) = \langle Q_r(\hat{n}_1)Q_r(\hat{n}_2)\rangle$ and $C^{UU}(\theta) = \langle U_r(\hat{n}_1)U_r(\hat{n}_2)\rangle$. The Stokes parameters appearing in the correlation functions are defined with respect to a reference frame on the tangent plane with axes parallel and perpendicular to the great arch connecting $\hat{n}_1$ and $\hat{n}_2$. As in [85] we choose one point to be the north pole and the other on $\phi = 0$ longitude. This choice is denoted by the suffix r in the above definitions of the correlations functions, which will be omitted for the rest of the chapter to simplify the notation. The coordinate system is hence fixed and the correlation functions depend only on the separation θ between $\hat{n}_1$ and $\hat{n}_2$. The definition of $S_{1/2}$ in polarisation is analogous to the temperature case,

$$S_{1/2}^{QQ,UU} \equiv \int_{-1}^{1/2} d(\cos\theta)[C^{QQ,UU}(\theta)]^2, \tag{3.15}$$

but it is useful again to rewrite it in terms of the angular power spectrum. We start writing the Q and U correlation funtions in terms of the C_ℓ^{EE} and C_ℓ^{BB}

computed in (2.79):

$$C^{QQ}(\theta) = -\sum_{\ell} \frac{2\ell+1}{4\pi} \left(\frac{2(\ell-2)!}{(\ell+2)!} \right) [C_\ell^{EE} G^+_{\ell 2}(\cos(\theta)) + C_\ell^{BB} G^-_{\ell 2}(\cos(\theta))], \tag{3.16a}$$

$$C^{UU}(\theta) = -\sum_{\ell} \frac{2\ell+1}{4\pi} \left(\frac{2(\ell-2)!}{(\ell+2)!} \right) [C_\ell^{BB} G^+_{\ell 2}(\cos(\theta)) + C_\ell^{EE} G^-_{\ell 2}(\cos(\theta))], \tag{3.16b}$$

where

$$G^+_{\ell m}(\cos\theta) = -\left(\frac{\ell - m^2}{\sin^2\theta} + \frac{\ell(\ell+1)}{2} \right) \mathcal{P}_\ell^m(\cos\theta) + (\ell+m)\frac{\cos\theta}{\sin^2\theta}\mathcal{P}_{l-1}^m(\cos\theta), \tag{3.17a}$$

$$G^-_{\ell m}(\cos\theta) = \frac{m}{sin^2\theta} \left((\ell-1)\cos(\theta)\mathcal{P}_\ell^m(\cos\theta) - (\ell+m)\mathcal{P}_{l-1}^m(\cos\theta) \right), \tag{3.17b}$$

being the $\mathcal{P}_\ell^m(\cos\theta)$ the associated Legendre polynomials. Plugging eq. (3.16) into (3.15) we obtain the following expression:

$$S_{1/2}^{QQ} = \sum_{\ell=2}^{\ell_{max}} \sum_{\ell'=2}^{\ell'_{max}} \frac{2\ell+1}{8\pi} \frac{2\ell'+1}{8\pi} \left(C_\ell^{EE} I^{(1)}_{\ell\ell'} C_{\ell'}^{EE} + C_\ell^{BB} I^{(3)}_{\ell\ell'} C_{\ell'}^{BB} + C_\ell^{EE} I^{(2)}_{\ell\ell'} C_{\ell'}^{BB} + C_\ell^{EE} I^{(4)}_{\ell\ell'} C_{\ell'}^{BB} \right), \tag{3.18}$$

where we have followed the notation of [70]. For $S_{1/2}^{UU}$ matrices $I^{(3)}_{\ell\ell'}$ and $I^{(1)}_{\ell\ell'}$ are swapped. More details on this calculation as well as the definition of the $I^{(X)}_{\ell\ell'}$ matrices are given in Appendix *0.2*.

3.2.1.3 *Two-point correlation functions for E- and B-modes*

An alternative to Q and U is to express the polarization in terms of local E- and B-modes. Their use has been suggested by [70] in the context of polarization correlation functions to complement the information given by Q and U, as we will show in the next section. The local correlation functions for E and B are defined as:

$$C^{\hat{E}\hat{E}}(\theta) = \langle \hat{E}(\hat{n}_1)\hat{E}(\hat{n}_2) \rangle, \tag{3.19a}$$

$$C^{\hat{B}\hat{B}}(\theta) = \langle \hat{B}(\hat{n}_1)\hat{B}(\hat{n}_2) \rangle, \tag{3.19b}$$

where the $\hat{B}(\hat{n})$ and $\hat{E}(\hat{n})$ functions are expanded as:

$$\hat{E}(\hat{n}) = \sum_{\ell,m} \sqrt{\frac{(\ell+2)!}{(\ell-2)!}} a^{E}_{\ell,m} Y_{\ell,m}(\hat{n}), \tag{3.20a}$$

$$\hat{B}(\hat{n}) = \sum_{\ell,m} \sqrt{\frac{(\ell+2)!}{(\ell-2)!}} a^{B}_{\ell,m} Y_{\ell,m}(\hat{n}). \tag{3.20b}$$

The two-point angular correlation functions can be written in terms of the angular power spectrum, in analogy with temperature:

$$C^{\hat{E}\hat{E}}(\theta) = \sum_{\ell} \frac{2\ell+1}{4\pi} \frac{(\ell+2)!}{(\ell-2)!} C^{EE}_{\ell} \mathcal{P}_{\ell}(\cos\theta), \tag{3.21a}$$

$$C^{\hat{B}\hat{B}}(\theta) = \sum_{\ell} \frac{2\ell+1}{4\pi} \frac{(\ell+2)!}{(\ell-2)!} C^{BB}_{\ell} \mathcal{P}_{\ell}(\cos\theta), \tag{3.21b}$$

and the expressions for the estimators $S^{EE}_{1/2}$ and $S^{BB}_{1/2}$ are:

$$S^{XX}_{1/2} = \sum_{\ell=2}^{\ell_{max}} \sum_{\ell'=2}^{\ell'_{max}} \frac{2\ell+1}{4\pi} \frac{(\ell+2)!}{(\ell-2)!} \frac{2\ell'+1}{4\pi} \frac{(\ell'+2)!}{(\ell'-2)!} C^{XX}_{\ell} I_{\ell,\ell'} C^{XX}_{\ell'}, \tag{3.22}$$

where X can be E or B and $I_{\ell\ell'}$ is the same kernel defined in eq. (3.14) above.

3.3 Results

In this section we present results obtained for the correlation functions and for the distribution of the $S_{1/2}$ estimators, for the Q, U and local E-modes fields. For the sake of brevity, we only show plots for constrained simulations, while in Table 3.1 we report the results for both the constrained and unconstrained case. We start by discussing our results on the Q, U and local E-modes correlation functions, which are needed to better highlight the specificity of the $S^{QQ}_{1/2}$, $S^{UU}_{1/2}$ and $S^{EE}_{1/2}$ estimators.

We show in Fig. 3.3 and 3.4 the QQ and UU angular correlation functions for both the *Planck* LFI+WMAP and *Planck* HFI 100×143 datasets, along with mean values and confidence intervals derived from constrained simulations, setting $\ell_{max} = 10$. In Fig. 3.5 we show instead the correlation function for local

E-modes. Note that only in this latter case the different noise levels of the *Planck* LFI+WMAP and *Planck* HFI 100×143 datasets clearly show up in the plots. Such behaviour can be ascribed to the weights applied to each multipole when computing the correlation functions out of power spectra. In order to further clarify this aspect we show in Fig. 3.6 the geometrical weights of C_ℓ^{EE} in the definition of Q and local E-modes correlation functions, see eq. (3.17a):

$$W_Q(\theta) = \sum_\ell \frac{2\ell+1}{4\pi}\left(\frac{2(\ell-2)!}{(\ell+2)!}\right) G^+_{\ell 2}(\cos(\theta)), \tag{3.23a}$$

$$W_{\hat{E}}(\theta) = \sum_\ell \frac{2\ell+1}{4\pi}\frac{(\ell+2)!}{(\ell-2)!}\mathcal{P}_\ell(\cos\theta) \tag{3.23b}$$

Here $G^+_{\ell 2}$ is defined as in eq. (3.17a). Both quantities entering the definition of the weights (i.e. the angle θ and the multipole ℓ) are binned and the plots show the total weight inside each bin. To highlight the contribution of the quadrupole it is shown without applying any binning. Fig. 3.6 shows how the Q and U correlation functions are dominated by very low multipoles, in particular by the quadrupole, while the correlation function of local E-modes is more susceptible to variations at high multipoles considered here. This has a clear impact on the variance of the correlation function itself. If the Q correlation function is computed only from the quadrupole, *Planck* LFI+WMAP is more sensitive than *Planck* HFI 100×143 (see Fig. 3.7), being the latter dominated by residual dipole leakage, as shown in Fig. 3.2. For all the higher multipoles, instead, *Planck* HFI 100×143 is clearly more constraining (see Fig. 3.8), partially, but not completely, compensating the quadrupole behaviour. Analogous results can be obtained for U Stokes field. The same multipole split for local E modes does not show the same trend, as the variance of the correlation function remains substantially unchanged if the quadrupole is excluded. E modes can be defined in terms of the power spectrum directly as scalar quantities, see equation 19 of [70]. These non-local E modes behave similarly to the Q and U correlation functions, as also in this case the geometrical weights applied to the C_ℓ^{EE} mainly insist on the lowest multipoles, especially the quadropule. For this reason we decided to omit the non-local E modes case in the our work.

In figures 3.9, 3.10 and 3.11 we plot in light grey the distribution of the $S_{1/2}$ estimators for the Q and U fields respectively and for the local E modes, as defined in eq. (3.18) and (3.22). The red line represents the value of the estimators on data. In all figures the panel on the left refers to the *Planck* HFI 100×143 dataset and the one on the right to the *Planck* LFI+WMAP dataset.

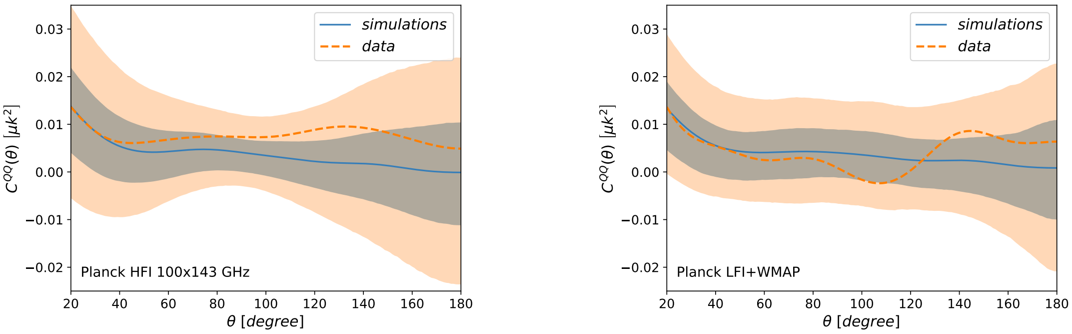

Figure 3.3: *Two point angular QQ correlation function. The orange dashed line represents data while the blue line is the mean of 250000 constrained simulations. The shaded region represents the 68% and 95% C.L.. The datasets employed are Planck HFI 100×143 on the left and Planck LFI+WMAP on the right. The analysis has been performed up to* $\ell = 10$.

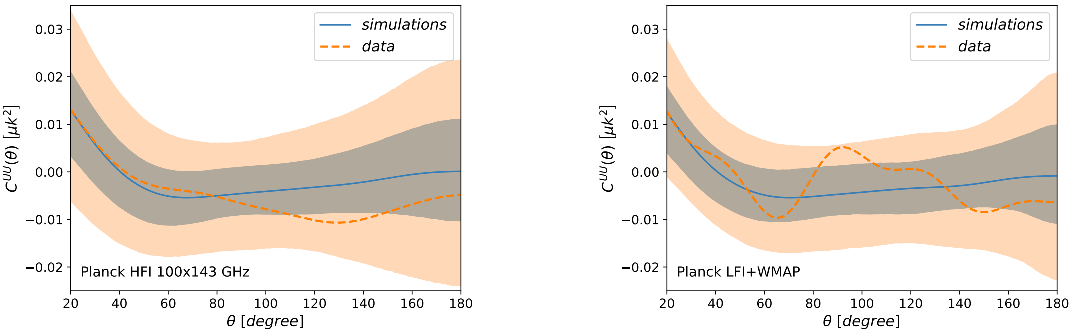

Figure 3.4: *As in Fig. 3.3 above but for the UU correlation function instead of QQ.*

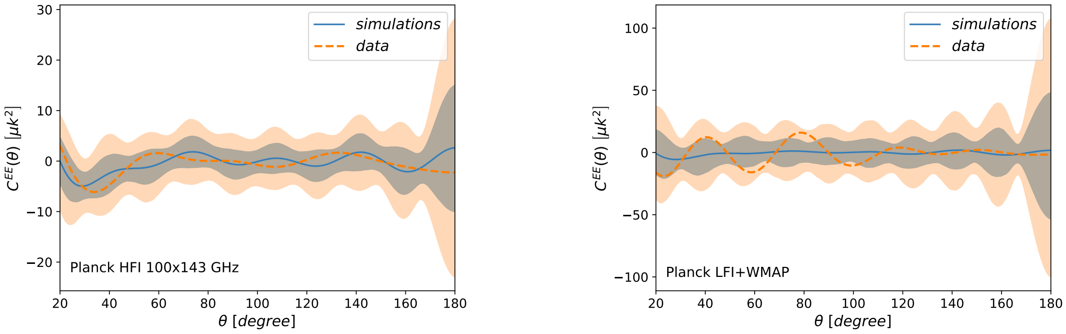

Figure 3.5: *As in Fig. 3.3 above but for the two-point angular correlation function built from E-modes.*

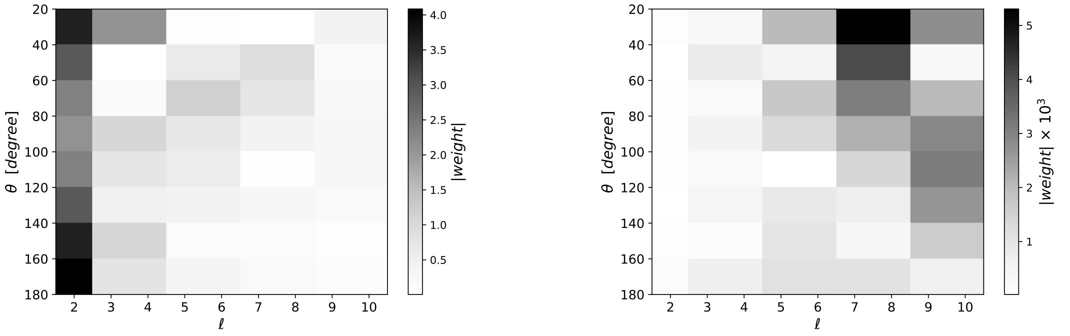

Figure 3.6: *Absolute value of binned geometrical weights applied to* C_ℓ^{EE}*s entering in the definition of the Q Stokes parameter (left panel) and of the local E-modes (on the right) correlation functions.*

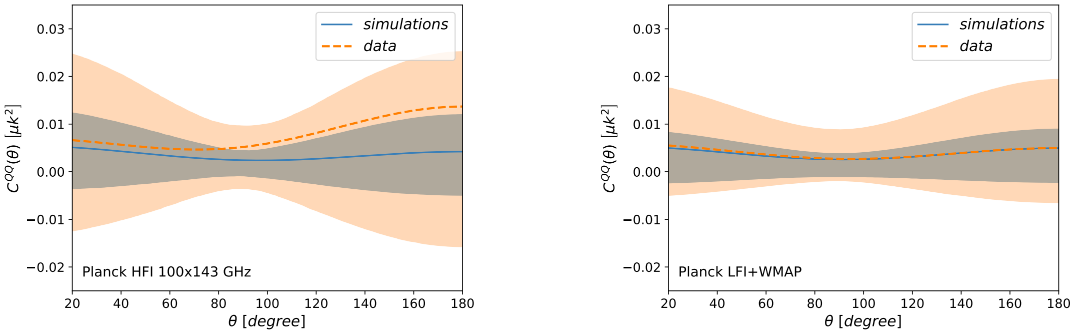

Figure 3.7: *Two point angular Q correlation function computed only with the quadrupole contribution. The shaded region represents the 68% and 95% C.L. The datasets employed are Planck HFI 100×143 on the left and Planck LFI+WMAP on the right.*

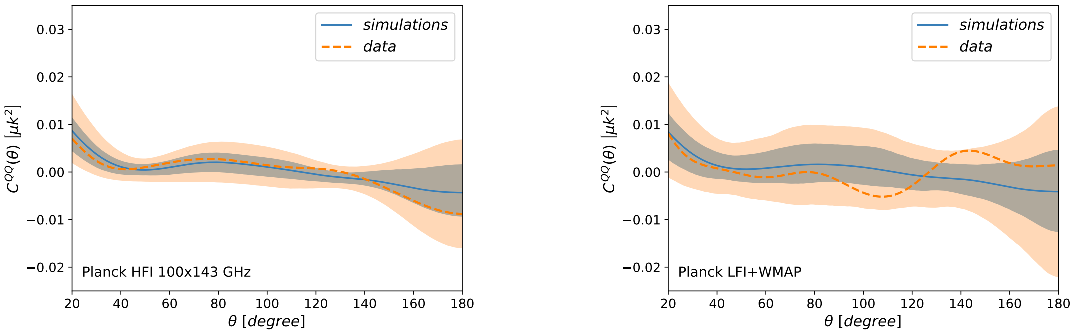

Figure 3.8: *Two point angular Q correlation function computed starting from the octupole. The shaded region represents the 68% and 95% C.L. The datasets employed are Planck HFI 100×143 on the left and Planck LFI+WMAP on the right. The analysis has been performed up to* $\ell_{\max} = 10$.

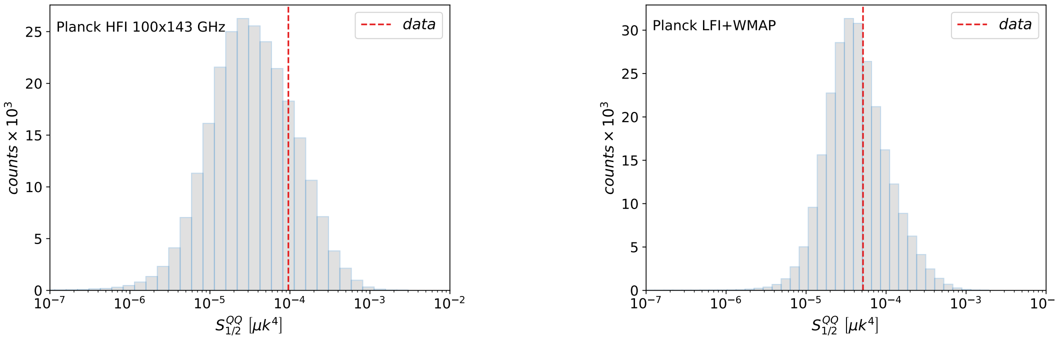

Figure 3.9: *Empirical distribution for* $S_{1/2}$ *values from simulations (grey) and data (red). The estimator has been computed on* Q *correlation function. The maximum multipole used is* $\ell_{max} = 10$*. The left panel is for Planck HFI 100×143 dataset and the right one for Planck LFI+WMAP .*

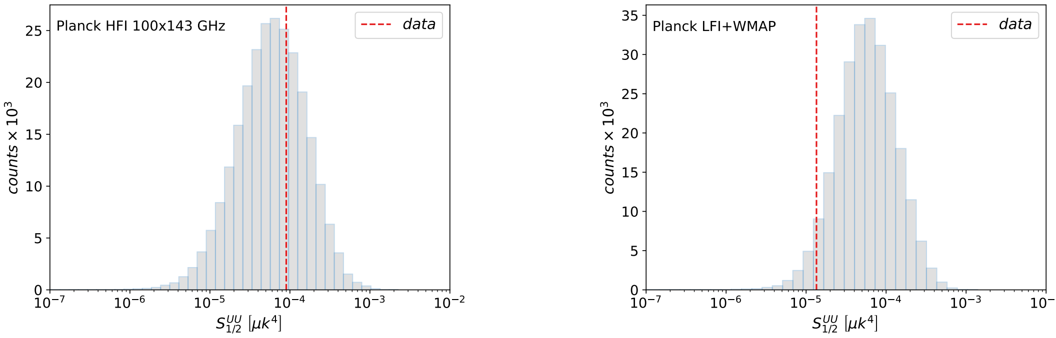

Figure 3.10: *Same as in Figure 3.9 but for* U*.*

Specifically, we computed the integrals in eq. (3.14) and (126), involved in the computation of $I_{\ell\ell'}$ matrices, in the angular range $60° - 180°$, coherently with previous analysis (see [48], [68]). We note that figure 3.5 shows that the expected correlation function for local E modes in ΛCDM appears to be oscillating around zero, a behaviour different from what we see in the temperature case. However this does not forbid the use of the $S_{1/2}$ estimator for local E-modes, which, of course, still quantifies the distance of the correlation function from zero.

In Table 3.1 we report the value of $S_{1/2}$ estimator on data for the analysed datasets, both with and without the quadrupole contribution. We also show the percentage of simulations having a value of $S_{1/2}$ larger than data, the values reported in brackets refer to the unconstrained simulations case. As previously discussed, the local E modes estimator does not sizeably depend on the inclusion of the quadrupole, differently from what happens for Q and U. As the *Planck* HFI 100×143 dataset has a higher signal to noise ratio with respect to *Planck*

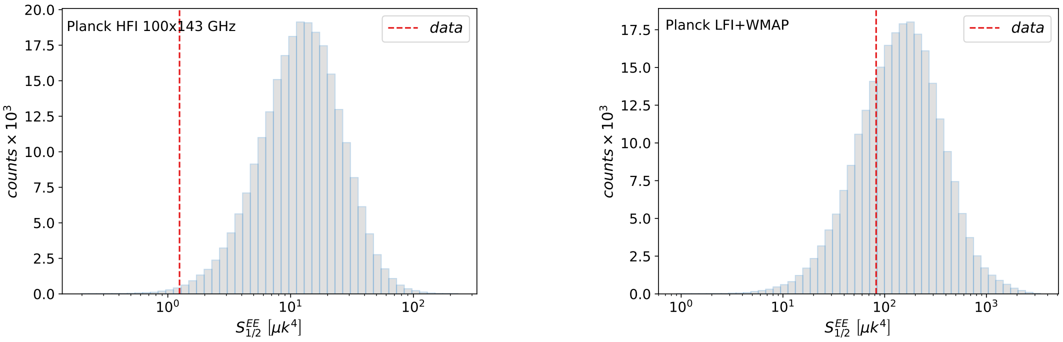

Figure 3.11: *Same as in Figure 3.9 but for E-modes.*

	$S_{1/2}^{data}$	$S_{1/2} > S_{1/2}^{data}$	$S_{1/2}^{data_{\ell>2}}$	$S_{1/2}^{\ell>2} > S_{1/2}^{data_{\ell>2}}$ [%]
	[μK^4]	[%]	[μK^4]	[%]
EE *Planck* HFI 100×143	1.25	99.5 (99.6)	1.30	99.5 (99.6)
EE *Planck* LFI+WMAP	82.4	71.6 (72.3)	82.7	71.5 (72.2)
	$10^5 \times [\mu$K$^4]$	[%]	$10^5 \times [\mu$K$^4]$	[%]
QQ *Planck* HFI 100×143	9.57	19.6 (31.7)	0.85	48.8 (49.0)
UU *Planck* HFI 100×143	9.0	34.2 (41.8)	3.21	49.2 (53.3)
QQ *Planck* LFI+WMAP	5.14	39.4 (50.2)	3.33	25.5 (27.3)
UU *Planck* LFI+WMAP	1.35	95.0 (95.6)	2.25	75.2 (77.6)

Table 3.1: *$S_{1/2}$ measured on data (second column including the quadrupole term and fourth column excluding the quadrupole term) and percentage of simulations with value of the estimator larger than the one found on data (third column including the quadrupole term and fifth column excluding the quadrupole term). The values reported in parenthesis refer to unconstrained simulations. The sensitivity associated to the percentage of simulations with $S_{1/2}$ higher than data is $\sim 0.2\%$.*

LFI+WMAP, we rely on it to make an assessment on the significance of the anomaly for E-modes. The value of the estimator on data is $S_{1/2}^{data} = 1.25\ \mu k^4$ for *Planck* HFI 100×143, with a lower tail probability of 0.5%, which suggests a low power in polarization data up to $\ell = 10$. This result might appear surprising at first, given that in Fig. 3.5 both the ΛCDM expectation for the correlation function, as computed on simulations, and the one that is actually realized in the data are consistent with zero. However, the $S_{1/2}$ estimator actually depends on the integral of the square of $C^{EE}(\theta)$, which somehow quantifies the distance of the correlation function from zero. We verified that actual $(C^{EE}(\theta))^2$ computed on data lies in the lower tail of the distribution reconstructed from simulations. In other words, the observed correlation function is much closer to zero (as measured by $S_{1/2}$) with respect to most simulations.

As previously noted, the correlation functions for Q and U change significantly when the quadrupole is excluded from the analysis. The higher variance due to residual dipole on the quadrupole in the *Planck* HFI 100×143 dataset suggests to base our considerations on the *Planck* LFI+WMAP dataset. The trend of the latter dataset seems to indicate that the contribution of $\ell = 2$ increase the power of the low multipoles in the data with respect to simulations. This effect is highlighted by the decrease of the percentage of simulations with a value of $S_{1/2}^{data}$ higher than data when excluding the quadrupole from the analysis (compare III and V columns in table 3.1 for the QQ case of *Planck* LFI+WMAP dataset). This conclusion holds for both constrained and unconstrained simulations.

To further investigate the contribution of each multipole in determining the relative power of data with respect to the empirical distributions, we computed the value of the estimators on constrained simulations and data gradually increasing the maximum multipole included in the analysis. As expected, the quadrupole dominates the Q and U results which therefore cannot be taken as representative of the behaviour of the other low multipoles. On the contrary, the local E-modes are not very sensitive to the quadrupole and exhibit a decreasing lower tail probability as a function of ℓ_{max} as shown in Figure 3.12. This is true for the *Planck* HFI 100×143 dataset but also for the *Planck* LFI+WMAP dataset, pending some scattering which can be ascribed to the lower signal-to-noise of the latter. For multipoles above $\ell \sim 10$ both datasets are noise-dominated and any trend is lost. Taking here the *Planck* HFI 100×143 dataset as our benchmark, due to its higher signal-to-noise, we found a lower-tail probability of 0.5%. Note that, in spite of the fact that, the quadrupole for this dataset exhibits extra variance, as explained above, yet we have chosen it as our benchmark given the fairly low sensitivity of the local E-modes $S_{1/2}$ estimator to the value of the quadrupole itself.

As a final test, we have studied the joint distribution of the $S_{1/2}$ estimators in temperature[5] and polarization. In Figure 3.13, we show the distribution in the $(S_{1/2}^{EE}, S_{1/2}^{TT})$ plane of $N_{\rm sims} = 500$ unconstrained *Planck* HFI 100×143 simulations (grey dots), compared to values computed on the actual *Planck* HFI 100×143 data (red dot). For each simulation the value of the estimator in temperature is

---

[5] The $S_{1/2}^{TT}$ estimator used here is computed in harmonic space, see Eq. (3.13), coherently with the polarization estimator. A real-space calculation, based on Eq. (3.12), was instead perfomed in the analysis from the Planck Collaboration [68], considering 71% of the sky. We have verified through simulations that the two procedures, when applied on the Commander data, produce statistically consistent results.

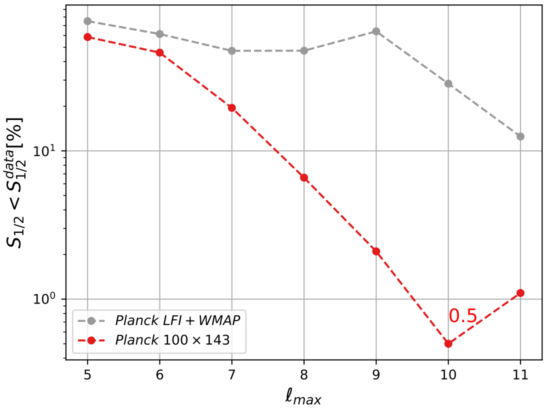

Figure 3.12: *Lower tail probability for the local E modes estimator computed on data w.r.t constrained simulations for both Planck HFI 100×143 (red curve) and Planck LFI+WMAP (grey curve) datasets. The region of multipoles higher than 11 is excluded from the plot as considered dominated by noise.*

normalized to the empirical mean of the $S_{1/2}^{TT}$ simulations distributions and the value of the estimator in polarization is normalized to the empirical mean of the $S_{1/2}^{EE}$ simulations distributions. The same normalization is applied to data.

Given the relatively small number of simulations available, we have sought to compress the information encoded in the two-dimensional joint distribution into a single, one-dimensional estimator. To this purpose, we extended the use of the $S_{1/2}$ estimator from one to two dimensions, computing the distance of the points from zero as in equation 3.24:

$$S_{1/2}^{EE,TT} = \sqrt{\left(\frac{S_{1/2}^{TT}}{\langle S_{1/2}^{TT}\rangle}\right)^2 + \left(\frac{S_{1/2}^{EE}}{\langle S_{1/2}^{EE}\rangle}\right)^2} \tag{3.24}$$

The resulting distribution is shown in figure 3.14. We repeated an identical analysis for the Q and U correlation functions. In figure 3.15 we see the scatter plot in the ($S_{1/2}^{QQ}$, $S_{1/2}^{TT}$) plane (left panel) and ($S_{1/2}^{UU}$, $S_{1/2}^{TT}$) plane (right panel) for the 500 *Planck* HFI 100×143 dataset simulations. In figure 3.16 we show the distribution for the $S_{1/2}^{QQ,TT}$ estimator (left panel) and $S_{1/2}^{UU,TT}$ estimator (right panel).

In the case of local E modes we found that no simulations have values of $S_{1/2}^{EE,TT}$ lower than data. Given that the sensitivity associated to our Monte Carlo is $1/N_{\rm sims} = 0.002$, we can quote this number as an upper limit to the lower tail probability associated to the $S_{1/2}^{EE,TT}$ value measured on the data. Instead, for

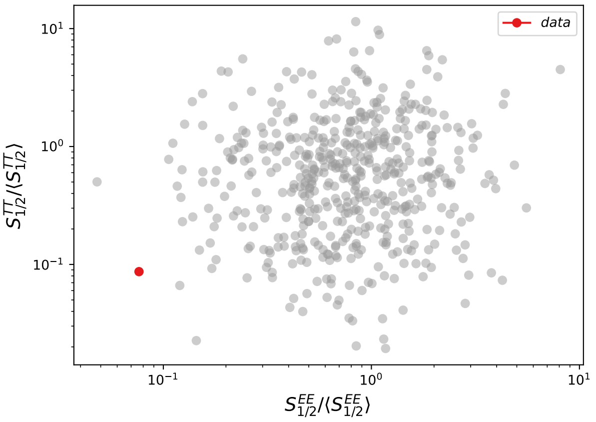

Figure 3.13: *Joint behaviour of the $S_{1/2}$ estimator in temperature and polarization for* 500 *unconstrained simulations (grey dots) and data (red dot) of Planck HFI 100×143 dataset. All values of the estimator in temperature and polarization reported here are normalized to the empirical mean of the corresponding distribution. The position of data with respect to the simulations suggests a low combined power of T and E correlation functions.*

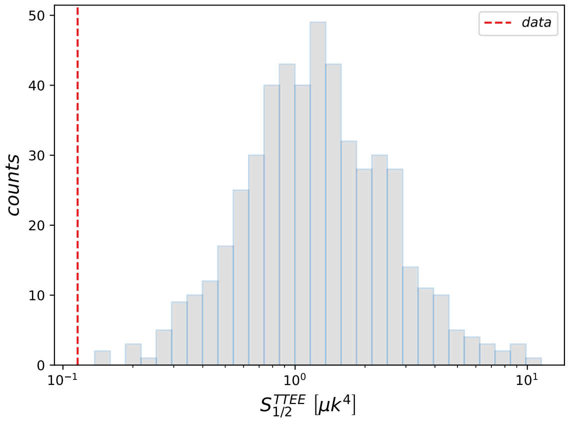

Figure 3.14: *Distribution of the $S^{EE,TT}_{1/2}$ estimator for* 500 *Planck HFI 100×143 simulations (grey) and data (red vertical line). The upper limit of the lower tail probability of the estimator computed on simulations with respect to data is* 0.2%.

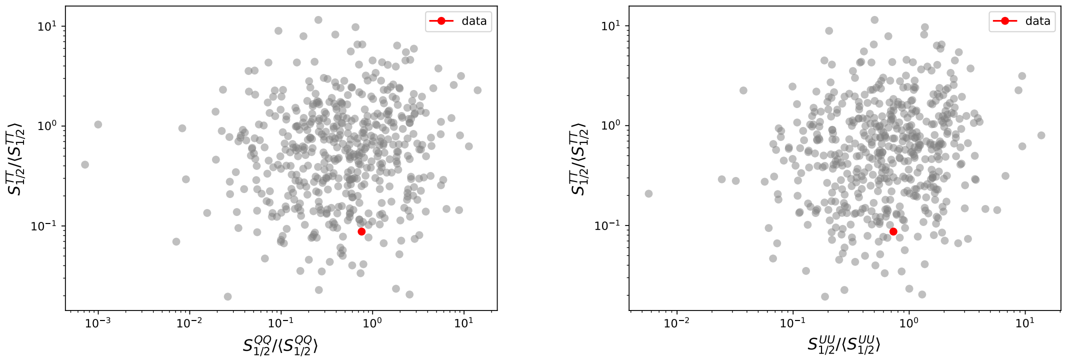

Figure 3.15: *Joint behaviour of the $S_{1/2}$ estimator in temperature and polarization for 500 unconstrained simulations (grey dots) and data (red dot) of Planck HFI 100×143 dataset. The values on x-axes are those of the $S^{QQ}_{1/2}$ estimator on the left and of the $S^{UU}_{1/2}$ estimator on the right, while on the y-axis we see the $S^{TT}_{1/2}$ estimator in both panels. All values of the estimator in temperature and polarization reported here are normalized to the empirical mean of the corresponding distribution.*

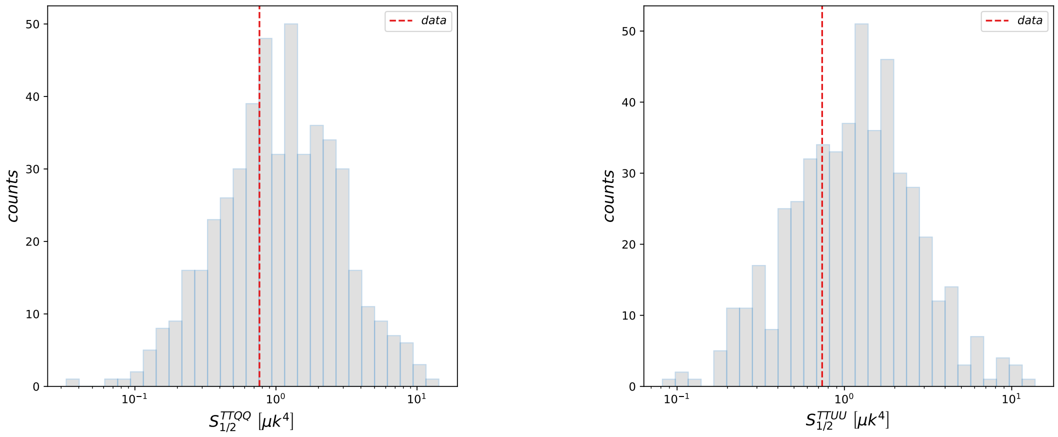

Figure 3.16: *Distribution of the $S^{QQ,TT}_{1/2}$ estimator (left) and $S^{UU,TT}_{1/2}$ estimator (right) for 500 Planck HFI 100×143 simulations (grey) and data (red vertical line). The sensitivity associated to the Montecarlo is 0.2%.*

$S_{1/2}^{QQ,TT}$ and $S_{1/2}^{UU,TT}$ estimators, data are well compatible with the simulations distribution with a lower tail probability of 37% and 30.4% respectively.

In order to summarize the results we underly the peculiarity of the correlation function on local E-modes with respect to that of the Q and U stokes parameters: the first is more sensitive to the ℓ_{max} used in the analysis and gives information on the integrated power of the lower multipoles, the latters are, instead, largely dominated by the quadrupole. In the first case we showed that including higher multipoles, up to $\ell = 10$, has the effect of lowering the lower tail probability of data with respect to simulations in both datasets considered. As opposite, in the case of the Stokes parameters we did not see any anomalous behaviour in the $S^{1/2}$ estimator, except for a mild 2σ anomaly in the case of *Planck* LFI+WMAP U correlation function. For the reasons stated above, this result does not change including higher multipoles in the analysis. This scenario is replicated when considering the joint estimator of temperature and local E modes on the *Planck* HFI 100×143 dataset: the lower tail probability associated to the data is less than 0.002. As opposite, when combining temperature with the Q or U estimators, we found consistency between data and simulations. The whole picture suggests that a mild anomalous behaviour of the data with respect to the expectations of the ΛCDM model emerges when including in the analysis the integrated power of all the lower multipoles, while the quadrupole is not anomalously low in data. It is worth noting, however, that both datasets include non negligible uncertainties, in particular on the quadrupole. In the conclusions of this thesis we will describe how this issue will be hopefully overcome by the next generation of CMB polarization data.

4

Probing the baryonic matter distribution through observations of the millimeter and sub-millimeter sky

Millimeter and submillimeter data are a mine of cosmological information. While CMB is fundamental to constrain cosmological parameters and test the Standard Model, other emissions can tell us how cosmic structures form and evolve. In the work presented in this chapter we analysed data from the South Pole Telescope (SPT) [86], [87] and the Spectral and Photometric Imaging REceiver (SPIRE), mounted on the Hershel Space Observatory [88], in six frequency bands: 95, 150, 220, 600, 857, 1200 GHz. The dataset will be described in detail in the following. For the moment, we just mention that the power spectrum we considered can be modelled as:

$$C_\ell^{tot} = C_\ell^{CMB} + C_\ell^{tSZ} + C_\ell^{kSZ} + C_\ell^{CIB_P} + C_\ell^{CIB_C} + C_\ell^{tSZ-CIB} + C_\ell^{rad} + C_\ell^{cirr}. \quad (4.1)$$

From equation (4.1) we see that the total power in data is given by the sum of several contributions. The CMB spectrum, C_ℓ^{CMB}, is combined with the secondary anisotropies: the thermal Sunyaev Zeldovich (tSZ) and kinetic Sunyaev Zeldovich (kSZ) effect, called respectively C_ℓ^{tSZ} and C_ℓ^{kSZ}. Other contributions to the total power spectrum come from extragalactic emission of radio sources, C_ℓ^{rad}, and dusty star forming galaxies (DSFGs). These galaxies generate the Cosmic Infrared Background (CIB) clustering and poisson effect, denoted in equation (4.1) as $C_\ell^{CIB_P}$ and $C_\ell^{CIB_C}$ respectively. To conclude, the total power includes a contribution from galactic sources emission, i.e. galactic cirrus, C_ℓ^{cirr}. Our aim was to build a coherent modelling for all foregrounds at all frequencies. The code we have developed has been widely validated [46, 89, 90], it is modular and easy to use. For details see Appendix *0.3*. The accurate modelling of every component of these power spectra has a key role both for the 'foreground cleaning' of the CMB maps and for clustering studies. The CMB on small scales provides a lot of information about the physics of the early Universe, encoded in the positions and the height of the high order acoustic peaks. Despite these scales are less affected by cosmic variance, extracting information from them is complicated by the presence of additional power coming from the other emissions. From this perspective, all components other than CMB are considered as contaminants, and are usually called *foregrounds*. These contaminats can be divided into two categories: secondary anisotropies and additional power due to astrophysical emissions. In the first case the CMB anisotropy field is distorted by the interaction of CMB photons with the galactic plasma. In the second case, the emission of galactic or extragalactic sources overlaps in some frequency bands with the CMB and what we observe is the sum of the two emissions. The proper modelling of the foregrounds then allows to clean CMB maps in order to extract the information about the early Universe, which is contained in the primary anisotropy. To have some details on the cosmological results, see [91–94].

Another field in which the accurate modelling of the galactic and extragalactic emission is of great utility is the one concerning the clustering studies: the galaxies generating these radiations are tracers of the matter distribution in the Universe and can then be used to understand the formation and evolution of the Large Scale Structures (LSS). In this work we decided to use the code for the second purpose: we fixed the cosmology and fit for the parameters describing the foregrounds, in order to derive information on the clustering properties of the CIB galaxies. We can do this as we implemented a physical description of the CIB emission and the tSZ effect. Differently from many previous work [95, 96], which used for these foregounds a phenomenological parametrization[1], we used an 'halo-model' approach, which is able to give fundamental information on the clustering properties of dark matter and galaxies. This chapter will be devoted to the description of the foregrounds model implemented in our code, as well as its comparison with data. In the first section we describe the adopted halo model, in the second we will enter the details of the modelling employed for each foreground. In the last section we will instead describe the value of the parameters we obtain through the fit of the model to SPT and SPIRE data.

---

[1] The angular dependence is given by a fixed template, both for the tSZ and CIB. The spectral dependence is parametrized as a gray body, for the CIB, and using equation (4.96), for the tSZ.

4.1 The halo model

We have already mentioned that equation (2.135) describes the power spectrum of linear perturbations, but, to study the LSS of the Universe, we have to deal with the non linear behaviour of the matter field. Indeed, the scales on which non linearities dominates correspond to those of the fundamental blocks of cosmic structures: halos. In the halo approach [6, 97–101] all matter in the Universe is contained in virialized structures of dark matter, separated by distances much larger than their tipical size. In this paradigm all scales smaller than the tipical size of halos are described by the matter distribution within themselves, and all scales larger than that size are described by the spatial distribution of the halos. If this is the case, then the entire non linear density field may be reconstructed by summing contributions from individual halos.

4.1.1 The spherical collapse model

The spherical collapse model is based on the idea that non-linear objects form through the spherical collapse of initially tophat density perturbations. These initial perturbations occupy a Lagrangian region R_0 with an initial overdensity δ_i. We suppose that initial fluctuations were Gaussian, with an rms on scale R_0 much less than unity. If this is the case, we are most likely in the condition in which $|\delta_i| \ll 1$ and the mass in the R_0 region is:

$$M_0 = \frac{4\pi R_0^3}{3}\bar{\rho}(1+\delta_i) \approx \frac{4\pi R_0^3}{3}\bar{\rho}, \tag{4.2}$$

where $\bar{\rho}$ is the comoving background density. As the Universe evolves, also the size of the region changes. The density within the region is defined as $(R_0/R)^3 \equiv (1+\delta)$, where R denotes the comoving size of the region at a given time. In a flat universe, described by a FLRW metric, the ratio between the size at redshift z and the initial size of the region considered is given by:

$$\frac{R(z)}{R_0} = \frac{(1+z)}{5/3|\delta_0|}\frac{1-\cos\theta}{2}, \tag{4.3}$$

where δ_0 denotes the initial density δ_i extrapolated with linear theory to the present time. Using:

$$\frac{1}{1+z} = \left(\frac{3}{4}\right)^{2/3}\frac{(\theta-\sin\theta)^{2/3}}{(5/3)|\delta_0|}, \tag{4.4}$$

we obtain:

$$\frac{R_0}{R(z)} = \frac{6^{2/3}}{2}\frac{(\theta - \sin\theta)^{2/3}}{(1-\cos\theta)}. \tag{4.5}$$

The process starts at $\theta = 0$ and undergoes a 'turnaround' at $\theta = \pi$, where the evolving radius starts to decrease with respect to the initial one. At $\theta = 2\pi$ the ratio tends to infinty as the denominator is zero, and this would cause the density of the collapsing region to diverge. In practice, though, the collapse stops before and the halo virializes. The density of the virialized object is computed assuming that the virial radius is half the turnaround radius. At turnaround $\theta = \pi$ and from equation (4.5) we get $[R_0/R(z_{ta})]^3 = (3\pi/4)^2$. As $R_{vir} = R_{ta}/2$, the virialized object is 8 times denser than it was at turnaround. Moreover, in the time between turnaround and collapse, Universe expands by a factor $(a_{col}/a_{ta}) = (1 + z_{ta})/(1 + z_{col}) = 2^{2/3}$, see equation (4.4). Considering the equation for the background evolution, $\rho \propto a^3$, we find then that the zero order density at turnaround is $(2^{2/3})^3 = 4$ times the background density at time of virialization. Putting all together we obtain the ratio between the virialized and background density:

$$\Delta_{vir} \equiv (9\pi^2/16) \times 8 \times 4 = 18\pi^2 \sim 178. \tag{4.6}$$

The initial overdensity of the halo region at the time of collapse can be obtained from equation (4.4) setting $\theta = 2\pi$:

$$\frac{\delta_c(z)}{1+z} = \frac{3}{5}\left(\frac{3\pi}{2}\right)^{2/3}. \tag{4.7}$$

Here δ_c is the critical overdensity for collapse, extrapolated using linear theory to the time in which the halo region starts to collapse. At present time, when $z = 0$, the critical overdensity for collapse is $\delta_c = 1.686$. One of the most important features of the spherical collapse model is that it provides a relation between the actual overdensity, δ, and the one predicted by linear theory, δ_0, as $1/\delta_0 \propto (R_0/R)^3 \equiv (1+\delta)$. This relation is valid for all R_0 and, given that $M \propto R^3$, this means that the critical density for collapse, δ_c, is the same for all objects, independent on their mass.

4.1.2 The halo mass function

The halo mass function, dn/dM, gives the comoving number density of bound objects of mass m at redshift z and it is related to the number of regions, in the initial density field, which were dense enough to start the collapse. The halo aboundance can then be predicted using a function describing the mass fraction of matter in peaks of a given height [102], which is defined as:

$$\nu \equiv \frac{\delta_c^2}{\sigma^2}, \tag{4.8}$$

where δ_c is the critical overdensity for collapse at redshift zero. The quantity $\sigma^2(m)$ is the variance in the initial density fluctuations field, when smoothed with a tophat filter of scale $R = (3m/4\pi\bar{\rho})$, extrapolated to the present time through linear theory:

$$\sigma^2_{lin}(m) = \int \frac{dk}{k} \frac{k^3 P^{lin}(k)}{2\pi^2} |W(kR)|^2. \tag{4.9}$$

Here P_{lin} is the matter linear power spectrum we have obtained in equation (2.134), while $W(kR)$ is the spatial filter [103]:

$$W(x = kR) = \left(\frac{3}{x^3}\right) [\sin(x) - x\cos(x)]. \tag{4.10}$$

A simple model to relate the halo mass function to the function describing the number density of the peaks, $\nu f(\nu)$, is provided by the Press and Schetcher formalism [104, 105]:

$$\frac{m^2 n(m,z)}{\bar{\rho}} \frac{dm}{m} = \nu f(\nu) \frac{d\nu}{\nu}. \tag{4.11}$$

A parametrization of $\nu f(\nu)$ is given by Sheth & Tormen [106].

$$\nu f(\nu) = A(p)\left(1 + (q\nu)^{-p}\right)\left(\frac{q\nu}{2\pi}\right)^{1/2} \exp(-q\nu/2), \tag{4.12}$$

with $p = 0.3$, $A(p) = 0.322$ and $q = 0.707$. The shape of the halo mass function can be divided in two different regimes: a power law at low masses and an exponential cut-off at high masses. This is due to the fact that very massive halos are rare, so that high mass bins are poorly populated. Other than the Sheth & Tormen mass function the code we developed include an alternative parametrization elaborated by Tinker [107], which is the one we mainly used in the fit to data:

$$\frac{dn}{d\ln M} = -\frac{1}{2} f(\sigma, z) \frac{\bar{\rho}}{M} \frac{d\ln\sigma^2}{d\ln M}. \tag{4.13}$$

In this case we have:

$$f(\sigma) = A\left[\left(\frac{\sigma}{b}\right)^{-a} + 1\right] e^{-c/\sigma^2}. \tag{4.14}$$

The parameter A represents the overall amplitude of the mass function, while a and b give respectively the amplitude and the slope of the low mass power law. The parameter c, instead, determinates the cut-off scale at which the halo abundance exponentially decreases. The parameters are functions of redshift and density contrast and have been calibrated through simulations and observations, see for example [108]. The density contrast with respect to the background, Δ, allows to identify a bound object as a halo. For redshift $z = 0$ and $\Delta = 200$ the parameters of equation (4.14) are:

$$A_0 = 0.186, \quad a_0 = 1.47, \quad b_0 = 2.57, \quad c_0 = 1.19. \tag{4.15}$$

The redshift evolution of A, a, b and c parameters derives from two contributions: the first is given by the evolution of the density contrast with z. The value 200 is an approximation of the number computed in equation (4.6), which is the density contrast required for collapse. But, to be precise, this quantity depends sligthly on cosmological parameters and, in particular:

$$\Delta = 200/\Omega_m(z) \tag{4.16}$$

So, to obtain the value of A_0, a_0, b_0 and c_0 at a given redshift, one has to interpolate these functions among the values computed by simulations (which usually are $\Delta = 200, 400, 800, 1600, 3200$). In addition to this, the $f(\sigma)$ parameteres have an explicit dependence on redshift, parametrized again by [107]:

$$A(z) = A_0(1+z)^{-0.14}, \tag{4.17}$$

$$a(z) = a_0(1+z)^{-0.06}, \tag{4.18}$$

$$b(z) = b_0(1+z)^{-\alpha}, \tag{4.19}$$

$$\log \alpha(\Delta) = -\left(\frac{0.75}{\log(\Delta/75)}\right)^{1.2}. \tag{4.20}$$

In figure 4.1 we show the halo mass function as function of mass for three different redshift values: $z = 0.1, 1.4, 4.5$. In the left panel we compare two different cosmologies, while in the right panel we compare the Tinker model with the Seth & Tormen one. In both panels the differences between the curves grow with redshift.

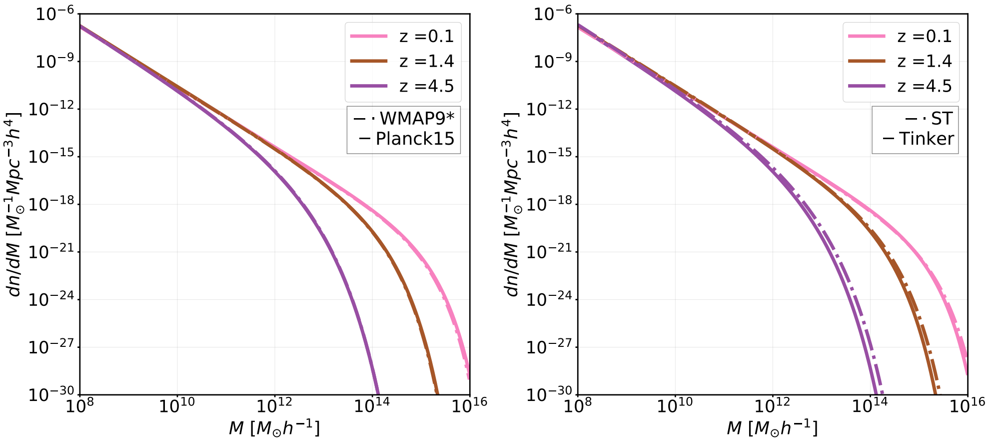

Figure 4.1: Halo mass function as function of the halo mass for two different sets of cosmological parameters (left panel) and modelling (right panel). The difference is more evident when considering higher redshifts.

The set of cosmological parameters in the left panel of the figure are those of WMAP9 and Planck15. They have been chosen as they are implemented both in *Astropy* [109] and in the *HaloMod* [46]. The only modification we have introduced regards the scalar spectral index, which has been set $n_s = 1$ in the case of WMAP9 cosmology, to highlight its eventual impact on the halo mass function. For this reason we will refer to this set of parameters as WMAP9*. The parameter values used are given in table 4.1:

	H_0	Ω_m	Ω_b	n_s
Planck15	67.7	0.307	0.0486	0.9593
WMAP9*	69.3	0.286	0.0463	1

Table 4.1: List of the main cosmological parameters corresponding to WMAP9* and Planck15 cosmology.

4.1.3 Halo bias

In this section we relate the overdensity of halos on large cells to the overdensity of the mass [110]. We start computing the number density of halos in dense regions. Imagine to divide the space in cells of comoving volume V. Different cells may contain different amount of mass, depending on their inner density. We write the relation between mass and density expliciting the mass overdensity δ:

$$\frac{M}{V} \equiv \bar{\rho}(1+\delta). \tag{4.21}$$

We write the overdensity of halos in such cells as:

$$\delta_h(m, z_1|M, V, z_0) = \frac{N(m, z_1|M, V, z_0)}{\frac{dn(m,z_1)}{dm}V} - 1. \tag{4.22}$$

In this equation $dn(m, z_1)/dm$ is the halo mass function computed in the previous section and calculated at some given value of mass and redshift: (m, z_1). The function $N(m, z_1|M, V, z_0)$, instead, represents the average number of halos of mass m, which collapsed at redshift z_1 and occupy cells of size V and mass M at present redshift z_0. We need to find an expression for it. As a halo is a region which, at some redshift, was sufficiently overdense that it collapsed, the halo number in a cell is equal to the number density of overdense region times the comoving volume of the cell. We can then write:

$$N(m, z_1|M, V, z_0) = \frac{dn(m, z_1|M, V, z_0)}{dm}V(1+\delta), \tag{4.23}$$

where $dn(m, z_1|M, V, z_0)/dm$ gives the average number of halos in the mass and redshift bins (m, z_1), conditioned to the fact that those halos have to occupy a cell of mass M and volume V at present time, i.e conditioned to an environment with a precise density. To compute the average number density appearing in equation (4.23) we consider that the halo mass function depends on the critical overdensity for collapse at the time chosen: $\delta_c(z_1)$. Denser cells, i.e. those which favour the formation of halos, have densities closer to the critical one. Then, a good approximation to compute $dn(m, z_1|M, V, z_0)/dm$ is obtained by replacing $\delta_c(z)$ in the computation of the dn/dm with $\delta_c(z_1) - \delta_0(\delta, z_0)$. In this case the peaks height needed to reach the collapse phase is lower and the formation of bound objects is easier. The quantity $\delta_0(\delta, z_0)$ denotes the initial overdensity, extrapolated using linear theory, that a region must have had so to have overdensity δ at z_0. We cannot simply use δ as it has been derived with non linear theory from initial condition, differently from δ_c, which instead has been extrapolated using linear theory [2]. Following this argument we can give an

---

[2] For clarity we summarize the different definition of the overdensity:

- δ: mass overdensity;

estimate of the density of halos of mass m, virialized at z_1, and occupying the cell identified by the values M, V and z_0:

$$\frac{m^2 dn(m, z_1|M, V, z_0)/dm}{\bar{\rho}} \frac{dm}{m} = \nu_{10} f(\nu_{10}) \frac{d\nu_{10}}{\nu_{10}}, \tag{4.24}$$

where

$$\nu_{10} = \frac{[\delta_c(z_1) - \delta_0(\delta, z_0)]^2}{\sigma^2(m) - \sigma^2(M)}, \tag{4.25}$$

and $f(\nu)$ can be given by equation (4.14) or (4.12). The very large scale limit of equation (4.24) is given by the conditions $V \to \infty, M \to \infty$. It returns back the halo mass function $dn(m, z_1)/dm$ as $\sigma^2(M) \to 0$ and $|\delta| \to 0$. On the other hand, the very small scale limit, given by the conditions $V \to 0, \delta \to \infty, \delta_0 \to \delta_c(z_0)$, is related to halo evolution. A small region containing a mass M, indeed, can be considered itself a halo of mass M. Thus, the number of subclusters of mass m obtained computing $N(m, z_1|M, V = 0, z_0)$ is the mass function of the halo progenitors, which eventually have merged to form the present halo. In the large scale limit the rms density fluctuation in the cells is much smaller than unity. This means that $\delta \ll 1$ most likely. Also in this case, similarly to the extreme limit seen before, $M \gg m$, where m is the typical mass of a halo. This causes $\sigma(M) \ll \sigma(m)$ and again $\sigma(M) \to 0$. For more details on this treatment see [111, 112]. We can write the conditional average number density as an expansion around the unconditioned one (obtained in the extreme large scale case):

$$n(m, z_1|M, V, z_0) \approx n(n, z_1) - \delta_0(\delta, z_0) \left(\frac{\partial (dn(m, z_1)/dm)}{\partial \delta_c} \right)_{\delta_c(z_1)}, \tag{4.26}$$

which, in terms of overdensity, becomes:

$$\delta_h(m, z_1|M, V, z_0) \approx \delta - (1 + \delta)\delta_0(\delta, z_0) \left(\frac{\partial \ln \left(dn(m, z_1)/dm\right)}{\partial \delta_c} \right)_{\delta_c(z_1)}. \tag{4.27}$$

- δ_h: halo overdensity;
- δ_c: critical overdensity for collapse, derived from linear theory;
- δ_0: initial overdensity, derived from linear theory.

Focusing on the lowest order of expansion and plugging in equation (4.27) the expression of the halo mass funtion, we obtain:

$$\delta_h(m, z_1|M, V, z_0) \approx \delta \left(1 + \frac{q\nu - 1}{\delta_c(z_1)} + \frac{2p/\delta_c(z_1)}{1 + (q\nu)^p}\right) = b(m, z_1)\delta, \tag{4.28}$$

if the $f(\nu)$ function is a Seth & Tormen [106]. In the case of Tinker modelling instead [113]:

$$b(m, z_1) = 1 - A\frac{\nu^a}{\nu^a + \delta_c^a} + B\nu^b + C\nu^c, \tag{4.29}$$

where, for a $\Delta = 200$ halo, we have:

$$A = 1.04, \quad a = 0.132, \quad B = 0.183, \quad b = 1.5, \quad C = 0.262, \quad c = 2.4. \tag{4.30}$$

Equation (4.28) states that the relation between the overdensity of the halos and that of the mass field in very large cell is linear [114]. The constant of proportionality, called halo bias and denoted with $b(m, z_1)$, depends on the masses of the haloes and the redshift they virialized. The result above also leads to:

$$n(m|\delta) \approx [1 + b(m)\delta]n(m). \tag{4.31}$$

As $b(m) \gg 1$ for the most massive haloes, they occupy the densest cells. It is also known that densest regions are more clustered than those of average density. This means that most massive objects are more clustered and that the environment has a great effect on the inner structure of the halo. In figure 4.2 we show the halo bias as function of the halo mass obtained with our code. On the left panel we compare two different set of cosmological parameters, see Table 4.1, while on the right panel we compare the Tinker and Seth & Tormen modelling.

4.1.4 Halo density profile

The inner structure of a halo, described by its radial density profile, is related to the time of formation and to the initial density distribution of the region which collapsed. The theory predicts that dark matter collapses first in small mass haloes, which eventually merge together and form larger haloes. Low mass halos are significantly denser than more massive systems, a correlation that reflects the higher collapse redshift of small halos. The characteristic density of an equilibrium halo is proportional to the density of the Universe at the time it was assembled. This means that early forming structures tends to be more concentrated than late time structures, which tend to be larger and less

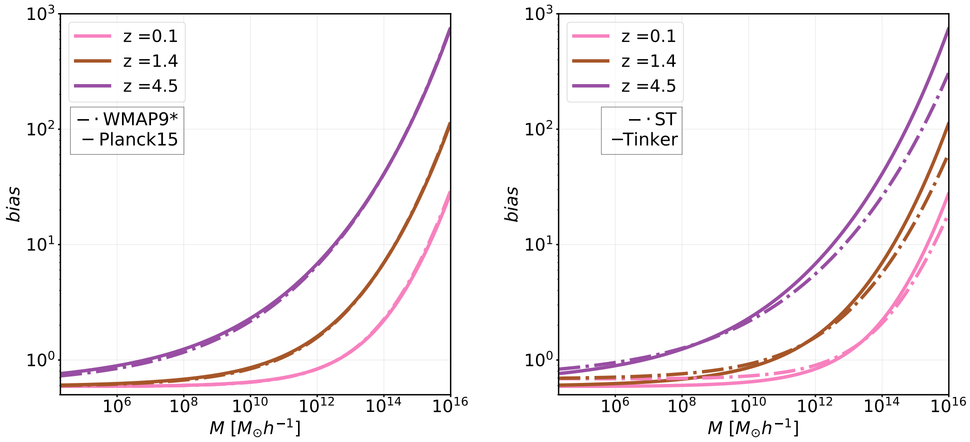

Figure 4.2: *Halo bias as function of the halo mass for two different sets of cosmological parameters (left panel) and modelling (right panel). Using different cosmologies has a minor impact on the halo bias with respect to the choice of the model. As in the case of the halo mass function, the difference between Tinker and Seth & Tormen modelling increases with redshift.*

concentrated. To describe the density profile of an halo as function of its radius we use a Navarro-Frenk-White (NFW) profile [115]:

$$\rho(r|m) = \frac{\rho_s}{(r/r_s)^\alpha (1 + r/r_s)^\beta}, \tag{4.32}$$

with $(\alpha, \beta) = (1, 2)$. The quantity r_s is a scale radius, while ρ_s is the density at that scale radius. We define the halo mass as:

$$m \equiv \int_0^{r_{vir}} dr 4\pi r^2 \rho(r|m). \tag{4.33}$$

For a NFW profile, the integral in equation (4.33) becomes:

$$m = 4\pi \rho_s r_s^3 \left[\ln(1 + c) - \frac{c}{1 + c} \right]. \tag{4.34}$$

Here $c \equiv r_{vir}/r_s$ is the concentration parameter. We note that the integral for the mass in equation (4.33) has been truncated to the virial radius. This is necessary as the NFW profile falls as r^{-3} at large radii, and the integral mass diverges logarithmically. Truncating the profile at the virial radius ensures convergence and a corrispondance between the mass computed from the density profile and that obtained from the halo mass function. In order to compute the concentration parameters we rely on the result of simulations, which shows that concentrations of haloes of the same mass are described by a log-normal distribution:

$$p(c|m,z)dc = \frac{d\ln c}{\sqrt{2\pi\sigma_c^2}} \exp\left\{ -\frac{\ln^2[c/\bar{c}(m,z)]}{2\sigma_{\ln c}^2} \right\}, \tag{4.35}$$

The mean concentration, $\bar{c}(m,z)$, depends on halo mass and redshift. The width of the distribution, σ_c^2, does not, even if recent papers show it is influenced by the large scale environment in which the halo forms [116]. For a NFW profile the mean concentration parameter is given by the parametrization of [117]:

$$\bar{c}(m,z) = \frac{9}{1+z}\left[\frac{m}{m_\star(z)}\right]^{-0.13} \quad \text{and} \quad \sigma_{\ln c} \approx 0.25, \tag{4.36}$$

where $m_\star(z)$ is a characteristic mass scale at which $\nu(m,z) = 1$. Different shapes for the concentration profile can be found in [118–124] . Equation (4.36) quantifies what stated at the beginning: there is an inverse proportionality between concentration and mass i.e. increasing the mass of the halo implies a decrese of its concentration. Actually, in the following calculations we will not need directly the density profile but rather its Fourier transform:

$$u(\mathbf{k}|m) = \frac{\int d^3\mathbf{x}\rho(\mathbf{x}|m)\exp\{-i\mathbf{k}\cdot\mathbf{x}\}}{\int d^3\mathbf{x}\rho(\mathbf{x}|m)}. \tag{4.37}$$

For spherically simmetric profiles truncated at the virial radius, equation (4.37) becomes:

$$u(k,m) = \int_0^{r_{vir}} dr 4\pi r^2 \frac{\sin kr}{kr}\frac{\rho(r|m)}{m}. \tag{4.38}$$

Expliciting ρ in equation (4.38) for the NFW profile we obtain:

$$\begin{aligned} u(k,m) = \frac{1}{\ln(1+c) - \frac{c}{1+c}} \Bigg(& \sin(kr_s)[\mathrm{Si}([1+c]kr_s) - \mathrm{Si}(kr_s)] - \frac{\sin(ckr_s)}{(1+c)kr_s} \\ & + \cos(kr_s)[\mathrm{Ci}([1+c]kr_s) - \mathrm{Ci}(kr_s)] \Bigg), \end{aligned} \tag{4.39}$$

where the integrals denoted as Si and Ci are:

$$\mathrm{Ci}(x) = -\int_x^\infty \frac{\cos(t)}{t}dt, \quad \mathrm{Si}(x) = \int_0^x \frac{\sin(t)}{t}dt. \tag{4.40}$$

The Fourier transform of the density profile is a function of halo concentration. Pratically the concentration used to compute the $u(k, m)$ is the mean of the distribution given in equation (4.36), which depends only on halo mass. In figure 4.3 it is shown the Fourier transform of the Navarro-Frenk-White profile truncated at the virial radius. The three curves represents three different halo masses (left panel) or redshifts (right panel).

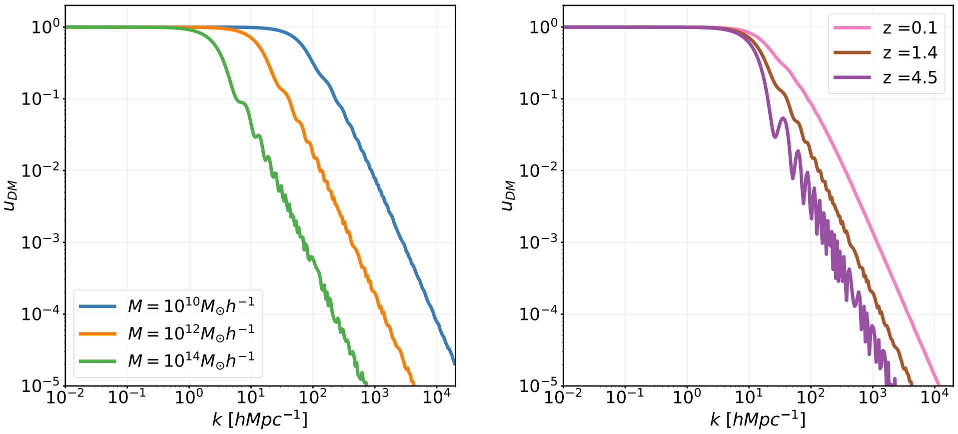

Figure 4.3: *Fourier transform of the Navarro-Frenk-White profile truncated at the virial radius. On the left panel the three curves represent three different halo masses. All of them have been computed at a redshift* $z = 1.4$ *assuming a Planck15 cosmology. On the right panel the three curves represents three different redshifts. The mass of the halo in this case is fixed to* $M = 10^{12} [M_\odot h^{-1}]$.

4.1.5 Dark matter power spectrum

The halo model predicts that all mass is bound up into halos, whose population is determined by the mass function and the density profile described in the previous sections. If this is the case, the density at position $\mathbf{x}$ is given by summing up the contribution of each halo:

$$\begin{aligned}\rho(x) &= \sum_i \rho(\mathbf{x} - \mathbf{x}_i | m_i) \equiv \sum_i m_i u(\mathbf{x} - \mathbf{x}_i | m_i) \\ &= \sum_i \int dm d^3x' \delta(m - m_i) \delta^3(\mathbf{x}' - \mathbf{x}_i) m u(\mathbf{x} - \mathbf{x}' | m),\end{aligned} \tag{4.41}$$

where ρ parametrizes the density profile as function of the halo mass and the distance from the center of the halo, which is denoted with $\mathbf{x}$. The second equality replaces the density profile with its normalized version, u, which is obtained as ρ divided by the total mass contained in the profile, so that we have:

$$\int d^3\mathbf{x}' u(\mathbf{x}-\mathbf{x}'|m) = 1. \tag{4.42}$$

We also define the number density of the halos of mass m to be:

$$\langle \sum_i \delta(m-m_i)\delta^3(\mathbf{x}'-\mathbf{x}_i)\rangle \equiv \frac{dn}{dm}, \tag{4.43}$$

where $\langle ... \rangle$ denotes the ensamble average. The mean density can be computed as:

$$\begin{aligned}\bar{\rho} = \langle \rho(\mathbf{x})\rangle = \langle \sum_i m_i u(\mathbf{x}-\mathbf{x}_i|m_i)\rangle = \int dm \frac{dn}{dm} m \int d^3\mathbf{x}' u(\mathbf{x}-\mathbf{x}_i|m_i) \\ = \int dm \frac{dn}{dm} m.\end{aligned} \tag{4.44}$$

Here the ensamble average has been replaced by an average over the halo mass function dn/dm and the density profile. In order to know the spatial distribution of dark matter we use the power spectrum. Turning to Fourier space, indeed, allows us to replace complicated convolutions with simple multiplications between the halo profiles. The dark matter power spectrum is the sum over two contributions [99]:

$$P(k) = P^{1h}(k) + P^{2h}(k), \tag{4.45}$$

where the term denoted as $1h$ describes the case in which the regions considered reside in the same halo, and the term denoted as $2h$ represents the case in which the two contributions are from different halos. The one-halo term is computed as:

$$P^{1h}(k) = \int dm \frac{dn}{dm} \left(\frac{m}{\bar{\rho}}\right)^2 |u(k,m)|^2, \tag{4.46}$$

while the two-halo term is:

$$\begin{aligned}P^{2h}(k) = \int dm_1 \left(\frac{dn}{dm}\right)_1 \left(\frac{m_1}{\bar{\rho}}\right) |u(k,m_1)| \times \\ \int dm_2 \left(\frac{dn}{dm}\right)_2 \left(\frac{m_2}{\bar{\rho}}\right) |u(k,m_2)| P_{hh}(k|m_1,m_2).\end{aligned} \tag{4.47}$$

The function $u(k|m)$ is the Fourier transform of the halo density profile and $P_{hh}(k|m_1,m_2)$ represents the power spectrum of halos of mass m_1 and m_2. Following the results of the previous section on the bias relating the background and the clustered structure overdensities, we can write:

$$P_{hh}(k|m_1, m_2) \approx \prod_{i=1}^{2} b(m_i) P^{lin}(k). \tag{4.48}$$

In equation (4.48) we have used the linear power spectrum P^{lin} as the two-halo term dominates on very large scales. The factors proportional to m in equations (4.47) are related to the average number of dark matter particles at a given halo mass, as $\langle N_{dm}|m \propto m\rangle$. For the one halo term, equation (4.46), we use instead $\langle (N_{dm}(N_{dm}-1))/2|m \propto m^2\rangle$. The $(N_{dm}-1)$ factor is needed to exclude self combinations, and the multiplication by $1/2$ avoids the double counting of particles pairs contribution. These considerations are valid in the limit in which the number of dark matter particles in a halo follows a Poisson distribution.

4.1.6 Galaxy clustering

The halo model predicts that baryonic gas can cool and form stars only if it resides in virialized dark matter halos potential wells. More massive halos are expected to host higher numbers of galaxies while smallest haloes may not contain galaxies, but, in any case, all galaxies are expected to be embedded in dark halos. The properties of the galaxy populations are determined by environmental factors, such as the cooling rate and the star formation rate, which themselves depend on the mass and angular momentum of the hosting halo. Extending the halo model framework to luminous matter allows to determine how many galaxies form within an halo and how these galaxies are distributed around the halo center [125]. If we assume that, similarly to dark matter, also the number of galaxies follows a poisson distribution, we can modify equations (4.46) and (4.47) and obtain:

$$P^{1h}_{gal}(k) = \int dm \frac{dn}{dm} \frac{\langle N_{gal}(N_{gal}-1)|m\rangle}{\bar{n}^2_{gal}} |u_{gal}(k,m)|^p, \tag{4.49}$$

$$P^{2h}_{gal}(k) \approx P^{lin}(k) \left[\int dm \frac{dn}{dm} b(m) \frac{\langle N_{gal}|m\rangle}{\bar{n}_{gal}} |u_{gal}(k,m)| \right]^2. \tag{4.50}$$

Also in this case the sum of the two contributions gives the total power spectrum:

$$P_{gal}(k) = P^{1h}_{gal}(k) + P^{2h}_{gal}(k). \tag{4.51}$$

In figure 4.4 it is shown the galaxy power spectrum at redshift $z = 0.1$, divided in the $1h$ and $2h$ contributions:

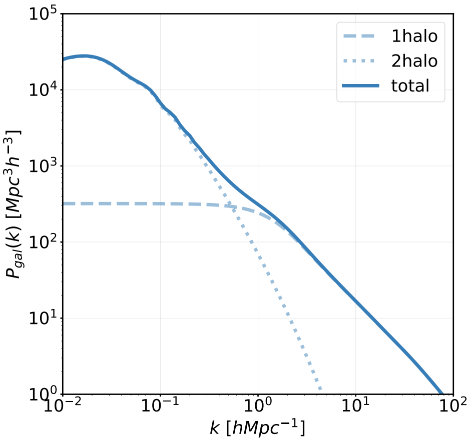

Figure 4.4: *Galaxy power spectrum at redshift $z = 0.1$ assuming a Planck15 cosmology. The dotted line represents the $2h$ term, which dominates at large scales (small k), while the dashed line is the $1h$ term, dominant at small scales (large k). The sum of these two contribution gives the total power spectrum (solid line).*

In equations (4.49) and (4.50) $\bar{n}_{gal}$ denotes the mean number of galaxies:

$$\bar{n}_{gal} = \int dm \frac{dn}{dm} \langle N_{gal}|m \rangle. \tag{4.52}$$

On large scales, where the two halo term dominates and $|u_{gal}(k, m)| \to 1$, the galaxy power spectrum becomes:

$$P_{gal}(k) \approx b_{gal}^2 P^{lin}(k), \tag{4.53}$$

where

$$b_{gal} = \int dm \frac{dn(m)}{dm} b(m) \frac{\langle N_{gal}|m \rangle}{\bar{n}_{gal}} \tag{4.54}$$

is the mean galaxy bias. The term $u_{gal}(k, m)$ denotes the Fourier transform of the density run of galaxies around the halo center. Though in principle it differs from $u_{dm}(k, m)$, a common appproximation is to set it to be the same of the dark matter case. To choose the value of the power p of the density profile we have to introduce a formalism which will be used later: it predicts that the first galaxy that forms within an halo resides in its center. After the generation of the central one, all other galaxies that eventually fill the halo are called satellites.

Only satellites galaxies are then associated to the density profile of the halo. As a consequences, pairs of galaxies of the central-satellite type are multiplied by $u_{gal}(k,m)$, while pairs of galaxies of the satellite-satellite type are multiplied by $u_{gal}(k,m)^2$. We can start from the above consideration to derive the weight to the mass function appearing in equation (4.49). Such weight must be proportional to:

$$\sum_{N_{gal}>1} p(N_{gal}|m) \left[(N_{gal}-1) u_{gal}(k|m) + \frac{(N_{gal}-1)(N_{gal}-2)}{2} u_{gal}(k|m)^2 \right], \tag{4.55}$$

where $p(N_{gal}|m)$ is the probability that a halo of mass m contains N_{gal} galaxies, and the sum starts from 2, as at least a pair is needed to give a contribution to the one-halo term. The first term in parenthesis represents the central-satellite pairs while the sencond term gives the satellite-satellite pairs. Performing the sum over N_{gal} we obtain:

$$\begin{aligned} \left[\langle N_{gal}-1|m\rangle + p(0|m) \right] & \left[u_{gal}(k,m) - u_{gal}(k,m)^2 \right] \\ & + \langle (N_{gal}(N_{gal}-1))/2|m\rangle u_{gal}(k,m)^p, \end{aligned} \tag{4.56}$$

with $p = 1$ or 2. In the limit of very small halos, which likely don't contain galaxies, the leading term in the sum above is $p(2|m) u_{gal}(k|m)$. In this limit we can write:

$$\langle N_{gal}(N_{gal}-1)|m\rangle \equiv \sum N_{gal}(N_{gal}-1) p(N_{gal}|m) \approx 2p(2|m). \tag{4.57}$$

The leading order term can be well approximated by:

$$p(2|m) \approx \langle N_{gal}(N_{gal}-1)/2|m\rangle. \tag{4.58}$$

Similarly, in the limit of large number of galaxies per halo, we can set $p(0|m) \ll 1$. The expression (4.56) becomes:

$$\langle N_{gal}-1|m\rangle \left[u_{gal}(k,m) - u_{gal}(k,m)^2 \right] + \langle (N_{gal}(N_{gal}-1))/2|m\rangle u_{gal}(k,m)^p. \tag{4.59}$$

For Poisson counts $\langle n(n+1)\rangle = \langle n^2\rangle$, so the last term of equation (4.59) dominates the sum. This implies that, both in the limit of large or low occupation number, the leading term of the weights is proportional to $\langle (N_{gal}(N_{gal}-1))|m\rangle$, as it is found in equation (4.49). Following [126] we can elaborate more on the expression of the weight just computed. As anticipated we assume:

$$\langle N_{gal}|m\rangle = \langle (N_{cent} + N_{sat})|m\rangle. \tag{4.60}$$

Then we have:

$$\langle N_{gal}(N_{gal}-1)\rangle = \langle (N_{cen}(N_{cen}-1))\rangle + 2\langle N_{cen}N_{sat}\rangle + \langle N_{sat}(N_{sat}-1)\rangle. \tag{4.61}$$

Having just one central galaxy, the first term on the right of equation (4.61) is null and, assuming a Poissonian distribution for N_{sat}, we obtain:

$$\langle N_{gal}(N_{gal}-1)\rangle = 2\langle N_{cen}N_{sat}\rangle + \langle N_{sat}\rangle^2. \tag{4.62}$$

Equation (4.49) becomes:

$$P^{1h}_{gal}(k) = \int dm \frac{dn}{dm} \frac{2\langle N_{cen}N_{sat}\rangle |u_{gal}(k,m)| + \langle N_{sat}\rangle^2 |u_{gal}(k,m)|^2}{\bar{n}^2_{gal}}. \tag{4.63}$$

An approximate shape for $\langle N_{gal}\rangle$ can be obtained considering that galaxies are made by baryons. Baryonic matter is a fixed fraction of the mass of the dark matter of the hosting halo. We can then assume $\langle N_{gal}|m\rangle \propto m^{\alpha}$. Considering $\langle N_{gal}\rangle$ as a function of the halo mass, we can place a further constraint on its form: one might expect that there is a minimum halo mass below which galaxies cannot be found, which corresponds to a truncation of the $\langle N_{gal}\rangle$ function. This is due to the energy feedback from supernovae: these stars are generated during an initial burst of star formation whithin the halo and their explosions may be sufficient to expel the baryons from the shallower potential wells of low mass halos. In our code we implemented two functional forms for the halo occupation distribution (HOD). Both of them rely on the assumptions we have just described. The simplest one is that of Zehavi et al. [127] and reads:

$$\begin{cases} N_{cen} = 1 \quad \text{if} \quad M > M_{min}, \\ 0 \quad \text{otherwise}, \end{cases} \tag{4.64}$$

and

$$\begin{cases} N_{sat} = \left(\frac{M}{M_{sat}}\right)^{\alpha} \quad \text{if} \quad M > \max(M_{min}, M_{sat}), \\ 0 \quad \text{otherwise}. \end{cases} \tag{4.65}$$

The number of central galaxies, N_{cent}, is described by a simple step function, which becomes equal to unity if the halo is massive enough to host a galaxy, i.e. $M > M_{min}$. As expected, the number of satellites is given by a power law. The quantity M_{sat} is the minimum mass required to an halo to host a satellite galaxy, in addition to the central one. The condition on the right ensures that the halo starts to host satellites only after having placed a galaxy in its center. The second model we coded is based on Tinker & Wetzel [128]. The central galaxy is parametrized as:

$$\langle N_{cent}\rangle_M = \frac{1}{2}\left[1 + \mathrm{erf}\left(\frac{\log M - \log M_{min}}{\sigma_{\log M}}\right)\right]. \tag{4.66}$$

This parametrization allows for a smooth transition between halos that are too small to contain galaxies and halos that are massive enough to host at least the central galaxy at their center. In this case, M_{min} is defined as the halo mass at which a galaxy has a 50% probability of containing a central galaxy. The parameter $\sigma_{\log M}$ represents the scatter in the logarithm of galaxy baryonic mass at fixed halo mass. This quantity regulates how rapid the transition is between having zero and one central galaxy. The satellite occupation function, instead, is parametrized as follows:

$$\langle N_{sat}\rangle_M = \frac{1}{2}\left[1 + \mathrm{erf}\left(\frac{\log M - \log 2M_{min}}{\sigma_{\log M}}\right)\right]\left(\frac{M}{M_{sat}}\right)^{\alpha}. \tag{4.67}$$

In the halos that are more massive than the minimum mass scale the number of satellite galaxies grows with a power law. The factor M_{sat} is the same that we find in equation (4.65). The cut-off has the same functional form as $\langle N_{cen}\rangle_M$, but with a transition mass twice the one of the central galaxy. This is needed to prevent halos with a low probability of containing a central galaxy from hosting satellites. In figure 4.5 we show the halo occupation distribution of galaxies, as function of the halo mass, obtained with our code. Tinker & Wetzel and Zehavi HODs [127, 128] are represented on the left and right panel respectively. The main difference between the two parametrizations consists in the cut of the HOD function at low masses, which is smoothed in the Tinker model and sharp in the Zehavi one. To have furter details on the HOD modelling, see [126, 129–131]. In figure 4.6 we show the one and two halo term of the galaxy power spectrum obtained with our code. The two halo term dominates at large scales, while the one halo term is prominent at smaller scales. On the left panel we compare two different sets of cosmological parameters, see Table 4.1. On the right panel we compare the galaxy power spectrum obtained using two different formalism for the halo mass function and the halo bias: Tinker (solid line) and Seth & Tormen (dash-dotted line). In both cases we used a NFW model for the halo density profile and a Tinker & Wetzel parametrization for the HOD.

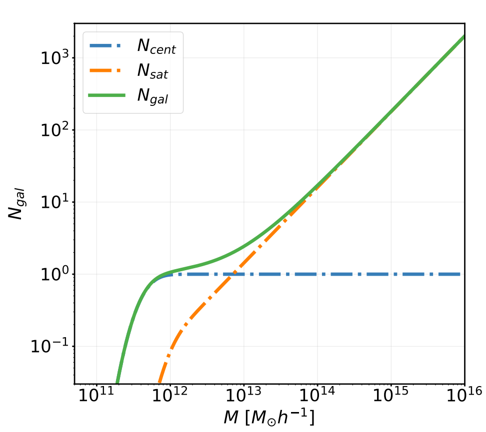

Figure 4.5: *Halo occupation distributions computed with Tinker & Wetzel modelling (left panel) and Zehavi modelling (right panel). Both panel show the contribution of the central galaxy (blue) and the satellites (orange). The sum of these two contributions gives the total number of galaxies in the halo,* N_{gal} *(green).*

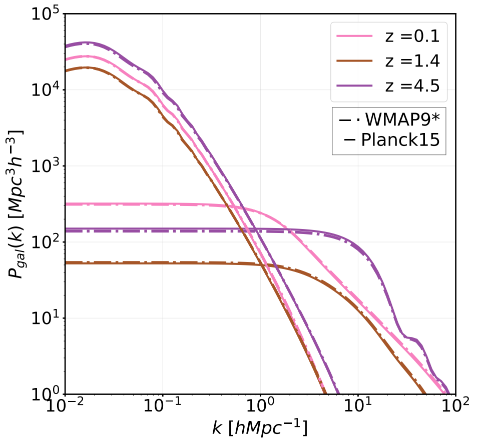

Figure 4.6: *One and two halo terms for three different redshift values. On the left panel we compare WMAP9** *and Planck15 cosmology. On the right panel we compare the galaxy power spectrum obtained using two different formalism for the halo mass function and bias: Tinker (solid line) and Seth & Tormen (dash-dotted line). The difference between the two model seems to increase with redshift (purple line) and is more evident on the one halo term.*

4.2 Secondary emission

In the previous section we described the distribution of galaxies within the dark matter structures. Now we will describe the emission of these galaxies, that generates the infrared background we observe at submillimeter wavelenghts. We will also use the main blocks which enter in the computation of the halos power spectrum to compute the halo model for the SZ effect. Moreover, considering the fact that CIB and SZ are tracer of the same underlying matter distribution, we will model their correlation always in the context of the halo model formalism. To conclude we will describe the empirical model used for the CIB poisson term at low frequencies, for the radio sources and for the galactic cirrus emission.

4.2.1 Unit convention

Usually, data at lower frequencies (95, 150, 220 GHz) are given in CMB units, while data at higher frequencies (600, 857, 1200 GHz) are in Jansky. For this reason, before starting with the description of the model, it is useful to focus on the unit of measure. For convention, the flux density unity is the Jansky, which is defined as:

$$Jy = 10^{-26} W m^{-2} Hz \tag{4.68}$$

and obtained by integrating over the solid angle of the source. For extended sources, the surface brightess is described in Jy per unit solid angle, $Jy sr^{-1}$, and the spectrum is given in unit of $Jy^2 sr^{-1}$. Nevertheless, in some cases the flux is given in CMB unit, which reports a signal as a deviation from the CMB blackbody, δT_{CMB}. To convert from $Jy sr^{-1}$ into δT_{CMB} μk, as a function of frequency we use:

$$\delta T_\nu = \left(\frac{\delta B_\nu}{\delta T}\right)\Bigg|_{T_{CMB}}, \tag{4.69}$$

where

$$\frac{\delta B_\nu}{\delta T}\Bigg|_{T_{CMB}} = \frac{2k}{c^2}\left(\frac{kT_{CMB}}{h}\right)^2 \frac{x^2 e^x}{(e^x-1)^2}. \tag{4.70}$$

4.2.2 Cosmic Infrared Background

The Cosmic Infrared Background (CIB) emission [132–134] originates from galaxies experiencing an active phase of star formation. The radiation, emitted at high frequencies by young and hot stars, is absorbed by dust and re-emitted at lower frequencies.

While the evolution of dark matter halos within the ΛCDM paradigm is quite well understood thanks to N-body simulations, the connection between the dark matter halo and the visible objects is not clear, especially in the sub-millimeter wavelenghts. The formalism we used in this project for the dusty galaxies has been originally created by Granato et al. [135] and then further developed by Cai et al. [136], hereafter C13. This model has been chosen as it provides a good fit to the multi−wavelength data (from the mid−IR to millimeter waves) on luminosity functions and number of counts at different redshifts. In our work we just use the final product of the C13 work, i.e. the luminosity functions, necessary for the computation of the CIB power spectrum. Nevertheless, for completeness, in the following sub-sections we briefly describe the Cai et al. formalism, see also [137–139].

The starting point of the model is the observed difference in stellar populations belonging to early-type and late-type galaxies. Early-type galaxies are massive spheroids, composed of relatively old stellar populations, characterized by a formation redshift $z \gtrsim 1 - 1.5$ [140]. In their early stage of formation the early-type galaxies were highly starforming and dust obscured. Their star formation phase has been quenced by AGNs feedback and lasted around $5 - 7 \times 10^8$ yr. As opposite, late-type denotes spiral or irregular galaxies. They formed at redshift $z < 1.5$ and are charcterized by younger stellar populations. Their star formation phase is regulated by supernovae feedback and can continue for few Gyr. We expect that galaxies co-evolve with the active nuclei at their centers. Since we do not have a physical model for the evolution of late type galaxies and AGN, Granato et al developed a hybrid approach, combining a physical model for the spheroidal galaxies and the early evolution of the AGNs with a phenomenological model for the late type galaxies and the low redshift AGNs evolution.

4.2.2.1 Luminosity function for early-type galaxies

In C13 modelling, the bolometric luminosity function (LF) of proto-spheroids can be obtained convolving the halo formation rate, $dn_{ST}(M_{vir})/d\ln M/dt$, with the galaxy luminosity distribution. At redshift higher than 1.5 the halo formation rate can be computed as the positive term of cosmic time derivative of the halo mass function, $dn/d\ln M$, which is written using the Seth & Tormen parametrization. The authors rewrite the analytical expression of the halo mass function accounting for a redshift evolution of the critical density for collapse:

$$dN_{ST} = \frac{dn_{ST}(M_{vir}, z)}{d\ln M} dM_{vir} = \frac{\bar{\rho}_{m,0}}{M_{vir}^2} f_{ST}(\nu) \frac{d\ln\nu}{d\ln M_{vir}} dM_{vir}. \tag{4.71}$$

Here again $\bar{\rho}_{m,0}$ is the present-day Universe mean comoving matter density and $\nu \equiv (\delta_c(z)/\sigma(M_{vir}))^2$ is the peak height. The redshift evolution of the critical overdensity for collapse is given by:

$$\delta_c(z) = \frac{\delta_0(z)D(0)}{D(z)}, \tag{4.72}$$

with

$$\delta_0(z) \simeq 1.686[1 + 0.0123 \log \Omega_m(z)], \tag{4.73}$$

as in [141]. The linear growth factor can be approximated following [142, 143] as:

$$D(z) = \frac{5\Omega_m(z)}{2(1+z)} \left[\frac{1}{70} + \frac{209}{140}\Omega_m(z) - \frac{1}{140}\Omega_m^2(z) + \Omega_m^{4/7}(z)\right]^{-1}. \tag{4.74}$$

Also the mass variance of the perturbation field, $\sigma(M_{vir})$, is given as an analytical approximation [144, 145]:

$$\begin{aligned}\sigma(M_{vir}) = \frac{0.8}{0.84}[&14.110393 - 1.1605397x - 0.0022104939x^2 \\ &+ 0.001331746x^3 - 2.1049631 \times 10^{-6}x^4],\end{aligned} \tag{4.75}$$

with $x \equiv \log M_{vir}/M_\odot$. Authors in C13 then write the expression for f_ν:

$$f_{ST}(\nu) = A(1 + (a\nu)^{-p}) \left(\frac{a\nu}{2}\right)^{1/2} \frac{e^{-a\nu/2}}{\pi^{1/2}}, \tag{4.76}$$

where $A = 0.322$, $p = 0.3$ and $a = 0.707$. The halo formation rate can be computed as the time derivative of the halo mass function:

$$\begin{aligned}\frac{dN_{ST}(M_{vir}, z)}{dt} &= N_{ST}(M_{vir}, z)\frac{d\ln f_{ST}(\nu)}{dt} \\ &\simeq N_{ST}(M_{vir}, z)\left[\frac{a\nu}{2} + \frac{p}{1 + (a\nu)^p}\right]\frac{d\ln\nu}{dz}\left|\frac{dz}{dt}\right|,\end{aligned} \tag{4.77}$$

with $dz/dt = -H_0(1+z)\sqrt{\Omega_{\Lambda,0} + \Omega_{m,0}(1+z)^3}$. The second block needed to build the luminosity function is the galaxy luminosity distribution computed at redshift z, inside a halo of mass M_{vir} and virialized at redshift z_{vir}, $P(\log L, z, M_{vir}, z_{vir})$. The total luminosity of a galaxy is the sum of the stellar component and the active nucleus. For each component, the model assumes a log-normal luminosity distribution:

$$P(\log L|\log \bar{L})d\log L = \frac{\exp\{-\log^2(L/\bar{L})/2\sigma^2\}}{\sqrt{2\pi\sigma^2}} d\log L, \tag{4.78}$$

where σ is the dispersion around the mean luminosity, $\bar{L}$, and it assumes different values for the stellar and AGN components. The distribution of the total luminosity, $L_{tot} = L_\star + L_{AGN}$, is then:

$$\begin{aligned} &P(\log L_{tot}|\log \bar{L}_\star, \log \bar{L}_{AGN})d\log L = d\log L_{tot} \\ &\times \int_{-\infty}^{\log L_{tot}} \frac{dx}{2\pi\sigma_\star\sigma_{AGN}} \frac{L_{tot}}{L_{tot}-10^x} \exp\{-(x-\log \bar{L}_\star)^2/2\sigma_\star^2\} \\ &\times \exp\{-[\log(L_{tot}-10^x) - \log \bar{L}_{AGN}]^2/2\sigma_{AGN}\}. \end{aligned} \tag{4.79}$$

Combining the two ingredients in equations (4.77), (4.79) C13 authors compute the comoving differential luminosity function, i.e., the number density of galaxies per unit luminosity interval at a given redshift. It is given by:

$$\begin{aligned} \Phi(\log L, z) = &\int_{M_{vir}^{min}}^{M_{vir}^{max}} dM_{vir} \int_{z}^{z_{vir}^{max}} dz_{vir} \left|\frac{dt_{vir}}{dz_{vir}}\right| \frac{dN_{ST}}{dt_{vir}}(M_{vir}, z_{vir}) \\ &\times P(\log L, z; M_{vir}, z_{vir}). \end{aligned} \tag{4.80}$$

A reasonable virialization redshift is $z_{vir}^{min} = 1.5$, as, after that epoch, the proto-spheroidal galaxies evolve toward the passive phase and their bolometric LF rapidly declines. More massive is the halo, faster is the decline, as the timescale of star formation is shorter in massive structures.

4.2.2.2 Luminosity function for late-type galaxies

As we don't have a theoretical model for the evolution of the low redshift galaxies, we consider an empirical parametrization of the luminosity function. In C13 authors adopt two late type galaxy sub-populations: "warm" starburst galaxies and "cold" late-type galaxies. For both these sub-populations they adopt the functional form suggested by [146]:

$$\begin{aligned} \Phi(\log L_{IR}, z)d\log L_{IR} = \Phi^\star \left(\frac{L_{IR}}{L^\star}\right)^{1-\alpha} \\ \times \exp\left[-\frac{\log^2(1+L_{IR}/L^\star)}{2\sigma^2}\right] d\log L_{IR}, \end{aligned} \tag{4.81}$$

where α is the low-luminosity slope and σ is the dispersion of each population, while $\Phi^\star$ and $L^\star$ are the characteristic density and luminosity. The values used for these parameters are reported in table 1 of C13.
In order to compute the monochromatic LF the authors make use of the spectral energy distribution (SED). For the stellar component they have:

$$\bar{\mathcal{L}}_{\star,\nu} \equiv \nu f_\star(\nu)\bar{L}_{\star,IR}, \tag{4.82}$$

where IR stands for infrared: the region of the spectrum in which we observe the emission connected to the star formation. In [137] it is shown that the submillimeter data coming from proto-spheroidal galaxies can be reproduced using a single SED. The reason for this is that the IR-emission coming from high redshifts is almost entirely generated by dust in molecular clouds, heated by the newly formed stars. This is not true for low z galaxies, in which there are other contributions to account for, as the cirrus emission. Although the contribution of contaminants affects the infrared emission in low redshift galaxies, the SED templates used to compute the luminosity function are just two: one for the cold and one for the warm population. We report figure 4 and 6 of C13 (Fig. 4.7 and 4.8 respectively) to show the SED template used, both for early and late type populations, and the luminosity function of all galaxies and AGN populations that contribute to the infrared emission.

4.2.2.3 Source counts and emissivity function

The luminosity function is used when computing the surface density of sources per unit flux density and redshift interval:

$$\frac{d^3N(S_\nu, z)}{dS_\nu dz d\Omega} = \frac{\Phi(\log L_{\nu'}, z)}{L_{\nu'} \ln 10} \frac{dL_{\nu'}}{dS_\nu} \frac{dV}{dz d\Omega}, \tag{4.83}$$

where $\nu' = \nu(1+z)$, and the flux S_ν can be calculated through the use of the luminosity distance D_L as:

$$S_\nu = \frac{(1+z)L_{\nu'}}{4\pi D_L^2(z)}. \tag{4.84}$$

The comoving volume per unit solid angle, in equation (4.83), can be computed as:

$$\frac{d^2V}{dz d\Omega} = \frac{c}{H_0} \frac{(1+z)^2 D_A^2(z)}{\sqrt{\Omega_\Lambda + (1+z)^3\Omega_m}}, \tag{4.85}$$

where D_A is the angular diameter distance. The cosmological and astrophysical information we are looking for is encoded in the power spectrum of the CIB inten-

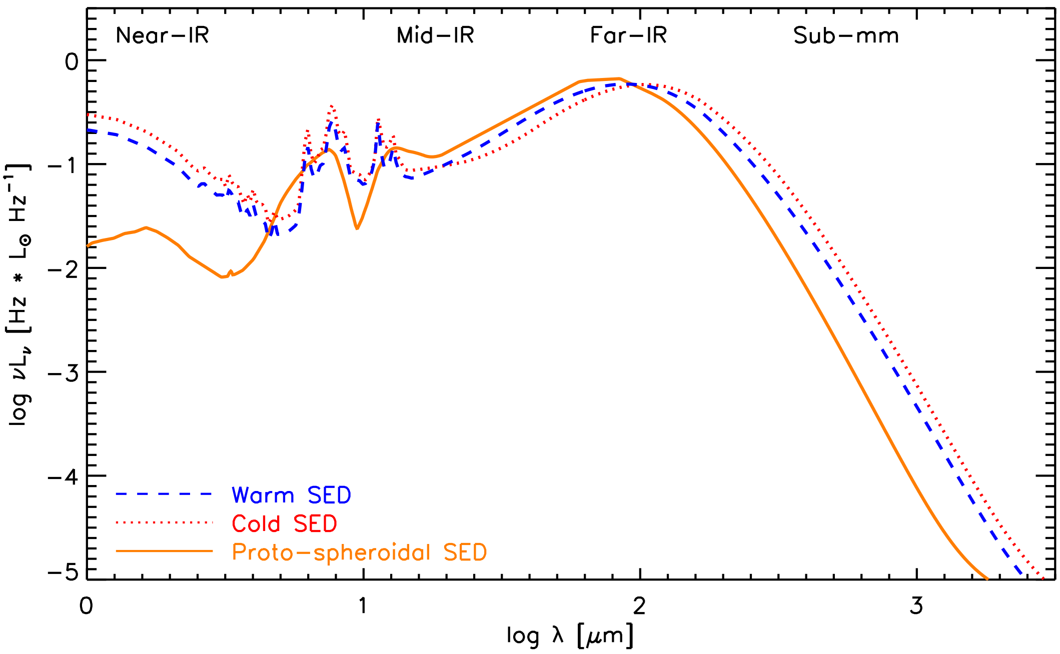

Figure 4.7: *SEDs template described in C13 for proto-spheroidal galaxies (solid orange), warm late-type (dashed blue) and cold late-type poulations (dotted red). The three SEDs are normalized to the same total IR luminosity* $log(L_{IR}/L_{\odot}) = 1$.

sity fluctuations. A key quantity involved in CIB power spectrum computation is the emissivity function, i.e. the redshift distribution of the cumulative flux density of sources below the detection limit, $S_{\nu,lim}$. It is defined as:

$$\frac{d^2S_\nu}{dzd\Omega} = \int_0^{S_{\nu,lim}} \frac{d^3N(S_\nu, z)}{dS_\nu dzd\Omega} S_\nu dS_\nu. \tag{4.86}$$

In figure 4.9 we show the emissivity function at six different frequencies, as function of redshift, both for early-type galaxies (solid line) and late-type galaxies (dashed line). See more details on the emissivity function computation in [147]. In order to model the infrared emission we can write its power spectrum as the sum of two components [148]:

$$C^{CIB}_{\ell,\nu,\nu'} = C^{clust}_{\ell,\nu,\nu'} + C^{shot}_{\ell,\nu,\nu'}. \tag{4.87}$$

The quantity $C^{shot}_{\ell,\nu,\nu'}$ is called the shot noise term, and quantifies the contribution of the distribution of the sources below the detection limit, which is assumed to be poissonian. The quantity $C^{clust}_{\ell,\nu,\nu'}$ is, instead, the contribution coming from the

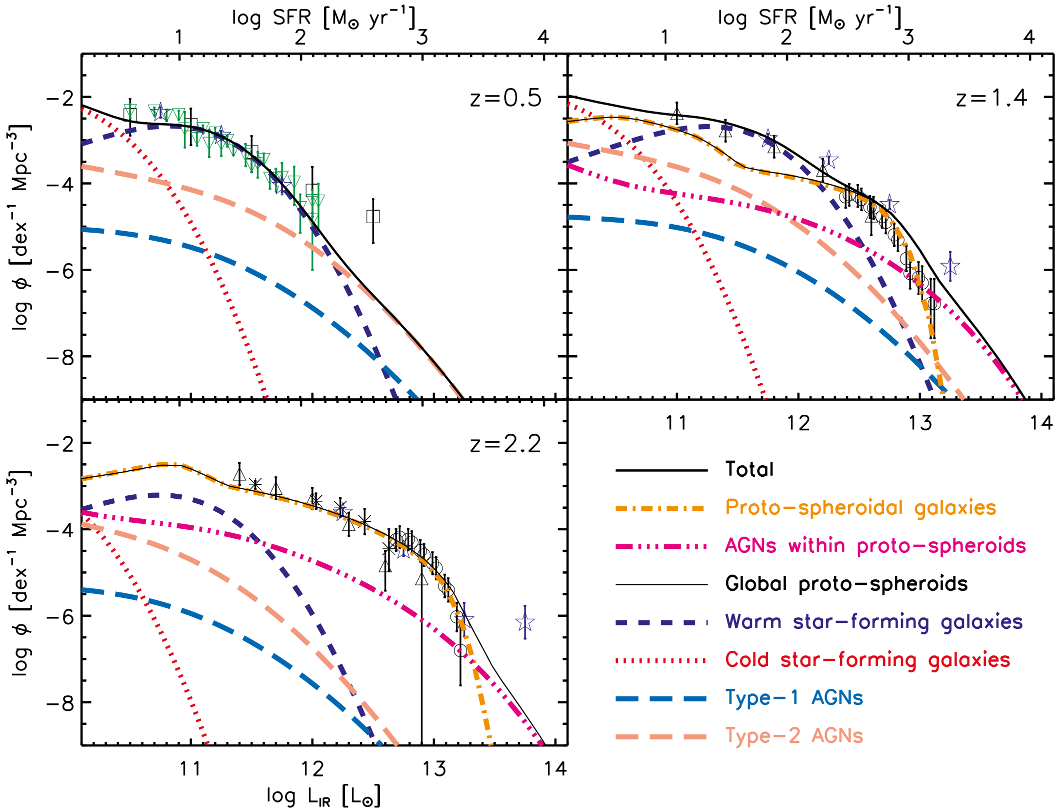

Figure 4.8: *Comparison between IR LF model and data, as shown in C13. The legend reports all the stellar and AGN populations that are taken into account. The stellar contribution is always dominant, apart for the very bright end tail. While at low redshift data are well described with the use of the cold and warm late-type populations, increasing with redshift the proto-spheroidal contribution becomes dominant.*

clustering of those sources.

The clustering term is related to the overdensities in the background that trace the dark matter distribution. It can then be described using the formalism of the halo model that we have presented in detail in the previous section. That formalism tells us how galaxies occupy the dark matter halos, while the emissivity function, equation (4.86), describes how those galaxies emit. The combination of these two fundamental blocks allows the computation of the clustering term of the CIB power spectrum:

$$C^{clust}_{\ell,\nu,\nu'} = \int \frac{dz}{\chi^2}\frac{dz}{d\chi}\frac{dS_\nu}{dz}\frac{dS_{\nu'}}{dz}P_{gal}(k=\ell/\chi,z). \qquad (4.88)$$

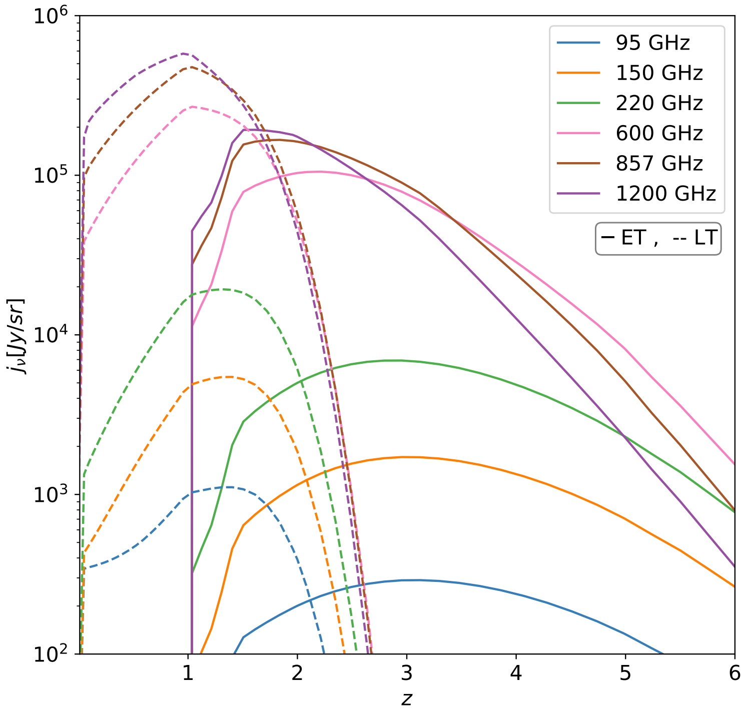

Figure 4.9: *Emissivity function at six different frequencies, as function of redshift. Low frequencies bands (95, 150, 220 GHz) are covered by the South Pole Telescope experiment (SPT), while high frequencies (600, 857, 1200 GHz) are the nominal bands of the SPIRE experiment. Early type galaxies (solid line) have their peak of star formation around $z \sim 2.5$. After redshift $z \sim 1$ this population undergoes a phase of passive evolution, as can be seen from the truncation of their infrared emissivity. The late-type population (dashed line), instead, has its active phase of star formation at lower redshift and shows its peak of emission at redshift $z \sim 1$.*

In this notation χ is the comoving distance and $\frac{dS_\nu}{dz}$ is the emissivity function, where we have neglected the dependence on the solid angle for simplicity. The term P_{gal} denotes the galaxy-galaxy power spectrum, as computed in equation (4.51). In the P_{gal} term, which includes both the one and the two halo terms, we used the *Limber approximation* [149, 150], and projected the three dimensional galaxy power spectrum to compute the angular one.
In figure 4.10 it is shown the CIB clustering power spectrum, computed with our code, at 150 (left panel) and 1200 GHz (right panel). Late-type (LP) population is in orange, while the early-type (EP) is in blue.

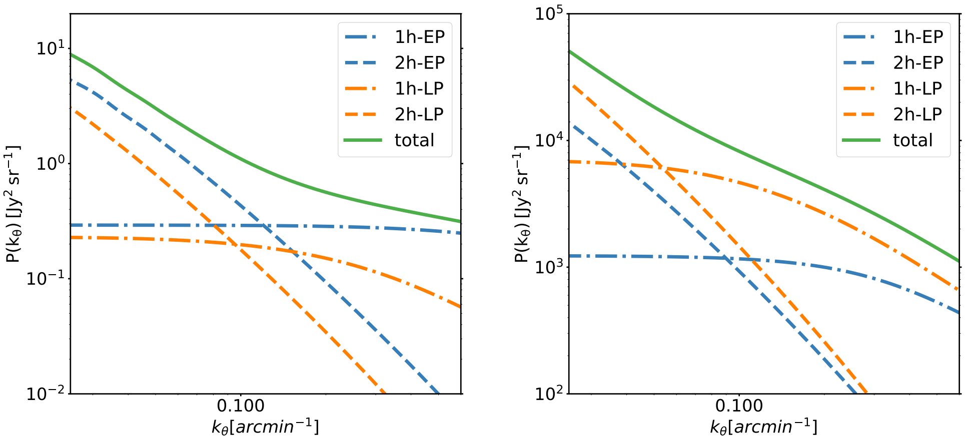

Figure 4.10: *CIB clustering power spectrum at 150 (left) and 1200 GHz (right). Late-type (LP) population is in orange, while the early-type (EP) is in blue. The hosting halo minimum mass is $M = 10^{12} M_\odot h^{-1}$ for the EP population and $M = 10^{11} M_\odot h^{-1}$ for the LP one, as these galaxies usually occupy less massive structures, with respect to the proto-spheroids. In both panels we see the two halo term (dashed line), the one halo term (dash-dotted line) and the total power spectra (green solid line). The two halo term is dominant at larger scales, while the one halo term becomes more relevant at smaller scales. While the early type emission dominates the power spectrum at low frequencies, at higher frequencies we observe the near Universe, so the late-type contribution becomes more relevant.*

The power spectrum of the poisson (shot) noise term is instead independent on the angular scale and can be computed as:

$$C_{\ell,\nu}^{shot} = \int_0^{S_{lim}} S_\nu^2 \frac{dN}{dS_\nu}(S_\nu) dS_\nu, \tag{4.89}$$

where S_{lim} is the flux density level above which sources are detected and consequently masked. The term dN/dS_ν in equation (4.89) represents the differential number counts. i.e. the number of galaxies per unit interval of flux density, at an observed frequency ν, and per unit solid angle:

$$\frac{dN}{dS_\nu d\Omega}(S_\nu) = \int_{z_{min}}^{z_{max}} dz \frac{\Phi(\log L_{\nu'}, z)}{L_{\nu'} \ln 10} \frac{dL_{\nu'}}{dS_\nu} \frac{d^2V}{dz d\Omega}. \tag{4.90}$$

4.2.2.4 Poisson noise: high frequency modelling

We use two different procedures to determine the level of the shot noise at SPIRE frequencies. The first one is based on previous analysis, which simply fit for the value of the shot noise within a flat prior [151]. The second procedure is designed to relate the value of the shot noise directly to the measured numbers of counts. It uses resolved data from [152–155] and model them as the sum of two functions: a Schechter function, dominating the faint flux densities, and a power law to describe the bright flux densities. The sum of these two functions is fitted to data in each of the three SPIRE frequency bands and the shot noise is computed as a byproduct. The fit to data is performed with a MCMC, as implemented in [156], and returns a distribution of values of the shot noise. The mean and standard deviation of those distributions has been computed[3] and we use them to impose a gaussian prior on level of the Poisson noise. The values of the mean and standard deviation of the shot noise distributions are reported in Table 4.2.

Frequency	Poisson noise
[GHz]	[$\mathrm{Jy}^2\mathrm{sr}^{-1}$]
600	2479 ± 75
857	6205 ± 133
1200	9833 ± 172

Table 4.2: *Mean and standard deviation of the shot noise distributions derived from the fit to number counts. To fit for CIB data at Hershel/SPIRE frequencies we impose a gaussian prior centered in the mean value and large three times the standard deviation.*

In figure 4.11 we show the fit to number counts obtained with the sum of a Schechter function and a power law.

4.2.2.5 Poisson noise: low frequency modelling

Except for the brightest flux densities, at the South Pole Telescope working frequencies (95, 150, 220 GHz) we do not have enough constraints on the number counts. Therefore, in order to model the poissonian term of the CIB emission, we use an empirical modelling, i.e. a flat angular template and a modified black body spectral dependence. At these frequencies, the poisson term of the CIB power specturm can be written as:

$$D^P_{\ell,\nu,\nu'} = D^P_{3000}\epsilon_{\nu\nu'}\frac{\eta_\nu\eta_{\nu'}}{\eta_0\eta_0}\left(\frac{\ell}{3000}\right)^2, \tag{4.91}$$

---

[3] Mattia Negrello, private comunication.

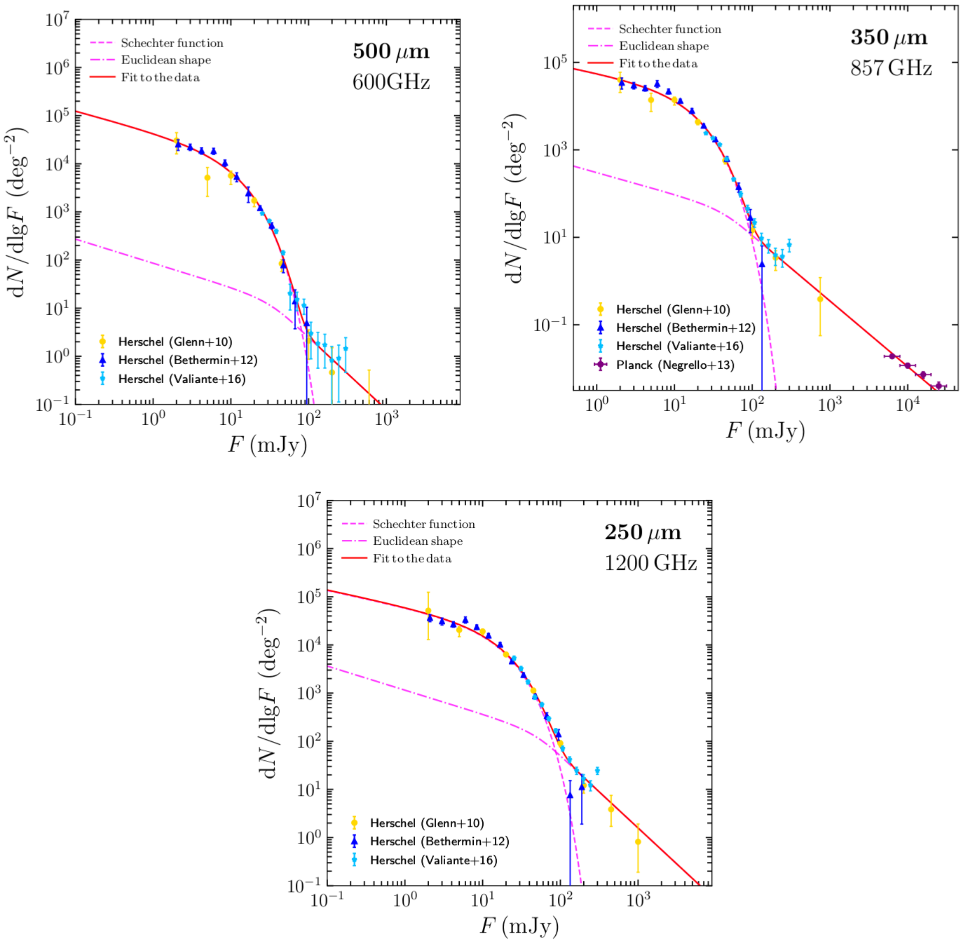

Figure 4.11: *Fit to the number of counts from three different datasets. The bright flux densities are described with a power law, while the faint flux densities with a Schechter function.*

where D^P_{3000} is the amplitude of the power spectrum at $\ell = 3000$ and frequency ν_0. The CIB poisson emission in equation 4.91 is written in flux units, despite the result is in μK^2. This is possible through the use of the quantity ϵ, which converts between the power at the normalization frequency, ν_0, and the power in a cross spectrum $\nu \times \nu'$, providing the result in CMB temperature units. It is defined as:

$$\epsilon_{\nu,\nu'} \equiv \frac{\frac{dB}{dT}\big|_{\nu_0} \frac{dB}{dT}\big|_{\nu_0}}{\frac{dB}{dT}\big|_{\nu} \frac{dB}{dT}\big|_{\nu'}}, \tag{4.92}$$

where B is the CMB black-body specific intensity, evaluated at T_{CMB}, while ν and ν' are the effective frequencies of the experiment under analysis. The quantity dB/dT is defined in equation 4.70, while η_ν describes how the CIB brigtness scales with frequencies and is parametrized with a modified black body:

$$\eta_\nu = \nu^\beta B_\nu(T). \tag{4.93}$$

Here $B_\nu(T)$ is again the black-body spectrum for temperature T, while β is the effective dust emissivity index. We followed the choice of George et al [96], hereafter G15, and fixed the temperature of the dust at 20K, while we let the spectral index to vary within a flat prior, $\beta \in [0.5, 3.5]$.

4.2.3 Sunyaev Zeldovich Effect

The Sunyaev-Zeldovich effect [9] arises when CMB photons are scattered by high energy electrons in intracluster gas. The high temperature, $\sim 10^8$ K, of the gas in clusters ensures it is ionized and free electrons interact with CMB photons through inverse Compton scattering. The energy transfer involved in the process causes a distortion of the black body distribution: photons are moved from the Rayleigh-Jeans part of the CMB spectrum to the Wien region, though preserving the total amount of photons. It is possible to compute the decrease of intensity in the Rayleigh-Jeans tail, which depends on the physical properties of the cluster [157]:

$$\Delta T(x) = \Delta T_{thermal}(x, y) + \Delta T_{kinetic}(x, \tau, v_p), \tag{4.94}$$

with $x = h\nu/kT_{cmb}$. The first term in equation (4.94) is the thermal distortion of the CMB intensity spectrum, while the second term arises when the electrons have high kinetic energy due to bulk motions and, in particular, present a net peculiar velocity along the line of sight. Figure 4.12 shows the spectral distortion of the CMB radiation due to the SZ effect.

Thermal Sunyaev Zeldovich
The tSZ distortion can be written as:

$$\frac{\Delta T_{thermal}(x, y)}{T_{CMB}} = y g(x). \tag{4.95}$$

The quantity $g(x)$ is the thermal distortion spectral shape:

$$g(x) = \left(x \frac{e^x + 1}{e^x - 1} - 4 \right), \tag{4.96}$$

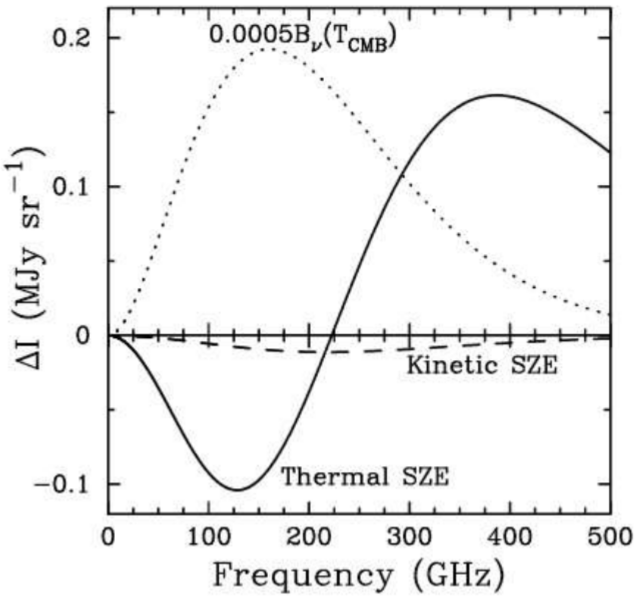

Figure 4.12: *Spectral distortion of the CMB spectrum due to the SZ effect. The thick solid line is the tSZ and the dashed line is the kSZ. For reference the* 2.7 *K thermal spectrum for the CMB intensity, scaled by* 0.0005*, is shown by the dotted line. Figure taken from [158].*

while y is its amplitude, given by the Compton parameter:

$$y = \frac{\sigma_T}{m_e c^2} \int dl n_e k T_e. \tag{4.97}$$

Here m_e and n_e are the mass and number density of the electron, while σ_T is the Thomson scattering cross section. The integral is computed along the line of sight, dl. From equation (4.97) we can also deduce one of the main property of the tSZ effect: its surface brightness is redshift indipendent. This makes it useful not only for cosmological analysis, but also for high redshift clusters study. Decomposing a SZ map in spherical harmonics, $Y_{\ell,m}$, we obtain:

$$y(\mathbf{n}) = \sum_{\ell,m} y_{\ell,m} Y_{\ell,m}(\mathbf{n}). \tag{4.98}$$

The adimensional angular power spectrum of the Compton parameter map is then [159]:

$$C_\ell^{tSZ} = \frac{1}{2\ell+1} \sum_m y_{\ell,m} y^\star_{\ell,m}. \tag{4.99}$$

From the large scale structure point of view, the tSZ effect is described with a halo model formalism, similarly to the CIB. The clusters originating the tSZ effect are usually located at redshift less than 1.5, in very massive and clustered structures. For this reason, the density contrast required to identify an halo hosting a SZ-cluster is $500\rho_c$. Note that it was $200\rho_c$ for CIB, as the level of clustering needed to host star-forming galaxies is expected to be lower. The general formalism for the thermal SZ halo model can be found in [6, 160–165]. The one and two halo terms take the form:

$$C_\ell^{yy-1h} = \int \frac{dV}{dz} dz \int dM \frac{dN}{dM} \tilde{y}_\ell(M,z)^2, \tag{4.100}$$

$$\begin{aligned} C_\ell^{yy-2h} = \int \frac{dV}{dz} dz P_{lin}(k=\ell/\chi, z) \\ \left[\int dM \frac{dN}{dM} b(M) \tilde{y}_\ell(M,z)\right]^2 . \end{aligned} \tag{4.101}$$

Here dV/dz is the comoving volume element defined in equation (4.85) and P_{lin} is the linear matter power spectrum. The halo mass function, dN/dM, and the halo bias, $b(M)$, are computed with Tinker et al. [166] parametrization. Following this reference, in the case of the bias, we need to replace the constants inside equation (4.29) with a new set of parameters:

$$\begin{aligned} A &= 1.0 + 0.24y \exp\left[-(4/y)^4\right], \\ a &= 0.44y - 0.88, \\ B &= 0.183, \\ b &= 1.5, \\ C &= 0.019 + 0.107y + 0.19 \exp\left[-(4/y)^4\right], \\ c &= 2.4, \end{aligned} \tag{4.102}$$

with $y \equiv \log_{10}\Delta$. The Fourier transform of the halo density profile, used for galaxy clustering, is replaced with the Fourier transform of the 3D Compton parameter [167]:

$$\tilde{y}_\ell(M,z) = \frac{\sigma_T}{m_e c^2} \frac{4\pi r_{500}}{\ell_{500}^2} C P_0 \int dx x^2 \frac{\sin(\ell x/\ell_{500})}{\ell x/\ell_{500}} P_e(x). \tag{4.103}$$

Here $x \equiv r/r_{500}$ and $\ell_{500} \equiv D_A/r_{500}$, where the subscript denotes the density contrast within that radius. The quantity P_e is the electron pressure profile, for which we use a standard generalized Navarro-Frenk-White parametrization

[115, 168]:

$$P_e(x) = (c_{500}x)^{-\gamma}\left[1 + (c_{500}x)^{\alpha}\right]^{(\gamma-\beta)/\alpha}, \tag{4.104}$$

with P_0, α, β, γ fixed to a constant. We use the best fit values computed in [169] and reported in Table 4.3.

P_0	c_{500}	γ	α	β
6.41	1.81	0.31	1.33	4.13

Table 4.3: *Electron pressure profile parameters.*

The parameter C is, instead, a function of the halo mass:

$$C = 1.65\left(\frac{h}{0.7}\right)^2\left(\frac{H}{H_0}\right)^{\frac{8}{3}}\left[\frac{(h/0.7)\tilde{M}_{500c}}{3\times 10^{14}M_\odot}\right]^{\frac{2}{3}+0.12}. \tag{4.105}$$

The mass used in equation (4.105), $\tilde{M}_{500c}$, is called *hydrostatic mass* and do not necessarily concide with the true mass. It can contain a bias due to non-thermal pressure, observational effects, and other uncertainties in the cluster pressure modelling. We then introduce the bias parameter B, which relates the true and hydrostatic mass: $\tilde{M}_{500c} = M_{500c}/B$. Accordingly with Planck notation [170], we actually use the parameter b, which relates to the bias as:

$$B = (1-b)^{-1}. \tag{4.106}$$

As $\ell_{500} \propto 1/r_{500}$ and $r_{500} \propto M_{500}^{1/3}$, the bias does not only affect the power spectrum normalization but also the angular dependence. The total tSZ adimensional power spectrum is then given by:

$$C_\ell^{yy} = C_\ell^{yy-1h} + C_\ell^{yy-2h}, \tag{4.107}$$

which can be converted in the tSZ power spectrum, expressed in CMB units, multiplying by the CMB temperature and spectral dependence reported in equation (4.96):

$$C_{\ell,\nu,\nu'}^{tSZ} = T_{CMB}^2 g(\nu)g(\nu')C_\ell^{yy} \tag{4.108}$$

In figure 4.13 it is shown the Compton parameter power spectrum. The one halo term is in blue, while the subdominant two halo term in orange.

Kinetic Sunyaev Zeldovic

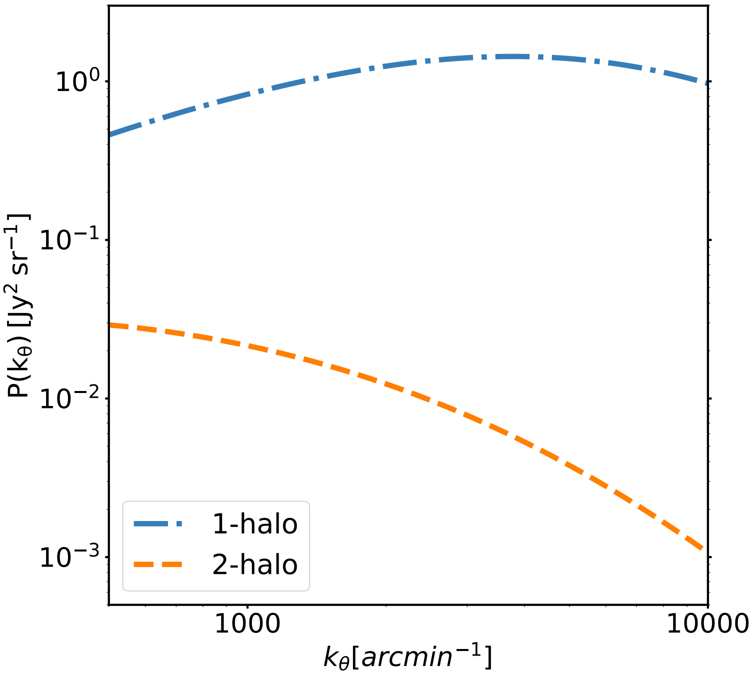

Figure 4.13: *Compton parameter power spectrum. Unlike the CIB, the tSZ power is dominated by the one halo term (blue) at all scales, while the two halo term (orange) is more than an order of magnitude lower, due to the scarcity of high massive tSZ clusters.*

The kinetic distortion in the last term of equation (4.94) has no spectral dependence. It is given by:

$$\Delta T_{kinetic}(x, \tau, v_p) = -\beta\tau. \tag{4.109}$$

The amplitude of this effect is regulated by $\beta = v_p/c$ and τ. The first is the average line-of-sight streaming velocity of the gas, defined with a positive sign if the gas is approaching the observer. The second is the Thomson scattering optical depth:

$$\tau = \sigma_T \int d\ell n_e. \tag{4.110}$$

Usually the kSZ is modelled through the use of an angular template multiplied by a free amplitude. We used the template of G15, which split the kSZ into two contributions: the "homogeneous kSZ" and the "patchy kSZ". The first one arises after the Reionization epoch, in a fully ionized Universe [171]. The second component, instead, comes from the peculiar motion of the partially ionized gas during Reionization [172]. The template power spectrum for homogeneus

Reionization is obtained by means of hydrodynamical simulations, including cooling and star formation. It has been computed through measurements of the power spectrum of gas fluctuations in simulations over a chosen range of redshifts. The approximate scaling of this template with cosmological parameters is given by:

$$\begin{aligned} D^{kSZ} \propto & \left(\frac{h}{0.71}\right)^{1.7}\left(\frac{\sigma_8}{0.80}\right)^{4.7}\left(\frac{\Omega_b}{0.044}\right)^{2.1} \\ & \times \left(\frac{\Omega_m}{0.264}\right)^{-0.4}\left(\frac{n_s}{0.96}\right)^{-0.2}. \end{aligned} \tag{4.111}$$

The dependence on cosmological parameters does not affect our analysis, as the template we used has been precomputed at fixed cosmology and rescaled to one at $\ell = 3000$. The patchy kSZ is also derived from simulations: once identified, the ionized regions forming during the Reionization epoch are correlated with the density and velocity fields to determine the kSZ power spectrum. The kSZ amplitude resulting from these simulations depends mainly on the midpoint and total duration of Reionization. As opposite, the shape of the patchy kSZ power spectrum is quite robust with respect to changes in duration and timing of Reionization. The dependence of patchy kSZ on cosmological parameters is the same of homogeneus kSZ, see equation (4.111).
The template we used assumes that reionization starts at $z = 11$ and ends at $z = 8$. As anticipated, the amplitude of the template is normalized to $1\mu k^2$ at $\ell = 3000$ and then left as a free parameter in the fit to data:

$$D_\ell^{kSZ} = a_{kSZ} D_{0,\ell}^{kSZ}, \tag{4.112}$$

where a_{kSZ} is the fitted amplitude and $D_{0,\ell}^{kSZ}$ is the normalized template.

4.2.4 tSZ-CIB correlation

The unresolved clusters, contributing to the SZ effect, and the dusty sources, emitting the CIB, are both tracers of the dark matter distribution within halos, although showing different dependence on the halo properties. For this reason we expect to find a certain degree of correlation between these two observables [173]. Addison et al. [174], hereafter A12, have modelled this correlation and found values between 10% and 50%, depending on the multipole and the separation between the two frequency used in the computation of the cross-spectrum. The uncertainty on the amount of tSZ-CIB correlation is dominated by the lack of precise knowledge about the mass of the halos hosting the CIB sources and their redshift ditribution. As the tSZ-CIB power does not vary significantly with frequencies in the SPT bands, it is somewhat degenerate with the kSZ. An imprecise modelling of the correlation between CIB and tSZ would then give wrong contraints on the kSZ. In our code we used a halo model to describe the tSZ-CIB correlation. The one halo term provides the correlation between the CIB sources and the tSZ within the same halo. The two halo term, instead, arises due to the correlation between a dusty galaxies in one halo and a tSZ clusters in another halo. As for the tSZ, the two halo term is subdominant, but still not negligible. Consider the scenario in which a massive halo, contributing to the tSZ, has no star formation happening within it. This implies no CIB sources and consequently no tSZ-CIB correlation from the one halo term. Still, there can be a contribution from the two halo term, arising from some overlap in the redshift distribution between dusty galaxies and the tSZ halos. We write our formalism in order to be coherent with A12 notation and we introduce the mean source flux density $\langle S_\nu(M,z)\rangle$. In general this quantity depends on redshift and mass. We followed A12 and C13 and neglect the dependence of the flux density on the mass of the source, considering only the redshift dependence. Starting from the emissivity we can obtain an expression for $\langle S_\nu(z)\rangle$:

$$\frac{dS_\nu(z)}{dz} = s_\nu(z)\frac{dV}{dz}, \tag{4.113}$$

where

$$s_\nu(z) = \int dM \frac{dN}{dM} S_\nu^w(z)\langle N_{gal}\rangle = S_\nu^w(z) n_{gal}. \tag{4.114}$$

Equation (4.113) becomes:

$$\frac{dS_\nu(z)}{dz} = S_\nu^w(z) n_{gal}\frac{dV}{dz}. \tag{4.115}$$

We can then derive a number-counts weighted emissivity:

$$S_\nu^w(z) = \frac{\frac{dS_\nu(z)}{dz}}{n_{gal}\frac{dV}{dz}} = \frac{\int \frac{dN}{dS_\nu dz} S_\nu dS_\nu}{n_{gal}\frac{dV}{dz}}. \tag{4.116}$$

The halo terms parameterization then becomes:

$$\begin{aligned} C_{\ell,\nu,\nu'}^{tSZ\times CIB-1h} = T_{CMB} \int \frac{dV}{dz} dz \left(g(\nu) S_{\nu'}^{w} + g(\nu') S_{\nu}^{w} \right) \\ \int dM \frac{dN}{dM_{500}} \tilde{y}_{\ell}(M_{500}, z) u_{gal} \langle N_{gal} \rangle, \end{aligned} \tag{4.117}$$

$$\begin{aligned} C_{\ell,\nu,\nu'}^{tSZ\times CIB-2h} = T_{CMB} \int \frac{dV}{dz} dz P_{lin}(k = \ell/\chi, z) \left(g(\nu) S_{\nu'}^{w} + g(\nu') S_{\nu}^{w} \right) \\ \left[\int dM \frac{dN}{dM_{500}} b_{500}^{SZ}(M_{500}) \tilde{y}_{\ell}(M_{500}, z) \right] \\ \left[\int dM \frac{dN}{dM} b(M) u_{gal} \langle N_{gal} \rangle \right]. \end{aligned} \tag{4.118}$$

The quantities denoted with the subscript $'500'$ are computed using a density contrast of $500\rho_{crit}$, as explained in the SZ modelling treatment. In order to compute the bias b^{SZ} we are using equation (4.102). In the model described, the functions involved in the computation of SZ and CIB are also used to obtain their correlation. Previous studies, such as Dunkley et al. [95] and G15, used a template approach for the tSZ-CIB correlation. Their parametrization requires the introduction of a correlation coefficient, ξ^{G}, which is the same on all angular scales. In addition to being more physically motivated with respect to G15 approach, our model does not need the introduction of new parameters and can eventually account for the scale dependence of the tSZ-CIB correlation. In figure 4.14 we show the tSZ-CIB correlation power spectrum at 150 GHz. As the massive clusters that cause the tSZ effect are located at low redshift, the correlation with CIB is higher for the late-type population (orange) with respect to the early-type one (blue).

4.2.5 Other contaminants

4.2.5.1 Radio sources

We included in the model a poisson term for the radio sources [175, 176] below the detection limit, as in G15. The flux density threshold has been set at ~ 6.4 mJy at 150 GHz, because, in SPT maps, all sources brighter than this flux density, and with spectral index consistent with a synchrotron emission, are identified as radio galaxies and masked. The Poisson term for radio emission is

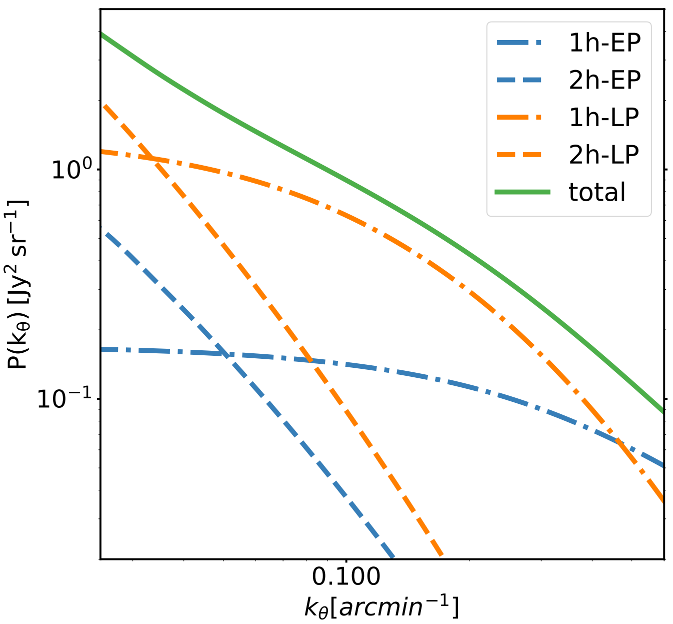

Figure 4.14: *tSZ-CIB correlation power spectrum at 150 GHz. As in the CIB case the early-type population (orange) is computed assuming $M_{min} = 10^{12} M_\odot h^{-1}$, while for the late-type population (blue) we assumed $M_{min} = 10^{11} M_\odot h^{-1}$. As the massive clusters thats cause the tSZ effect are located at low redshift, the correlation with CIB is higher for the late-type population. Massive clusters are rare and for this reason the one halo term (dash-dotted line) is the dominant contribution, especially for the late-type population.*

then:

$$D^r_{\ell,\nu,\nu'} = D^r_{3000} \epsilon_{\nu,\nu'} \left(\frac{\nu\nu'}{\nu_0^2}\right)^{\alpha_r} \left(\frac{\ell}{3000}\right)^2 . \tag{4.119}$$

The quantity D^r_{3000} is the amplitude of the power spectrum at $\ell = 3000$ and frequency ν_0, while α_r is the effective spectral index of the radio source population. The unit conversion factor, $\epsilon_{\nu,\nu'}$, is computed in equation (4.92). We neglected the clustering of the radio galaxies, as it is expected to be well below the uncertainty on the clustered CIB signal at SPT frequencies [177]. We did not even consider the correlation between radio sources and tSZ signal. Indeed, [178, 179] have shown that the number of radio sources with significant flux density in the mm range of the spectrum and correlated with galaxy clusters is expected to be low, well under the tSZ-CIB correlation amplitude.

4.2.5.2 Galactic cirrus emission

Galactic cirrus is the less relevant foreground term we included in the model [180]. We tested two different parametrizations for this emission. The first can be found in [95] and reads:

$$D^{cir}_{\ell,\nu,\nu'} = D^{cir}_{3000,\nu,\nu'}\left(\frac{\ell}{3000}\right)^{-1.2} \tag{4.120}$$

The amplitude can both be varyed or fixed to the measured value at $\ell = 3000$: 0.16, 0.21, 2.19 μK^2 at 95, 150, 220 GHz. These values represent the autospectra powers, and the cross-frequency amplitudes are the geometric means of these parameters.
The second modelling is taken by G15 and Fixsen et al. [133]. The authors model the cirrus similarly to the Poisson noise of the CIB:

$$D^{cir}_{\ell,\nu,\nu'} = D^{cir}_{3000}\epsilon_{\nu\nu'}\frac{\eta_\nu\eta_{\nu'}}{\eta_0\eta_0}\left(\frac{\ell}{3000}\right)^{\alpha_{cir}} \tag{4.121}$$

The quantity D^r_{3000} is the amplitude of the power spectrum at $\ell = 3000$ and frequency ν_0. Again the unit conversion $\epsilon_{\nu\nu'}$ is given by equation (4.92), while η_ν is the modified black body defined as in equation (4.93). The temperature of the cirrus dust is fixed at $T = 29$K and the spectral index at $\beta = 0.69$. The angular template has the same index as the former modelling, $\alpha_{cir} = -1.2$. The amplitude of the galactic cirrus can in principle be varied, but we decided to fix it to G15 best fit and set $D^{cir}_{3000} = 0.65$.

4.3 Constraints on the parameters of the foregrounds

In this section we use the model detailed above to describe data at millimeter and sub-millimeter wavelenghts. We have chosen to investigate two datasets: the first includes data from the SPT and has been released by G15. The SPT nominal frequencies are 95, 150, 200 GHz. The second dataset is comprehensive of both the SPT and Hershel/SPIRE bandpowers, with the SPIRE working frequencies assuming the nominal values of 600, 750, 1200 GHz. This dataset has been released by Viero et al. in 2019 and, from now on, will be denoted as V19. The high frequencies give reliable contraints on the clustering parameters of both early and late type star forming galaxies. Moreover they allow a deep study of the shot noise term both from power spectra analysis and from galaxy number counts. Also the low frequencies can be used to study the clustering parameters of the CIB sources, mainly for the early type population. Moreover they are necessary to constrain the parameters describing the tSZ, the kSZ and the radio sources. The G15 dataset has been chosen in order to ensure the possibility to have a direct comparison between the results of our model with those obtained by the authors in G15 analysis. On this dataset, which have a well-behaving covariance matrix, we could explore the degeneracies among the parameters of the model. The baseline is made by seven parameters: the hydrostatic mass bias, b, the clustering parameters of the early type population, $Log_{10}(M_{min}^{EP})$ and α_{EP}, the amplitude and spectral index of the poisson noise, A_p and β, the amplitude of the kSZ and of the radio sources, A_{kSZ} and A_r. After an investigation on the degeneracy between the kSZ and the tSZ-CIB correlation, we added two parameters to the fit: $Log_{10}(M_{min}^{LP})$ and α_{LP}. This allows to improve the modelling of the local sources, those more correlated with the SZ effect. The V19 dataset had never been used for model fitting before our analysis. In the work presented here we performed a study only of the SPT and SPIRE portion separately, while leaving the joint study for a future work. The SPT part of this dataset is derived on the same maps of the G15 dataset and serves as test to confirm the conclusions drawn in the G15 case. The added information comes from the SPIRE frequencies. In this case the baseline model includes the clustering parameters of both populations ($Log_{10}(M_{min}^{EP})$, α_{EP}, $Log_{10}(M_{min}^{LP})$, α_{LP}) and the level of the shot noise for the three SPIRE autospectra ($PN_{600\times600}$, $PN_{857\times857}$, $PN_{1200\times1200}$).

4.3.1 SPT-SZ survey: dataset and results

The South Pole Telescope is a 10 meter diameter telescope operating at the Amundsen-Scott South Pole station in Antarctica [87]. The telescope is designed for conducting large-area millimeter surveys of faint emissions, as required to map primary and secondary anisotropies in the CMB. As already mentioned, the first analysis we present is on the dataset released by G15. Here we briefly describe the dataset, but we refer to the aforementioned paper for all the details. The dataset used comes from the 2540 deg^2 of sky observed with the SPT-SZ camera from 2008 to 2011. The SPT-SZ camera consists of 960 horn-coupled spiderweb bolometer. Its field of view was divided into 19 contiguous sub-patches, called fields, for observations. Seventeen of the 19 fields were observed to an approximate depth of 18 μK-armcin at 150 GHz. The noise levels at 95 and 220 GHz, instead, vary significantly between the years of observation. For details on the telescope, the receiver, the detectors see [181–184]. A complete overview of the time-ordered data (TOD), filtering and map-making procedure can be found instead in [92]. The SPT beams are measured using a combination of bright point sources in each field, Venus and Jupiter. The main lobes of the SPT beam at 95, 150, 220 GHz have $1.7'$, $1.2'$ and $1.0'$ gaussian FWHM. The observation-to-observation relative calibration of the TOD are determined from the measurements of a galactic HII, RCW38, several time per days. The absolute calibration is determined by comparing the SPT power spectrum and the Planck CMB power spectrum per each frequency [185]. The comparison is performed in ℓ-bins over the multipole range $\ell \in [670, 1170]$, chosen as dominated by the primary CMB power at these observation frequencies. The pseudo-C_ℓ method [186–188] has been used to estimate the power specturm from the Fourier transform of the maps. The whole analysis is performed in flat sky approximation, replacing the spherical harmonics transform with the Fourier transform. The MASTER algorithm [186] has been employed to account for beam, apodization, filtering and limited sky fraction. In addition to the autospectra computed by the use of MASTER, also the cross-spectra are estimated in order to eliminate the noise bias. The cross spectra are obtained from the combination of maps at two different frequencies in Fourier space. The maps used are smoothed at the edges through a window function and depurated by point sources with flux density higher than ~ 6.4 mJy at 150 GHz by means of proper masking. They are also weighted by an array including the theoretical power spectrum from simulations and the noise power. The obtained C_ℓ are averaged within the bins to obtain the cross band powers, details in [91,94]. The covariance matrix includes instrumental noise variance and sample variance, which is estimated from signal-only simulations. The authors mention that the off-diagonals blocks in the estimated covariances can be large compared to the true covariance. For this reason they compute analytically the off-diagonals blocks from the diagonal elements, following Appendix A of [91]. The covariance containing the sample variance and the instrumental noise is then added to the beam and calibration covariance, to obtain a full description of the uncertainties. The nominal frequencies at which SPT operates are 95, 150 and 220 GHz, but the effective band center can vary with the source spectrum. A radio-like source spectrum ($\alpha = -0.5$) have band centers of 95.3, 150.5 and 214.0 GHz. For a dust-like source spectrum ($\alpha = 3.5$), which characterizes CIB and cirrus emission, the effective frequencies are 97.9, 154.1 and 219.6 GHz. When considering a tSZ power spectrum we have 97.6, 153.1 and 218.1 GHz. In the

modelling of some of these foregrounds we need a normalization frequencies. We always use the central band of each of the different components, except for the cirrus modelling, where the normalization frequency is $\nu_0 = 219.6$ GHz.
In the following we present the model fit to data. We vary the parameters of the foregrounds, while keeeping the cosmology fixed to the best fit parameters obtained by G15: $H_0 = 68.15$, $\Omega_m = 0.30$ and $n_s = 0.9611$. This choice is made in order to allow a direct comparison with the results of G15. We sampled the parameters distributions using the Monte Carlo engine, available in the package Cobaya [189]. The convergence is assessed through a generalized version of the Gelman-Rubin statistic denoted as R-1, see [190].

Before starting to comment the results, we underly that our modelling is the same of G15 for the radio source emission, the CIB poisson term and the kSZ, while we used the halo model for the CIB clustering, the tSZ and the correlation between the two [4]. For the tSZ effect we fit for the hydrostatic mass bias. For what concern the CIB, we fixed the clustering parameters of the late-type population, as done in C13, to the values of $Log_{10}(M^{LP}_{min}) = 10.8 M_{\odot} h^{-1}$, $\alpha_{LP} = 1$, $scale_{LP} \equiv M^{LP}_{sat}/M^{LP}_{min} = 20$, $\sigma_{LP} = 0.1$. We also fixed two of the early-type population HOD parameters: $scale_{EP} \equiv M^{EP}_{sat}/M^{EP}_{min} = 20$, $\sigma_{EP} = 0.1$, in order to reduce the degeneracies in the determination of the one halo term. We instead vary the minimum mass M_{min} and α for the early-type population. We also fit for the amplitude and spectral index of the CIB poisson noise, A_P and β_P, the amplitude of the radio galaxy emission, A_r, and of the kSZ, A_{kSZ}. We fixed the radio sources spectral index to the best fit value of G15, $\alpha_r = -0.945$, and impose on the amplitude a gaussian prior of $1.28 \pm 0.19\ \mu K^2$, based on [191] source counts model. In figure 4.15 we see the posterior distributions of the parameters, while in table 4.4 we report the mean and standard deviation of these distributions.

For the poisson term of the CIB, G15 found $D^{p}_{3000} = 9.16 \pm 0.36\ \mu K^2$ and $\beta_p = 1.505 \pm 0.077$, which are values well in agreement with our result. The quoted amplitude of the radio sources was $1.06 \pm 0.17\ \mu K^2$, again in agreement with our results. If we compute the amplitude of the clustering of the CIB at $\ell = 3000$ and $\nu = 150$ GHz, we get $D^{c}_{3000} \sim 3.65\ \mu K^2$, which is within the error

---

[4] In G15 the parameters of the model are: the amplitude of the CIB clustering term, D^{CIBc}_{3000}, the effective dust emissivity index (for the clustering term), β_c, the amplitude of the CIB poisson term, D^{CIBp}_{3000}, the effective dust emissivity index (for the poisson term), β_p, the effective dust temperature, T_d, the amplitude of the tSZ, D^{tSZ}_{3000}, the amplitude of the kSZ, D^{kSZ}_{3000}, the amplitude of the radio sources, D^{r}_{3000}, the radio sources spectral index, α^{r}_{3000}, the amplitude of the galactic cirrus, D^{cirr}_{3000}, the amplitude of the tSZ-CIBc correlation, ξ^{G}.

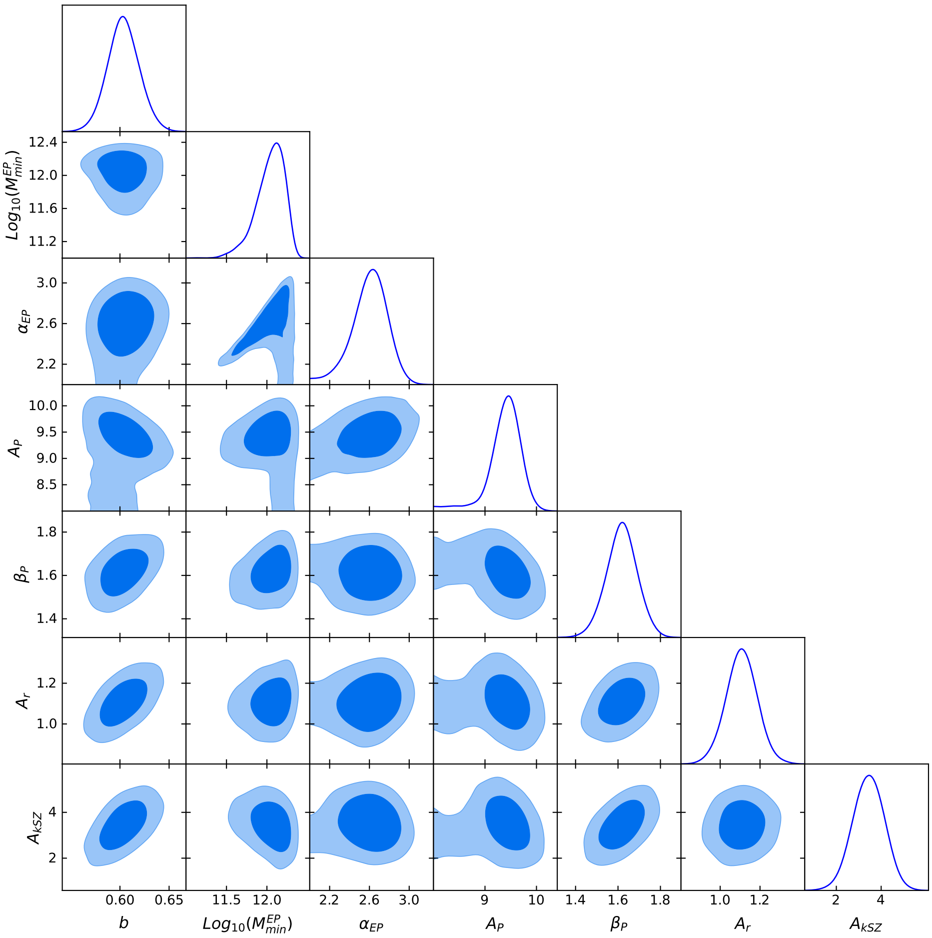

Figure 4.15: *Distributions of the parameter posteriors. We put a gaussian prior only on the amplitude of the radio sources power spectrum, while all other parameters are just varyed within a flat prior.*

of the G15 value, who gave $D^c_{3000} \sim 3.46 \pm 0.54\ \mu K^2$. The tSZ amplitude at $\ell = 3000$ can be computed from the halo model, introducing hydrostatic mass bias found in our fit. We obtain $D^{tSZ}_{3000} \sim 2.55\ \mu K^2$, while G15 quoted a higher value: $D^{tSZ}_{3000} = 4.38^{+0.83}_{-1.04}\ \mu K^2$. This first fit shows some issue that it is useful to comment in order to understand the degeneracies between the parameters of the model and to explore the physics behind them. The first is that the value of the kSZ is higher than predicted by previous analysis and, more important, the null hypothesis is excluded at more than five sigma. This is really unlikely, as all previous analysis on these maps found an upper limit on the kinetic term [95,192]. The high value of the kSZ causes a suppression of the power in the tSZ, which then shows the aforementioned discrepancy with respect to G15. Moreover, the

parameter	priors	result
b	[0.05, 0.95]	0.60±0.016
$Log_{10}(M^{EP}_{min}/M_{\odot}h^{-1})$	[11, 12.8]	12.01±0.2
α_{EP}	[0.2, 3.5]	2.4±0.47
$A_P\ [\mu K^2]$	[0.2, 16]	9.14±0.88
β_P	[0, 6]	1.62±0.07
$A_r\ [\mu K^2]$	1.28±0.19	1.11±0.08
$A_{kSZ}\ [\mu K^2]$	[0, 13]	3.44±0.7

Table 4.4: *Mean and standard deviation of the parameters distributions. In this case $R-1=0.01$. We also apply to the chains a burn in equal to 0.4. The value of α_{EP} for the early type population is higher then predicted by semi-analytical model. Moreover, differently from the results of previous studies on the same dataset, the amplitude of the kSZ excludes the null value at more than five sigma.*

value of α_{EP} found is well above the prediction of semi-analytic models, $\alpha \leq 1$ (see [193, 194]).

The unrealistic value of the kSZ effect can be adressed starting from the considerations of A12 and [192]: the uncertainty in the modelling of the tSZ-CIB can significantly mislead the constraints on the kSZ. We use the Equation 28 of A12 to compute the so-called correlation parameter:

$$\xi_\ell = \frac{C^{tSZ\times CIBc}_{\ell,\nu_1,\nu_2}}{\sqrt{C^{tSZ}_{\ell,\nu_1,\nu_1}C^{CIBc}_{\ell,\nu_2,\nu_2}} + \sqrt{C^{tSZ}_{\ell,\nu_2,\nu_2}C^{CIBc}_{\ell,\nu_1,\nu_1}}}. \tag{4.122}$$

Here $C^{tSZ}_{\ell,\nu_2,\nu_2}$ is the absolute value of the tSZ power spectrum, $\ell = 3000$ and $\nu_1 = \nu_2 = 150$ GHz. In G15 the amplitude of the tSZ-CIBc correlation is computed inverting equation 4.122. In the baseline model of G15 the correlation parameter is varyed within uniform prior and it is unique at all angular scales: we will denote it as ξ^G in the following. Using the values of table 4.4, we obtain $\xi_{3000} = -0.46$. This value is almost twice the degree of correlation expected for that frequency and multipole, which is $\xi_\ell \sim 0.2$. In order to verify if the wrong value of the kSZ is a consequence of a degeneration with the tSZ-CIB correlation, we first performed a diagnostic test, fitting for an additional parameter γ directly mutiplied to the correlation power spectrum. If the prediction of A12 are correct, we should see a deviation from one of the correlation parameter. The result is shown in figure 4.16.

We obtained a mean value of the correlation parameter around $\gamma = 0.36$. With

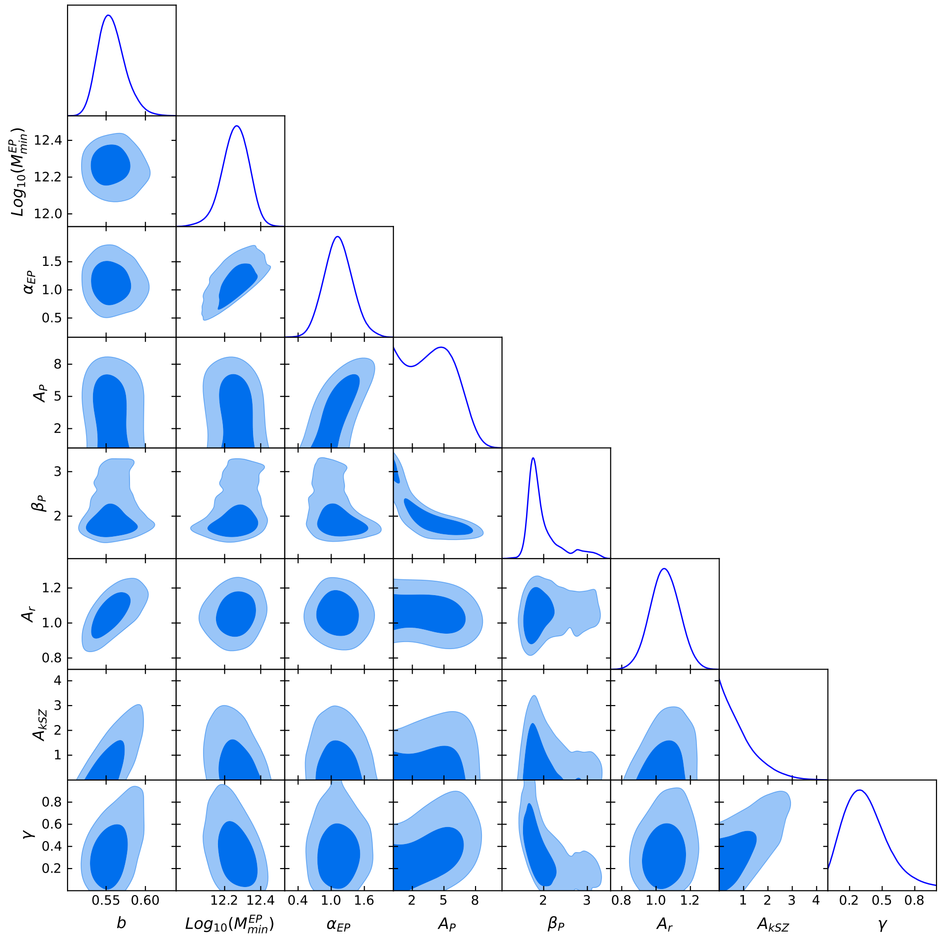

Figure 4.16: *Distributions of the parameter posteriors. To test the impact of the tSZ-CIB correlation on the kSZ constraints we fit also for the γ parameter.*

this configuration the tSZ effect slightly increase: $b = 0.56 \pm 0.18$, which means an amplitude of $D_{3000}^{tSZ} \sim 3.6\ \mu K^2$, now compatible with the G15 result. We also correct the kinetic term: $D_{3000}^{kSZ} < 2.3\ \mu K^2$ at 95% C.L., compatile with G15 baseline model results, $D_{3000}^{kSZ} < 5.4\ \mu K^2$, for the same confidence level. In our modelling, the halo approach employed to describe the tSZ and the CIB should prevent from the use of the γ parameter: the value of the correlation is determined by the mass bias, b, and, most of all, by the clustering parameters of the CIB. We have already mentioned that the tSZ-CIB correlation power is higher at low redshift, where the massive SZ clusters are located. This observable is then dominated by the late-type population of star forming galaxies. We then decided to fit also for $Log_{10}(M_{min}^{LP})$ and α_{LP}, while keeping $scale_{LP} = 20$ and

$\sigma_{LP} = 0.1$. In figure 4.17 we see the posterior distributions of the parameters, while their mean and standard deviation are reported in table 4.5.

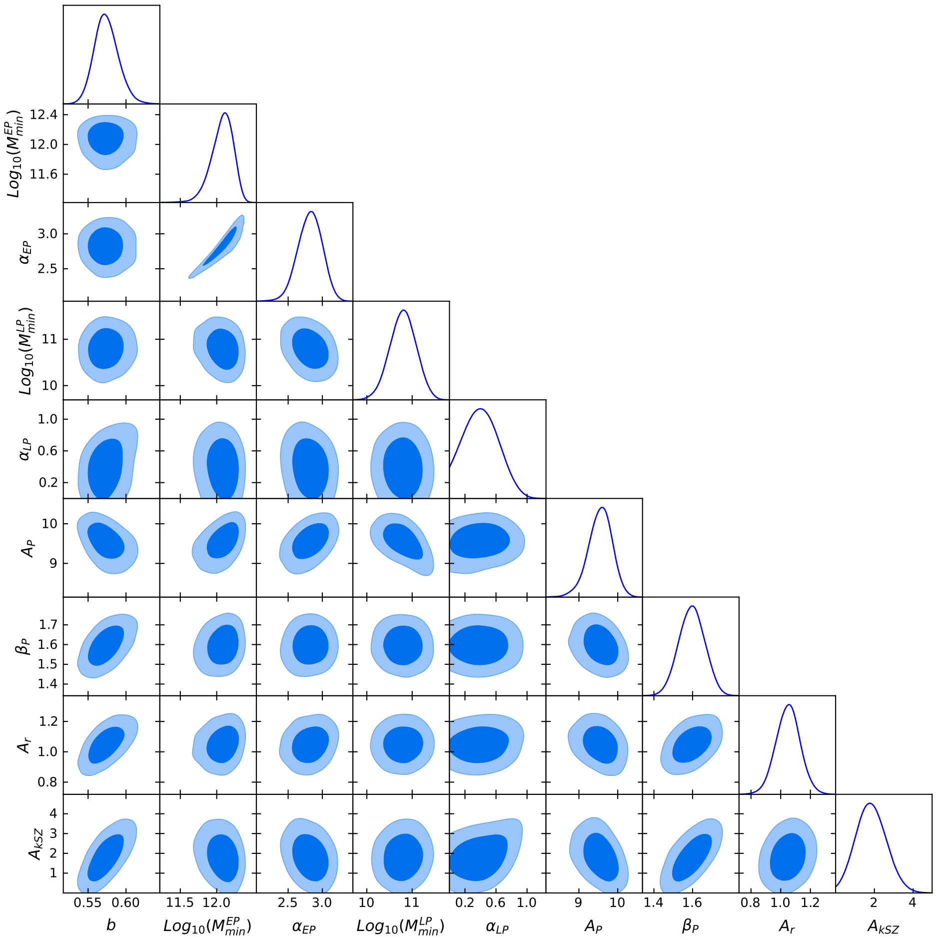

Figure 4.17: *Distributions of the parameter posteriors. We put a gaussian prior only on the amplitude of the radio sources power spectrum, while all other parameters are just varyed within a flat range. We included in the fit also the minimum mass and α of the late-type population.*

In this case, the value of the mass bias is $b = 0.57 \pm 0.016$ and the resulting amplitude of the tSZ is compatible with what found by G15. We detected the kSZ at 95% C.L. and found $D_{3000}^{kSZ} = 1.9^{+2.6}_{-1.0}\ \mu K^2$. This result is within the upper limit found by G15 and in line with what obtained by Reichartd et al. 2020. In [195] the authors performed a measurement of the secondary CMB anisotropies combining the G15 maps and the low-noise 500 deg^2 SPTpol survey and found $D_{3000}^{kSZ} = 3.0 \pm 1.0\ \mu K^2$ at 3σ. In our work, the combination of an improved modelling of the CIB late type population and the implementation of an halo

parameter	priors	result
b	[0.05, 0.95]	0.57±0.016
$Log_{10}(M_{min}^{EP}/M_\odot h^{-1})$	[11, 12.8]	12.07±0.15
α_{EP}	[0.2, 3.5]	2.8±0.2
$Log_{10}(M_{min}^{LP}/M_\odot h^{-1})$	10.8±0.3	10.8±0.3
α_{LP}	0.5±0.3	$<$ 0.88 (95%C.L.)
A_P $[\mu K^2]$	[0.2, 16]	9.53±0.3
β_P	[0, 6]	1.59±0.07
A_r $[\mu K^2]$	1.28±0.19	1.0±0.08
A_{kSZ} $[\mu K^2]$	[0, 13]	$1.9^{+2.6}_{-1.0}$

Table 4.5: *Mean and standard deviation of the parameters distributions. For the kSZ amplitude we report the 68% C.L.. Again we apply to the chains a burn in equal to 0.4 and $R-1=0.007$. We fit also for the clustering parameter of the late-type population: for the minimum mass we obtain a value similar to what predicted by C13, while we found just an upper limit on the index of the power law regulating the satellite galaxy accretion. Varying the clustering parameters of the late-type population, we found a upper limit for the kSZ effect, coherently with G15.*

model for the tSZ-CIB correlation allow to boost the constraints on the kSZ already on G15 bandpowers. To conclude, the value of the correlation is now lower, approaching the prediction of previous literature: $\xi_{3000}^{150\times150}=-0.29$. The halo model successfully reproduces current limit on the kSZ effect without the use of a correlation parameter, replaced by a physically motivated description of the late-type population of low redshift star forming galaxies. We have also shown that data prefer a suppression of the one halo term for the late-type population and are oriented to lower values of α, with respect to those used in literature.

In figure 4.18 we show the comparison between data and the model obtained with the parameters quoted in table 4.5. We also plot the contribution given by every foreground. In particular the curves represent: the radio galaxy emission (green solid line), the tSZ and kSZ effect (solid and dashed blue line respectively), the CIB poisson and clustering emission (solid and dashed orange lines respectively) and the correlation between the tSZ effect and the CIB clustering (pink dashed line). To conclude, the CMB is represented by the red line and the galactic cirrus are in yellow. For sake of clarity we do not show the decomposition of the CIB clustering into the two populations or dividing the one and two halo terms and just show the total contribution of this foreground. The chi-square of this model is 99.9 for 77 degrees of freedom. It corresponds to a reduced $\chi^2=1.3$ and $p-value=0.04$: the model is in agreement with data around 2σ.

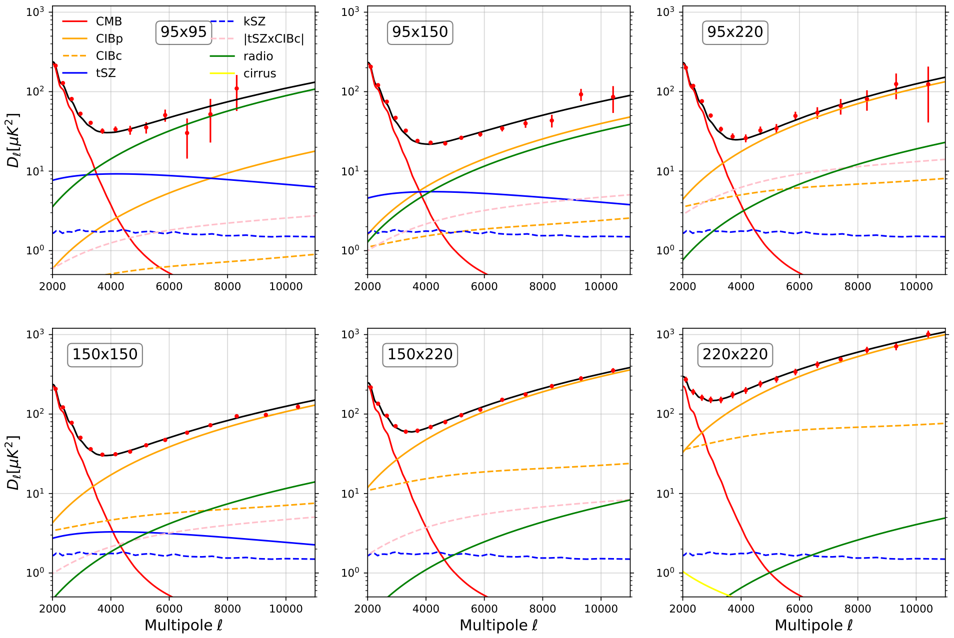

Figure 4.18: *Comparison between data and the model obtained with the parameters in table 4.5. The curves represent: the radio galaxy emission (green solid line), the tSZ and kSZ effect (solid and dashed blue line respectively), the CIB poisson and clustering emission (solid and dashed orange lines respectively) and the correlation between the tSZ effect and the CIB clustering (pink dashed line). The model has a reduced* $\chi^2 = 1.3$ *and* $p - value = 0.04$*: it is in agreement with data at* $\approx 2\sigma$.

To conclude the investigation of the degenerations that affect the kSZ effect, we decided to place a gaussian prior on the hydrostatic mass bias, which determines the amplitude of the tSZ. The value that b should assume is still debated: numerical simulations give $b \sim 0.2$. On the other hand, the value used to alleviate the inconsistency with the constraints derived from the analysis based on primary CMB anisotropies is $b \sim 0.4$ [196]. We have chosen to center the prior on this second value, imposing $b = 0.4 \pm 0.05$, as it is given by analysis similar to what we are doing here. We show the distribution of the parameters posterior in 4.19.The mean and standard deviation of the parameters distributions are listed in table 4.6.

The value of the hydrostatic mass bias obtained from the fit is in tension with the prior, around three sigma. Nevertheless it returns an amplitude of the tSZ power spectrum in line with G15, $D_{3000}^{tSZ} \sim 3.6\ \mu K^2$. We again detected the kSZ

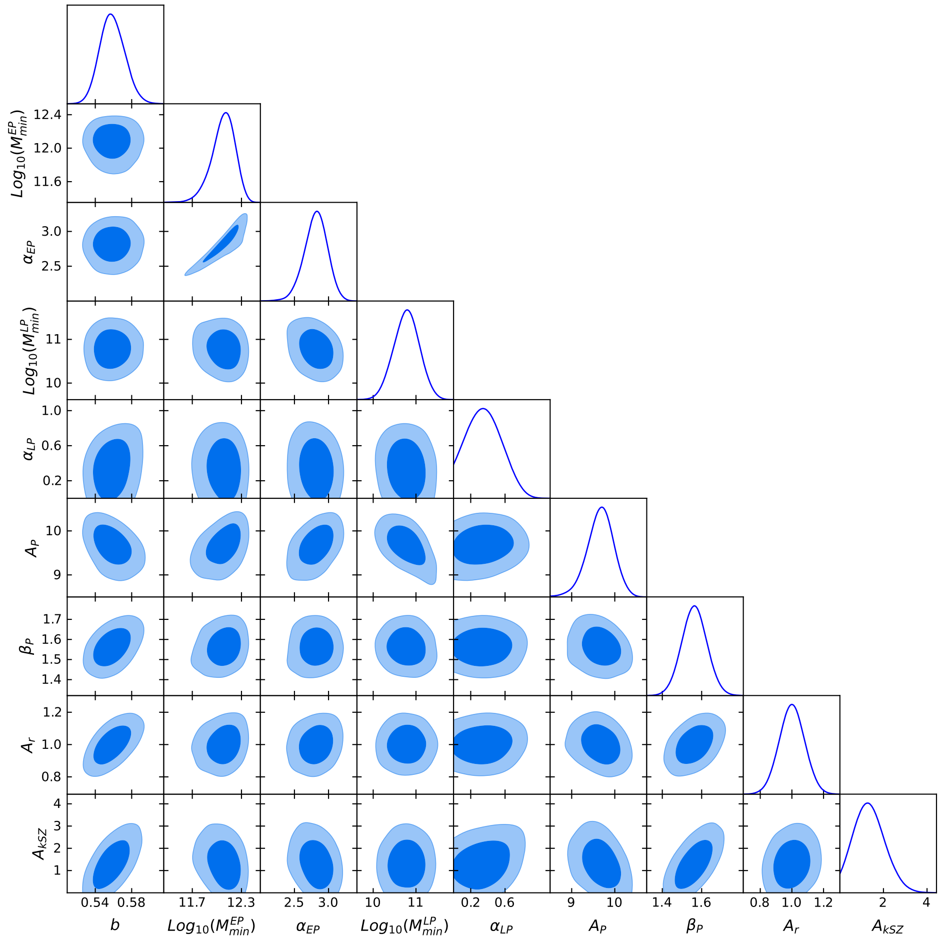

Figure 4.19: *Distributions of the parameter posteriors. We imposed a prior on the b parameter, i.e. on the amplitude of the tSZ power spectrum, in order to break the degeneracy with the kSZ.*

effect at 95% C.L. and found $D_{3000}^{kSZ} = 1.4^{+2.0}_{-0.5}$.
The chi-square of this model is 99.6 for 76 degrees of freedom. It corresponds to a reduced $\chi^2 = 1.3$ and $p - value = 0.036$: the model is in agreement with data between 2 and 3σ.

We have anticipated that the value of α_{EP} is in strong disagreement with the value given by semi-analytical models, ≈ 1. It is also far from the results of previous studies: C13 obtained $\alpha = 1.55 \pm 0.05$, while Xia et al. [197] $\alpha = 1.81 \pm 0.04$. We underly that these values are obtained on high frequencies datasets (250, 350, 500 μm) and thus they are not fully comparable with the present case, but still they strengthen the evidence of a tension between the value

parameter	priors	result
b	0.40±0.05	0.56±0.014
$Log_{10}(M_{min}^{EP}/M_{\odot}h^{-1})$	[11, 12.8]	12.07±0.14
α_{EP}	[0.2, 3.5]	2.8±0.2
$Log_{10}(M_{min}^{LP}/M_{\odot}h^{-1})$	10.8±0.3	10.8±0.3
α_{LP}	0.5±0.3	< 0.79 (95%C.L.)
A_P $[\mu K^2]$	[0.2, 16]	9.62±0.35
β_P	[0, 6]	1.56±0.06
A_r $[\mu K^2]$	1.28±0.19	1.0±0.08
A_{kSZ} $[\mu K^2]$	[0, 13]	$1.4^{+2.0}_{-0.5}$

Table 4.6: *Mean and standard deviation of the parameters distributions. For the kSZ amplitude we report the 68% C.L.. Again we apply to the chains a burn in equal to 0.4 and $R - 1 = 0.007$. The value of b is high with respect to the prior, suggesting that data strongly requires a lower value of the tSZ, with respect to what found in [196]. The resulting amplitude of the tSZ power spectrum is in line with the results of G15. Imposing a prior on b, we tightened a bit the upper limit on the kinetic SZ amplitude, with respect ot the case reported in 4.5.*

we found and what expected.
A possible explanation can be found in the choice we made when implementing the dependence of the clustering on luminosity [7,198]. Indeed, we can think that more luminous galaxies should contribute more to the total power spectrum with respect to faint galaxies. This assumption affects the number of satellites needed to reproduce the radiation coming from halos, which is regulated by α. In our model, we included the dependence of clustering on luminosity through the split of the late and early-type populations, assuming different clustering properties for the massive proto-spheroids and the smaller local galaxies. To understand if we can correct for the high values of α_{EP} without a deep modification of the model, we imposed a gaussian prior on the index of the satellite accretion power law, based on the results of C13 at higher frequencies, $\alpha = 1.55 \pm 0.3$. We show the result in figure 4.20.

The effect of decresing α has an impact on the Poisson level, which decreases to $D^p_{3000} \sim 7.4 \pm 1.5$ μK^2 and enlarges its error bars. This is expected as the poisson noise and the one halo term of the CIB clustering are degenerate at small scales. As we mentioned while presenting the modelling, at these frequencies the numbers of counts can not give strong constraint on the value of the Poisson noise, so, in principle, the value we obtain from the distribution in figure 4.20 can not be excluded. Nevertheless, the problem arises when considering the

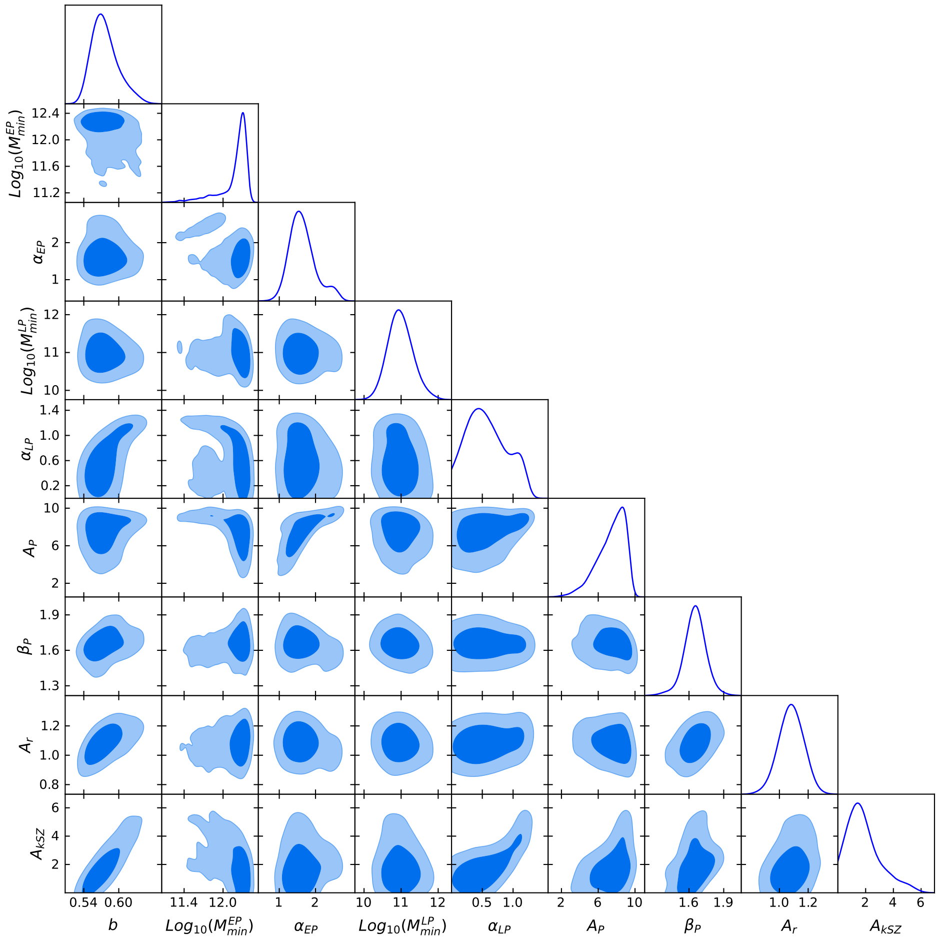

Figure 4.20: *Distributions of the parameter posteriors. We imposed a gaussian prior on* α^{EP} *parameter, centered on the value found by C13 at SPIRE frequencies. This prior has an impact on the values of the CIB poisson noise, highliting the degeneracy between the shot noise and the one halo contribution of the clustering term, especially at small scales.*

comparison to data: figure 4.21 represents the model obtained for the parameters corresponding to the mean of the distributions shown in figure 4.20, compared to data. The legend of the plot is the same of figure 4.18.

From this plot it is visually clear that the model underestimates the data for the 150 × 220 and 220 × 220 autospectra. This is validated from the increase of the chi-square, up to 162, which exclude the model at several sigma. The result suggests that, in this framework, and related to this specific dataset, there is no short way to lower the value of α_{EP} without spoiling the accordance between model and data. The conclusion we draw is that a more sophisticated implementation of the dependence of clustering on luminosity is required for this

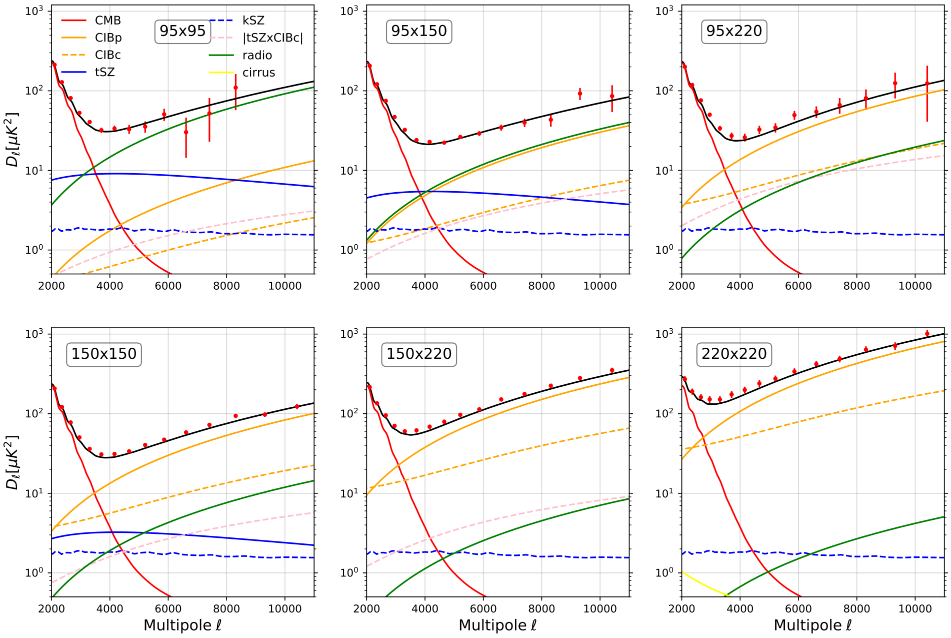

Figure 4.21: *Comparison between data and the model obtained from the mean of the posterior distribution of the parameters shown in 4.20. The plot legend is the same of figure 4.18. The model underestimates data for the* 150×220 *and* 220×220 *autospectra. The model shows a* $p - value < 0.001$ *and is consequently rejected.*

dataset.

4.3.2 SPT-SZ and Hershel/SPIRE: dataset and results

As anticipated, the second dataset we used has been released by Viero et al in 2019 [199](V19). It combines millimeter data observed with the SPT at 95, 150, 220 GHz and submillimeter data imaged with the SPIRE instrument on the Herschel Space Observatory [200]. SPIRE works at higher frequencies with respect to the SPT, and in particular at 600, 857, 1200 GHz. The spectra are obtained from observations covering roughly 100 deg^2 of the sky: 102 deg^2 are used for SPT-only bandpowers, 90 deg^2 for the SPIRE-only bandpowers, while 86 deg^2 are dedicated to the cross-frequencies bandpowers, denoted from now as SPT×SPIRE. In all cases the power spectra are extracted using a pseudo$-C_\ell$ method, as we will see a bit more in detail in the next subsection.

4.3.2.1 Dataset

The field used to derive SPT bandpowers is approximately $10° \times 10°$ centered at 23^h30^m, -55^d00^m and was observed in 2008 and 2010. The data and the power spectrum analysis are identical to the G15 case, described before. The only difference lies in the absolute calibration, which is determined by comparing the SPT maps to Planck maps over the same footprint. The uncertainty in the SPT calibration at 95, 150, 220 GHz are 0.43%, 0.34%, 0.84%. The beam and calibrations uncertainties are included as a correlation matrix in the data release. SPIRE maps are obtained at the nominal frequencies of 600, 857, 1200 GHz [201]. They are derived from observations designed to target the large scales. The full observation consists of twelve 10×13 degrees scans, half in a direction and half in the perpendicular one. The full 100 deg^2 map is built from a mosaic of these 12 scans. Data are reduced with standard ESA software and the costum software package, SMAP [7, 202]. Maps are made using and iterative map-maker, which is designed to separate large scale noise from signal and includes an updated calibration procedure with respect to previous studies [201, 203]. The absolute calibration uncertainty is 5% and, similarly for the SPT case, is accounted for in the beam and calibration correlation matrix. Two sets of maps with different pixel size are obtained: the one at high resolution, with pixels $15''$, is used for the SPIRE-only analysis. The set of coarser maps, with pixels $30''$, is used for the SPT×SPIRE map-making, in order to match the lower resolution provided by the SPT.

The SPIRE maps noise leves are 5.6, 4.0, 2.8 mJy arcmin, and the instrument effective beams are $36.6''$, $25.2''$, $18.1''$ FWHM at 600, 857, 1200 GHz. Maps are converted from Jybeam^{-1} to Jysr^{-1}, by dividing by the effective beam areas. SPIRE beams are measured with Neptune, which is a point source to SPIRE. As the effective beam is sensitive to the source spectrum through the band pass, the effective solid angle have to be color corrected [204, 205]. Following the SPIRE Observers Manual [5], the authors of V19 found that the effective solid angles are 3.878, 1.873, and 1.080×10^8 sr at 600, 857, 1200 GHz. At SPIRE frequencies the signal is dominated by the CIB emission: differently from the SPT case, in which we needed to know the effective frequencies for every component, in this case we just need the effective frequencies for a dust like source. The effective band centers for the SPIRE are then 546.0, 796.0 and 1092.4 GHz.

In order to compute the bandpowers, a cross-spectrum-based pseudo-C_ℓ method has been used both for the SPT-only, SPIRE-only and SPT×SPIRE cases. In

---

[5] `http://herschel.esac.esa.int/Docs/SPIRE/html/spireom.html`

the SPT-only case the bandpowers have been obtained following the procedure of G15, that we have briefly described in the previous section. The SPIRE-only bandpowers are obtained as in [7]: the power spectrum is estimated from the cross-correlation of jack-knife map-pairs, exploiting the fact that noise is mostly uncorrelated between frequencies. Actually the uncorrelated white noise dominates at $k_\theta \gtrsim 0.2$ arcmin^{-1}, while at larger angular scales maps are affected by the correlated $1/f$ noise. To minimize this contamination, the map-pairs are constructed by dividing the timestreams in half by time. This ensures that maps are derived from observations taken at time intervals corresponding to very large scales.
The one dimensional power spectrum results then from the azimuthal average of the two dimensional power spectrum of the map-pairs in $k-$space. The procedure for SPT×SPIRE is similar to the SPIRE-only case. The only minor difference is that full coadded maps for each experiment are used in this case, as the noise in SPT and SPIRE maps are uncorrelated.
The spectra obtained from the maps have to be corrected for the transfer function, masking and instrumental beam. A unique mask has been construct for each cross-frequency spectrum, which has values of unity only in the region in which the two maps overlap and zero outside. The mask is used to cover sources with flux densities greater than 300 mJy at 1200 GHz and local extended sources for the SPIRE maps and sources with flux densities greater than 6.4 mJy at 150 GHz for SPT maps. The filtering procedure is applyed during map making to correct for the $1/f$ noise. It has an higher impact on the SPT power spectrum which suffers more from large scales atmospheric noise. To correct for the effect of filtering and for the beam, transfer functions are computed on simulated maps, made with the same map-making pipelines applyed on mock data. The covariance matrix is estimated as in G15 in the case of SPT-only band powers. The covariance estimator changes when also SPIRE data are included. Firstly, many realizations of the sky signal and noise terms are generated through a Monte Carlo simulation. These realizations are analysed with the same pipeline of real data and the ensemble of the estimated binned power spectra obtained is used to measure the covarianche matrix, see equation 1 of V19. The sky realizations include both Gaussian fields (CMB, tSZ, kSZ, radio galaxies) and non-Gaussian field (CIB) [153]. The presence of non-Gaussian field led to the appearance of substantial off-diagonal terms in the covariance matrix. The covariance matrix obtained from these simulations contains the signal and noise uncertainties. To obtain the total uncertainty we have to combine the beam and calibration correlation matrix to the model bandpowers and then add it to the

covariance matrix. We mention here that we have opted for a simplified analysis, using a block diagonal version of the covariance matrix. This choice is due to the substantial off-diagonal terms present in the SPIRE part of the covariance matrix, which tend to bias the computation of the best fit model. In this sense, we partially followed the path of [151] in their analysis on the SPIRE dataset. The authors assumed gaussian uncorrelated error bars for measurement uncertainties, i.e. a diagonal covariance matrix. In the following we present the model fit to data. In this thesis we describe the results for the SPT and SPIRE block of the dataset separately, while leaving the global fit for a future work. We varied the parameters of the foregrounds, while keeeping the cosmology fixed to the Planck 2018 best fit parameters: $H_0 = 67.7$, $\Omega_m = 0.31$ and $n_s = 0.9667$. We sampled the parameters distributions using the Polychord engine, available in the Cobaya package. Polychord is a nested sampler, tailored for high dimensional parameter space. In order to sample the parameter space, Polychord draws from the prior range a certain number of *live points*. At each iteration the point with the lowest likelihood is replaced by a new live point, uniformly drawn from the prior, with the constraint that its likelihood is larger than that of the discarded point. The convergence is reached when the evidence of the live points is a fraction, 10^{-2}, of the total evidence.

4.3.2.2 SPT-only: results

We have isolated the bandpowers corresponding to the SPT frequencies in the V19 dataset and the associated portion of the covariance matrix. We directly include the clustering parameters of the late-type population in the fit, relying on the conclusions drawn in the case of the G15 dataset. At first we impose only one prior, on the amplitude of the radio sources. However, we obtained high values of the kSZ effect, which caused a strong decrease of the amplitude of the tSZ, with values of the hydrodynamical mass bias larger than 0.7. To investigate this issue we compared the bandpowers for the auto and cross spectra of the G15 and V19 datasets and found that the latter presents an eccess of power in the 95×220 GHz. In figure 4.22 we show the comparison between the two datasests for that cross frequency. The blue triangles, representing the G15 bandpowers, have lower values with respect to the orange squares, corresponding instead to the V19 data, especially at $\ell > 3000$.

The two datasets are obtained with the same procedure on the same maps, so we attributed the difference in the bandpowers to the variation of the sky fraction. The cross spectrum of the 95×220 GHz is dominated by the CIB

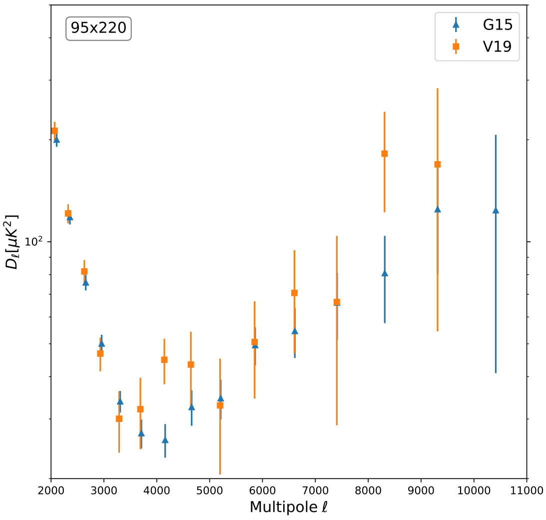

Figure 4.22: *Comparison between G15 and V19 datasets for the* 95×220 *GHz cross-frequency. G15 bandpowers (blue triangles) have lower values with respect to V19 data (orange squares).*

emission (in particular from the poisson term) and by the radio sources. The parameters determining the amplitude of both these components are mainly constrained from the fit to the 220×220 GHz auto-spectrum, for the CIB, and to the 95×95 GHz frequency channel, for the radio sources. The only remaining degree of freedom to vary, in order to fit the high power in data, is the amplitude of the kSZ, which is then pushed to unrealistically high values. Because of the degeneration between the amplitude of the kSZ and the mass bias, the increase of A_{kSZ} causes the reduction of the amplitude of the tSZ, with the large values of the bias mentioned before. To cure this issue, we imposed a gaussian prior on the value of the mass bias, centered in the value ontained by the Planck analysis, as we did in the last test performed on the G15 dataset. The posterior distribution for the parameters of the model are shown in figure 4.23. The mean and standard deviation of the distributions are reported in table 4.7.

The values of the minimum mass for both the galaxy populations and the upper limit derived for the α^{LP} are compatible with those obtained in the analysis of G15 dataset. Interestingly, the value of the α^{EP} is now compatible with the value found by Cai13, probably as a consequence of the degradation of the constraint on the Poisson noise. The value of the mass bias is $\sim 2 - 3\sigma$ away from the center of the prior, confirming that this dataset strongly requires a lower

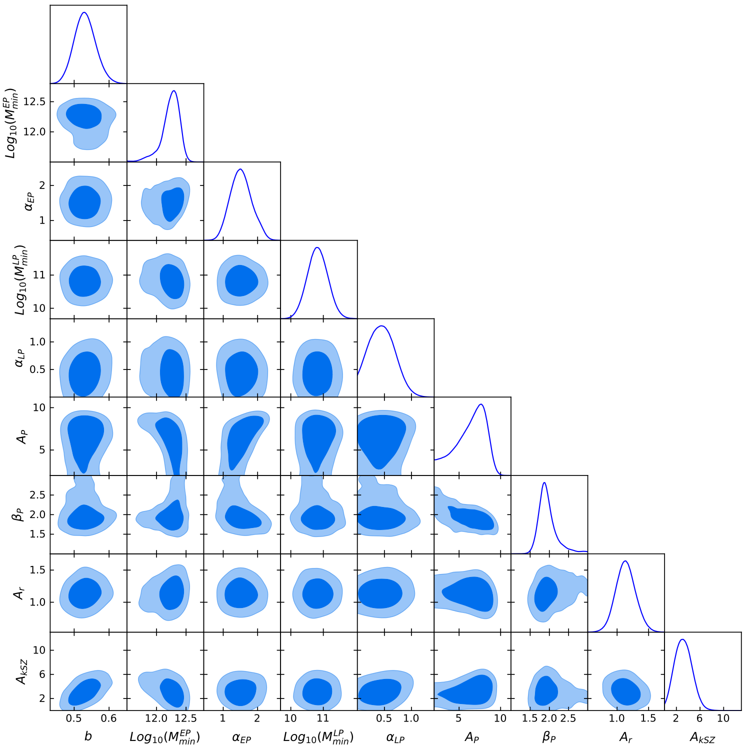

Figure 4.23: *Distributions of the parameter posteriors. We imposed a gaussian prior on the b parameter,* $b = 0.4 \pm 0.05$, *in order to cure the effect of suppression of the tSZ caused by the eccess of power in data at* 95×220 *GHz.*

value of the tSZ with respect to that inferred by Planck analysis. The constraint on the amplitude of the kSZ degradates with respect to G15 and we attribute this worsening to the difference in the cross-spectra bandpowers, explained before. The value found, $D^{kSZ}_{3000} = 3.2^{+4.5}_{-1.6}$, is, however, compatible with [195] results. In figure 4.24 we show the comparison between data and the model obtained with the parameters quoted in table 4.7. We also plot the contribution given by the single foreground.

The chi-square of this model is 92.6 for 78 degrees of freedom. It corresponds to a reduced $\chi^2 = 1.18$ and $p - value = 0.12$: the model is in agreement with data between 1 and 2σ.

4.3.2.3 SPIRE-only: results

At SPIRE frequencies the only foregrounds that contribute to the signal are the CIB (both clustering and poissonian terms) and the galactic cirrus. This

parameter	priors	result
b	0.40±0.05	0.53±0.03
$Log_{10}(M^{EP}_{min}/M_{\odot}h^{-1})$	[11, 12.8]	12.19±0.5
α_{EP}	[0.2, 3.5]	1.5±0.3
$Log_{10}(M^{LP}_{min}/M_{\odot}h^{-1})$	10.8±0.3	10.8±0.3
α_{LP}	0.5±0.3	$<$ 0.93 (95%C.L.)
A_P $[\mu K^2]$	[0.2, 16]	$<$ 9.1 (95%C.L.)
β_P	[0, 6]	2.0±0.3
A_r $[\mu K^2]$	1.28±0.19	1.1±0.2
A_{kSZ} $[\mu K^2]$	[0, 13]	$3.2^{+4.5}_{-1.6}$

Table 4.7: *Mean and standard deviation of the parameters distributions. For the kSZ amplitude we report the 68% C.L.. The run has converged i.e. the posterior mass contained in the live points is equal to the 1% of the total evidence. Again we apply to the chains a burn in equal to 0.4. The value of b is high with respect to the prior, suggesting that data strongly requires a lower value of the tSZ, with respect to what found in [196]. With respect to G15 dataset, the constraints on both A_P and A_{kSZ} degradate, while the value of α_{EP} is now compatible with previous literature.*

dataset is already cleaned from the presence of the cirrus so we can fit only for the CIB. We vary both the early and late type population minimum mass and α parameters. Similarly to what we have done for the low frequencies, the satellite mass is derived multiplying the minimum mass by a factor 20, as in Xia et al. [197] (hereafter X12). We also fit the value of the shot noise for the auto-spectra of the three frequencies, denoted in the following triangle plots as $PN_{\nu\times\nu'}$. In the first run we decided to vary all parameters without gaussian priors. The result is in figure 4.25, while the mean and standard deviation of the parameters distributions are reported in table 4.8.

For the minimum mass of the halos hosting the early type population, C13 finds $Log_{10}(M^{EP}_{min}/M_{\odot}) = 12.15 \pm 0.04$, which in our units translate into $Log_{10}(M^{EP}_{min}/M_{\odot}h^{-1}) \sim 12.0$, while X12 gives as result $Log_{10}(M^{EP}_{min}/M_{\odot}) = 12.24 \pm 0.06$ i.e. $Log_{10}(M^{EP}_{min}/M_{\odot}h^{-1})1 \sim 12.1$. Our value seems to be higher, but it is still within the range of value present in literature. Manyar et al. [151] indeed attribute to the typical dark matter halo, hosting DSFGs at $z = 2$, a mass of $Log_{10}(M^{EP}_{min}/M_{\odot}) = 12.77^{+0.128}_{-0.125}$, while Planck collaboration [206], with a slight different model, gives value between $10^{11.5}$ to $10^{12.5}$ $M_{\odot}h^{-1}$. The value of α_{EP} given by C13 and X12 are respectively $\alpha_{EP} = 1.55 \pm 0.05$ and $\alpha_{EP} = 1.81 \pm 0.04$. In this case we found a lower value, which is, however, in line with the prediction of the semi-analytical models [7]. For what concern the clustering parameters

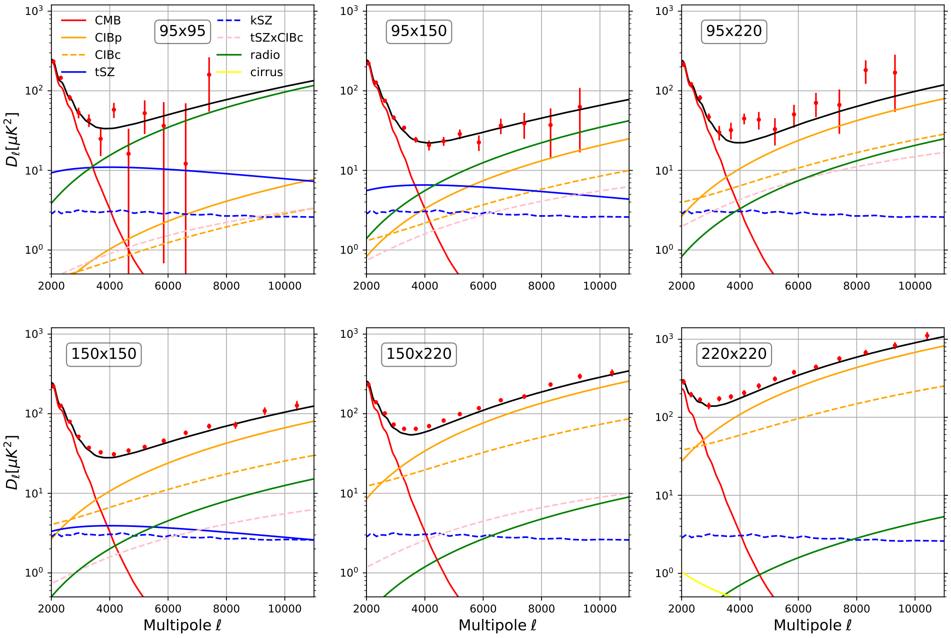

Figure 4.24: *Comparison between data and the model obtained with the parameters in table 4.7. The plot legend is the same of figure 4.18. The errorbars are the diagonal elements of the matrix given by the sum of the covariance matrix plus the correlation matrix multiplied by the theory bandpowers. The covariance matrix contains the uncertainties related to signal and noise, while the correlation matrix accounts for beam and calibration errors.*

of the low redshift population, in literature they are usually fixed at a mass of $Log_{10}(M^{LP}_{min}/M_\odot) = 11$ and $\alpha_{LP} = 1$. In our fit we constrained the clustering parameters of the late type population for the first time. The value of the minimum mass we found is ten times lower than that of the early-type population. This validates the prediction that the early-type galaxies are hosted in more massive structures than the late-type ones.

The values of the shot noise, reported in table 4.8, differ from the values computed by fitting the number of counts and listed in table 4.2. In all cases the value obtained by the fit of the counts is higher that that given by the fit of the power spectra, but with some differences among the frequencies. In particular, we observe that, for the 1220 GHz frequency, the values obtained through the two procedures are compatible at 1σ. For the two lower frequencies, instead, the values differs more than 2σ. The explanation of this behaviour can be traced

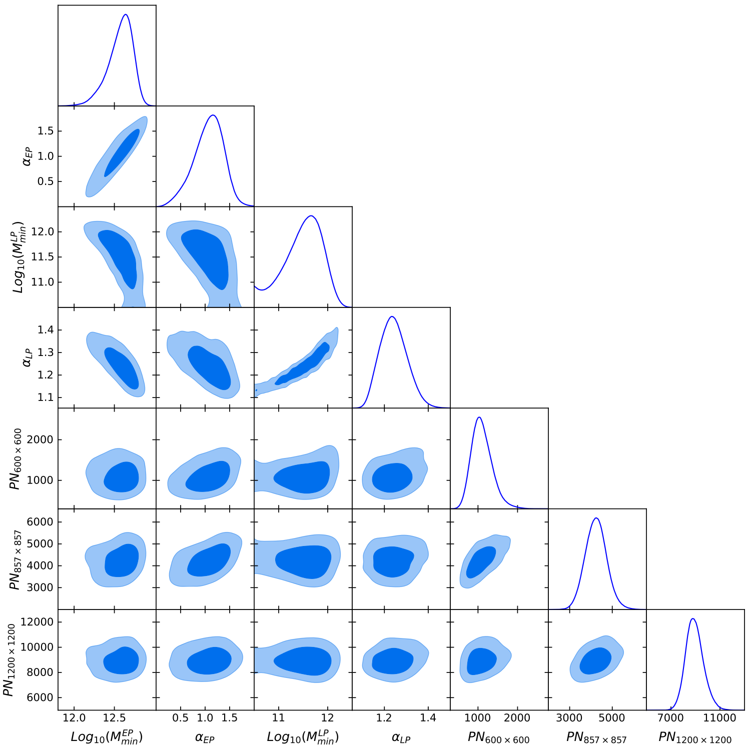

Figure 4.25: *Posterior distributions for the clustering and shot noise parameters in SPIRE-only analysis. All parameters in this fit have been varyed within uniform priors.*

back to resolution effects: Bethermin et al. [207] analyse the impact of resolution effects at SPIRE wavelenghts by means of simulations. They have shown that the number counts measured by Hershel between 5 and 50 mJy are biased towards high values by a factor of ~ 2, which is indeed what we found, in particular at 600 GHz. In figure 4.26 we show the SPIRE-only spectra of the V19 dataset, along with the model computed with the values reported in table 4.8. The solid black curve is the total power, computed as the sum of clustering and poisson terms. The black dotted line is the scale independent poisson term, while the blue dotted line is the clustering. The clustering is computed as the sum of the late-type (green) and early-type (orange) populations. For both populations the plot shows the 2 halo term (solid line) and the 1 halo term (dash-dotted line).

The model well reproduces the data except in the case of the 1200×1200 GHz auto-spectrum and the 600×857 GHz cross-spectrum, for which we observe an excess of power in the model with respect to data at small scales. The total reduced chi-square is $\chi^2 = 1.3$, with a p-value of 0.01. The model is consistent

parameter	priors	result
$Log_{10}(M_{min}^{EP}/M_{\odot}h^{-1})$	[11, 12.8]	12.57±0.16
α_{EP}	[0.2, 3.5]	1.07±0.3
$Log_{10}(M_{min}^{LP}/M_{\odot}h^{-1})$	[10.5, 12.5]	11.5±0.4
α_{LP}	[0.2, 3.5]	1.24±0.06
$PN_{600\times600}$	[300, 2779]	1098±261
$PN_{857\times857}$	[2000, 6605]	4235±496
$PN_{1200\times1200}$	[5000, 13000]	8934±724

Table 4.8: *Mean and standard deviation of the parameters distributions. The run has converged i.e. the posterior mass contained in the live points is equal to the* 1% *of the total evidence. Again we apply to the chains a burn in equal to* 0.4*. Both clustering and shot noise parameters in this fit have been varyed within uniform priors.*

with data between 2 and 3σ, similarly to what found by [148] with a similar modelling. The high value of the chi-square is mainly due to the presence of substantial off-diagonal terms in the covariance matrix, as can be seen by the high degree of correlation in data at small scales.
In order to better explore the descrepancy between the level of the shot noise computed through the fit of the number of counts and the value obtained with the power spectra analysis, we repeated the fit imposing a Gaussian prior on the Poisson levels, centered in the values given by the number of counts, see Table 4.2, and large three times the value of sigma obtained with the same procedure. The resulting distributions are shown in figure 4.27.

The dashed vertical line in the subplots representing the marginal distributions of the poisson noise levels are the values derived from the number counts fit. In the case of the 1200 × 1200 GHz spectrum the distribution matches the value given by the number counts. For the two lower frequencies the distributions are still compatible with the center value of the prior between 1 and 2σ, but have their peaks at lower values. This behaviour mimics what seen in the case in which the shot noise could vary freely, though mitigated by the presence of the prior. The mean and standard deviation of these distributions are listed in table 4.9.

Focusing on the clustering parameters we observe that the value of α is now higher than 2, i.e. not consistent with previous literature and with semi-analytical model predictions. At the same time, the value of the minimum mass for the late type population increases to the value of $\approx 10^{12}M_{\odot}$. A qualitative explanation comes with the following consideration: in a halo of $\approx 10^{12.5}M_{\odot}$ and a scale

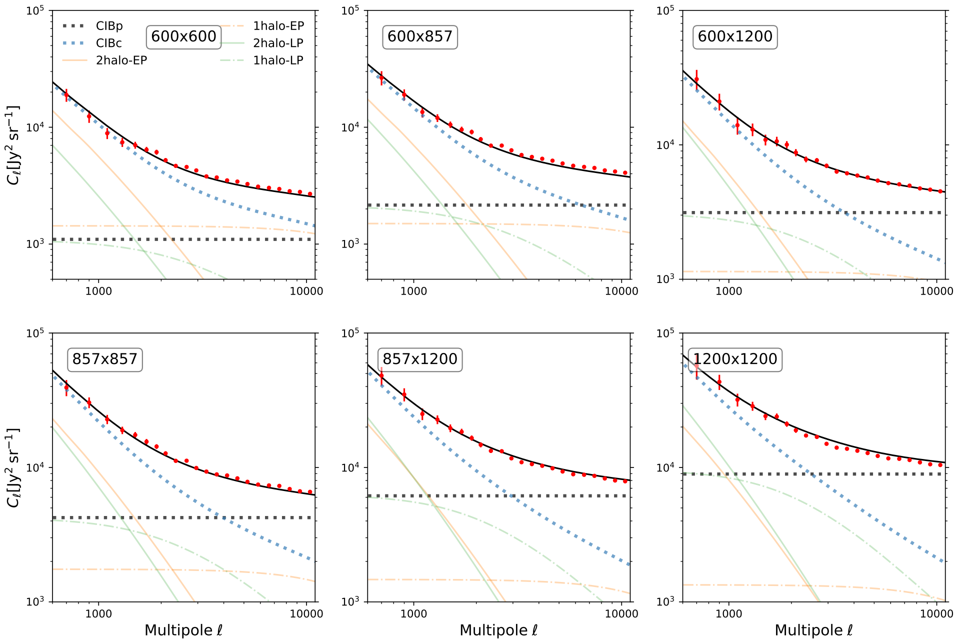

Figure 4.26: *SPIRE-only spectra of the V19 dataset, along with the model computed with the values corresponding to the mean of the parameters distributions. The solid black curve is the total power, computed as the sum of clustering and poisson terms. The black dotted line is the scale independent poisson term, while the blue dotted line is the clustering. The clustering is computed as the sum of the late-type (green) and early-type (orange) populations. For both populations the plot shows the 2 halo term (solid line) and the 1 halo term (dash-dotted line).*

factor of 20, an increase of α causes a decrease of the one halo term. As we are constraining the shot noise to higher values, in particular at low frequencies, an artificial dump of the clustering at small scales is required: this causes α to reach values higher than two. At this point at 1200 GHz we are left with some power missing and this is accounted for with an increase of the minimum mass of the late-type population. In figure 4.28 we show the SPIRE-only spectra of the V19 dataset, along with the model computed with the values reported in table 4.9. The legend is the same of figure 4.26.

The effect of the prior on the value of the shot noise can be appreciated by comparing the top left panel of figure 4.26 and 4.28, which correspond to the autospectra of 600 GHz. In the first case the shot noise term is lower and the one halo term of the early-type population dominates, in the second case the

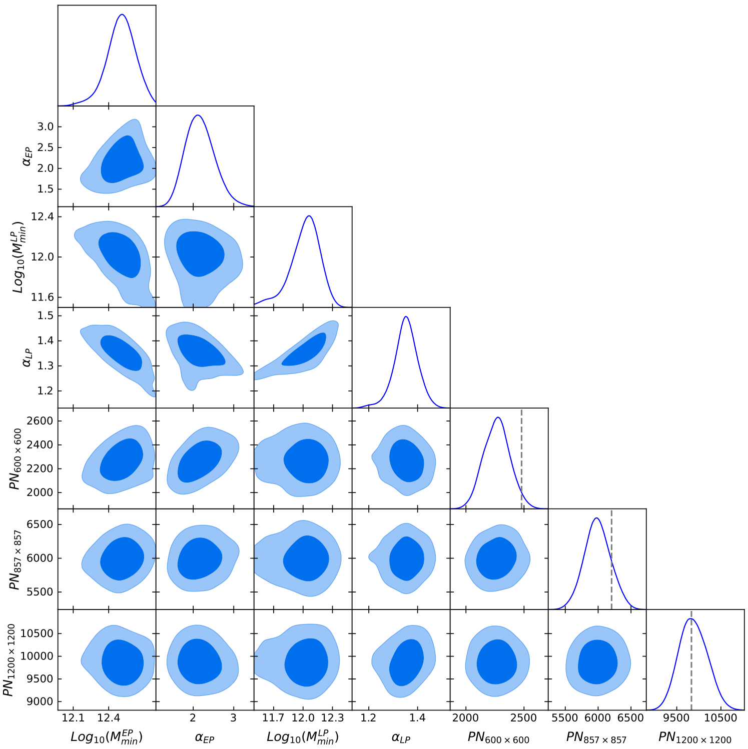

Figure 4.27: *Parameters distributions for the clustering and poisson terms of the CIB emission in the only-SPIRE portion of the V19 dataset. The dashed vertical line in the subplots representing the marginal distributions of the poisson noise levels are the value derived from the number counts fit.*

situation is reversed, with a higher shot noise term and a negligible one halo term for the high redshift galaxies. The consequence of this can be seen by comparing instead the bottom right panels of the two figures, i.e. the auto-spectra of the 1200 GHz. To match the large scale data bandpowers we need more power in the model, which is obtained with an increase of the late-type two halo term (solid green line), through an increase of the hosting halo minimum mass.

Apart from the variations in the parameters value, from figure 4.28 one can see that the fit worsen visibly, in particular for the two higher frequencies. The total reduced chi-square is $\chi^2 = 1.4$, with a p-value lower than 0.002. The conclusion that we can draw is that the present clustering model is not able to reproduce the power spectrum data in presence of constraints on the poisson term. A possible future development of the project is to implement the dependence of clustering on luminosity in a more sophisticated way than what we have done here with the separation of the two galaxy populations, see for example [7].

parameter	priors	result
$Log_{10}(M_{min}^{EP}/M_{\odot}h^{-1})$	[11, 12.8]	12.50±0.14
α_{EP}	[0.2, 3.5]	2.16±0.39
$Log_{10}(M_{min}^{LP}/M_{\odot}h^{-1})$	[10.5, 12.5]	11.98±0.24
α_{LP}	[0.2, 3.5]	1.35±0.55
$PN_{600\times600}$	2479±150	2265±124
$PN_{857\times857}$	6205±250	5991±215
$PN_{1200\times1200}$	9833±400	9882±346

Table 4.9: *Mean and standard deviation of the parameters distributions. The run has converged i.e. the posterior mass contained in the live points is equal to the 1% of the total evidence. Again we apply to the chains a burn in equal to 0.4. Clustering parameters in this fit have been varyed within flat priors, while on shot noise parameters we have imposed a gaussian prior derived by the source-counts analysis.*

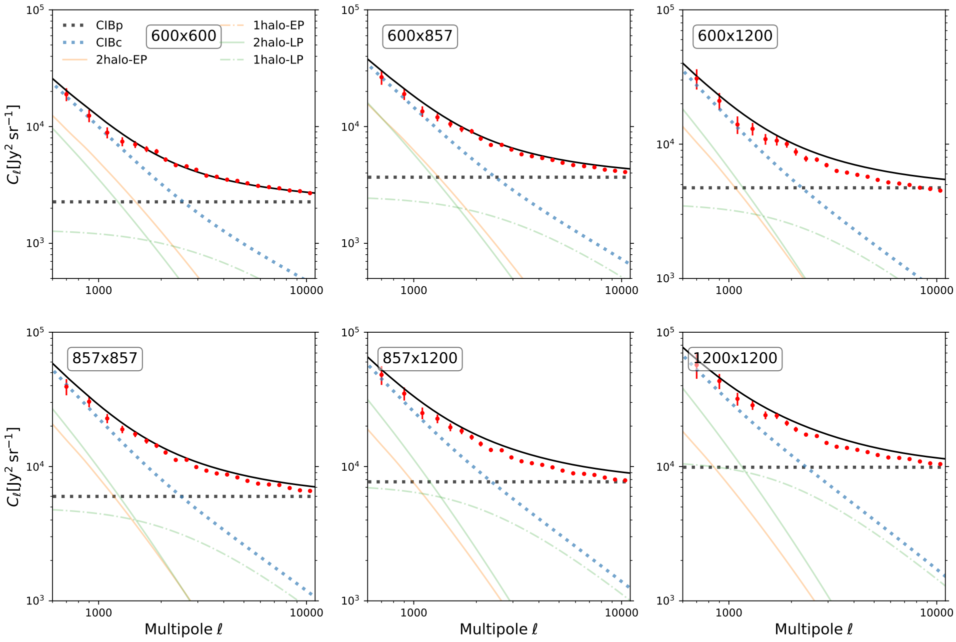

Figure 4.28: *SPIRE-only spectra of the V19 dataset, along with the model computed with the values corresponding to the mean of the parameters distributions. The plot legend is the same of figure 4.26. Imposing a gaussian prior on the shot noise level causes an excess of power in the model with respect to data, especially at 1200 GHz.*

To conclude this paragraph we outline some of the main results: we built a code able to fit data in a large range of frequencies through a physically motivated description of the main foregrounds emitting in millimeter and submillimeter wavelenghts. Data at millimeter wavelenghts (G15 dataset and the SPT portion of V19 dataset) are used to constrain the tSZ and kSZ, the radio sources amplitude and the CIB emission. First we underly that the SPT portion of the V19 dataset, which is obtained with the same procedure and on the same maps of G15, presents an excess of power in the 95×220 GHz cross-spectrum, probably due to a reduced sky fraction. Despite this, the two datasets gave similar results. We found that the kSZ is strongly degenerate with both the tSZ and its correlation with the CIB. Despite data at these frequencies hardly constrain the clustering parameters of the local population of starforming galaxies, a proper modelling of the late type population of the CIB is necessary to avoid misleading the constraints on the kSZ. For the hydrostatic mass bias we found, in both datasets, higher values than those released by Planck analysis, still, the tSZ amplitude obtained with such values is compatible with previous analysis on SPT data, i.e. G15. The V19 dataset is already cleaned from galactic cirrus. Consequently, at SPIRE frequencies, the only contribution to the total power spectrum comes from the CIB. In this case we succesfully constrained the clustering parameters for both early and late type population, confirming that the first is hosted in halos almost ten time more massive than the latter. We also confirmed that there is a discrepancy between the value of the poisson noise computed from power spectrum analysis and that obtained from the galaxy number counts. This is true in particular at 600 GHz, where the number counts measured by Hershel are biased towards high values between 5 and 50 mJy. Beyond the results described here, our code can be used to fit for cosmological parameters and, moreover, it will be of great utility in the analysis of future datasets, as we will describe while drawing the conclusions of this thesis.

Conclusions and future prospects

In this thesis we have explored the two extremes of the Cosmic Microwave Background (CMB) angular power spectrum. We employed the large scales of CMB polarization correlation function to investigate the concordance of low-ℓ CMB measurements with our cosmological model. We used, instead, small scales of millimeter and submillimeter data, focusing on temperature anisotropies, to investigate the distribution of matter in the Universe.

In the first two chapters we briefly reviewed the theory of our standard cosmology, describing the components of the Universe, the main phases of the cosmic history and the origin and evolution of the matter and radiation cosmological perturbations.

In chapter three we extended the study of the lack-of-power anomaly to the CMB polarization field, analysing the most constraining large-scale datasets currently available, which are the *Planck* LFI+WMAP dataset [73] and the *Planck* HFI 100×143 dataset [72]. Adopting a frequentist approach, we assumed *Planck* 2018 + `SRoll2` cosmological fiducial model [67] and in particular a specific value for reionization optical depth $\tau = 0.0591$, which is an important choice for the angular scales probed. The value of τ used is also compatible with that obtained by [73] when using the WMAP+LFI dataset in polarization, together with the `Commander` 2018 solution in temperature. We employed the $S_{1/2}$ estimator [70], which is based on the two-point correlation function of Q and U, see eq. (3.18), and of the local E-modes, see eq. (3.22). We computed such estimators on both data and realistic simulations, which contain signal, noise and residual systematic effects, and compared empirical distributions from simulations with data results. We employed fully polarised signal, considering both Planck CMB temperature constrained and unconstrained simulations, and limit most of the analysis to $\ell_{max} = 10$, a multipole above which both datasets are fully noise-dominated. We calculated the correlation function for Q and U and showed that it is largely dominated by the quadrupole. This clearly impacts the results obtained, which show negligible variation when the maximum multipole included in the analysis is varied.

For both datasets considered, we did not see any anomalous behaviour, except for a mild 2σ anomaly in the case of *Planck* LFI+WMAP U correlation function. This suggests that the power in the very low multipoles, in particular in the quadrupole, is not anomalously low in data. It is worth noting however, that both datasets include non negligible uncertainties at $\ell = 2$, mostly of systematic origin for *Planck* HFI 100×143 and mostly statistical for *Planck* LFI+WMAP. These uncertainties likely affect the constraining power of a possible polarisation anomaly.

On the other hand the estimator involving local E-modes behaves differently being more sensitive to the ℓ_{max} used in the analysis, and thus giving information on the integrated power of the lower multipoles. In Figure 3.12 we showed that the lower tail probability for the two datasets follows the same descending trend and in particular the *Planck* HFI 100×143 seems to suggest a low power in data with respect to the simulations considered.

The behaviour of the $S_{1/2}$ estimators on Q, U and local E-modes in the case of unconstrained simulations appears to be similar to what described for the constrained case. In particular the lower tail probability for $\ell_{max} = 10$ of the *Planck* HFI 100×143 dataset is 0.4%, indicating again a low power of data with respect to simulations.

These results suggest that the large-angle CMB polarisation data behave in a similar way to temperature, exhibiting a mild low power anomaly, presumably originating not only from the quadrupole but rather than from the combined behaviour of all the multipoles $\ell \leq 10$.

This conclusion is strengthened by the joint behaviour of the $S_{1/2}$ estimators in temperature and polarization, investigated through 500 unconstrained simulations of the *Planck* HFI 100×143 dataset. For the joint estimator of temperature and local E modes, the lower tail probability associated to the data is $< 0.2\%$. When combining temperature with the Q or U estimators, instead, we found consistency between data and simulations. This confirms that the hint of an anomalous behaviour of the data with respect to the expectations of the ΛCDM model emerges when including in the analysis the integrated power of all the lower multipoles through the use of local E modes estimators.

The analysis has been carried out with the best datasets currently available at large angular scales, which are however limited by the still significant amount

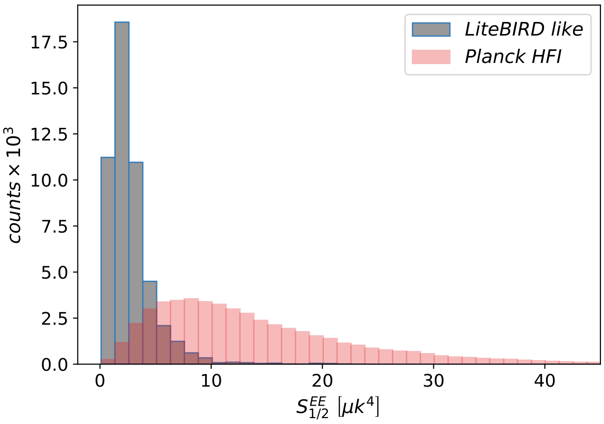

Figure 4.29: *Distributions comparison between LiteBIRD like experiment (grey) and Planck HFI 100×143 dataset (magenta) simulations. The lower width and the left shift of the peak of the grey distribution are due to the lower level of noise which turns into an increase of constraining power for LiteBIRD like experiment.*

of noise in polarisation observations. This issue will be hopefully overcome by the advent of new data, such as those from LiteBIRD [5,208], which are expected to be cosmic variance limited at all scales. LiteBIRD is a satellite-mission proposed by the japanese space agency JAXA, which is expected to be launched in the middle of the 2020s. Unlike Planck, whose target were the temperature anisotropies, LiteBIRD is optimize for polarization. It is designed to measure the anisotropies over the full sky in the multipole range $2 \leq \ell \leq 200$. The mission will last three years, during which LiteBIRD will map the sky in 15 microwave frequency bands, from 34 to 448 GHz. The satellite will use a Low Frequency Telescope (LFT) and an High Frequency Telescope (HFT). Each telescope is equipped with a half-wave plate system for polarization signal modulation and a focal plane filled with polarization-sensitive TES bolometers. We have tried to predict the impact of the advent of LiteBIRD data on our analysis. Through a rough estimate of the noise level from the three most sensitive LiteBIRD bands, we expect to increase of five times the constraining power of our test, in the case of polarization E modes, see Fig. 4.29. The perspectives for shedding light on this subject are thus high.

In the fourth and last chapter we presented a extended analysis of the millimeter and submillimeter data power spectrum relased by the South Pole Telescope (SPT) and the Hershel/SPIRE. We used two different datasets, the first has been published by George et al. in 2015, G15, and includes only the SPT frequencies, while the second has been released by Viero et al. in 2019, V19, and combines together both SPT and SPIRE frequency bands. As we outlined in the chapter, the SPT part of the two datasets has been built through the same pipeline, with some minor variations in the calibration procedure. The main difference is the sky fraction, which goes from 2540 of G15 to 102 deg^2 of V19. We also described the way in which SPIRE×SPIRE and SPT×SPIRE bandpowers of V19 are obtained, along with the covariance matrix. For this dataset, the computation of the total uncertainty required the inclusion of a beam and calibration correlation matrix, multiplied by the theory bandpowers. We specified that the high off-diagonal terms in the total matrix bias the result of the fit, so we decided to consider only the block-diagonal portion of the covariance plus beam-calibration matrix.

Data at millimeter and submillimeter wavelenghts combine the CMB, the thermal Sunyaev Zeldovich (tSZ) and kinetic Sunyaev Zeldovich (kSZ) effect, the Cosmic Infrared Backgorund (CIB), the radio sources and cirrus emission. Such a richness of observables implies a variety of possible investigations we can do on that power spectra. To constrain cosmological parameters we have to clean data from all emissions and effects, also known as *foregrounds*, other from the CMB primary anisotropy. The proper modelling of the foregrounds is then essential for cosmological studies. Looking from another perspective, however, these emissions are not just contaminants to remove, but an additional source of information, mainly from an astrophysiscal point of view. The sources that generate these radiations are galaxies or clusters, located inside dark matter halos. They are then tracers of the large scale matter distribution of the Universe and can be used to study the evolution of cosmic structures. The CIB traces the distribution of dark matter structures hosting the so-called dusty star forming galaxies, up to the mid-far Universe. The SZ effect, instead, sheds light on the distribution of massive galaxy clusters located in the near Universe. In our work we adopted this perspective and investigated the information contained in the foregrounds emission, while keeping the cosmology fixed.

We built a model able to fit for both millimeter and submillimeter data. We adopted an hybrid approach, implementing both an phenomenological modelling for the radio sources and the kSZ effect and a physically motivated model for the tSZ, the CIB and their correlation. In particular the modelling of the CIB clustering term employ a halo model based on the Tinker parametrization for the mass function, the bias and the halo occupation distribution. The model includes two populations of star forming galaxies: one at low redshift, called early-type population and one in the local universe, named late-type population. For the poisson noise, we used the model described in G15 at SPT frequencies, while we fit for the shot noise level at each frequency when considering the SPIRE bandpowers. In the chapter we described in detail the model used and the result of its comparison to data. For what concern the V19 dataset, in this thesis we described the results for the SPT and SPIRE portion of the dataset separately, while leaving the global fit for a future work.

Focusing on the G15 dataset we improved the constraints on the kSZ obtained by previous analysis, detecting it at the 2σ level, $D_{3000}^{kSZ} = 1.9^{+2.6}_{-1.0}\ \mu K^2$. We confirmed what found by A12 about the degeneration between the amplitude of the kSZ and the tSZ-CIB correlation. In particular, we showed that the proper modelling of dusty sources at low redshift is required in order to avoid misleading the constraints on the kSZ amplitude. For the poisson noise term and the radio sources, our results are compatible with literature, while data seem to prefer a high value of the hydrostatic mass bias, $b = 0.57 \pm 0.16$, with respect to Planck analysis [196]. In any case, the amplitude of the tSZ obtained with this value of the mass bias is compatible with that obtained by G15. We found a minimum mass of $10^{12.1}[M_{\odot}h^{-1}]$ and $10^{10.8}[M_{\odot}h^{-1}]$ for the early and late-type population respectively, confirming that the early-type population is hosted in more massive halos. For what concern the index of the power law that regulates the galaxies accretion within the halo, α, we found that data prefer values higher than two in the case of the early-type population. These values are in disagreement with previous literature and with the prediction of semi-analytical models. We attribute this discrepancy to the lack of a sophisticated implementation of the dipendence of clustering on luminosity in our model.

The SPT portion of the V19 dataset shows an excess of power in the 95×1200 cross frequency, which causes a degradation of the constraints on the parameters, in particular on the amplitude of the kSZ. Despite this, the values of the parameters obtained for G15 dataset and V19 SPT×SPT bandpowers are compatible and confirms the conclusions previously outlined.

V19 dataset is already cleaned from galactic cirrus. Consequently, at SPIRE frequencies, the only contribution to the total power spectrum comes from the CIB. The fit to data confirms the results found at millimeter wavelenghts: in particular, the early-type galaxies are hosted in giant halos, ten time more massive than those occupied by the late-type population. We found a minimum mass of $10^{12.5}[M_{\odot}h^{-1}]$ for the early-type population and, for the first time, we constrained the mass of the late-type population at these frequencies to the value of $10^{11.4}[M_{\odot}h^{-1}]$. Moreover, also the Poisson term has revealed some interesting informations. The values of the shot noise resulting from the power spectra fit are strongly in disagreement with the those obtained from the galaxy number counts.

The explanation of this behaviour can be traced back to resolution effects: [207] claims that the number counts measured by Hershel are biased towards high values by a factor of almost two between 5 and 50 mJy. This is approximately the factor we found, in particular at 600 GHz.

The results displayed are obtained using the state of the art dataset available. However, our code has been widely validated [46], it is modular and easy to use, so it will be of great utility in the analysis of future datasets. Several projects have already been planned to start over the next decade. Among them, let us mention the Simons Observatory, CMB-Stage 4 and CONCERTO.

The Simons Observatory (SO) is a new CMB ground-based experiment, and it is expected to start observations in the early 2020s. SO is located in the Atacama Desert (in Chile), sharing the site with other ground-based experiments, such as ACT, CLASS and the planned CMB-Stage 4.

The SO collaboration is building a Large Aperture Telescope (LAT) with a 6-meter primary and three 0.5-meter refracting Small Aperture Telescopes (SATs). The initial plan is to deploy a total of around 60 000 detectors, approximately evenly split between the LAT and the set of SATs. The plan for sky coverage is to observe $\sim 40\%$ of the sky with the LAT, and $\sim 10\%$ with the SATs. This amount of detectors represents a record, as it is about more than an order of magnitude over the size of current microwave detector arrays. With this equipment, SO will observe the sky in six frequency bands: 27, 39, 93, 145, 225 and 280 GHz [10]. SO has the capability to explore the small angular scales, ranging from an arcmin to tens of degrees. This will allow us to shed light on the phenomena affecting the damping tail (high-ℓ region) of the CMB power spectra both in temperature and in polarization.

CMB-Stage 4 (CMB-S4) is another CMB ground-based experiment, covering more than 50% of the sky, over the frequency range $\sim 20 - 280$ GHz [209]. CMB-S4 collaboration targets to deploy $\sim 500\,000$ detectors, so more than an order of magnitude over the SO number. Again, these detectors will be almost equally split among LAT and SATs, and they will be located in both the Atacama Desert and the South Pole.
Small telescopes have the role of setting the most sensitive constraints on the degree scale, *i.e.* on the recombination peak of polarization power spectra. Large telescope, instead, will have primary apertures in the $2-10\,m$ diameter range, in order to achieve angular scales between $1-4$ arcminutes: CMB-S4 will provide us measurements of CMB power spectra up $l_{max} \sim 5000$ [210].

CONCERTO, which saw its first light in April 2021, is one of the instruments on the Atacama Pathfinder Experiment (APEX), operated by ESO and located in the 5100-metre high Chanjantor plateau in the Chilean Andes. It is a spectrometer operating at frequencies between infrared and radio waves (specifically, between 130 and 310 GHz). This is the window into which the radiation is emitted by ionised carbon atoms, one of the most valuable tracers of star formation in the early cosmic ages. With a resolution of 30 arcsec and a field of view of some degrees, CONCERTO can perform both imaging and spectroscopy. It uses a very innovative tecnique, called *intensity mapping* [211], which measures signal fluctuations produced by the combined emission of the galaxy populations on large regions of the sky in a wide frequency (i.e. redshift) band. This tecnique is designed to increase sensitivity to faint sources. CONCERTO intensity mapping will measure the $3-$D fluctuations of the [CII] line at redshifts more than 4.5. CONCERTO is specifically designed to study the epoch of formation of the first generation of stars, i.e the Reionization epoch [212–214]. This target is of extreme importance, as one of the main uncertainties we have in the interpretation of the millimeter and submillimeter data is related to the emission of the dusty sources. Moreover it will allow a deep investigation of the kSZ, as the constraints we obtained with our model depend also on the kSZ angular template and, thus, on the model adopted for the duration and timing of Reionization.

To conclude, we underly that the analysis we have presented in this thesis is perfectly coherent with the main fields of investigation which will be active in Cosmology in the near future. Our effort is aimed to build and optimize a tool that will be useful in the context of new data to analyse, while making a point on what we know or don't know to now on the millimeter and submillieter data interpretation.

Ringraziamenti

A Luca e Mattia, per tutto quello che mi avete insegnato e trasmesso in questi anni di lavoro assieme. A Luca, in particolare, per la sua disponibilità. Grazie di aver dimostrato flessibilità e comprensione nel momento difficile di chiusura della tesi. A Mattia, in particolare, per la pazienza nell'avermi introdotta ad un campo per me completamente nuovo. A tutto il gruppo di Ferrara: Paolo, Massimiliano, Martina, Alessandro, per aver favorito un ambiente in cui ho imparato molto. A Erminia, per avermi dato l'opportunità di impegnarmi in un progetto che mi ha fatta sudare, ma mi ha anche appassionata molto.

Agli amici di Ferrara: Linda, Francesco, Benry, Erica, Alessandro, Umberto, Serena, Luca, Shaz, Marco, Anna, Pari e tutti i nuovi dottorandi, per avermi fatta sentire accolta in città e aver condiviso con me la quotidianità di questi anni.

A Daniele, per essere sempre così generoso e tenero. Sapere che siamo vicini di casa rende persino Roma un po' più piccola.

A Margherita, per tutto l'affetto, per tutto il disagio. Perché condividere la tristezza la trasforma in goliardia e ti permette di fare un passo avanti anche quando pensi di non sentirtela.

Ad Arianna, perchè, per quanto le nostre strade si siano divise già anni fa, riesci sempre a starmi vicina.

Agli amici dell'ADI Ferrara e in particolare a Lorenzo, per avermi fatto ritrovare il senso dell'organizzarsi in un momento di stanca del mio attivismo.

Grazie alla mia famiglia per la vicinanza in questi anni non sempre semplici. Ci sono affetti che non hanno bisogno di parole, ma una la voglio dire. Alla nostra Camilla. L'Astronomia è incomparabilmente bella e spero che un giorno potrò contribuire a fartela apprezzare. Ora sei immersa tra le prime paroline e i giochi, ma io ci tengo lo stesso a darti un avvertimento per il futuro. Molte persone vivono la Scienza come una forma di competizione tra il proprio intelletto e la Natura, poveri pazzi! Tu non fare così: sentirsi piccoli di fronte all'immensità del Cosmo è un privilegio e io ti auguro di affrontare lo studio con la passione e l'incanto di chi è messo a parte di un segreto meraviglioso.

Ai miei nuovi colleghi e colleghe, siete stati una splendida scoperta. Ho cambiato città, vita e prospettive nel giro di due fatidici giorni nel dicembre del 2021. Credo che sarei uscita pazza se non avessi trovato voi. Nelle mille strade che molti di noi prenderanno, cerchiamo di non perderci e di conservare il ricordo della follia che abbiamo vissuto e che ha reso unici questi mesi.

Ai compagni e alle compagne di Roma, per la pazienza che portate in un adattamento che si sta rivelando più difficile del previsto. Me ne sono andata dalla capitale sei anni fa. Tornare oggi e vedere ciò che avete costruito su quelli che allora erano soltanto sogni, mi riempie il cuore di gioia. Conoscervi mi dà il privilegio di tornare dopo tanto tempo e non dover cercare cosa è rimasto, ma scoprire cosa è cambiato.

0.1 Appendix: Comparison between pixel and harmonic based $S_{1/2}^{TT}$ estimator

The two-point correlation functions built in harmonic space and pixel space are equivalent only in the full sky case. When a mask is applied, the two estimators are different: in particular the "masked" harmonic-based estimator recovers the function obtained in the full sky case whereas the "masked" pixel-based estimator deviates from the full sky case. When we propagate this to the lack-of-correlation estimator used, we find that the $S_{1/2}^{TT}$ estimator built with the pixel-based $C(\theta)$ is systematically lower than that built with the harmonic-based $C(\theta)$. In figure 30 we see the scatter plot of 500 simulations: on the y-axis and x-axis we have the pixel-based and harmonic-based $S_{1/2}^{TT}$ estimator respectively. On the left panel we display the comparison for an ideal full sky no-noise analysis, while on the right we compute the $S_{1/2}^{TT}$ for simulations based on the Planck Commander solution, with an $f_{sky} = 86\%$ in temperature. In the ideal case, all simulations accumulate along the diagonal, in the masked case instead there is a bias between the two methods, as the estimator computed in real space gives sistematically lower values than the other. This difference has to be taken into account when comparing pixel and harmonic based estimators.

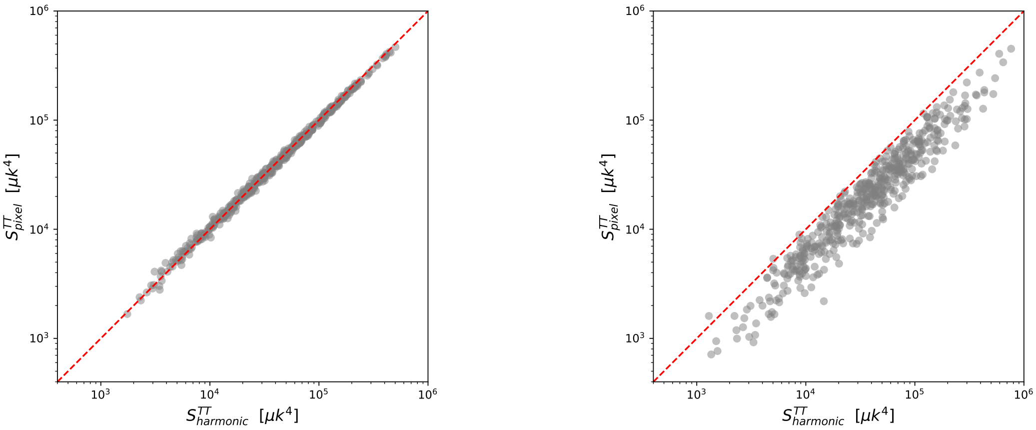

Figure 30: *Scatter plot for 500 simulations. On the y-axis and x-axis we have the pixel-based and harmonic-based $S_{1/2}^{TT}$ estimates respectively, obtained for the same realization. We can qualitatively note that while in the ideal case (left panel) all simulations lie near the diagonal, in the masked case (left panel) there is a bias for the pixel-based estimator that shows lower magnitude with respect to the harmonic-based one.*

0.2 Appendix: calculation of $S_{1/2}^{QQ}$ and $S_{1/2}^{UU}$ in terms of power spectrum

Writing $S_{1/2}^{QQ}$ and $S_{1/2}^{UU}$ in terms of power spectrum is useful to ease computation. To obtain an analytic expression of these estimators we express the $G_\ell^{\pm}(\cos(\theta))$ functions in terms of the reduced Wigner matrices. We define

$$D_\ell^+ = \frac{4(\ell-2)!}{(\ell+2)!} G_{\ell 2}^+(\cos\theta); \tag{123a}$$

$$D_\ell^- = \frac{4(\ell-2)!}{(\ell+2)!} G_{\ell 2}^-(\cos\theta), \tag{123b}$$

and rewrite the $S_{1/2}^{QQ}$ statistic in terms of the power spectrum in the following way

$$\begin{aligned} S_{1/2}^{QQ} &\equiv \int_{-1}^{1/2} d(\cos\theta)[C^{QQ}(\theta)]^2 \\ &= \sum_{\ell=2}^{\ell_{max}} \frac{2\ell+1}{8\pi}\frac{2\ell'+1}{8\pi} \int_{-1}^{1/2} d(\cos\theta)[D_\ell^+ C_\ell^{EE} + D_\ell^- C_\ell^{BB}][D_{\ell'}^+ C_{\ell'}^{EE} + D_{\ell'}^- C_{\ell'}^{BB}]. \end{aligned} \tag{124}$$

Going further in the calculation we obtain:

$$S_{1/2}^{QQ} = \sum_{\ell=2}^{\ell_{max}} \frac{2\ell+1}{8\pi}\frac{2\ell'+1}{8\pi}\left(C_\ell^{EE}C_{\ell'}^{EE}I_{\ell\ell'}^{(1)}+C_\ell^{BB}C_{\ell'}^{BB}I_{\ell\ell'}^{(3)}+C_\ell^{EE}C_{\ell'}^{BB}I_{\ell\ell'}^{(2)}+C_\ell^{BB}C_{\ell'}^{EE}I_{\ell\ell'}^{(4)}\right), \tag{125}$$

where the $I_{\ell\ell'}^{(X)}$ matrices are defined as:

$$\begin{aligned} I_{\ell\ell'}^{(1)} &= \int_{-1}^{1/2} d(\cos\theta) D_\ell^+ D_{\ell'}^+ \quad I_{\ell\ell'}^{(3)} = \int_{-1}^{1/2} d(\cos\theta) D_\ell^- D_{\ell'}^-; \\ I_{\ell\ell'}^{(2)} &= \int_{-1}^{1/2} d(\cos\theta) D_\ell^+ D_{\ell'}^- \quad I_{\ell\ell'}^{(4)} = \int_{-1}^{1/2} d(\cos\theta) D_\ell^- D_{\ell'}^+. \end{aligned} \tag{126}$$

We write now $D_\ell^\pm$ in terms of the reduced Wigner rotation matrices, $d_{2,\pm 2}^\ell$:

$$D_\ell^\pm(\cos\theta) \equiv [d_{2,2}^\ell(\theta) \pm d_{2,-2}^\ell(\theta)] \tag{127}$$

and define

$$I_{\ell\ell'}^{\pm\pm} \equiv \int_{-1}^{1/2} dx\, d_{2,\pm 2}^\ell(x) d_{2,\pm 2}^{\ell'}(x), \tag{128}$$

with $x = \cos(\theta)$. The final expression for the $I_{\ell\ell'}^{(X)}$ matrices is then given by

$$\begin{aligned} I_{\ell\ell'}^{(1)} &= I_{\ell\ell'}^{++} + I_{\ell\ell'}^{+-} + I_{\ell\ell'}^{-+} + I_{\ell\ell'}^{--}; \\ I_{\ell\ell'}^{(2)} &= I_{\ell\ell'}^{++} - I_{\ell\ell'}^{+-} + I_{\ell\ell'}^{-+} - I_{\ell\ell'}^{--}; \\ I_{\ell\ell'}^{(3)} &= I_{\ell\ell'}^{++} - I_{\ell\ell'}^{+-} - I_{\ell\ell'}^{-+} + I_{\ell\ell'}^{--}; \\ I_{\ell\ell'}^{(4)} &= I_{\ell\ell'}^{++} + I_{\ell\ell'}^{+-} - I_{\ell\ell'}^{-+} - I_{\ell\ell'}^{--}. \end{aligned} \tag{129}$$

The matrices $I_{\ell\ell'}^{\pm\pm}$ can be calculated from the relation between Wigner matrices and Clebsch-Gordan coefficients [215], as shown in Appendix A of [70].

0.3 Tool for analysis of millimeter and sub-millimeter data

The code developed is modular and organized to separate the computation of the spectral and angular dependence of the theory power spectrum of each foreground. This allows to increase the flexibility of the code and makes debugging easier. For what concern the halo model (in particular for the CIB) a specific portion of the whole code is devoted to the matter power spectrum calculation, while another computes the halo occupation distributions, necessary to model the galaxy power spectrum. This choice derives from the fact that, considering a given set of cosmological parameters, the matter power spectrum is fixed, while the clustering parameters are varied to perform the fit. In detail, the code is made of four main blocks:

- *spectral-dependence*: allows the computation of the frequency dependence of each foreground together with the conversion factors from μK^2 to Jy^2. Within this block, one can load and interpolate a precomputed emissivity function;
- *HODS*: calculate the halo occupation distribution and mean galaxy density of both early and late type populations;
- *utils*: is devoted to the computation of the halo mass function, the halo bias and the halo density and pressure profiles;
- *power-spectrum*: compute the theory curves for the CIB halo model, the tSZ halo model, the tSZ-CIB correlation, the radio sources, the cirrus emission, the kSZ and the level of the shot noise.

The final spectra of the foregrounds are summed to the CMB power spectrum, computed through the use of CAMB, which is integrated in the present code. Two more functions complete the pictures: the first combines the theory power spectra with the window functions in order to obtain the theory bandpowers. The second computes the likelihood and includes the call to Cobaya to perform the fit. The likelihood used is:

$$-2\ln\mathcal{L} = (C_b^{th} - C_b^{data})^T\Sigma^{-1}(C_b^{th} - C_b^{data}) + \ln det\Sigma. \tag{130}$$

The quantity Σ is the bandpower covariance matrix, C_b^{data} are the data bandpowers, while C_b^{th} are the theory bandpowers. They are computed from the theory power spectrum, C_ℓ^{th}, as:

$$C_b^{th} = \sum_\ell w_{b\ell} C_\ell^{th}, \tag{131}$$

where $w_{b\ell}$ is the bandpower window function.

Bibliography

[1] Arno A. Penzias and Robert Woodrow Wilson. A Measurement of excess antenna temperature at 4080-Mc/s. *Astrophys. J.*, 142:419–421, 1965.

[2] John C. Mather et al. Measurement of the Cosmic Microwave Background spectrum by the COBE FIRAS instrument. *Astrophys. J.*, 420:439–444, 1994.

[3] Licia Verde et al. First year Wilkinson Microwave Anisotropy Probe (WMAP) observations: Parameter estimation methodology. *Astrophys. J. Suppl.*, 148:195, 2003.

[4] Francois R. Bouchet. Looking at the universe with Planck. *PoS*, ICHEP2010:532, 2010.

[5] H. Ishino et al. LiteBIRD: lite satellite for the study of B-mode polarization and inflation from cosmic microwave background radiation detection. *Proc. SPIE Int. Soc. Opt. Eng.*, 9904:99040X, 2016.

[6] Asantha Cooray and Ravi K. Sheth. Halo Models of Large Scale Structure. *Phys. Rept.*, 372:1–129, 2002.

[7] M. P. Viero et al. HerMES: Cosmic Infrared Background Anisotropies and the Clustering of Dusty Star-Forming Galaxies. *Astrophys. J.*, 772:77, 2013.

[8] A. S. Maniyar, M. Béthermin, and G. Lagache. Simple halo model formalism for the cosmic infrared background and its correlation with the thermal Sunyaev-Zel'dovich effect. *Astron. Astrophys.*, 645:A40, 2021.

[9] R. A. Sunyaev and Ya. B. Zeldovich. Microwave background radiation as a probe of the contemporary structure and history of the universe. *Ann. Rev. Astron. Astrophys.*, 18:537–560, 1980.

[10] Peter Ade et al. The Simons Observatory: Science goals and forecasts. *JCAP*, 02:056, 2019.

[11] Kevork Abazajian et al. CMB-S4 Science Case, Reference Design, and Project Plan. 7 2019.

[12] P. Ade et al. A wide field-of-view low-resolution spectrometer at APEX: Instrument design and scientific forecast. *Astron. Astrophys.*, 642:A60, 2020.

[13] Caterina Chiocchetta, Alessandro Gruppuso, Massimiliano Lattanzi, Paolo Natoli, and Luca Pagano. Lack-of-correlation anomaly in CMB large scale polarisation maps. *JCAP*, 08:015, 2021.

[14] Edward W. Kolb and Michael S. Turner. *The Early Universe*, volume 69. 1990.

[15] Chung-Pei Ma and Edmund Bertschinger. Cosmological perturbation theory in the synchronous and conformal Newtonian gauges. *Astrophys. J.*, 455:7–25, 1995.

[16] Giovanni Montani, Marco Valerio Battisti, Riccardo Benini, and Giovanni Imponente. *Primordial cosmology.* World Scientific, Singapore, 2009.

[17] Daniel Baumann. Inflation. In *Theoretical Advanced Study Institute in Elementary Particle Physics: Physics of the Large and the Small*, pages 523–686, 2011.

[18] William H. Kinney. TASI Lectures on Inflation. 2 2009.

[19] Alan H. Guth. The Inflationary Universe: A Possible Solution to the Horizon and Flatness Problems. *Adv. Ser. Astrophys. Cosmol.*, 3:139–148, 1987.

[20] Andrei D. Linde. A New Inflationary Universe Scenario: A Possible Solution of the Horizon, Flatness, Homogeneity, Isotropy and Primordial Monopole Problems. *Adv. Ser. Astrophys. Cosmol.*, 3:149–153, 1987.

[21] Alexei A. Starobinsky. Multicomponent de Sitter (Inflationary) Stages and the Generation of Perturbations. *JETP Lett.*, 42:152–155, 1985.

[22] Patrick Peter and Jean-Philippe Uzan. *Primordial Cosmology.* Oxford Graduate Texts. Oxford University Press, 2 2013.

[23] L. Knox, N. Christensen, and C. Skordis. The age of the universe and the cosmological constant determined from cosmic microwave background anisotropy measurements. *Astrophys. J. Lett.*, 563:L95–L98, 2001.

[24] Scott Dodelson and Jay M. Jubas. Reionization and its imprint on the cosmic microwave background. *Astrophys. J.*, 439:503–516, 1995.

[25] Peter Coles and Francesco Lucchin. Cosmology, the origin and evolution of cosmic structure. *Chichester: Wiley, |c1995*, -1, 01 1995.

[26] Peter W. Higgs. Broken Symmetries and the Masses of Gauge Bosons. *Phys. Rev. Lett.*, 13:508–509, 1964.

[27] D. Boyanovsky. Phase transitions in the early and the present universe: From the big bang to heavy ion collisions. In *International School of Astrophysics 'Daniel Chalonge' 8th Course: Opening the 3rd Millennium, Phase Transitions in the Early Unverse: Theory and Observations*, pages 3–44, 2 2001.

[28] Gary Steigman. Big bang nucleosynthesis: Current status. In *2nd Oak Ridge Symposium on Atomic and Nuclear Astrophysics*, 3 1998.

[29] R. H. Dicke, P. J. E. Peebles, P. G. Roll, and D. T. Wilkinson. Cosmic Black-Body Radiation. *Astrophys. J.*, 142:414–419, 1965.

[30] D. J. Fixsen, E. S. Cheng, J. M. Gales, John C. Mather, R. A. Shafer, and E. L. Wright. The Cosmic Microwave Background spectrum from the full COBE FIRAS data set. *Astrophys. J.*, 473:576, 1996.

[31] C. L. Bennett et al. Nine-Year Wilkinson Microwave Anisotropy Probe (WMAP) Observations: Final Maps and Results. *Astrophys. J. Suppl.*, 208:20, 2013.

[32] P. A. R. Ade et al. Planck 2015 results. XIII. Cosmological parameters. *Astron. Astrophys.*, 594:A13, 2016.

[33] Wayne Hu and Scott Dodelson. Cosmic Microwave Background Anisotropies. *Ann. Rev. Astron. Astrophys.*, 40:171–216, 2002.

[34] W. L. Freedman, editor. *Measuring and modeling the universe. Proceedings, Symposium, Pasadena, USA, November 17-22, 2002*, 2004.

[35] Joseph Silk. Cosmic black body radiation and galaxy formation. *Astrophys. J.*, 151:459–471, 1968.

[36] John David Jackson. *Classical Electrodynamics.* Wiley, 1998.

[37] R. K. Sachs and A. M. Wolfe. Perturbations of a cosmological model and angular variations of the microwave background. *Astrophys. J.*, 147:73–90, 1967.

[38] Arthur Kosowsky, Milos Milosavljevic, and Raul Jimenez. Efficient cosmological parameter estimation from microwave background anisotropies. *Phys. Rev. D*, 66:063007, 2002.

[39] N. Aghanim et al. Planck 2018 results. I. Overview and the cosmological legacy of Planck. *Astron. Astrophys.*, 641:A1, 2020.

[40] Matias Zaldarriaga and Uros Seljak. An all sky analysis of polarization in the microwave background. *Phys. Rev. D*, 55:1830–1840, 1997.

[41] Antony Lewis and Anthony Challinor. Weak gravitational lensing of the CMB. *Phys. Rept.*, 429:1–65, 2006.

[42] N. Aghanim et al. Planck 2018 results. I. Overview and the cosmological legacy of Planck. *Astron. Astrophys.*, 641:A1, 2020.

[43] Volker Springel, Carlos S. Frenk, and Simon D. M. White. The large-scale structure of the Universe. *Nature*, 440:1137, 2006.

[44] Antony Lewis and Anthony Challinor. CAMB: Code for Anisotropies in the Microwave Background, February 2011.

[45] Daniel J. Eisenstein and Wayne Hu. Baryonic features in the matter transfer function. *Astrophys. J.*, 496:605, 1998.

[46] Steven G. Murray, Benedikt Diemer, Zhaoting Chen, Anton Glenn Neuhold, M. A. Schnapp, Tia Peruzzi, Daniel Blevins, and Trent Engelman. TheHaloMod: An online calculator for the halo model. *Astron. Comput.*, 36:100487, 2021.

[47] Dominik J. Schwarz, Craig J. Copi, Dragan Huterer, and Glenn D. Starkman. CMB Anomalies after Planck. *Class. Quant. Grav.*, 33(18):184001, 2016.

[48] D. N. Spergel, L. Verde, H. V. Peiris, E. Komatsu, M. R. Nolta, C. L. Bennett, M. Halpern, G. Hinshaw, N. Jarosik, A. Kogut, and et al. First-year wilkinson microwave anisotropy probe(wmap) observations: Determination of cosmological parameters. *The Astrophysical Journal Supplement Series*, 148(1):175–194, Sep 2003.

[49] Armando Bernui, Thyrso Villela, Carlos A. Wuensche, Rodrigo Leonardi, and Ivan Ferreira. On the cmb large-scales angular correlations. *Astron. Astrophys.*, 454:409–414, 2006.

[50] Craig Copi, Dragan Huterer, Dominik Schwarz, and Glenn Starkman. The Uncorrelated Universe: Statistical Anisotropy and the Vanishing Angular Correlation Function in WMAP Years 1-3. *Phys. Rev. D*, 75:023507, 2007.

[51] Craig J. Copi, Dragan Huterer, Dominik J. Schwarz, and Glenn D. Starkman. No large-angle correlations on the non-Galactic microwave sky. *Mon. Not. Roy. Astron. Soc.*, 399:295–303, 2009.

[52] Craig J. Copi, Dragan Huterer, Dominik J. Schwarz, and Glenn D. Starkman. Large angle anomalies in the CMB. *Adv. Astron.*, 2010:847541, 2010.

[53] P. A. R. Ade et al. Planck 2013 results. XVI. Cosmological parameters. *Astron. Astrophys.*, 571:A16, 2014.

[54] N. Aghanim et al. Planck 2015 results. XI. CMB power spectra, likelihoods, and robustness of parameters. *Astron. Astrophys.*, 594:A11, 2016.

[55] A. Gruppuso, N. Kitazawa, M. Lattanzi, N. Mandolesi, P. Natoli, and A. Sagnotti. The Evens and Odds of CMB Anomalies. *Phys. Dark Univ.*, 20:49–64, 2018.

[56] A. Gruppuso, N. Kitazawa, N. Mandolesi, P. Natoli, and A. Sagnotti. Pre-Inflationary Relics in the CMB? *Phys. Dark Univ.*, 11:68–73, 2016.

[57] A. Gruppuso and A. Sagnotti. Observational Hints of a Pre–Inflationary Scale? *Int. J. Mod. Phys. D*, 24(12):1544008, 2015.

[58] C. Monteserin, R. B. Belen Barreiro, P. Vielva, E. Martinez-Gonzalez, M. P. Hobson, and A. N. Lasenby. A low CMB variance in the WMAP data. *Mon. Not. Roy. Astron. Soc.*, 387:209–219, 2008.

[59] M. Cruz, P. Vielva, E. Martinez-Gonzalez, and R. B. Barreiro. Anomalous variance in the WMAP data and Galactic Foreground residuals. *Mon. Not. Roy. Astron. Soc.*, 412:2383, 2011.

[60] A. Gruppuso, P. Natoli, F. Paci, F. Finelli, D. Molinari, A. De Rosa, and N. Mandolesi. Low Variance at large scales of WMAP 9 year data. *JCAP*, 07:047, 2013.

[61] Jessica Muir, Saroj Adhikari, and Dragan Huterer. Covariance of CMB anomalies. *Phys. Rev. D*, 98(2):023521, 2018.

[62] A. Gruppuso. Two-point correlation function of Wilkinson Microwave Anisotropy Probe 9-yr data. *Monthly Notices of the Royal Astronomical Society*, 437(3):2076–2082, 11 2013.

[63] Craig J. Copi, Dragan Huterer, Dominik J. Schwarz, and Glenn D. Starkman. Lack of large-angle TT correlations persists in WMAP and Planck. *Mon. Not. Roy. Astron. Soc.*, 451(3):2978–2985, 2015.

[64] P. A. R. Ade et al. Planck 2013 results. XXIII. Isotropy and statistics of the CMB. *Astron. Astrophys.*, 571:A23, 2014.

[65] P. A. R. Ade et al. Planck 2015 results. XVI. Isotropy and statistics of the CMB. *Astron. Astrophys.*, 594:A16, 2016.

[66] U. Natale, A. Gruppuso, D. Molinari, and P. Natoli. Is the lack of power anomaly in the CMB correlated with the orientation of the Galactic plane? *JCAP*, 12:052, 2019.

[67] L. Pagano, J. M. Delouis, S. Mottet, J. L. Puget, and L. Vibert. Reionization optical depth determination from Planck HFI data with ten percent accuracy. *Astron. Astrophys.*, 635:A99, 2020.

[68] Y. Akrami et al. Planck 2018 results. VII. Isotropy and Statistics of the CMB. *Astron. Astrophys.*, 641:A7, 2020.

[69] C. J. Copi, D. Huterer, D. J. Schwarz, and G. D. Starkman. Large-Angle CMB Suppression and Polarization Predictions. *Mon. Not. Roy. Astron. Soc.*, 434:3590–3596, 2013.

[70] Amanda Yoho, Simone Aiola, Craig J. Copi, Arthur Kosowsky, and Glenn D. Starkman. Microwave background polarization as a probe of large-angle correlations. *Physical Review D*, 91(12), Jun 2015.

[71] M. Billi, A. Gruppuso, N. Mandolesi, L. Moscardini, and P. Natoli. Polarisation as a tracer of CMB anomalies: Planck results and future forecasts. *Phys. Dark Univ.*, 26:100327, 2019.

[72] J. M. Delouis, L. Pagano, S. Mottet, J. L. Puget, and L. Vibert. SRoll2: an improved mapmaking approach to reduce large-scale systematic effects in the Planck High Frequency Instrument legacy maps. *Astron. Astrophys.*, 629:A38, 2019.

[73] U. Natale, L. Pagano, M. Lattanzi, M. Migliaccio, L. P. Colombo, A. Gruppuso, P. Natoli, and G. Polenta. A novel CMB polarization likelihood package for large angular scales built from combined WMAP and Planck LFI legacy maps. *Astron. Astrophys.*, 644:A32, 2020.

[74] N. Aghanim et al. Planck 2018 results. III. High Frequency Instrument data processing and frequency maps. *Astron. Astrophys.*, 641:A3, 2020.

[75] Y. Akrami et al. Planck 2018 results. II. Low Frequency Instrument data processing. *Astron. Astrophys.*, 641:A2, 2020.

[76] C. L. Bennett, D. Larson, J. L. Weiland, N. Jarosik, G. Hinshaw, N. Odegard, K. M. Smith, R. S. Hill, B. Gold, M. Halpern, E. Komatsu, M. R. Nolta, L. Page, D. N. Spergel, E. Wollack, J. Dunkley, A. Kogut, M. Limon, S. S. Meyer, G. S. Tucker, and E. L. Wright. Nine-year wilkinson microwave anisotropy probe (wmap) observations: Final maps and results. *The Astrophysical Journal Supplement Series*, 208(2):20, Sep 2013.

[77] L. Page et al. Three year Wilkinson Microwave Anisotropy Probe (WMAP) observations: polarization analysis. *Astrophys. J. Suppl.*, 170:335, 2007.

[78] N. Aghanim et al. Planck 2018 results. V. CMB power spectra and likelihoods. *Astron. Astrophys.*, 641:A5, 2020.

[79] K. M. Górski, E. Hivon, A. J. Banday, B. D. Wandelt, F. K. Hansen, M. Reinecke, and M. Bartelman. HEALPix - A Framework for high resolution discretization, and fast analysis of data distributed on the sphere. *Astrophys. J.*, 622:759–771, 2005.

[80] Andrea Zonca, Leo Singer, Daniel Lenz, Martin Reinecke, Cyrille Rosset, Eric Hivon, and Krzysztof Gorski. healpy: equal area pixelization and spherical harmonics transforms for data on the sphere in Python. *Journal of Open Source Software*, 4(35):1298, 2019.

[81] K. Benabed, J. F. Cardoso, S. Prunet, and E. Hivon. TEASING: a fast and accurate approximation for the low multipole likelihood of the Cosmic Microwave Background temperature. *Mon. Not. Roy. Astron. Soc.*, 400:219, 2009.

[82] N. Aghanim et al. Planck intermediate results. XLVI. Reduction of large-scale systematic effects in HFI polarization maps and estimation of the reionization optical depth. *Astron. Astrophys.*, 596:A107, 2016.

[83] Max Tegmark and Angelica de Oliveira-Costa. How to measure CMB polarization power spectra without losing information. *Phys. Rev. D*, 64:063001, 2001.

[84] A. Gruppuso, A. De Rosa, P. Cabella, F. Paci, F. Finelli, P. Natoli, G. de Gasperis, and N. Mandolesi. New estimates of the CMB angular power spectra from the WMAP 5 yrs low resolution data. *Mon. Not. Roy. Astron. Soc.*, 400:463–469, 2009.

[85] Marc Kamionkowski, Arthur Kosowsky, and Albert Stebbins. Statistics of cosmic microwave background polarization. *Phys. Rev. D*, 55:7368–7388, 1997.

[86] J. D. Vieira, T. M. Crawford, E. R. Switzer, P. A. R. Ade, K. A. Aird, M. L. N. Ashby, B. A. Benson, L. E. Bleem, M. Brodwin, J. E. Carlstrom, and et al. Extragalactic millimeter-wave sources in south pole telescope survey data: Source counts, catalog, and statistics for an 87 square-degree field. *The Astrophysical Journal*, 719(1):763–783, Jul 2010.

[87] K. T. Story, C. L. Reichardt, Z. Hou, R. Keisler, K. A. Aird, B. A. Benson, L. E. Bleem, J. E. Carlstrom, C. L. Chang, H.-M. Cho, and et al. A measurement of the cosmic microwave background damping tail from the 2500-square-degree spt-sz survey. *The Astrophysical Journal*, 779(1):86, Nov 2013.

[88] G. L. Pilbratt et al. Herschel Space Observatory - An ESA facility for far-infrared and submillimetre astronomy. *Astron. Astrophys.*, 518:L1, 2010.

[89] Julien Lesgourgues. The cosmic linear anisotropy solving system (class) i: Overview, 2011.

[90] Diego Blas, Julien Lesgourgues, and Thomas Tram. The cosmic linear anisotropy solving system (class). part ii: Approximation schemes. *Journal of Cosmology and Astroparticle Physics*, 2011(07):034–034, Jul 2011.

[91] M. Lueker, C. L. Reichardt, K. K. Schaffer, O. Zahn, P. A. R. Ade, K. A. Aird, B. A. Benson, L. E. Bleem, J. E. Carlstrom, C. L. Chang, H. M. Cho, T. M. Crawford, A. T. Crites, T. de Haan, M. A. Dobbs, E. M. George, N. R. Hall, N. W. Halverson, G. P. Holder, W. L. Holzapfel, J. D. Hrubes, M. Joy, R. Keisler, L. Knox, A. T. Lee, E. M. Leitch, J. J. McMahon, J. Mehl, S. S. Meyer, J. J. Mohr, T. E. Montroy, S. Padin, T. Plagge, C. Pryke, J. E. Ruhl, L. Shaw, E. Shirokoff, H. G. Spieler, B. Stalder, Z. Staniszewski, A. A. Stark, K. Vanderlinde, J. D. Vieira, and R. Williamson. Measurements of Secondary Cosmic Microwave Background Anisotropies with the South Pole Telescope. *apj*, 719(2):1045–1066, August 2010.

[92] E. Shirokoff, C. L. Reichardt, L. Shaw, M. Millea, P. A. R. Ade, K. A. Aird, B. A. Benson, L. E. Bleem, J. E. Carlstrom, C. L. Chang, H. M. Cho, T. M. Crawford, A. T. Crites, T. de Haan, M. A. Dobbs, J. Dudley, E. M. George, N. W. Halverson, G. P. Holder, W. L. Holzapfel, J. D. Hrubes, M. Joy, R. Keisler, L. Knox, A. T. Lee, E. M. Leitch, M. Lueker, D. Luong-Van, J. J. McMahon, J. Mehl, S. S. Meyer, J. J. Mohr, T. E. Montroy, S. Padin, T. Plagge, C. Pryke, J. E. Ruhl, K. K. Schaffer, H. G. Spieler, Z. Staniszewski, A. A. Stark, K. Story, K. Vanderlinde, J. D. Vieira, R. Williamson, and O. Zahn. Improved Constraints on Cosmic Microwave Background Secondary Anisotropies from the Complete 2008 South Pole Telescope Data. *apj*, 736(1):61, July 2011.

[93] C. L. Reichardt et al. A measurement of secondary cosmic microwave background anisotropies with two years of South Pole Telescope observations. *Astrophys. J.*, 755:70, 2012.

[94] R. Keisler, C. L. Reichardt, K. A. Aird, B. A. Benson, L. E. Bleem, J. E. Carlstrom, C. L. Chang, H. M. Cho, T. M. Crawford, A. T. Crites, and et al. A measurement of the damping tail of the cosmic microwave background power spectrum with the south pole telescope. *The Astrophysical Journal*, 743(1):28, Nov 2011.

[95] J. Dunkley et al. The Atacama Cosmology Telescope: likelihood for small-scale CMB data. *JCAP*, 07:025, 2013.

[96] E. M. George et al. A measurement of secondary cosmic microwave background anisotropies from the 2500-square-degree SPT-SZ survey. *Astrophys. J.*, 799(2):177, 2015.

[97] J. Neyman, E. L. Scott, and C. D. Shane. On the Spatial Distribution of Galaxies: a Specific Model. *apj*, 117:92, January 1953.

[98] J. A. Peacock and R. E. Smith. Halo occupation numbers and galaxy bias. *Mon. Not. Roy. Astron. Soc.*, 318:1144, 2000.

[99] Uroš Seljak. Analytic model for galaxy and dark matter clustering. *mnras*, 318(1):203–213, October 2000.

[100] Chung-Pei Ma and James N. Fry. Deriving the nonlinear cosmological power spectrum and bispectrum from analytic dark matter halo profiles and mass functions. *Astrophys. J.*, 543:503–513, 2000.

[101] Marc Davis, George Efstathiou, Carlos S. Frenk, and Simon D. M. White. The Evolution of Large Scale Structure in a Universe Dominated by Cold Dark Matter. *Astrophys. J.*, 292:371–394, 1985.

[102] A. Jenkins, C. S. Frenk, Simon D. M. White, J. M. Colberg, S. Cole, August E. Evrard, H. M. P. Couchman, and N. Yoshida. The Mass function of dark matter halos. *Mon. Not. Roy. Astron. Soc.*, 321:372, 2001.

[103] Kwan Chuen Chan, Ravi K. Sheth, and Román Scoccimarro. Effective window function for lagrangian halos. *Phys. Rev. D*, 96:103543, Nov 2017.

[104] William H. Press and Paul Schechter. Formation of galaxies and clusters of galaxies by selfsimilar gravitational condensation. *Astrophys. J.*, 187:425–438, 1974.

[105] J. R. Bond, S. Cole, G. Efstathiou, and Nick Kaiser. Excursion set mass functions for hierarchical Gaussian fluctuations. *Astrophys. J.*, 379:440, 1991.

[106] Ravi K. Sheth and Giuseppe Tormen. Large-scale bias and the peak background split. *Monthly Notices of the Royal Astronomical Society*, 308(1):119–126, Sep 1999.

[107] Jeremy L. Tinker, Andrey V. Kravtsov, Anatoly Klypin, Kevork Abazajian, Michael S. Warren, Gustavo Yepes, Stefan Gottlober, and Daniel E. Holz. Toward a halo mass function for precision cosmology: The Limits of universality. *Astrophys. J.*, 688:709–728, 2008.

[108] M. M. Cueli, L. Bonavera, J. González-Nuevo, and A. Lapi. A direct and robust method to observationally constrain the halo mass function via the submillimeter magnification bias: Proof of concept. *Astron. Astrophys.*, 645:A126, 2021.

[109] Thomas P. Robitaille et al. Astropy: A Community Python Package for Astronomy. *Astron. Astrophys.*, 558:A33, 2013.

[110] Shaun Cole and Nick Kaiser. Biased clustering in the cold dark matter cosmogony. *Mon. Not. Roy. Astron. Soc.*, 237:1127–1146, 1989.

[111] Andrew R. Zentner. The Excursion Set Theory of Halo Mass Functions, Halo Clustering, and Halo Growth. *Int. J. Mod. Phys. D*, 16:763–816, 2007.

[112] M. Manera, Ravi K. Sheth, and R. Scoccimarro. Large-scale bias and the inaccuracy of the peak-background split. *Monthly Notices of the Royal Astronomical Society*, 402(1):589–602, Dec 2009.

[113] Jeremy L. Tinker, Risa H. Wechsler, and Zheng Zheng. Interpreting the clustering of distant red galaxies. *The Astrophysical Journal*, 709(1):67–76, Dec 2009.

[114] H. J. Mo and Simon D. M. White. An Analytic model for the spatial clustering of dark matter halos. *Mon. Not. Roy. Astron. Soc.*, 282:347, 1996.

[115] Julio F. Navarro, Carlos S. Frenk, and Simon D. M. White. A Universal density profile from hierarchical clustering. *Astrophys. J.*, 490:493–508, 1997.

[116] Corentin Cadiou, Andrew Pontzen, Hiranya V. Peiris, and Luisa Lucie-Smith. The causal effect of environment on halo mass and concentration. *Mon. Not. Roy. Astron. Soc.*, 508(1):1189–1194, 2021.

[117] James S. Bullock, Tsafrir S. Kolatt, Yair Sigad, Rachel S. Somerville, Andrey V. Kravtsov, Anatoly A. Klypin, Joel R. Primack, and Avishai Dekel. Profiles of dark haloes. Evolution, scatter, and environment. *Mon. Not. Roy. Astron. Soc.*, 321:559–575, 2001.

[118] Frank C. van den Bosch. The universal mass accretion history of cdm haloes. *Mon. Not. Roy. Astron. Soc.*, 331:98, 2002.

[119] Risa H. Wechsler, James S. Bullock, Joel R. Primack, Andrey V. Kravtsov, and Avishai Dekel. Concentrations of dark halos from their assembly histories. *Astrophys. J.*, 568:52–70, 2002.

[120] Donghai Zhao, Houjun Mo, Yipeng Jing, and Gerhard Boerner. The growth and structure of dark matter haloes. *Mon. Not. Roy. Astron. Soc.*, 339:12–24, 2003.

[121] Benedikt Diemer, Surhud More, and Andrey V. Kravtsov. The pseudo-evolution of halo mass. *The Astrophysical Journal*, 766(1):25, Mar 2013.

[122] Benedikt Diemer and Michael Joyce. An accurate physical model for halo concentrations. *Astrophys. J.*, 871(2):168, 2019.

[123] Aaron D. Ludlow, Julio F. Navarro, Michael Boylan-Kolchin, Philip E. Bett, Raul E. Angulo, Ming Li, Simon D. M. White, Carlos Frenk, and Volker Springel. The Mass Profile and Accretion History of Cold Dark Matter Halos. *Mon. Not. Roy. Astron. Soc.*, 432:1103, 2013.

[124] Neal Dalal, Yoram Lithwick, and Michael Kuhlen. The origin of dark matter halo profiles, 2010.

[125] Risa H. Wechsler and Jeremy L. Tinker. The Connection between Galaxies and their Dark Matter Halos. *Ann. Rev. Astron. Astrophys.*, 56:435–487, 2018.

[126] Zheng Zheng, Andreas A. Berlind, David H. Weinberg, Andrew J. Benson, Carlton M. Baugh, Shaun Cole, Romeel Dave, Carlos S. Frenk, Neal Katz, and Cedric G. Lacey. Theoretical models of the halo occupation distribution: Separating central and satellite galaxies. *Astrophys. J.*, 633:791–809, 2005.

[127] Idit Zehavi et al. The Luminosity and color dependence of the galaxy correlation function. *Astrophys. J.*, 630:1–27, 2005.

[128] Jeremy L. Tinker and Andrew R. Wetzel. What does clustering tell us about the buildup of the red sequence? *The Astrophysical Journal*, 719(1):88–103, Jul 2010.

[129] Guinevere Kauffmann, Adi Nusser, and Matthias Steinmetz. Galaxy formation and large scale bias. *Mon. Not. Roy. Astron. Soc.*, 286:795–811, 1997.

[130] Roman Scoccimarro, Ravi K. Sheth, Lam Hui, and Bhuvnesh Jain. How many galaxies fit in a halo? Constraints on galaxy formation efficiency from spatial clustering. *Astrophys. J.*, 546:20–34, 2001.

[131] Andreas A. Berlind, David H. Weinberg, Andrew J. Benson, Carlton M. Baugh, Shaun Cole, Romeel Dave, Carlos S. Frenk, Adrian Jenkins, Neal Katz, and Cedric G. Lacey. The Halo occupation distribution and the physics of galaxy formation. *Astrophys. J.*, 593:1–25, 2003.

[132] Göran Pilbratt. The FIRST Mission: Science Objectives, Baseline, And Operations. In *32nd Rencontres de Moriond: Extragalactic Astronomy in the Infrared*, pages 579–588, Paris, 1997. Edition Frontieres.

[133] D. J. Fixsen, E. Dwek, J. C. Mather, C. L. Bennett, and R. A. Shafer. The spectrum of the extragalactic far-infrared background from thecobefiras observations. *The Astrophysical Journal*, 508(1):123–128, Nov 1998.

[134] Andrew W. Blain, Ian Smail, R. J. Ivison, J. P. Kneib, and David T. Frayer. Submillimeter galaxies. *Phys. Rept.*, 369:111–176, 2002.

[135] Gian Luigi Granato, Gianfranco De Zotti, Laura Silva, Alessandro Bressan, and Luigi Danese. A physical model for the co-evolution of qsos and of their spheroidal hosts. *Astrophys. J.*, 600:580–594, 2004.

[136] Zhen-Yi Cai, Andrea Lapi, Jun-Qing Xia, Gianfranco De Zotti, Mattia Negrello, Carlotta Gruppioni, Emma Rigby, Guillaume Castex, Jacques Delabrouille, and Luigi Danese. A hybrid model for the evolution of galaxies and Active Galactic Nuclei in the infrared. *Astrophys. J.*, 768:21, 2013.

[137] A. Lapi and A. Cavaliere. Self-Similar Dynamical Relaxation of Dark Matter Halos in an Expanding Universe. *Astrophys. J.*, 743:127, 2011.

[138] A. Lapi et al. Herschel-ATLAS Galaxy Counts and High Redshift Luminosity Functions: The Formation of Massive Early Type Galaxies. *Astrophys. J.*, 742:24, 2011.

[139] J. Mao, A. Lapi, G. L. Granato, G. de Zotti, and L. Danese. The role of the dust in primeval galaxies: A simple physical model for lyman break

galaxies and lyα emitters. *The Astrophysical Journal*, 667(2):655–666, Oct 2007.

[140] David Elbaz et al. The reversal of the star formation-density relation in the distant Universe. *Astron. Astrophys.*, 468:33–48, 2007.

[141] T. T. Nakamura and Y. Suto. Strong gravitational lensing and velocity function as tools to probe cosmological parameters: Current constraints and future predictions. *Progress of Theoretical Physics*, 97(1):49–81, Jan 1997.

[142] Ofer Lahav, Per B. Lilje, Joel R. Primack, and Martin J. Rees. Dynamical effects of the cosmological constant. *Mon. Not. Roy. Astron. Soc.*, 251:128–136, 1991.

[143] Sean M. Carroll, William H. Press, and Edwin L. Turner. The Cosmological constant. *Ann. Rev. Astron. Astrophys.*, 30:499–542, 1992.

[144] James M. Bardeen, J. R. Bond, Nick Kaiser, and A. S. Szalay. The Statistics of Peaks of Gaussian Random Fields. *Astrophys. J.*, 304:15–61, 1986.

[145] Naoshi Sugiyama. Cosmic background anistropies in CDM cosmology. *Astrophys. J. Suppl.*, 100:281, 1995.

[146] W. Saunders, M. Rowan-Robinson, A. Lawrence, G. Efstathiou, N. Kaiser, R. S. Ellis, and C. S. Frenk. The 60-mu.m and far-infrared luminosity functions of IRAS galaxies. *mnras*, 242:318–337, January 1990.

[147] Matthieu Bethermin, Herve Dole, Guilaine Lagache, Damien Le Borgne, and Aurelie Penin. Modeling the evolution of infrared galaxies: A Parametric backwards evolution model. *Astron. Astrophys.*, 529:A4, 2011.

[148] Marco P. Viero, Peter A. R. Ade, James J. Bock, Edward L. Chapin, Mark J. Devlin, Matthew Griffin, Joshua O. Gundersen, Mark Halpern, Peter C. Hargrave, David H. Hughes, and et al. Blast: Correlations in the cosmic far-infrared background at 250, 350, and 500 μm reveal clustering of star-forming galaxies. *The Astrophysical Journal*, 707(2):1766–1778, Dec 2009.

[149] D. Nelson Limber. The Analysis of Counts of the Extragalactic Nebulae in Terms of a Fluctuating Density Field. *apj*, 117:134, January 1953.

[150] D. Nelson Limber. The Analysis of Counts of the Extragalactic Nebulae in Terms of a Fluctuating Density Field. II. *apj*, 119:655, May 1954.

[151] A. S. Maniyar, M. Béthermin, and G. Lagache. Star formation history from the cosmic infrared background anisotropies. *Astron. Astrophys.*, 614:A39, 2018.

[152] J. Glenn et al. HerMES: Deep Galaxy Number Counts from a P(D) Fluctuation Analysis of SPIRE Science Demonstration Phase Observations. *Mon. Not. Roy. Astron. Soc.*, 409:109, 2010.

[153] Matthieu Béthermin, Emanuele Daddi, Georgios Magdis, Mark T. Sargent, Yashar Hezaveh, David Elbaz, Damien Le Borgne, James Mullaney, Maurilio Pannella, Véronique Buat, and et al. A unified empirical model for infrared galaxy counts based on the observed physical evolution of distant galaxies. *The Astrophysical Journal*, 757(2):L23, Sep 2012.

[154] M. Negrello et al. Herschel-ATLAS: deep HST/WFC3 imaging of strongly lensed submillimetre galaxies. *Mon. Not. Roy. Astron. Soc.*, 440(3):1999–2012, 2014.

[155] E. Valiante et al. The Herschel -ATLAS data release 1 – I. Maps, catalogues and number counts. *Mon. Not. Roy. Astron. Soc.*, 462(3):3146–3179, 2016.

[156] Daniel Foreman-Mackey, David W. Hogg, Dustin Lang, and Jonathan Goodman. emcee: The MCMC hammer. *Publications of the Astronomical Society of the Pacific*, 125(925):306–312, mar 2013.

[157] N. Aghanim, S. H. Hansen, and G. Lagache. Trouble for cluster parameter estimation from blind sz surveys? *Astronomy & Astrophysics*, 439(3):901–912, Aug 2005.

[158] John E. Carlstrom, Gilbert P. Holder, and Erik D. Reese. Cosmology with the Sunyaev-Zel'dovich effect. *Ann. Rev. Astron. Astrophys.*, 40:643–680, 2002.

[159] G. Hurier and F. Lacasa. Combined analysis of galaxy cluster number count, thermal sunyaev-zel'dovich power spectrum, and bispectrum. *Astronomy & Astrophysics*, 604:A71, Aug 2017.

[160] Pengjie Zhang and Ue-Li Pen. Deprojecting Sunyaev-Zeldovich Statistics. *apj*, 549(1):18–27, March 2001.

[161] Hy Trac, Paul Bode, and Jeremiah P. Ostriker. Templates for the Sunyaev-Zel'dovich Angular Power Spectrum. *apj*, 727(2):94, February 2011.

[162] J. D. Cohn and Kenji Kadota. Uncertainties in the Sunyaev-Zel'dovich-selected Cluster Angular Power Spectrum. *apj*, 632(1):1–14, October 2005.

[163] Jonathan L. Sievers, Renée A. Hlozek, Michael R. Nolta, Viviana Acquaviva, Graeme E. Addison, Peter A. R. Ade, Paula Aguirre, Mandana Amiri, John William Appel, L. Felipe Barrientos, Elia S. Battistelli, Nick Battaglia, J. Richard Bond, Ben Brown, Bryce Burger, Erminia Calabrese, Jay Chervenak, Devin Crichton, Sudeep Das, Mark J. Devlin, Simon R. Dicker, W. Bertrand Doriese, Joanna Dunkley, Rolando Dünner, Thomas Essinger-Hileman, David Faber, Ryan P. Fisher, Joseph W. Fowler, Patricio Gallardo, Michael S. Gordon, Megan B. Gralla, Amir Hajian, Mark Halpern, Matthew Hasselfield, Carlos Hernández-Monteagudo, J. Colin Hill, Gene C. Hilton, Matt Hilton, Adam D. Hincks, Dave Holtz, Kevin M. Huffenberger, David H. Hughes, John P. Hughes, Leopoldo Infante, Kent D. Irwin, David R. Jacobson, Brittany Johnstone, Jean Baptiste Juin, Madhuri Kaul, Jeff Klein, Arthur Kosowsky, Judy M. Lau, Michele Limon, Yen-Ting Lin, Thibaut Louis, Robert H. Lupton, Tobias A. Marriage, Danica Marsden, Krista Martocci, Phil Mauskopf, Michael McLaren, Felipe Menanteau, Kavilan Moodley, Harvey Moseley, Calvin B. Netterfield, Michael D. Niemack, Lyman A. Page, William A. Page, Lucas Parker, Bruce Partridge, Reed Plimpton, Hernan Quintana, Erik D. Reese, Beth Reid, Felipe Rojas, Neelima Sehgal, Blake D. Sherwin, Benjamin L. Schmitt, David N. Spergel, Suzanne T. Staggs, Omelan Stryzak, Daniel S. Swetz, Eric R. Switzer, Robert Thornton, Hy Trac, Carole Tucker, Masao Uehara, Katerina Visnjic, Ryan Warne, Grant Wilson, Ed Wollack, Yue Zhao, and Caroline Zunckel. The Atacama Cosmology Telescope: cosmological parameters from three seasons of data. *jcap*, 2013(10):060, October 2013.

[164] Boris Bolliet, Barbara Comis, Eiichiro Komatsu, and Juan Francisco Macías-Pérez. Dark energy constraints from the thermal Sunyaev–Zeldovich power spectrum. *Mon. Not. Roy. Astron. Soc.*, 477(4):4957–4967, 2018.

[165] Laura Salvati, Marian Douspis, and Nabila Aghanim. Constraints from thermal sunyaev-zel'dovich cluster counts and power spectrum combined with cmb. *Astronomy & Astrophysics*, 614:A13, Jun 2018.

[166] Jeremy L. Tinker, Brant E. Robertson, Andrey V. Kravtsov, Anatoly Klypin, Michael S. Warren, Gustavo Yepes, and Stefan Gottlöber. The large-scale bias of dark matter halos: Numerical calibration and model tests. *The Astrophysical Journal*, 724(2):878–886, Nov 2010.

[167] E. Komatsu and U. Seljak. The sunyaev-zel'dovich angular power spectrum as a probe of cosmological parameters. *Monthly Notices of the Royal Astronomical Society*, 336(4):1256–1270, Nov 2002.

[168] Daisuke Nagai, Andrey V. Kravtsov, and Alexey Vikhlinin. Effects of Galaxy Formation on Thermodynamics of the Intracluster Medium. *apj*, 668(1):1–14, October 2007.

[169] P. A. R. Ade, N. Aghanim, C. Armitage-Caplan, M. Arnaud, M. Ashdown, F. Atrio-Barandela, J. Aumont, C. Baccigalupi, A. J. Banday, and et al. Planck2013 results. xxi. power spectrum and high-order statistics of theplanckall-sky compton parameter map. *Astronomy & Astrophysics*, 571:A21, Oct 2014.

[170] N. Aghanim et al. Planck 2015 results. XXII. A map of the thermal Sunyaev-Zeldovich effect. *Astron. Astrophys.*, 594:A22, 2016.

[171] Laurie D. Shaw, Douglas H. Rudd, and Daisuke Nagai. Deconstructing the kinetic sz power spectrum. *The Astrophysical Journal*, 756(1):15, Aug 2012.

[172] O. Zahn, C. L. Reichardt, L. Shaw, A. Lidz, K. A. Aird, B. A. Benson, L. E. Bleem, J. E. Carlstrom, C. L. Chang, H. M. Cho, and et al. Cosmic microwave background constraints on the duration and timing of reionization from the south pole telescope. *The Astrophysical Journal*, 756(1):65, Aug 2012.

[173] P. A. R. Ade, N. Aghanim, M. Arnaud, J. Aumont, C. Baccigalupi, A. J. Banday, R. B. Barreiro, J. G. Bartlett, N. Bartolo, and et al. Planck2015 results. *Astronomy & Astrophysics*, 594:A23, Sep 2016.

[174] Graeme E. Addison, Joanna Dunkley, and David N. Spergel. Modelling the correlation between the thermal Sunyaev Zel'dovich effect and the cosmic infrared background. *Mon. Not. Roy. Astron. Soc.*, 427:1741, 2012.

[175] Tom Mauch, T. Murphy, H. J. Buttery, J. Curran, R. W. Hunstead, B. Piestrzynski, J. G. Robertson, and E. M. Sadler. SUMSS: A wide-field

radio imaging survey of the southern sky. 2. The Source catalogue. *Mon. Not. Roy. Astron. Soc.*, 342:1117, 2003.

[176] L. M. Mocanu, T. M. Crawford, J. D. Vieira, K. A. Aird, M. Aravena, J. E. Austermann, B. A. Benson, M. Béthermin, L. E. Bleem, M. Bothwell, and et al. Extragalactic millimeter-wave point-source catalog, number counts and statistics from 771 deg2of the spt-sz survey. *The Astrophysical Journal*, 779(1):61, Nov 2013.

[177] Matthew K. Sharp, Daniel P. Marrone, John E. Carlstrom, Thomas Culverhouse, Christopher Greer, David Hawkins, Ryan Hennessy, Marshall Joy, James W. Lamb, Erik M. Leitch, and et al. A measurement of arcminute anisotropy in the cosmic microwave background with the sunyaev-zel'dovich array. *The Astrophysical Journal*, 713(1):82–89, Mar 2010.

[178] Yen-Ting Lin, Bruce Partridge, J. C. Pober, Khadija El Bouchefry, Sarah Burke, Jonathan Klein, Joseph Coish, and Kevin Huffenberger. Spectral Energy Distribution of Radio Sources in Nearby Clusters of Galaxies: Implications for Sunyaev-Zel'dovich Effect Surveys. *Astrophys. J.*, 694:992–1009, 2009.

[179] Neelima Sehgal, Paul Bode, Sudeep Das, Carlos Hernandez-Monteagudo, Kevin Huffenberger, Yen-Ting Lin, Jeremiah P. Ostriker, and Hy Trac. Simulations of the Microwave Sky. *Astrophys. J.*, 709:920–936, 2010.

[180] Sudeep Das et al. The Atacama Cosmology Telescope: temperature and gravitational lensing power spectrum measurements from three seasons of data. *JCAP*, 04:014, 2014.

[181] John E. Ruhl et al. The South Pole Telescope. *Proc. SPIE Int. Soc. Opt. Eng.*, 5498:11, 2004.

[182] J. E. Carlstrom et al. The 10 Meter South Pole Telescope. *Publ. Astron. Soc. Pac.*, 123:568–581, 2011.

[183] S. Padin, Z. Staniszewski, R. Keisler, M. Joy, A. A. Stark, P. A. R. Ade, K. A. Aird, B. A. Benson, L. E. Bleem, J. E. Carlstrom, C. L. Chang, T. M. Crawford, A. T. Crites, M. A. Dobbs, N. W. Halverson, S. Heimsath, R. E. Hills, W. L. Holzapfel, C. Lawrie, A. T. Lee, E. M. Leitch, J. Leong, W. Lu, M. Lueker, J. J. McMahon, S. S. Meyer, J. J. Mohr, T. E. Montroy, T. Plagge, C. Pryke, J. E. Ruhl, K. K. Schaffer, E. Shirokoff, H. G. Spieler,

and J. D. Vieira. South Pole Telescope optics. *ao*, 47(24):4418–4428, August 2008.

[184] Erik Shirokoff, Bradford A. Benson, Lindsey E. Bleem, Clarence L. Chang, Hsiao-Mei Cho, Abigail T. Crites, Matt A. Dobbs, William L. Holzapfel, Trevor Lanting, Adrian T. Lee, Martin Lueker, Jared Mehl, Thomas Plagge, Helmuth G. Spieler, and Joaquin D. Vieira. The South Pole Telescope SZ-Receiver Detectors. *IEEE Transactions on Applied Superconductivity*, 19(3):517–519, June 2009.

[185] P. A. R. Ade et al. Planck 2013 results. XV. CMB power spectra and likelihood. *Astron. Astrophys.*, 571:A15, 2014.

[186] E. Hivon, K. M. Gorski, C. B. Netterfield, B. P. Crill, S. Prunet, and F. Hansen. Master of the cosmic microwave background anisotropy power spectrum: a fast method for statistical analysis of large and complex cosmic microwave background data sets. *Astrophys. J.*, 567:2, 2002.

[187] Gianluca Polenta, D. Marinucci, A. Balbi, P. de Bernardis, E. Hivon, S. Masi, P. Natoli, and N. Vittorio. Unbiased estimation of angular power spectrum. *JCAP*, 11:001, 2005.

[188] M. Tristram, J. F. Macias-Perez, C. Renault, and D. Santos. Xspect, estimation of the angular power spectrum by computing cross power spectra. *Mon. Not. Roy. Astron. Soc.*, 358:833, 2005.

[189] Jesus Torrado and Antony Lewis. Cobaya: Code for Bayesian Analysis of hierarchical physical models. *JCAP*, 05:057, 2021.

[190] Antony Lewis. Efficient sampling of fast and slow cosmological parameters. *Phys. Rev. D*, 87(10):103529, 2013.

[191] G. De Zotti, R. Ricci, D. Mesa, L. Silva, P. Mazzotta, L. Toffolatti, and J. González-Nuevo. Predictions for high-frequency radio surveys of extragalactic sources. *Astronomy & Astrophysics*, 431(3):893–903, Feb 2005.

[192] C. L. Reichardt, L. Shaw, O. Zahn, K. A. Aird, B. A. Benson, L. E. Bleem, J. E. Carlstrom, C. L. Chang, H. M. Cho, T. M. Crawford, and et al. A measurement of secondary cosmic microwave background anisotropies with two years of south pole telescope observations. *The Astrophysical Journal*, 755(1):70, Jul 2012.

[193] Liang Gao, Simon D. M. White, Adrian Jenkins, Felix Stoehr, and Volker Springel. The Subhalo populations of lambda-CDM dark halos. *Mon. Not. Roy. Astron. Soc.*, 355:819, 2004.

[194] Sarah M. Hansen, Erin S. Sheldon, Risa H. Wechsler, and Benjamin P. Koester. The Galaxy Content of SDSS Clusters and Groups. *Astrophys. J.*, 699:1333–1353, 2009.

[195] C. L. Reichardt et al. An Improved Measurement of the Secondary Cosmic Microwave Background Anisotropies from the SPT-SZ + SPTpol Surveys. *Astrophys. J.*, 908(2):199, 2021.

[196] P. A. R. Ade et al. Planck 2013 results. XX. Cosmology from Sunyaev–Zeldovich cluster counts. *Astron. Astrophys.*, 571:A20, 2014.

[197] Jun-Qing Xia, M. Negrello, A. Lapi, G. De Zotti, L. Danese, and M. Viel. Clustering of sub-millimeter galaxies in a self-regulated baryon collapse model. *Mon. Not. Roy. Astron. Soc.*, 422:1324–1331, 2012.

[198] P. A. R. Ade et al. Planck 2013 results. XXX. Cosmic infrared background measurements and implications for star formation. *Astron. Astrophys.*, 571:A30, 2014.

[199] M. P. Viero et al. Measurements of the Cross Spectra of the Cosmic Infrared and Microwave Backgrounds from 95 to 1200 GHz. *Astrophys. J.*, 881(2):96, 2019.

[200] G. L. Pilbratt, J. R. Riedinger, T. Passvogel, G. Crone, D. Doyle, U. Gageur, A. M. Heras, C. Jewell, L. Metcalfe, S. Ott, and et al. Herschelspace observatory. *Astronomy and Astrophysics*, 518:L1, Jul 2010.

[201] G. P. Holder et al. A Cosmic Microwave Background Lensing Mass Map and Its Correlation with the Cosmic Infrared Background. *Astrophys. J. Lett.*, 771:L16, 2013.

[202] L. Levenson, G. Marsden, M. Zemcov, A. Amblard, A. Blain, J. Bock, E. Chapin, A. Conley, A. Cooray, C. D. Dowell, and et al. Hermes: Spire science demonstration phase maps. *Monthly Notices of the Royal Astronomical Society*, 409(1):83–91, Oct 2010.

[203] D. Hanson et al. Detection of B-mode Polarization in the Cosmic Microwave Background with Data from the South Pole Telescope. *Phys. Rev. Lett.*, 111(14):141301, 2013.

[204] G. J. Bendo et al. Flux calibration of the Herschel-SPIRE photometer. *Mon. Not. Roy. Astron. Soc.*, 433:3062–3078, 2013.

[205] M. J. Griffin, A. Abergel, A. Abreu, P. A. R. Ade, P. André, J. L. Augueres, T. Babbedge, Y. Bae, T. Baillie, J. P. Baluteau, M. J. Barlow, G. Bendo, D. Benielli, J. J. Bock, P. Bonhomme, D. Brisbin, C. Brockley-Blatt, M. Caldwell, C. Cara, N. Castro-Rodriguez, R. Cerulli, P. Chanial, S. Chen, E. Clark, D. L. Clements, L. Clerc, J. Coker, D. Communal, L. Conversi, P. Cox, D. Crumb, C. Cunningham, F. Daly, G. R. Davis, P. de Antoni, J. Delderfield, N. Devin, A. di Giorgio, I. Didschuns, K. Dohlen, M. Donati, A. Dowell, C. D. Dowell, L. Duband, L. Dumaye, R. J. Emery, M. Ferlet, D. Ferrand, J. Fontignie, M. Fox, A. Franceschini, M. Frerking, T. Fulton, J. Garcia, R. Gastaud, W. K. Gear, J. Glenn, A. Goizel, D. K. Griffin, T. Grundy, S. Guest, L. Guillemet, P. C. Hargrave, M. Harwit, P. Hastings, E. Hatziminaoglou, M. Herman, B. Hinde, V. Hristov, M. Huang, P. Imhof, K. J. Isaak, U. Israelsson, R. J. Ivison, D. Jennings, B. Kiernan, K. J. King, A. E. Lange, W. Latter, G. Laurent, P. Laurent, S. J. Leeks, E. Lellouch, L. Levenson, B. Li, J. Li, J. Lilienthal, T. Lim, S. J. Liu, N. Lu, S. Madden, G. Mainetti, P. Marliani, D. McKay, K. Mercier, S. Molinari, H. Morris, H. Moseley, J. Mulder, M. Mur, D. A. Naylor, H. Nguyen, B. O'Halloran, S. Oliver, G. Olofsson, H. G. Olofsson, R. Orfei, M. J. Page, I. Pain, P. Panuzzo, A. Papageorgiou, G. Parks, P. Parr-Burman, A. Pearce, C. Pearson, I. Pérez-Fournon, F. Pinsard, G. Pisano, J. Podosek, M. Pohlen, E. T. Polehampton, D. Pouliquen, D. Rigopoulou, D. Rizzo, I. G. Roseboom, H. Roussel, M. Rowan-Robinson, B. Rownd, P. Saraceno, M. Sauvage, R. Savage, G. Savini, E. Sawyer, C. Scharmberg, D. Schmitt, N. Schneider, B. Schulz, A. Schwartz, R. Shafer, D. L. Shupe, B. Sibthorpe, S. Sidher, A. Smith, A. J. Smith, D. Smith, L. Spencer, B. Stobie, R. Sudiwala, K. Sukhatme, C. Surace, J. A. Stevens, B. M. Swinyard, M. Trichas, T. Tourette, H. Triou, S. Tseng, C. Tucker, A. Turner, M. Vaccari, I. Valtchanov, L. Vigroux, E. Virique, G. Voellmer, H. Walker, R. Ward, T. Waskett, M. Weilert, R. Wesson, G. J. White, N. Whitehouse, C. D. Wilson, B. Winter, A. L. Woodcraft, G. S. Wright, C. K. Xu, A. Zavagno, M. Zemcov, L. Zhang, and E. Zonca. The Herschel-SPIRE instrument and its in-flight performance. *aap*, 518:L3, July 2010.

[206] P. A. R. Ade et al. Planck Early Results XVIII: The power spectrum of cosmic infrared background anisotropies. *Astron. Astrophys.*, 536:A18, 2011.

[207] Matthieu Bethermin, Hao-Yi Wu, Guilaine Lagache, Iary Davidzon, Nicolas Ponthieu, Morgane Cousin, Lingyu Wang, Olivier Dore, Emanuele Daddi, and Andrea Lapi. The impact of clustering and angular resolution on far-infrared and millimeter continuum observations. *Astron. Astrophys.*, 607:A89, 2017.

[208] M. Hazumi et al. LiteBIRD: A Satellite for the Studies of B-Mode Polarization and Inflation from Cosmic Background Radiation Detection. *J. Low Temp. Phys.*, 194(5-6):443–452, 2019.

[209] Kevork N. Abazajian et al. CMB-S4 Science Book, First Edition. 10 2016.

[210] Maximilian H. Abitbol et al. CMB-S4 Technology Book, First Edition. 6 2017.

[211] José Fonseca, Marta Silva, Mário G. Santos, and Asantha Cooray. Cosmology with intensity mapping techniques using atomic and molecular lines. *Mon. Not. Roy. Astron. Soc.*, 464(2):1948–1965, 2017.

[212] Wayne Hu, Douglas Scott, and Joseph Silk. Reionization and cosmic microwave background distortions: A Complete treatment of second order Compton scattering. *Phys. Rev. D*, 49:648–670, 1994.

[213] Naoshi Sugiyama, Joseph Silk, and Nicola Vittorio. Reionization and cosmic microwave anisotropies. *Astrophys. J. Lett.*, 419:L1, 1993.

[214] Intensity mapping of the [c ii] fine structure line during the epoch of reionization. 745(1).

[215] V. K. Khersonskii, A. N. Moskalev, and D. A. Varshalovich. *Quantum Theory Of Angular Momentum.* World Scientific Publishing Company, 1988.